Dissertation zur Erlangung des Doktorgrades

der Fakultät für Chemie und Pharmazie

der Ludwig-Maximilians-Universität München

Ionothermal Synthesis Opening New Avenues towards Highly Crystalline Carbon Nitrides for Artificial Photosynthesis

Hendrik Schlomberg

aus

Oberhausen, Deutschland

2021

Erklärung

Diese Dissertation wurde im Sinne von § 7 der Promotionsordnung vom 28. November 2011 von Frau Prof. Dr. Bettina V. Lotsch betreut.

Eidesstattliche Versicherung

Diese Dissertation wurde eigenständig und ohne unerlaubte Hilfe erarbeitet.

München, 28.09.2021

Hendrik Schlomberg

Dissertation eingereicht am	01.10.2021
1. Gutachterin:	Prof. Dr. Bettina V. Lotsch
2. Gutachter:	Prof. Dr. Konstantin Karaghiosoff
Mündliche Prüfung am	15.11.2021

Danksagung

Mein besonderer Dank gilt meiner Doktormutter Frau Prof. Bettina Lotsch. Sie hat mir das Privileg eröffnet, getrieben von der eigenen Neugier, ein sehr interessantes und vielfältiges Themengebiet im Rahmen meiner Doktorarbeit zu erforschen. Dabei war ihr großes Detailwissen und Gespür für die richtigen Fragen immer eine große Hilfe. Ohne diese Impulse hätte diese Arbeit nicht werden können, was sie ist.

Ebenso danke ich Herrn Prof. Konstantin Karaghiosoff für die Übernahme der Zweitbegutachtung dieser Arbeit. Darüber hinaus für die immer offene und interessierte Art, wenn man mit Fragen zu ihm kam.

Ich möchte auch Frau Prof. Lena Daumann, Frau Prof. Ivanović-Burmazović, Herrn Prof. Wolfgang Schnick und Herrn Prof. Joost Wintterlin meinen Dank aussprechen, für ihr Interesse an meiner Arbeit und ihre Bereitschaft Teil meines Prüfungskomitees zu sein.

Des Weiteren möchte ich mich bei all meinen Koautoren und Kooperationspartnern bedanken, die mich mit ihrem Wissen, Ideen und kritischen Fragen unterstützt haben. Insbesondere möchte ich Maxwell Terban und Sebastian Bette hervorheben, die mich mit ihrer lösungsorientierten und gelassenen Art nachhaltig beeindruckt haben. An dieser Stelle möchte ich auch der kleinen CN-subgroup Julia Kröger, Filip Podjaski, Andreas Gouder und Florian Binder danken für die Kooperationen, hilfreichen Diskussionen und die freundliche Aufnahme bei Stuttgart-Aufenthalten. Außerdem bedanke ich mich herzlich bei meinen Praktikanten Sabrina Hampel, Sonja Rieth, Simon Wanninger, Maximilian Halbauer und Carina Schmitt, die mich auf dem Weg zu dieser Doktorarbeit tatkräftig unterstützt haben.

Danke an alle Kolleginnen und Kollegen aus dem AK Lotsch in München und Stuttgart (natürlich auch die Ehemaligen!) für die angenehme und sehr harmonische Arbeitsatmosphäre, die große Hilfsbereitschaft, die Ausflüge (pre-Corona), die Mittagessen und Fachdiskussionen. Ihr wart die Jahre über eine sehr inspirierende Umgebung und ich konnte so auch viel über andere Themengebiete abseits der CN-Chemie lernen. Speziell möchte ich den anderen beiden Mitgliedern des Großhaderner Gitarrentrios, Leo Diehl und Sascha Harm, danken: Eure stets offene, interessierte und wertschätzende Art habe ich als sehr wertvoll empfunden. Dir, Leo nicht zuletzt auch für deine hilfreichen Kommentare beim Korrekturlesen.
Ein Dank geht auch an das Stuttgarter Büro Viola Duppel, Claudia Kamella und Roland Eger für die herzliche Aufnahme bei Dienstreisen. Claudia Kamella und Sigrid Fuhrmann danke ich auch für ihre Hilfe bei administrativen Angelegenheiten. Wertschätzen möchte ich auch die vielen anderen Mitarbeiterinnen und Mitarbeiter am MPI, die sich durch ihre Hilfsbereitschaft bei allerlei Messungen, Verwaltungsangelegenheiten oder Spezialanfertigungen ausgezeichnet haben.

Außerdem möchte ich mich bei den beiden Arbeitskreisen Schnick und Johrendt bedanken; für die kollegiale Zusammenarbeit, gemeinsame Ausflüge und Feiern, die unkomplizierte Hilfe untereinander und natürlich auch für die Möglichkeit Infrastruktur mitzubenutzen.

Apropos Geräte: ein herzliches Dankeschön an die Festangestellten Dr. Brigitte Breitenstein, Dr. Markus Döblinger, Susanne Ebert, Robert Eicher, Michi Gayer, Christian Minke, Dr. Peter Mayer, Christine Neumann, Jarka Obel, Dieter Rau und Wolfgang Wünschheim, die mich mit zahlreichen Messungen versorgt, oder auf anderen Wegen unterstützt haben. Danke auch an Susanne Hennig und das CeNS-Team für die Organisation der zahlreichen kurzweiligen Events und Workshops und die gelungene Vernetzung mit anderen Arbeitsgruppen.

Auch meinen Freunden aus dem Studium bin ich dankbar, dass sie mich auch in stressigen Phasen immer wieder mit netten Aktivitäten wie Kochabenden, „Stammtischen“, Reisen, Wanderungen etc. aus dem Arbeitsalltag entführt haben.

Mein tief empfundener Dank gilt meiner Familie und dir, Laura für die stete, uneingeschränkte Unterstützung und das Vertrauen in meine Fähigkeiten.

Seht ihr den Mond dort stehen? Er ist bloß halb zu sehen, und ist doch rund und schön.
So sind wohl manche Sachen, die wir getrost belachen, weil unsre Augen sie nicht sehn.

Abendlied – Matthias Claudius

Summary 1

1 Introduction 3

1.1 Historic background 5

1.2 Carbon nitride polymers 8

1.3 Photocatalysis 17

1.3.1 Photocatalysis Basics 17

1.3.2 Photocatalysis with carbon nitrides 21

1.3.3 “Dark Photocatalysis” with carbon nitrides 23

1.4 Objectives 25

1.5 References 26

2 Structural Insights into Poly(Heptazine Imides): A Light-Storing Carbon Nitride Material for Dark Photocatalysis 39

2.1 Introduction 39

2.2 Results and Discussion 40

2.3 Conclusions 50

2.4 Experimental Section 51

2.5 Associated Content 51

2.6 Author Information 51

2.7 Acknowledgments 52

2.8 References 53

3 K-CN-Phase – Autogenous pressure influences polymorphism in potassium poly(heptazine imides) affecting “dark photocatalysis” 57

3.1 Introduction 57

3.2 Results and Discussion 58

3.3 Conclusion 73

3.4 Acknowledgments 74

3.5 References 75

4 Ni-CN_x – An ionic carbon nitride storing and converting CO_2 by photothermal catalysis 79

4.1 Introduction 79

4.2 Results 80

4.3 Discussion and conclusion 96

4.4 Acknowledgments 98

4.5 References 99

5 Conclusion and outlook 105
- 5.1 References 109

6 Appendix A 111
- 6.18 References 168

7 Appendix B 171
- 7.1 References 181

8 Appendix C 183
- 8.1 References 192

9 Contributions and publications 194

Summary

Carbon nitrides combine the advantages of a cheap and abundant resource with semi-conducting properties. Although CN-materials could already prove their ability to split water into its elements, they still lack behind in terms of efficiency. Thus, more active variants and structural tuning is highly sought after for the successful implementation as environmentally benign photocatalysts. In this regard, it is vital to understand the structural basis of CN-polymers, which remains a challenging task, owing to their defective and overall low crystallinity. However, new synthetic approaches, utilizing eutectic salt melts, yield more defined CN-compounds and have been studied as part of this thesis. In the end, a thorough characterization is a key requirement for the deduction of structure–property–relationships.

In chapter 2, highly crystalline two-dimensional layered potassium poly(heptazine imide) (K-PHI) and the protonated variant (H-PHI) are reported on, based on an ionothermal synthetic approach with molecular precursors. A kaleidoscope of analytical techniques, including transmission electron microscopy and solid-state NMR spectroscopy, supported by quantum-chemical calculations, reveals a planar sheet-like arrangement of heptazine units interconnected via imide bridges with trigonal symmetry. Deeper insights, using PDF analysis and X-ray powder diffraction accompanied by simulations of various stacking scenarios of the PHI layers, suggest that the pore content is governing the structure in the third dimension. K-PHI exhibits a unidirectional layer offset, caused by the hydrated potassium ions within the pores of the PHI backbone. After acidic treatment and hence transformation to H-PHI, this long-range out-of-plane order is mostly lost and replaced by a random stacking sequence, reasoned by the weaker structure-directing influence of pore water opposed to that of potassium ions.

From photocatalytic tests for water splitting, we could derive the beneficial influence of smaller lateral particles sizes and higher amounts of cyanamide terminating groups on the overall activity, thus putting size-optimized H-PHI – with a photocatalytic hydrogen evolution rate of 3363 μmol/gh – on par with the most active carbon nitrides. Furthermore, K-PHI as well as H-PHI can reversibly be photoexcited in the presence of an electron donor, storing radiative energy in the form of a photoreduced state, which is stable for more than 6 h in the dark. The light-induced electrons can be further used to drive water reduction upon addition of a platinum cocatalyst. This chapter underlines the need for careful structural characterization in order to derive structure–property–relationships, and hence rationally improve a photocatalyst, such as K-PHI.

Sticking closely with the synthetic scheme as presented for K-PHI, in chapter 3, a change in reaction pressure led to the formation of the K-CN-phase, presenting a new member to the carbon nitride family. By combining pair distribution function analysis, solid-state NMR and infrared spectroscopy, we could identify a linearly arranged polymer, constituted of imide-bridged heptazine units. X-ray powder and electron diffraction techniques further revealed a close relationship to the prototypical carbon nitride polymer melon. In contrast to melon however, the imide-bridges are negatively charged and balanced by potassium cations in between the 1D polymeric strands. While the structure-directing influence of potassium ions results in a highly

crystalline material, the linear structural motifs with intercalated potassium ions render the identification of the stacking arrangement more difficult, as evidenced by an irregular intensity modulation for higher correlation distances in the PDF analysis. Analogous to K/H-PHI, the K-CN-phase can be protonated under mild acidic conditions, thus yielding a polymer deprived of alkali cations, which goes hand in hand with a loss of crystallinity. Indeed, the H-CN-phase features the spectroscopic imprint of a melon-type polymer. By means of this comparison and in combination with the findings in chapter 2, the universality of the structure-directing influence of potassium could be confirmed in another system. This investigation highlights the delicate equilibria, which are present in salt melt assisted carbon nitride syntheses and the importance of a close monitoring of reaction parameters to discover new crystalline materials.

Both the K-CN-phase as well as its protonated counterpart are active for photocatalytic hydrogen evolution, yet compared to K-PHI/H-PHI, with lower rates. Nevertheless, this study could corroborate the trend of higher activity for the protonated form, hinting at the necessity of relatively loosely bound H^+-ions for efficient water reduction. In contrast to K/H-PHI, the K/H-CN-phase is not able to adopt a photoreduced state upon irradiation in presence of an electron donor, thus yielding important insights on the necessary conditions responsible for the long-lived state. By combining different cues, we could tentatively identify the 2D arrangement of heptazine units as the likely structural element, accountable for charge storage on K-PHI, and hence the potential to perform dark photocatalysis.

In chapter 4, the concept of alkali salt assisted syntheses for CN-compounds has been transferred to the implementation of the transition metal nickel. Choosing a bottom-up approach with a $NiCl_2$/KCl melt, it was possible to directly incorporate the catalytically active element for CO_2 reduction. X-ray diffraction techniques, transmission electron microscopy and photoelectron spectroscopy reveal a needle-shaped, highly crystalline material with nickel in various oxidation states or coordination environments. The downside of the introduction of a paramagnetic nickel species is its detrimental effect on the characterization by solid-state NMR spectroscopy, thus aggravating the identification of CN-building blocks. Pair distribution function analysis hints at a triazine-based compound. However, while some evidence supports the presence of a polymeric triazine-based form, other factors point towards the existence of a molecular crystal. Thus, the final structural assessment remains partially elusive, but may be revisited once better crystals for single-crystal X-ray analysis can be obtained.

Nevertheless, the atomically dispersed nickel centers are active for the selective CO_2 reduction to CO in a photothermal setup. In this concept, driving the reaction relies both on resistive heating as well as local heating, induced by light irradiation. Ni-CN_x features a broad absorption profile over the visible light range, thus utilizing a substantial portion of incident sunlight. Despite the carbon nitride backbone primarily acting as a support for active nickel centers, its property to capture CO_2 by basic amino groups and its subsequent release, makes this catalyst suitable for temporally decoupling the substrate adsorption from the conversion.

1 Introduction

It does not take a genius to predict that the world will fundamentally have to change its way of producing energy to live up to the current and, especially, future demand. The necessity for renewable alternatives becomes apparent. Yet thinking of renewable energies, one has also to consider that for instance solar power is not constantly available and does not overlap with the consumption curve in the best way possible. Typically, in the morning and evening, when more power is needed, the incident solar irradiation is lowest. In turn, this imbalance leads to a drop in demand for other sources during times, when renewables energies are produced the most. This effect is especially pronounced for photovoltaics and leads to a shape of the demand curve resembling a duck (Figure 1.1).[1,2] Although it is undoubtedly a good idea to use sunlight whenever possible, the so called "duck curve" can cause severe problems: The more energy is provided by sunlight during midday, the steeper the conventional power plants have to ramp up their generators in the evenings, which is bound to technical limitations for many power plants. Strong fluctuations can also cause damage to the energy grid itself. In addition, coal and nuclear power plants only work efficient at a constant output, so that ironically an increase of renewable power can inadvertently lead to an increase in fossil fuel consumption.[1]

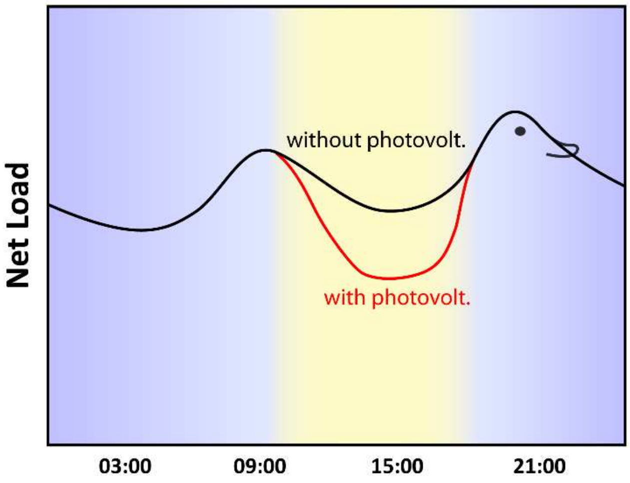

Figure 1.1. So called "duck curve" showing the mismatch of the demand and the solar power output during the day, thus forming a drop in demand for the energy grid.

Of course, these considerations should not offer any excuse to rely on the old ways, but rather encourage to follow a holistic approach to the global challenge. The future of energy generation, transportation and consumption will certainly be guided by multiple different channels. Those will not only include various ways of sustainable energy production – and a little counterintuitive, also new ideas to consume energy – but importantly, also means of intermediate and long-term storage of the harvested energy. One practical way to store energy for longer periods of time presents itself in the form of chemical bonds. Ultimately, the herein examined carbon nitrides may advance to cheap, earth-abundant, non-toxic and chemically stable materials for artificial photosynthesis, i.e. directly splitting water with sunlight into the universal energy carrier, hydrogen.[3,4] A great advantage of carbon nitrides comes with the fact that their precursors are geopolitically and environmentally more benign compared to other resources (i.e. noble metals). Hence, they are potentially interesting for poorer countries as well, which will be a key requirement in a globally concerted effort to mitigate climate change.[5]

The course being set, this dissertation is dedicated to the exploration of new carbon nitride materials obtained from a salt melt assisted synthetic route. The major guiding principle will be the detailed characterization of polymeric carbon nitrides, which in turn will lay the groundwork for a better understanding on a structural level and the ensuing fascinating properties. Within the scope of fundamental research, this work strives to add a puzzle piece on the journey towards sustainable energy generation.

1.1 Historic background

Figure 1.2 Pharao's serpent, pyrolysis of $Hg(SCN)_2$ under the fume hood.

Given the long-standing tradition of carbon nitride chemistry, it only seems reasonable to begin this thesis with a brief historic outline. In the early 19th century, the Swedish chemist *J. J. Berzelius* reported on a compound that was formed upon ignition of mercury(II) thiocyanate, also known as the pharao's serpent (Figure 1.2).[6,7] The self-propagating reaction lead to a carbon nitride decorated with mercury sulfide, which emerges like a snake from the ignited powder and was an attraction at fairs, though a poisonous one. Although Berzelius being the first to synthesize the carbon nitride compound, his contemporary chemist *J. v. Liebig* obtained this material with less impurities (i.e. HgS) by pyrolysis of $NH_4(SCN)$.[8] He was also the one to systematically report on various precursors, intermediates and byproducts (cyanamide, melamine, melam, melem, ammeline, ammelide; Scheme 1.1) that lead to *Berzelius'* compound, which he arbitrarily – neither from color nor property[8] – named melon and has become the most famous representative of this C/N/H-containing class of material. Since in those days systematic nomenclature has not yet been uniformly followed, it must be doubted whether he gauged how many undergraduate students would end up with images of ripe fruits upon their literature research via *Google*. Although it is fascinating what scientist could already apprehend with the limited available analytical techniques, the structural investigations of many of these compounds had to wait until the first half of the 20th century, when the crystal structures of cyanuric acid[9] and melamine[10] were the first carbon nitrides identified by diffraction techniques.

At the times there was ongoing discussion about what the structure of the larger carbon nitride molecules could look like.[11] After various initial descriptions, primarily based on chemical

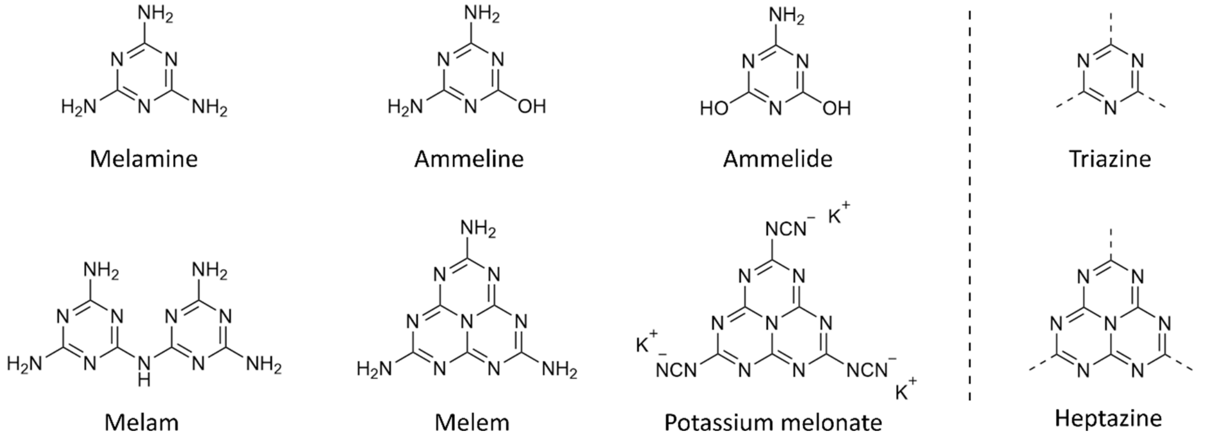

Scheme 1.1. Left: "*Liebig's* molecules": melamine, melam, melem, ammeline, ammelide, and "*Gmelin's*" potassium hydromelonate (more commonly known as potassium melonate). Right: s-triazine and heptazine (tri-s-triazine) nucleus, respectively.

composition analysis,[12] *L. Pauling* and *J. H. Sturdivant* applied quantum-chemical calculations (“molecular-orbital method”) leading to the correct model for the cyameluric nucleus (tri-*s*-triazine/heptazine) depicted in Scheme 1.1, which is still valid today.[13] The structural “blind spot” for larger CN-compounds is most probably related to the general low solubility of carbon nitrides and their relatively bad crystallinity. This dilemma – we shall see – is hitherto still one of the biggest impediments for researchers in the field.

In the second half of the 20th century it became quieter around carbon nitrides. As with many aspects of life, different areas of chemistry are subject to intervals of higher and lower interest of the research communities. However, when a prediction about an intriguing property is made, a drastic increase of scientific research in the corresponding field is often observed. For carbon nitride chemistry three major turning points can be identified, which significantly influenced the advancements in the field.

First, when *Liu* and *Cohen* predicted that hypothetical, three dimensional β-C_3N_4 (Figure 1.3) could potentially be harder or at least comparable to the bulk modulus of diamond (~443 GPa), the field of carbon nitride chemistry had been revived and researchers worldwide have worked with zeal towards this potential material.[15,16] The predicted material contains carbon and nitrogen atoms in a sp^3 hybridized arrangement, crystallizing isotypically to β-Si_3N_4 in a hexagonal space group ($P6_3/m$).[16,17] In the 1990s and early 2000s numerous researchers[18] jumped onto the train for the quest of ultrahard C_3N_4, leading to a soaring scientific output depicted in Figure 1.3. There have been many attempts to obtain the desired product ranging from high-temperature pyrolysis of nitrogen-rich precursors,[19–21] high-pressure (diamond anvil cells),[22,23] shockwave compression experiments,[24,25] chemical vapor deposition (CVD),[26] physical vapor deposition (PVD),[27] ion implantation[28,29] to laser ablation techniques[30]. Despite the theoretically calculated thermodynamic stability (or at least meta-stability) of binary CN-phases[31] and the promising attempts that have been made, until today no ultra-hard CN-material could be obtained in satisfactory quality and quantity. Although the successful synthesis of the desired materials has

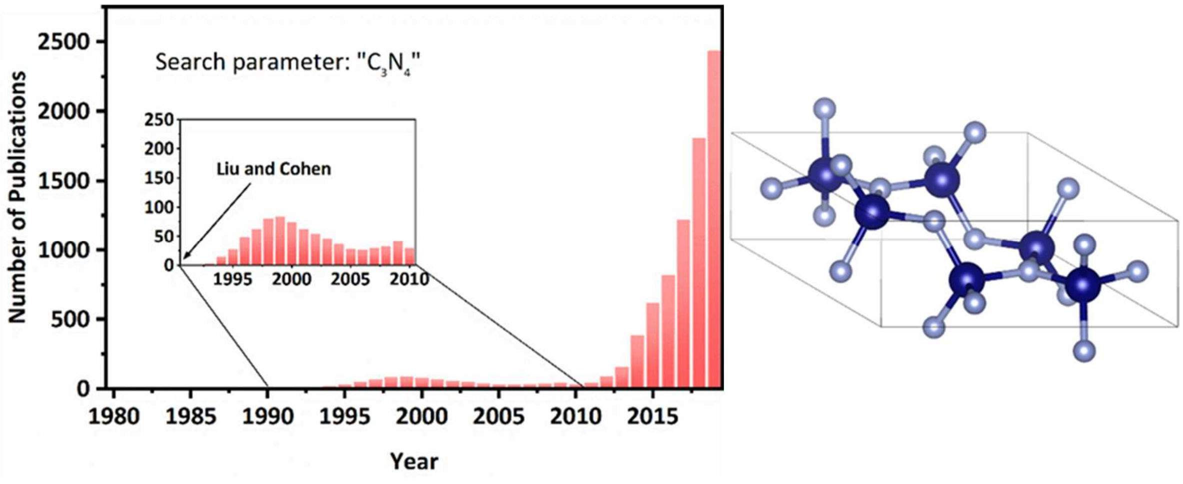

Figure 1.3. (a) Number of publications obtained from online search in Web of Science™ Database with search parameter: “C_3N_4”. Note, that the strong increase from 2010 on is due to increasing use of the term g-C_3N_4 as a synonym for largely amorphous CN-materials. (b) Crystal structure of β-Si_3N_4,[14] which is isotypical to sp^3 bonded β-C_3N_4; silicon and nitrogen atoms depicted as dark blue spheres and light blue spheres, respectively.

often been claimed, the majority of these studies resulted in amorphous materials with ill-defined composition (high heterogeneity) or very small crystalline domains, embedded in an amorphous matrix.[23,30,32] Fortunately, these developments not only served the quest for the ultra-hard material, but also lead to valuable insights and a drastically increased base of knowledge on carbon nitride polymers, which reframed the research focus at the turn of the millennium. In contrast to the more molecular oriented research of the second half of the 20th century, the engagement in polymeric carbon nitrides culminated in the second more recent disruption, in the field of photocatalysis.

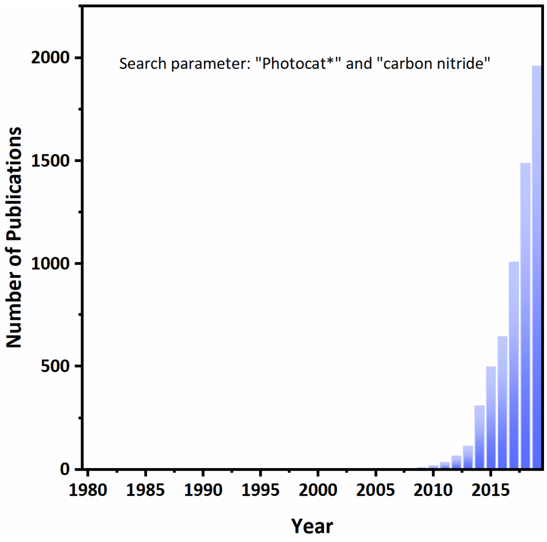

Figure 1.4. Number of publications obtained from online search in Web of Science™ Database with search parameter: "Photocat*" and "carbon nitride".

This branch of material chemistry is not new by any means, but in 2009 *Wang et al.* discovered that polymeric carbon nitrides exhibit a band gap, thus rendering them applicable for photocatalysis; i.e. the splitting of water into hydrogen and oxygen.[33] Mostly the fact that carbon nitrides are metal-free made this finding particularly interesting. CN-materials therefore do not rely on rare, expensive and potentially toxic transition metal elements nor higher homologues of main group elements as is the case for many other photocatalysts.[34–38] Furthermore, the material is also visible light active, hence exploiting sunlight more efficiently than UV-light dependent photocatalysts, such as the "prototype" photocatalytic material TiO_2. The promise of an environmentally and abundant photocatalyst, allowing regenerative fuel production just from sunlight and water raised a lot of attention and spurred research activities exponentially. Figure 1.4 illustrates the huge increase in publications related to the terms "carbon nitride" and "photocat*", reaching over 2000 new publications just in the year 2019.

The third important development – and most influential for this work – is the renewed effort of applying salt melts to access carbon nitride polymers. Of course, the concept of ionothermal syntheses is not new within the field of carbon nitride chemistry – only to mention the synthesis of potassium melonate by *Gmelin* nearly 200 years ago[39] –, but only in recent years the thorough investigations of the resulting polymeric type carbon nitrides, that can be isolated from these reactions, have been pushed forward. Hence, the novel two-dimensional carbon nitrides such as poly(triazine imide), PTI · LiCl,[40–42] poly(heptazine imide) (PHI) and anionic polymeric species compensated by various cations[43–46] could be added to the pool of polymeric structures and will be further discussed in the ensuing chapter.

1.2 Carbon nitride polymers

In this chapter the synthesis and structure of several important carbon nitride polymers are highlighted in terms of their structure and synthetic accessibility. As was alluded to in the previous chapter, the main synthetic approaches involve high-temperature pyrolysis reactions of nitrogen-rich precursors. Scheme 1.2 illustrates two potential mechanisms by *May*[47] and *Hosmane et al.*[48,49] on how the typical tri-*s*-triazine unit (melem) is formed during the pyrolysis of precursors such as dicyandiamide (DCDA) and melamine, respectively. Owing to the relatively high polarity of the CN bond in cyano-groups, it is likely that an nucleophilic attack occurs at this position with a subsequent release of ammonia.[50] Further extensive investigations on the reactivity of various other carbon nitride precursors such as guanylurea dicyanamide,[51] tricyanomelaminates,[52] ammonium cyanoureate[53] and ammonium dicyanamide[54] have been conducted by *Lotsch* and co-workers. They interestingly disclosed that in all investigated precursor systems, the formation of melamine is thermodynamically favorable and therefore represents an inevitable intermediate towards higher condensed structures.[55] Hence, it may be assumed that the choice of precursor rather influences the type and amount of the released side products such as ammonia, water, etc., than directly affecting the structure of the finally formed CN-polymers (i.e. dimensionality., triazine vs. heptazine, elemental composition). In turn, the released side products play an important role in closed reaction vessels, in which usually the occurring back reaction leads to smaller condensation fragments.

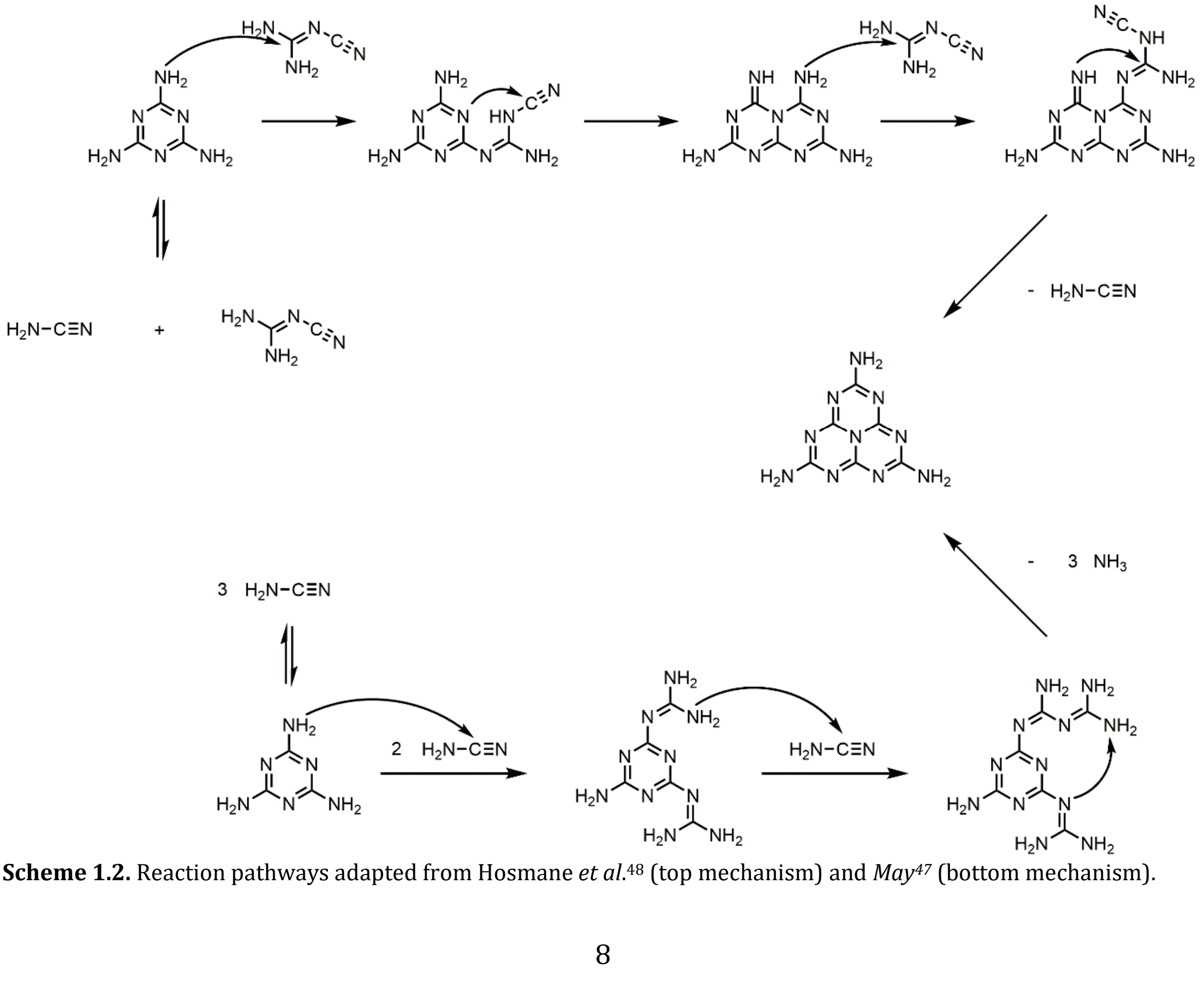

Scheme 1.2. Reaction pathways adapted from Hosmane *et al.*[48] (top mechanism) and *May*[47] (bottom mechanism).

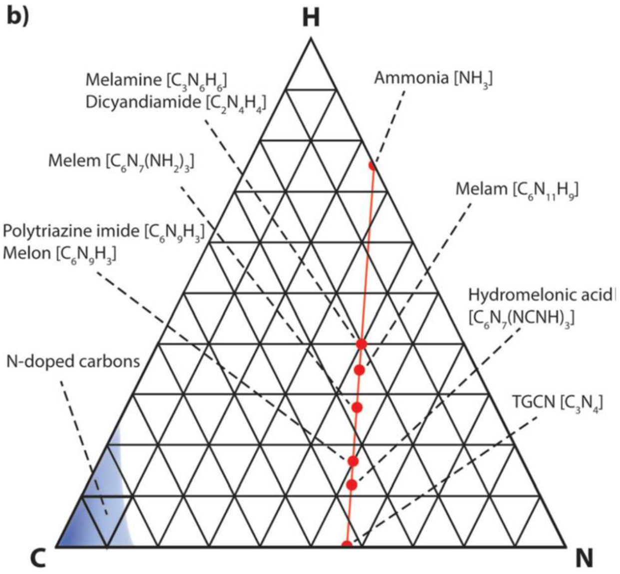

Figure 1.5. Ternary phase diagram for C/N/H. - Reproduced from Ref. https://doi.org/10.1039/C7CP02711G with permission from the PCCP Owner Societies.

Typically, carbon nitride precursors (i.e. dicyandiamide, melamine, urea, thiourea, ammonium thiocyanate, cyanamide and others) share the similarity that they contain preformed C-N or N-H bonds. In recent studies, *Savateev et al.*[56,57] extended this dogma by applying 5-aminotetrazole in CN-chemistry, which additionally features N-N-bonds. Admittedly, at the relevant temperatures for carbon nitride condensation (350-600 °C),[4] the preformed dinitrogen molecule within 5-aminotetrazole is released, which may act as a thermodynamic driving force for the subsequent polymerization.[58] In a similar fashion carbon disulfide is released from sulfur containing precursors (i.e. ammonium thiocyanate), although this process already occurs at lower temperatures of 180 °C.[59]

In general, the “phase corridor” in the ternary phase diagram for C/N/H compounds is fairly narrow as indicated by the red line in Figure 1.5, on which common carbon nitrides are allocated. The line from ammonia to the other extreme triazine-based carbon nitride (TGCN)[60] follows generally speaking a process of deammoniation. On the axis between carbon and nitrogen, the nitrogen-richest molecular carbon nitride is tri-azido-triazine (C_3N_{12}) while the other end is dominated by N-doped carbons and molecules such as nitrogen-containing fullerenes, respectively.[50,61] There are only few examples like tricyanoamine and dicyano-carbodiimide featuring neat C_3N_4 stoichiometry with carbon in oxidation state IV. But even these have only been observed as reactive intermediates that could be isolated in a nitrogen matrix.[62] Thus, transformation of these hydrogen-free precursors into the highly sought after polymeric C_3N_4 has not been achieved in a controlled fashion.

In a strict sense, carbon nitrides should be binary compounds consisting solely of carbon and nitrogen. However, the convention to consider compounds with C/N/H as carbon nitrides has gained wide acceptance within the research community. Unfortunately, this inaccuracy – though historically evolved – might have been one reason, why often CN-polymers that contain considerable amounts of hydrogen, are yet called graphitic carbon nitrides (g-C_3N_4), while their true stoichiometry can be rather displayed as $C_6N_9H_3$; de facto *Liebig's* melon (cf. chapter 1). Starting from the prototypical precursor melamine, the condensation to melon follows the cascade depicted in Scheme 1.3 (top). The shown reaction pathway is of course oversimplified in a sense that during the pyrolysis reaction, sensitive equilibria between various intermediates are formed. Depending on the ammonia back pressure and temperature, for instance formations of adduct phases between melamine–melem[63] and melam–melem[64] may be isolated, respectively. Insights gained over the course of this thesis, using isotopically enriched $KS^{13}C^{15}N$, suggest the

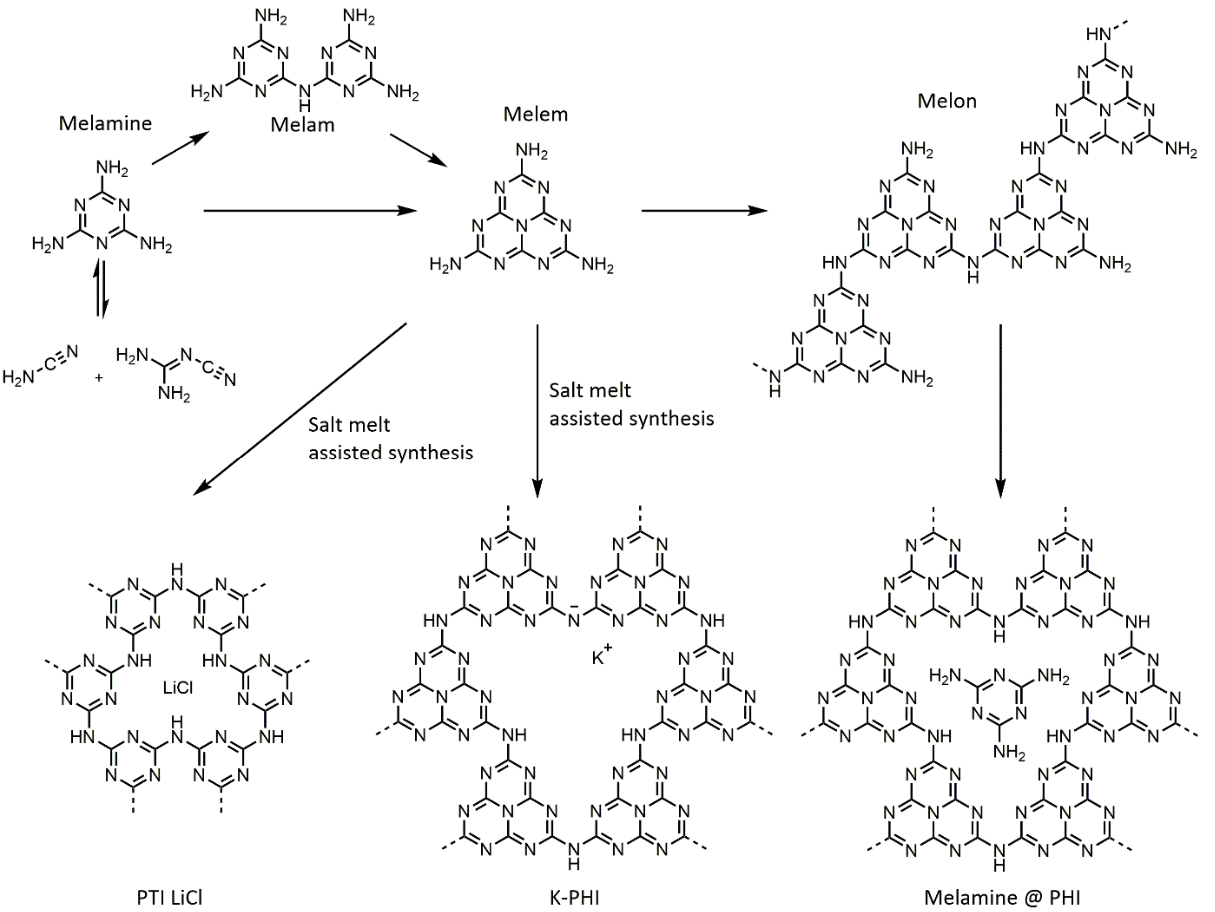

Scheme 1.3. Cascade of reaction for different carbon nitride polymers starting from melamine via melam, melem to melon and finally poly(heptazine imide), PHI with intercalated melamine. Ionothermal conditions lead to poly(triazine imide), PTI with intercalated LiCl or the ionic carbon nitride: potassium poly(heptazine imide), K-PHI.

partial decomposition and reformation of the constituting building blocks (i.e. heptazine) during a typical synthesis at temperatures around 500 °C. Hence, the isotopically labelled atoms are more or less evenly distributed within the carbon nitride polymer.

From the first syntheses in the 1830s, it took nearly 200 years to finally solve the structure of melon by electron diffraction techniques by *Lotsch et al.*[65] in 2007. Of course, considerable previous work has led to this success and in this regard, especially the work of *Komatsu* must be mentioned. He found a semi-crystalline solid synthesized by deammoniation of melon at 700 °C, which he named “cyameluric high polymer” and should, according to mass spectrometry, consists of 42 linearly arranged NH-bridged melem units.[66]

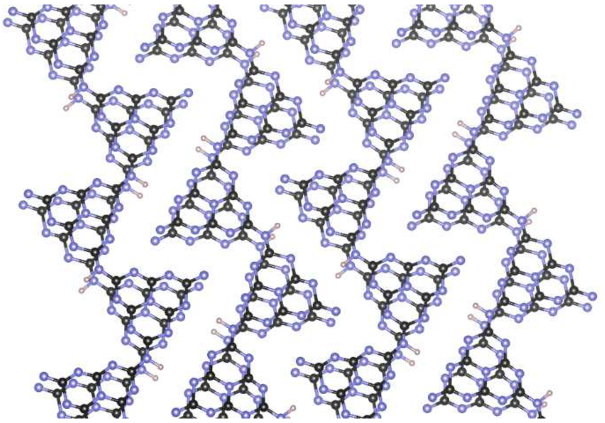

Figure 1.6. Crystal structure of melon, blue spheres are nitrogen atoms, black spheres are carbon atoms, white spheres are hydrogen atoms.

These investigations reveal a major problem, impeding a straightforward structural elucidation: What is called melon, is in truth rather a heterogeneous mixture of phases with respect to the given synthetic conditions. This induces non-conformity in terms of its nanocrystalline character, the variation of molecular weights and also different arrangements of heptazine based microstructures (e.g. strands, oligomers, and potentially even higher condensed structures).[55,67] The ideal structure of melon, as derived from thin crystallites in the electron microscope and complementary solid-state NMR (ssNMR) techniques, is composed of strands of condensed heptazine units forming the polymeric backbone (Figure 1.6). These strands are closely connected via interpolymeric hydrogen bonds between the NH_2-group on one strand and the cyameluric nuclei of the other strand, quasi forming a 2D network.[65] Studying the third dimension of melon is not trivial, because of the lacking long-range order in the crystallographic *c*-direction, resulting in the very broad, so called, stacking reflection observed at approx. 3.2 Å in X-ray powder diffraction patterns (XRPD). 2D solid-state NMR experiments supported by force field calculations suggest that these “layers” are stacked in no particular order, but such that heptazine units are shifted to the zigzag voids of the underlying layer; instead of an eclipsed arrangement. This finding for melon could be corroborated by our investigations for a heptazine based polymer, in detail discussed as part of chapter 2. The π-π interaction and corresponding regular stacking distance of the layers, that is typical for aromatic CN-systems[68,69] and the pseudo two-dimensional backbone owed to the hydrogen bonding, may explain the notorious habit of calling melon type polymers “graphitic carbon nitride”. Fortunately, it seems that awareness has spread and in more recent publications the better suited term polymeric carbon nitride (PCN) is increasingly used.

The example of melon already illustrates the weak point of the structural characterization for polymeric carbon nitrides, both figuratively and literally. The rather weak connectivity in the third dimension is one major reason why it is inherently difficult to grow larger crystals, which could be suited for single-crystal analysis.

Another issue is related to the very low solubility of CN-polymers, preventing access to highly crystalline and phase pure compounds. Typical reactions with open vessels merely yield largely amorphous products, and purification by chromatography or recrystallization are beyond question. One way to circumvent this problem is the use of autoclaves, confining the gaseous species that are formed during reaction, keeping the reaction under autogenous pressure.[64,70,71] So has the pyrolysis of melamine at 630 °C in a closed ampoule led to the formation of cyclic condensed heptazine units – poly(heptazine imide) – with the central pores being intercalated with melamine (Scheme 1.3, bottom right).[72] Note however, that this product could only be obtained as a minute side phase and therefore could only be investigated by electron diffraction.

Nevertheless, this study highlights the importance that the control of pressure has on the synthetic result, which will become an important factor for the discussion of chapter 3.

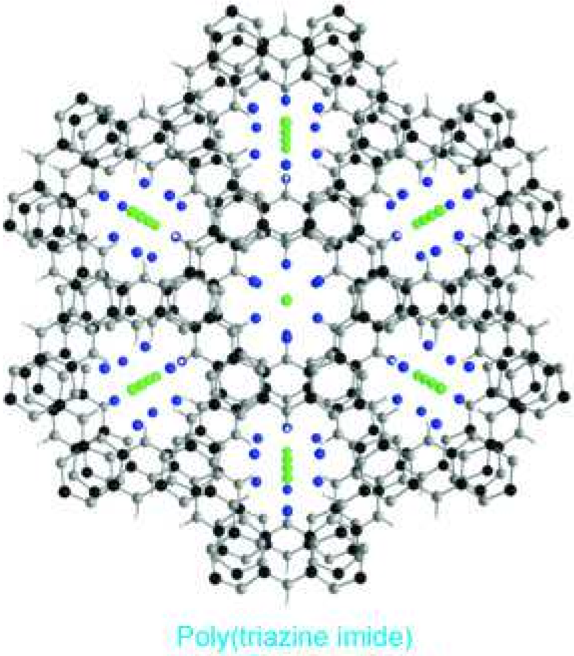

Figure 1.7. Crystal structure of poly(triazine imide) · LiCl; C (black), N (gray), Li (blue) , Cl (green). The blue lithium ions are only occupied by ⅓ for charge neutrality. Reproduced from https://doi.org/10.1002/chem.201002462 with permission of John Wiley and sons.

It is not surprising that the quest for methods allowing for the synthesis of well-defined polymers with long-range order runs like a golden thread through the efforts that have been put forth by numerous scientists. To this end, utilization of salt melts presented a promising pathway to achieve this goal, because of increased solubility of precursors and hence enhanced mass transport during crystallite formation. By this means, *Bojdys et al.* prepared a new crystalline member of CN-polymer family from a mixture of dicyandiamide (DCDA) and an eutectic mixture of LiCl and KCl, which was used to lower the melting point of the salt melt beneath the pyrolysis temperature.[73] The structural model that has been proposed was based on heptazine units forming a fully condensed planar sheet. However, a later reinvestigation by *Wirnhier et al.* employing X-ray powder diffraction and *Rietveld* refinement[74] revealed a triazine based structure composed of six triazine units fused by NH-bridges, forming a cavity in the center.[40] The triazine based layers are stacked in AB-fashion and the thus formed channels incorporate LiCl from the salt melt. The trigonal symmetry is retained by ⅓ occupation of lithium on three equivalent positions around the central chlorine atom, as depicted in Figure 1.7.[40] While the average structure could well be determined by this approach, still nuances of the PTI · LiCl structure have not been fully understood. Additional pair distribution function (PDF) analyses, paired with multidimensional ssNMR techniques, quantum-chemical modelling and automated electron diffraction tomography could show that the positions of protons and lithium atoms, respectively, may differ from pore to pore, and that protons can also be partially be substituted with lithium $[(C_3N_3)_2(NH_xLi_{1-x})_3\cdot LiCl]$, thus reducing the local crystal symmetry ($P2_12_12_1$).[75] The knowledge of these local variations is a key factor, when it comes to rationally improving the properties of carbon nitrides, for instance band gap engineering. The example of PTI · LiCl shows that only the combination of complementary analytical techniques leads to the desired structural elucidation. This extensive approach may serve as a paradigm for the structure determination of carbon nitrides in general, as will be seen for the structural elucidation of potassium poly(heptazine imide) in chapter 2.

When LiBr/KBr was used as eutectic salt mixture, it was found that the same network is formed, with LiBr intercalated as a salt inside the channels.[76] Lithium bromide can also be exchanged for ammonium fluoride, yielding PTI/F.[76] Depending on the ionic radii of the inserted halogens, the gallery height of the PTI layers is increased in the series F < Cl < Br, which is also a key parameter for successful exfoliation of PTI sheets.[77,78] In 2001 even before the synthetic realization of PTI · LiCl, a closely related compound has been discovered by *Wolf et al.* in a pressurized vessel reacting melamine and cyanuric chloride. Instead of the alkali salt, the structure formally contains HCl within the pores.[79] However, the relatively poor crystallinity hampered the structure solution from diffraction data. Additionally, the need for (high) pressures up to 1.5 GPa has probably hampered wide availability within the community.

Figure 1.8. CN-Compounds: potassium melonate (left), amorphous potassium poly(heptazine imide), K-PHI (center) and its protonated counterpart poly(heptazine imide), H-PHI (right).

Inspired by the auspicious results from poly(triazine imide), recently many studies have directed their attention towards the heptazine based analog: poly(heptazine imide). The story of potassium poly(heptazine imide) (K-PHI) impressively tells how a "new light on an old story" eventuates in discoveries of aspects that were either deemed uninteresting at the times or were too intricate to analyze, thus leaving new compounds and their respective properties unexposed. The treatment of melon in a KSCN melt results in a largely amorphous solid and a very crystalline molecular product: potassium melonate (Figure 1.8, left). As stated in the historic introduction, the described reaction has been carried out by *Gmelin* ca. 200 years ago, who was first to isolate potassium melonate,[39] but whose structure could be identified only in recent years (cf. Scheme 1.1).[80,81] However, in the scope of this work, the more important "byproduct" is the deep yellow, insoluble substance, called potassium poly(heptazine imide), K-PHI,[43,44] (Figure 1.8, center) obtained after washing away the potassium melonate and the residual KSCN. There are several other pathways (i.e. using KBr,[82] KCl,[45,83] LiCl/KCl[84–86] and others[87]), that result in the formation of the K-PHI species exhibiting slight variations with respect to the potassium content, functional groups, the level of defects and the stacking arrangement of polymer sheets. It must be noted that prolonged reaction times at the synthesis temperature of 500 °C can already lead to a beginning decomposition into oligomers, showing that the formation of K-PHI is presumably a kinetically controlled process, thus accounting for the frequently observed batch to batch differences. The high dynamics of these processes has recently been demonstrated by *Kessler et al.*, who obtained poly(triazine imide) under ionothermal conditions starting from heptazine-based melon. This necessarily involves the decomposition of the heptazine units to eventually yield the triazine based polymer.[88] While PTI · LiCl syntheses are usually conducted in closed reaction vessels, K-PHI is often obtained under inert, but atmospheric pressure. Although heptazine-based structures have been calculated to be thermodynamically more stable and are generally favored over their triazine counterparts,[69,89–91] it is vital to finely tune parameters like pressure, temperature and the salt melt stoichiometry (i.e. degree of solubility of precursors) in order to yield a crystalline PHI species. The underlying concept is that a constant decomposition and reformation is required to heal defects and form a crystalline material. Therefore, a closed vessel is favorable, in which the gaseous reaction species are contained to induce the back reaction.[40,43] As high temperatures of about 500 °C are needed to overcome the activation barrier for both PTI and PHI formation, the chemists main handle on the resulting product is the choice of the correct mixture of precursors, which in turn defines the N/C ratio and also simultaneously affecting the amount of released gases. Ultimately, this means that the used precursor and the reaction medium (i.e. salt melt versus classical solid-state approach) are probably the more important parameters to control the desired product and its crystallinity. The choice of the reaction surface has probably received less attention as a reaction parameter so far. Although there have not been many studies on this topic, the few existing reports,[60,72,92–94] the parallel observation of interfacial growth for covalent organic frameworks (COFs),[95,96] own observations and discussions with other researchers in the field, point towards the surface as the next major step in the synthetic control for CN-polymers. If, for instance, one could grow CN-materials directly on an – ideally conducting – substrate to prepare thin films, further use as electrochemical devices could greatly benefit implementations such as photovoltaics, sensing and catalysis, respectively.

Concerning the reaction time of carbon nitrides, it is likely that some of the products in salt melts like K-PHI are metastable and longer reaction may lead to a beginning decomposition into monomeric forms like potassium melonate. Therefore, the control of the reaction time should not be neglected. However, due to the similarities between distinct polymeric phases and the troublesome identification of oligomeric vs. polymeric materials, it remains very challenging to determine optimal reaction times.

The ionic nature of K-PHI allows for the exchange of the cations, such that beside the alkali-metal ions that are used during the ionothermal synthesis, also other ions can be intercalated such as alkaline earth and transition metals, demonstrating the versatile character of the network.[46] When K-PHI – or any other M-PHI[a] – is treated with diluted aqueous acids it is rapidly transformed into the protonated version, H-PHI.[43,97] This process is reversible to the effect that a suitable base (MOH) or excess salt (MCl) can be used to yield the corresponding M-PHI again; but comes at the cost of losing some long-range order. It has been suggested that during extraction (and reinsertion) of the ions the PHI sheets may shift to some extent, thus smearing out the 3D structure of the PHI sheets.[43]

For K-PHI, a number of structural models have been proposed, some of which are displayed in Scheme 1.4.[44,86,98–101] However, the convincing proofs for a certain model could not adequately be presented. Additionally, the 3D structures of these PHI related materials remain unclear, highlighting the need for a thorough structural investigation. Hence, the major objective of this thesis has been the structure elucidation of K-PHI, for which the main challenge lies in identifying the correct model, uniting a plethora of analytical tools and providing the best overlap between theoretical and experimental results. Accurate information on the structure of K/H-PHI is ultimately important for associating the photocatalytic performance to certain structural characteristics and will be discussed in detail in chapters 2 and 3.

---

[a] M-PHI symbolizes a variety of studied alkali (Li, Na, K, Rb, Cs), alkaline earth (Mg, Ca) and transition metal (Co, Ni, Zn, Ag) poly(heptazine imides).

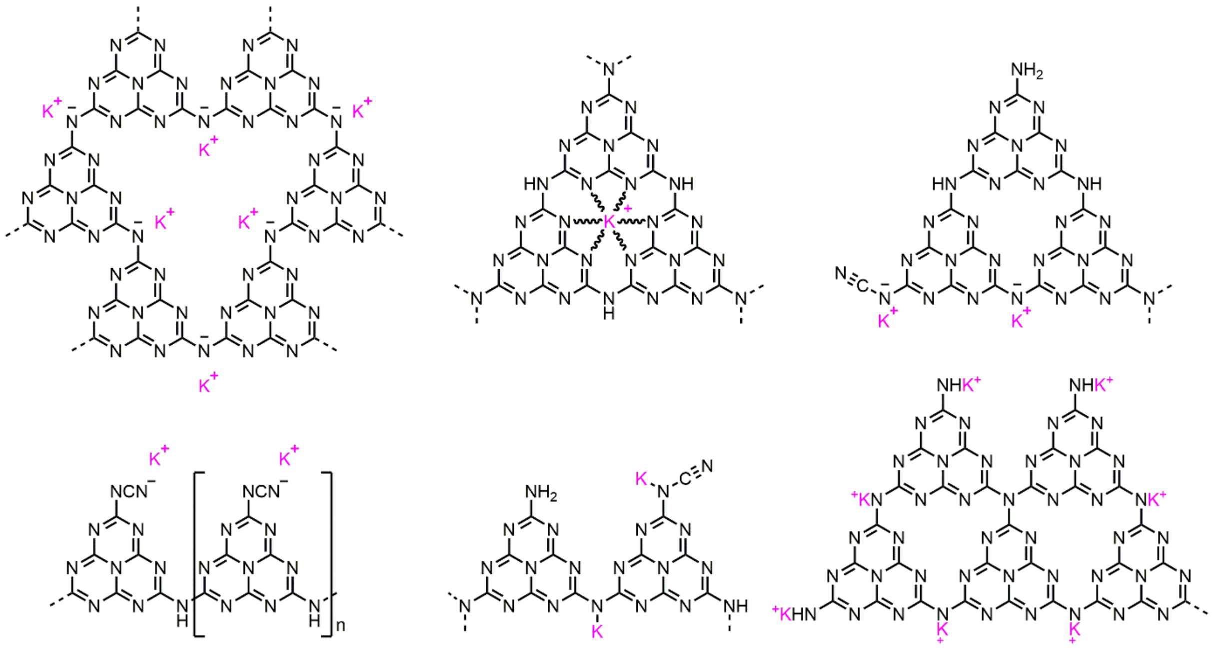

Scheme 1.4. Various structural models proposed for potassium poly(heptazine imide), underlining the need for a thorough structural assessment.

Finally, at the end of this section, we would like recap and carve out some of the technical reasons, why the structural identification of polymeric carbon nitrides generally proves challenging. A standard technique for analyzing solid matter is X-ray crystallography. Therefore, one would ideally try to grow single crystals of CN-polymers. However, this usually remains very difficult, as even the largest crystallites observed with transmission electron microscope (TEM) images are in the range of a few 100 nm,[43] which is too small for laboratory single crystal X-ray analysis.[40] Especially so, because usually thin platelet-shaped crystallites are formed, whose high aspect ratio prevents facile mounting on a specimen holder. Additionally, the light-weight elements, constituting the polymer, scatter X-rays weakly, such that even micro-focused X-ray sources (e.g. synchrotron) may not yield adequate scattering patterns. The two reasons listed above also impede the structural elucidation by electron diffraction. Carbon nitride crystallites are rapidly degraded in the electron beam even at low dosages and short acquisition times.[102] The high aspect ratios of the crystallites also cause a preferential orientation on the TEM grid, increasing the difficulty of observing diffraction patterns perpendicular to the preferential orientation.[43,65]

An important technique for the analysis of the local structure is NMR spectroscopy. The good news is that the three most common elements in carbon nitride polymers (C, H, N) are all NMR active with natural isotopes that come with a spin s = ½. Unfortunately, the natural abundance of ^{13}C- (ca. 1.1 %) and ^{15}N- (ca. 0.4 %) isotopes is quite low. While ^{1}H abundance is nearly 100%, it is accompanied by a very narrow range of chemical shifts and broad line-width, due to strong homonuclear dipolar interactions, which increase the difficulty of the identification of proton signals in solid-state NMR (ssNMR) spectroscopy.[103] The resolution can be increased by higher rotational frequencies of the magic angle spinning (MAS) technique, but this is also subject to practical limitations such as rotor design. Regarding ^{13}C-NMR, the chemical shifts for the main building units, heptazines and triazines, cover only a range of several ppm (approx. 155–175 ppm) and overlap with each other, hampering the correct quantification of the individual constituents in the polymer. Enriching the carbon nitride polymer with the corresponding NMR active nuclei can partly circumvent the low signal to noise ratio of ^{13}C- and ^{15}N- NMR spectra. However, this approach can become very expensive and impractical as a standard procedure, bearing in mind that a large portion of nitrogen and carbon is lost during typical syntheses in form of small molecules like NH_3, HCN, melamine, dicyanamide and other sublimed byproducts.

In summary, many carbon nitrides exhibit a large anisotropy with very rigid in-plane architecture by covalent bonding, while the structure in the third dimension is dominated by softer van der Waals- and π-stacking interactions. These very different circumstances can only be probed by using a variety of combined techniques (incl. X-ray/electron diffraction, IR/NMR spectroscopy, quantum-chemical calculations), that finally result in a credible structural model.

1.3 Photocatalysis

1.3.1 Photocatalysis Basics

The ensuing chapter will explain the concept of photocatalysis using the example of solar water splitting and will give an outline of the mechanisms and necessary premises. However, due to the complexity of the topic, this collection is not exhaustive and interested readers may be referred to additional sources covering the principles of photocatalysis.[104–107] The term photocatalysis itself is somewhat misleading, since catalysis in a strict sense increases the kinetics of exergonic reactions i.e. by lowering the activation energy.[107,108] By this stricter definition, photocatalytic processes would use light only to provide the activation energy or induce an intermediate state. However, the production of a chemical product with higher energy by using light would more correctly be termed photosynthesis, as observed in plants and algae, which generate sugars and oxygen from lower energetic substrates such as H_2O and CO_2. Nevertheless, for historical reasons and for the sake of consistency with many other studies, the term photocatalysis will be used synonymously in this thesis.

Water splitting is an endergonic process comprising the reduction (eq. 1.1) and oxidation (eq. 1.2) of water, respectively. The combined reactions are energetically uphill with a Gibb's free energy ΔG^0 = +237 kJ/mol or ΔE^0 = 1.23 V (eq. 1.3) translated into voltages.

$$2\ H_2O\ +\ 4\ e^-_{CB}\ \rightarrow\ 2\ H_2\ +\ 2\ O^{2-} \qquad 1.1$$

$$2\ H_2O\ +\ 4\ h^+_{VB}\ \rightarrow\ O_2\ +\ 4\ H^+ \qquad 1.2$$

$$2\ H_2O\ \rightarrow\ 2\ H_2\ +\ O_2 \qquad \Delta G^0 = 2 \cdot (+237\ \text{kJ/mol}) \qquad 1.3$$

Thus, the reaction towards hydrogen and oxygen does not occur spontaneously, but requires external energy input. To this purpose, classical electrolysis of water has been established as a technique already in the late 18th century.[109] However, in their pioneering work from 1972, *Honda* and *Fujishima* were the first to utilize a photoelectrochemical setup to convert water into O_2 and H_2 with TiO_2 as the oxidation photoelectrode and platinum as the reduction electrode, respectively.[110] The revolutionary idea was to use light to provide the required potential, which is otherwise supplied as electrical potential in classical electrolysis.

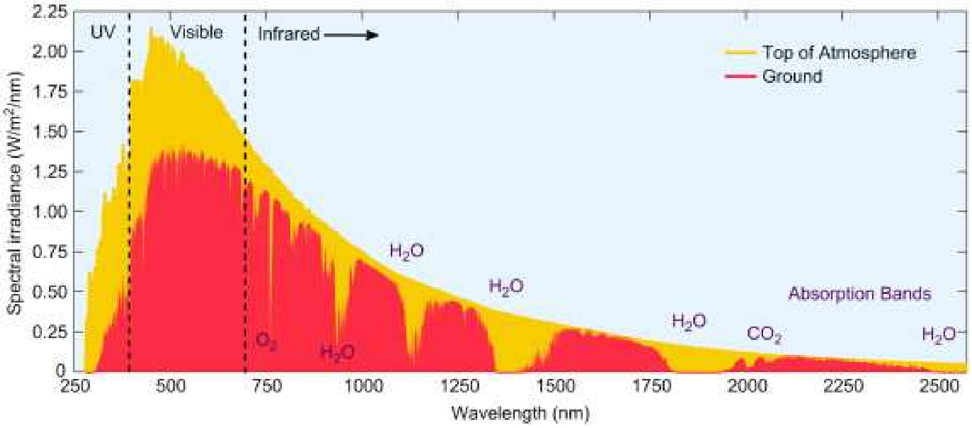

Figure 1.9. Extraterrestrial solar spectrum and corresponding spectrum at sea level with absorption effects by atmospheric molecules. Reprinted from ref. https://doi.org/10.1016/B978-0-08-046405-3.00010-3 with permission from Elsevier.

The following paragraphs lists the requirements and illustrates the stages during a photocatalytic cycle. Firstly, the band gap of the semiconductor must be sufficiently larger than the thermodynamically constraining limit of 1.23 eV (~1000 nm). The need for a larger band gap potential stems from the necessity of supplying enough driving force to overcome the overpotential, intrinsic to any form of photoconversions (incl. photovoltaics).[111,112] The various loss channels that lead to the overpotential will further be specified below. In order to drive both half reactions simultaneously, the valence- (VB) and conduction band (CB) of the photocatalyst (Figure 1.10a) must, furthermore, straddle the redox potentials of the water oxidation and reduction, respectively. While a large band gap provides sufficient energy for the process (incl. overpotentials) and facilitates the likelihood of suitable band positions on the thermodynamic scale, there has yet to be a trade-off between the size of the band gap and the provided energy by solar irradiation. With the highest photon flux from sunlight occurring in the visible spectrum (i.e. 400-700 nm),[113] the band gap should be as small as possible to harness the maximal solar power (Figure 1.9), while still providing enough driving force.

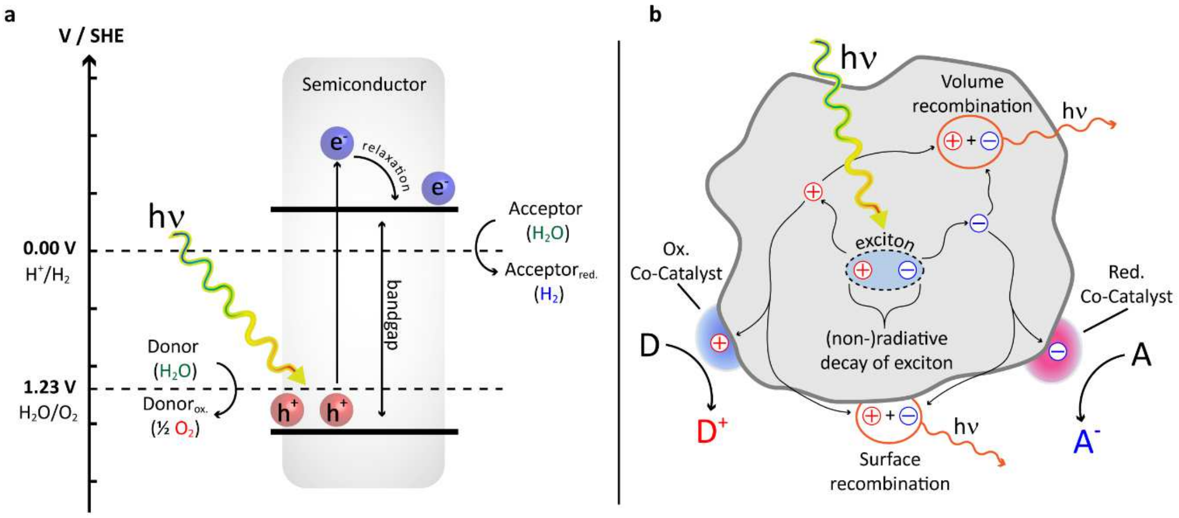

Figure 1.10. (a) Energy scheme referenced to the standard hydrogen electrode (SHE) showing the suitable conduction- and valance band positions required for photocatalytic transformation of water into hydrogen and oxygen. (b) Schematic representation of the photocatalytic cascade (absorption, exciton dissociation, charge migration and charge transfer to a substrate) and potential loss pathways occurring in the photocatalyst particle.

The actual photocatalytic cascade is dependent on four key steps that sequentially occur within the bulk and on the surface of the photocatalyst, respectively. The processes are summarized graphically in Figure 1.10b. In a first step, light of a specific wavelength is absorbed by the semiconducting material. During excitation an electron is promoted to the conduction band and leaves behind a positively charged hole in the valence band. Depending on the band structure this process may also involve relaxation of the electron to the lowest available level of the conduction band. Hence, the maximum potential energy of this electron equals the band gap of the semiconductor, which represents an important figure of merit for photocatalysis (cf. Figure 1.10a). However, during continuous illumination of a semiconductor another loss channel occurs, due to the formation of quasi-Fermi levels resulting from increased charge carrier concentrations in the conduction band and valence band, respectively.[114] These new levels lie below the conduction band and above the valence band, hence, the actual available energy is reduced to the so-called photopotential, i.e. the difference between the electron quasi-Fermi level and the hole quasi-Fermi level.

During the second step of the photocatalytic process, the thus created electron-hole pair, the so called exciton,[115] can diffuse through the crystallite. However, the charges are not yet free, but bound by electrostatic force: the exciton binding energy.[116] This energy, typically in the range of several hundred meV for low dielectric materials (such as CN-materials),[117] needs to be overcome in order to separate the individual charges and is unfortunately lost for the actual fuel generation.[118] Since most carbon nitrides suitable for water splitting are two-dimensional in nature, another parameter has to be taken into account when speaking of excitons. If the semiconductor sheets get thinner, quantum confinement effects (e-correlation) will cause the band gap to increase. At the same time less efficient screening of electron and hole leads to a more strongly bound exciton, which is detrimental for the catalysis.[119] The stronger the exciton is bound, the higher the chances are that it will recombine causing light emission instead of participating in the desired redox reactions. Thus, the separation of the electron and hole is pivotal. Creating a material, in which this separation easily happens at interfaces (i.e. heterojunctions), is highly desired for efficient devices.

The migration of the separated charges comprises the third step of the photocatalytic process. In general, high mobilities of charge carriers are desirable to ensure that the charges can reach the surface of the photocatalyst fast. If charges are not used fast enough, there is always the chance of recombination when opposing charges meet either en route through the crystallite or at surface sites, illustrated in Figure 1.10b.[104,120,121] The recombination behavior is also influenced by the size and shape of the semiconductor crystallite, owing to the difference in aspect ratios in bulk and nanomaterials.[122] The recombination of the charges can either take a non-radiative pathway dissipating heat, or a radiative pathway causing light emission, called photoluminescence.[123] Enhancing the carrier lifetimes is usually beneficial for photocatalytic efficiency, since the following redox reactions occur on a slower time scale with respect to the absorption process and charge separation.[104] Once the charge reaches the surface it is transferred to a cocatalyst, which is employed because of enhanced reaction kinetics for the individual redox reactions compared to the neat photocatalyst (photoabsorber). For the hydrogen evolution reaction (HER) typical electrocatalyst such as the noble metals Pt, Pd or Rh are employed. A good cocatalyst mainly excels by two important characteristics: At first the work function of the metal should be suitable to create a contact in which the generated electrons are extracted and "trapped" inside the cocatalyst particle, thus avoiding recombination of charges that otherwise may happen at the photoabsorber's surface.[124,125] This junction between the two materials can either form an ohmic contact or lead to a Schottky barrier, in which a barrier has to be overcome in order to inject electrons into the cocatalyst.[126,127] The other task of the cocatalyst is to lower the activation energy/overpotential and thus enhance the kinetics of the surface reaction.[127] In this regard a high exchange current density for the conversion reaction is desirable along with neither a too strong adsorption nor too weak adsorption for the atomic hydrogen species in case of HER.[128] This behavior (also known as Sabatier's principle) is often expressed graphically in so called volcano plots (Figure 1.11a–b).[127,129,130] It must be noted, that although the concept of volcano plots with one

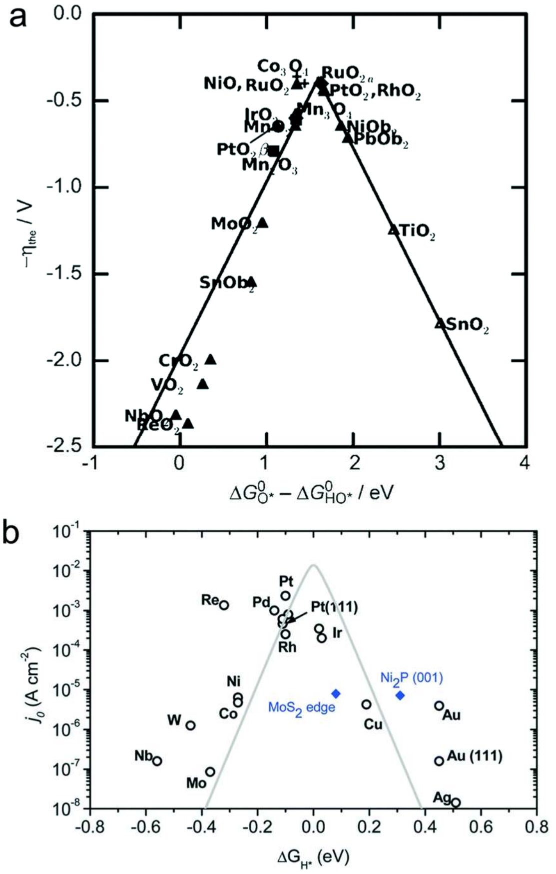

Figure 1.11. Volcano plots for the water oxidation (a) and reduction (b), respectively. In (a) the negative theoretical overpotential is plotted against the standard free energy of a reaction intermediate of the OER. In (b) the experimentally obtained exchange-current density is plotted against the DFT-calculated free energy of adsorbed atomic hydrogen.

Figure 1.11 a) is reprinted from ref. https://doi.org/10.1002/cctc.201000397 with permission from John Wiley and Sons. Figure 1.11 b) is reprinted from ref. https://doi.org/10.1039/C3CS60468C with permission from the Royal Society of Chemistry.

descriptor (adsorption energy) is a neat concept, it must be assumed that the complex processes on a cocatalyst's surface are additionally governed by multiple other parameters (e.g. diffusion processes, electrolyte interaction, correct orbital overlap) and that therefore the volcano plots certainly have their limitations.[131]

For the oxidation of water a set of other cocatalysts are employed, among which oxides such as RuO_2, IrO_2 CoO_x, and NiO are typical representatives.[127,130] Since we have seen that the charge separation and extraction to the corresponding catalysts is a major challenge in the photocatalytic cycle, it is beneficial for the overall performance when the complementary cocatalysts are deposited in close proximity. Ideally, only one cocatalyst (either for HER or OER) is decorated on the surface, while the photocatalyst itself is able to drive the respective other half reaction on its surface, as for instance could be shown with NiO@$NaTaO_3$ capable of full water splitting.[132] With powders as photocatalysts – which can be pictured as "short-circuited photoelectrochemical cells"[133] –, it is essential to separate OER and HER spatially to avoid the back reaction, since no external bias can be applied to compartmentalize the reactions as happening in a (photo-)electrochemical setup.[134,135] With that in mind, the proximity of reaction centers for efficient use of charges on the one side and the spatial separation of the reaction centers to avoid the pending back reaction on the other side must carefully be optimized.

Another factor, that profoundly influences the photocatalytic reaction, is the number of electrons transferred on the way to product formation (i.e. 2 e^- for H_2 and 4 e^- for O_2). The four electron transfer required in the OER is considered kinetically more demanding and thus presents the rate limiting step in water splitting.[136] Additionally, the longer the reaction intermediates remain on the surface of the cocatalyst/photocatalyst, the higher the chances are for the competing back reaction to water. That being said, many studies rely on so called sacrificial agents that are more easily reduced or oxidized than water and therefore enable the investigation of only one half reaction.[137] The idea behind this strategy is to ideally exclude any bottleneck by a rapid reaction of the sacrificial agent, so that the effect of changed parameters at the opposite half reaction can be observed. A recent study by *Kröger et al.* has drawn the attention towards the fact that in some cases the sacrificial donor may even become the kinetically limiting step in hydrogen evolution, because of adsorbed oxidation products, that block active sites for continuous hole extraction.[138] Additionally, when applying sacrifical agents, care should be taken that the sacrificial agent is not causing "current doubling", that would artificially enhance the rate of the studied reaction.[139,140]

1.3.2 Photocatalysis with carbon nitrides

Over the last years, carbon nitrides have attracted considerable attention as "metal-free" photocatalysts for multiple purposes such as hydrogen and oxygen evolution from water, CO_2 reduction, nitrogen fixation, dye/pollutant degradation and additionally as a photocatalyst for various organic reactions.

Photocatalytic hydrogen evolution with CN-materials has first been shown for amorphous melon by *Wang et al.* in 2009,[33] but has been accomplished with various other carbon nitride materials ever since. Among those the most important have been presented in chapter 1.2, comprising melon type systems along with the 2D materials, PTI and PHI. Usually, in these materials the photogenerated holes in the conduction band are quenched by sacrificial donors such as methanol,[43,44] 4-methylbenzyl alcohol (4-MBA),[141] triethanolamine (TEA)[41] and others, depending on the requirements of the photocatalytic reaction media.[142] Thus, most reports – including the ones in this thesis – study the hydrogen evolution half reaction decoupled from the water oxidation half reaction. However, lately, there have also been attempts to use this downside in order to create valuable chemicals on the oxidation site, i.e C-H thiolation of aryl compounds, selective alcohol oxidation to aldehydes and conversion of sulfides to sulfoxides, respectively.[141,143–145] Using waste materials like microplastics, that are oxidized over the course of the photocatalytic cycle, presents another fascinating concept to tackle the in itself unfavorable use of sacrificial agents.[146] Finally, there have also been studies, that show full water splitting with carbon nitrides, though at relatively low rates and mainly relying on excitation with wavelengths shorter than the visible light.[147,148] A particularly promising approach for full water splitting is the combination of a carbon nitride photocatalyst and carbon nanodots as a cocatalyst, completely avoiding expensive and toxic metal cocatalysts.[149] In this system the applied principle of a two electron/two electron pathway allows for the generation of H_2O_2, which is then rapidly decomposed to water and O_2 on the surface of the carbon nanodots, thereby avoiding poisoning of the catalyst surface by H_2O_2. In principle, the generation of H_2O_2 is thermodynamically unfavorable (1.78 eV), but can be kinetically advantageous due to the separated electron transfers (eq. 1.4 and 1.5) opposed to the full four electron process necessary for direct water splitting.

$$2\ H_2O \rightarrow H_2 + H_2O_2 \qquad (1.78\ \text{eV}) \tag{1.4}$$

$$H_2O_2 \rightarrow \frac{1}{2}O_2 + H_2O \qquad (-1.1\ \text{eV}) \tag{1.5}$$

Since based on earth abundant elements, cheap precursors and their inherent thermal, chemical and photochemical robustness, carbon nitrides could represent also an economically viable alternative for sustainable energy generation. The drawback is the comparably low efficiency of many carbon nitride photocatalysts, preventing their use in commercial applications so far.[150] Many strategies have been pursued to enhance the activity of CN_x compounds including heteroatom doping e.g. with boron,[151] nitrogen, oxygen,[152] fluorine,[153] phosphorus[154] and sulfur,[155] hard and soft templating,[156] nano-structuring and exfoliation aiming at an increased surface area (and electronically tuning the material by quantum confinement effects),[157] co-polymerization,[41] introducing heterojuction architectures (i.e. z-scheme photocatalysis),[158,159] sensitizing with dye molecules,[160] cocatalyst design[141,161,162] and defect engineering including the rational introduction of terminal groups.[44,138,163] The listed zoo of possible ways of adjustments emphasizes how many parameters must be investigated with each set of materials. While the mere improvement of materials is a legitimate goal, this thesis primarily focusses on the structural characterization of carbon nitride materials to provide a more reliable basis for the analysis and further improvement of the photocatalysts.

The importance of this endeavor is vividly illustrated by the example of melon, whose structural misinterpretation (fully condensed 2D sheets instead of the actual 1D polymer; see chapter 1.2) lead to numerous inaccurate calculations of the electronic structure.[164–166] The conclusions drawn from these theoretical results may ultimately compromise their benefit on the goal of rational catalyst design and can in part explain the regularly encountered deviations between calculation and experiment.[167]

In summary, carbon nitrides are versatile and promising candidates for many photocatalytic applications and substantial efforts for an increased efficiency have been undertaken. Yet, it is at least equally important to gain a more fundamental understanding of their individual structure, because only on that basis, rational advances by quantum-chemical calculation and experimental design can be made. As *Takanabe* points out, the photocatalytic process is dependent on numerous parameters, so it is essential to obtain a thorough structural understanding to begin from a solid basis.[104]

1.3.3 “Dark Photocatalysis” with carbon nitrides

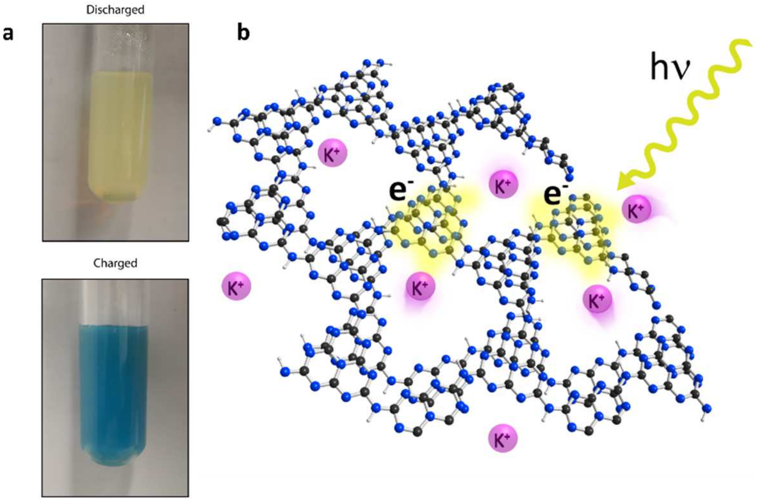

Figure 1.12. (a) Photography of the discharged (top) and charged (bottom) K-PHI in a suspension with an electron donor. (b) Schematic illustration how the charged network (yellow) is stabilized by potassium cations.

Potassium poly(heptazine imide) (K-PHI), shows a particularly interesting property: a long-lived photoreduced state.[168] Upon excitation with light, the holes in the valence band are quenched by an electron donor, while the electrons remain in a high energetic state within the valence band for hours or even days.[143,168] This process is accompanied by a change in color from yellow to dark blue depicted in Figure 1.12a. Subsequently, these electrons can be extracted in a dark reaction to produce hydrogen, once a cocatalyst such as platinum is added.[43,168] This process resembles the naturally occurring dark reaction in plants (Calvin-Benson-Bassham cycle) that uses stored energy in the form of ATP and NADPH to fixate carbon dioxide to sugars.[107] The negative charge (up to 45-60 $\mathrm{C\ g^{-1}}$) is stored on the carbon nitride backbone and is stabilized by potassium cations (Figure 1.12b).[169] The intermediately stored electrons on the polymer backbone may even be advantageous for the photocatalytic cycle that has been discussed in section 1.3.1. As the surface redox reactions are sluggish compared to the time frames of the light absorption, the long-lived electronic state could enhance the efficiency by constantly supplying electrons to the cocatalyst, that are not readily lost by recombination channels.

When contacted to a transparent electrode, K-PHI can also be exploited as a photoanode in a so-called “solar battery”,[169] which can be charged under illumination in the presence of a sacrificial electron donor and discharged in the dark. Consequently, this design allows for energy storage and delayed conversion into electricity, simultaneously. The battery can also be charged purely electrically, when applying a potential of ca. -700 mV vs Ag/AgCl without the need for light nor an electron donor. Accordingly, batteries made from K-PHI could help to store energy from other renewable sources such as wind power and thus help to overcome their inherent production intermittency without the need for scarce resources such as cobalt, nickel, etc., commonly incorporated in state-of-the-art batteries.

While the aspects described above paint a promising picture for a potential use of “dark photocatalysts”, still the mechanism causing the charge storage is not yet fully understood. While there is reasonable ground to suspect that ions are essential for stabilizing the charge, the exact necessary structural conditions for the photoreduced state itself are not yet clarified. In chapter 3 of this thesis, we will tackle this issue from a structural perspective. This once more emphasizes that the structural characterization is at the heart of any deliberate advance in photocatalysis.

1.4 Objectives

In the introductory chapters, it has been shown that first of all the structural elucidation of many carbon nitrides is highly ambiguous and that there is ongoing debate which structural model is correct. Secondly and equally important, we have seen that the photocatalytic process is governed by a very complicated interplay of a multitude of parameters, which for a good part are affected by the chemical structure. There are studies using the same material, but reaching very different values for activity, thus the comparability of studies may be questioned to a certain degree. Hence, this thesis' main objective can be described as the structural investigation of the very commonly used potassium poly(heptazine imide), K-PHI, a promising candidate for photocatalytic applications. This fundamental approach is necessary, because the field is growing so quickly and the return to a common basis is ever more difficult to achieve, but a thorough structural basis can help reconvene at this aim.

A second goal is the characterization of a new potassium containing carbon nitride phase that has been synthesized by an ionothermal approach. The ambition behind this structure elucidation is not only to add another member to the CN-family, but also to compare this new potassium containing network with the closely related K-PHI polymer and its intriguing property to store light in form of a photoreduced state. By means of this comparison, we may get a better understanding of what structural features cause this long-lived photoreduced state in K-PHI.

The third part of this thesis investigates a new carbon nitride species that has been synthesized from a $NiCl_2$/KCl salt melt. As nickel species are frequently used as cocatalysts for the CO_2 reduction reaction, the goal was to synthesize a catalyst with a directly incorporated metal species that would allow for the hydrogenation of CO_2. The method uses a gas mixture of hydrogen and carbon dioxide and aims at producing carbon monoxide, a highly relevant feedstock for the chemical industry.

Finally, my hope is that this thesis may also serve the purpose of an introduction on carbon nitrides and their use as photocatalysts, uncovering some of the common pitfalls and becoming a helpful basis for students new to the field. Since the field is progressing so fast, there is, unfortunately, sometimes a discrepancy between what is claimed and what is irrefutably known.

1.5 References

(1) Denholm, P.; O'Connell, M.; Brinkman, G.; Jorgenson, J. Overgeneration from Solar Energy in California: A Field Guide to the Duck Chart, NREL/TP-6A20-65023, National Renewable Energy Laboratory, https://www.nrel.gov/docs/fy16osti/65023.pdf, Accessed June 10, 2021.

(2) Jones-Albertus, B. Confronting the Duck Curve: How to Address Over-Generation of Solar Energy, U.S. Department of energy, https://www.energy.gov/eere/articles/confronting-duck-curve-how-address-over-generation-solar-energy, Accessed June 10, 2021.

(3) Zhou, L.; Zhang, H.; Sun, H.; Liu, S.; Tade, M. O.; Wang, S.; Jin, W. Recent advances in non-metal modification of graphitic carbon nitride for photocatalysis: a historic review. *Catal. Sci. Technol.* **2016**, *6* (19), 7002–7023. DOI: 10.1039/C6CY01195K.

(4) Kessler, F. K.; Zheng, Y.; Schwarz, D.; Merschjann, C.; Schnick, W.; Wang, X.; Bojdys, M. J. Functional carbon nitride materials — design strategies for electrochemical devices. *Nat. Rev. Mater.* **2017**, *2* (6), 17030. DOI: 10.1038/natrevmats.2017.30.

(5) Organization for economic co-operation and development. *Climate Change Mitigation, https://www.oecd.org/env/cc/41751042.pdf, Accessed on June 11, 2021*.

(6) Schlomberg, H.; Podjaski, F.; Kröger, J.; Lotsch, B. Von der Jahrmarktattraktion zur Energiequelle: Kohlenstoffnitride. *Nachr. Chem.* **2018**, *66* (12), 1157–1161. DOI: 10.1002/nadc.20184065088.

(7) Miller, T. S.; d'Aleo, A.; Suter, T.; Aliev, A. E.; Sella, A.; McMillan, P. F. Pharaoh's Serpents: New Insights into a Classic Carbon Nitride Material. *Z. anorg. allg. Chem.* **2017**, *643* (21), 1572–1580. DOI: 10.1002/zaac.201700268.

(8) Liebig, J. Ueber einige Stickstoff - Verbindungen. *Ann. Chem. Pharm.* **1834**, *10* (1).

(9) Wiebenga, E. H.; Moerman. N. F. Die Kristallstruktur der Cyanursäure $(HCNO)_3$. *Z. Kristallogr. Cryst. Mater.* **1938**, *99* (1), 217–229. DOI: 10.1524/zkri.1938.99.1.217.

(10) Hughes, E. W. The Crystal Structure of Melamine. *J. Am. Chem. Soc.* **1941**, *63* (6), 1737–1752. DOI: 10.1021/ja01851a069.

(11) Andreas Sattler. Investigations into s-Heptazine-Based Carbon Nitride Precursors, Doctoral Thesis, University of Munich (LMU) **2010**.

(12) Klason, P. Ueber Melamverbindungen. *J. prakt. Chem.* **1886**, *33* (1), 285–289. DOI: 10.1002/prac.18860330128.

(13) Pauling, L.; Sturdivant, J. H. The Structure of Cyameluric Acid, Hydromelonic Acid and Related Substances. *Proc. Natl. Acad. Sci.* **1937**, *23* (12), 615. DOI: 10.1073/pnas.23.12.615.

(14) *https://materialsproject.org/materials/mp-988/#; accessed on June 27, 2020*.

(15) Liu, A. Y.; Cohen, M. L. Structural properties and electronic structure of low-compressibility materials: Si_3N_4 and hypothetical C_3N_4. *Phys. Rev. B* **1990**, *41* (15), 10727–10734. DOI: 10.1103/PhysRevB.41.10727.

(16) Liu, A. Y.; Wentzcovitch, R. M. Stability of carbon nitride solids. *Phys. Rev. B* **1994**, *50* (14), 10362–10365. DOI: 10.1103/PhysRevB.50.10362.

(17) Schnick, W. Carbon(IV) Nitride C_3N_4 - A new Material Harder than Diamond? *Angew. Chem. Int. Ed.* **1993**, *32* (11), 1580–1581. DOI: 10.1002/anie.199315801.

(18) DeVries, R. C. Inventory on innovative research: the case of C_3N_4. *Mater. Res. Innov.* **1997**, *1* (3), 161–162.

(19) Todd, M.; Kouvetakis, J.; Groy, T. L.; Chandrasekhar, D.; Smith, D. J.; Deal, P. W. Novel Synthetic Routes to Carbon Nitride. *Chem. Mater.* **1995**, *7* (7), 1422–1426. DOI: 10.1021/cm00055a023.

(20) Martín-Ramos, P.; Martín-Gil, J.; Dante, R. C.; Vaquero, F.; Navarro, R. M.; Fierro, J.L.G. A simple approach to synthesize g-C_3N_4 with high visible light photoactivity for hydrogen production. *Int. J. Hydrog. Energy* **2015**, *40* (23), 7273–7281. DOI: 10.1016/j.ijhydene.2015.04.063.

(21) Maya, L.; Cole, D. R.; Hagaman, E. W. Carbon–Nitrogen Pyrolyzates: Attempted Preparation of Carbon Nitride. *J. Am. Ceram. Soc.* **1991**, *74* (7), 1686–1688. DOI: 10.1111/j.1151-2916.1991.tb07161.x.

(22) Zinin, P. V.; Ming, L. C.; Sharma, S. K.; Hong, S. M.; Xie, Y.; Irifune, T.; Shinmei, T. Synthesis of new cubic C_3N_4 and diamond-like BC_3 phases under high pressure and high temperature. *J. Phys. Conf. Ser.* **2008**, *121* (6), 62002.

(23) Stavrou, E.; Lobanov, S.; Dong, H.; Oganov, A. R.; Prakapenka, V. B.; Konôpková, Z.; Goncharov, A. F. Synthesis of Ultra-incompressible sp^3-Hybridized Carbon Nitride with 1:1 Stoichiometry. *Chem. Mater.* **2016**, *28* (19), 6925–6933. DOI: 10.1021/acs.chemmater.6b02593.

(24) Komatsu, T.; Samejima, M. Preparation of carbon nitride C_2N by shock-wave compression of poly(aminomethineimine). *J. Mater. Chem.* **1998**, *8* (1), 193–196. DOI: 10.1039/A707214G.

(25) Wixom, M. R. Chemical Preparation and Shock Wave Compression of Carbon Nitride Precursors. *J. Am. Ceram. Soc.* **1990**, *73* (7), 1973–1978. DOI: 10.1111/j.1151-2916.1990.tb05254.x.

(26) Han, H.-X.; Feldman, B. J. Structural and optical properties of amorphous carbon nitride. *Solid State Commun.* **1988**, *65* (9), 921–923. DOI: 10.1016/0038-1098(88)90732-6.

(27) Okada, T.; Yamada, S.; Takeuchi, Y.; Wada, T. Formation of carbon nitride films with high N/C ratio by high-pressure radio frequency magnetron sputtering. *Int. J. Appl. Phys.* **1995**, *78* (12), 7416–7418. DOI: 10.1063/1.360397.

(28) Hoffman, A.; Geller, H.; Gouzman, I.; Cytermann, C.; Brener, R.; Kenny, M. Formation of carbon nitride films by high-energy nitrogen ion implantation into glassy carbon. *Surf. Coat. Technol.* **1994**, *68-69*, 616–620. DOI: 10.1016/0257-8972(94)90226-7.

(29) Jagielski, J.; Moncoffre, N.; Delichère, P.; Marest, G. On the possibility of β-C_3N_4 carbon nitride synthesis via C and N implantation into copper. *J. Mater. Sci.* **1999**, *34* (12), 2949–2954. DOI: 10.1023/A:1004608107268.

(30) Niu, C.; Lu, Y. Z.; Lieber, C. M. Experimental realization of the covalent solid carbon nitride. *Science* **1993**, *261* (5119), 334–337. DOI: 10.1126/science.261.5119.334.

(31) Pickard, C. J.; Salamat, A.; Bojdys, M. J.; Needs, R. J.; McMillan, P. F. Carbon nitride frameworks and dense crystalline polymorphs. *Phys. Rev. B* **2016**, *94* (9), 94104. DOI: 10.1103/PhysRevB.94.094104.

(32) Martin-Gil, J.; Martin-Gil, F. J.; Sarikaya, M.; Qian, M.; José-Yacamán, M.; Rubio, A. Evidence of a low compressibility carbon nitride with defect-zincblende structure. *Int. J. Appl. Phys.* **1997**, *81* (6), 2555–2559. DOI: 10.1063/1.364301.

(33) Wang, X.; Maeda, K.; Thomas, A.; Takanabe, K.; Xin, G.; Carlsson, J. M.; Domen, K.; Antonietti, M. A metal-free polymeric photocatalyst for hydrogen production from water under visible light. *Nat Mater* **2009**, *8* (1), 76–80. DOI: 10.1038/nmat2317.

(34) Tsuji, I.; Kato, H.; Kobayashi, H.; Kudo, A. Photocatalytic H_2 Evolution Reaction from Aqueous Solutions over Band Structure-Controlled (AgIn)x$Zn_{2(1-x)}S_2$ Solid Solution Photocatalysts with Visible-Light Response and Their Surface Nanostructures. *J. Am. Chem. Soc.* **2004**, *126* (41), 13406–13413. DOI: 10.1021/ja048296m.

(35) Min, S.; Lu, G. Sites for High Efficient Photocatalytic Hydrogen Evolution on a Limited-Layered MoS_2 Cocatalyst Confined on Graphene Sheets—The Role of Graphene. *J. Phys. Chem. C* **2012**, *116* (48), 25415–25424. DOI: 10.1021/jp3093786.

(36) Maeda, K.; Teramura, K.; Lu, D.; Takata, T.; Saito, N.; Inoue, Y.; Domen, K. Photocatalyst releasing hydrogen from water. *Nature* **2006**, *440* (7082), 295. DOI: 10.1038/440295a.

(37) Kibria, M. G.; Zhao, S.; Chowdhury, F. A.; Wang, Q.; Nguyen, H. P. T.; Trudeau, M. L.; Guo, H.; Mi, Z. Tuning the surface Fermi level on p-type gallium nitride nanowires for efficient overall water splitting. *Nat. Commun.* **2014**, *5* (1), 3825. DOI: 10.1038/ncomms4825.

(38) Wang, Q.; Lian, J.; Li, J.; Wang, R.; Huang, H.; Su, B.; Lei, Z. Highly Efficient Photocatalytic Hydrogen Production of Flower-like Cadmium Sulfide Decorated by Histidine. *Sci. Rep.* **2015**, *5* (1), 13593. DOI: 10.1038/srep13593.

(39) Gmelin, L. Ueber einige Verbindungen des Melon's. *Ann. Pharm.* **1835** (15), 252–258.

(40) Wirnhier, E.; Döblinger, M.; Gunzelmann, D.; Senker, J.; Lotsch, B. V.; Schnick, W. Poly(triazine imide) with Intercalation of Lithium and Chloride Ions [$(C_3N_3)_2(NH_xLi_{1-x})_3 \cdot LiCl$]: A Crystalline 2D Carbon Nitride Network. *Chem. Eur. J.* **2011**, *17* (11), 3213–3221. DOI: 10.1002/chem.201002462.

(41) Schwinghammer, K.; Tuffy, B.; Mesch, M. B.; Wirnhier, E.; Martineau, C.; Taulelle, F.; Schnick, W.; Senker, J.; Lotsch, B. V. Triazine-based Carbon Nitrides for Visible-Light-Driven Hydrogen Evolution. *Angew. Chem. Int. Ed.* **2013**, *52* (9), 2435–2439. DOI: 10.1002/anie.201206817.

(42) McMillan, P. F.; Lees, V.; Quirico, E.; Montagnac, G.; Sella, A.; Reynard, B.; Simon, P.; Bailey, E.; Deifallah, M.; Corà, F. Graphitic carbon nitride $C_6N_9H_3 \cdot HCl$: Characterisation by UV and near-IR FT Raman spectroscopy. *J. Solid State Chem.* **2009**, *182* (10), 2670–2677. DOI: 10.1016/j.jssc.2009.07.030.

(43) Schlomberg, H.; Kröger, J.; Savasci, G.; Terban, M. W.; Bette, S.; Moudrakovski, I.; Duppel, V.; Podjaski, F.; Siegel, R.; Senker, J.; Dinnebier, R. E.; Ochsenfeld, C.; Lotsch, B. V. Structural Insights into Poly(Heptazine Imides): A Light-Storing Carbon Nitride Material for Dark Photocatalysis. *Chem. Mater.* **2019**, *31* (18), 7478–7486. DOI: 10.1021/acs.chemmater.9b02199.

(44) Lau, V. W.-h.; Moudrakovski, I.; Botari, T.; Weinberger, S.; Mesch, M. B.; Duppel, V.; Senker, J.; Blum, V.; Lotsch, B. V. Rational design of carbon nitride photocatalysts by identification of cyanamide defects as catalytically relevant sites. *Nat. Commun.* **2016**, *7*, 12165. DOI: 10.1038/ncomms12165.

(45) Chen, Z.; Savateev, A.; Pronkin, S.; Papaefthimiou, V.; Wolff, C.; Willinger, M. G.; Willinger, E.; Neher, D.; Antonietti, M.; Dontsova, D. "The Easier the Better" Preparation of Efficient Photocatalysts-Metastable Poly(heptazine imide) Salts. *Adv. Mater.* **2017**, *8*, 1700555. DOI: 10.1002/adma.201700555.

(46) Savateev, A.; Pronkin, S.; Willinger, M. G.; Antonietti, M.; Dontsova, D. Towards Organic Zeolites and Inclusion Catalysts: Heptazine Imide Salts Can Exchange Metal Cations in the Solid State. *Chem. Asian J.* **2017**, *15*, 783. DOI: 10.1002/asia.201700209.

(47) May, H. Pyrolysis of melamine. *J. Appl. Chem.* **1959**, *9* (6), 340–344. DOI: 10.1002/jctb.5010090608.

(48) Hosmane, R. S.; Rossman, M. A.; Leonard, N. J. Synthesis and structure of tri-s-triazine. *J. Am. Chem. Soc.* **1982**, *104* (20), 5497–5499. DOI: 10.1021/ja00384a046.

(49) Shahbaz, M.; Urano, S.; LeBreton, P. R.; Rossman, M. A.; Hosmane, R. S.; Leonard, N. J. Tri-s-triazine: synthesis, chemical behavior, and spectroscopic and theoretical probes of valence orbital structure. *J. Am. Chem. Soc.* **1984**, *106* (10), 2805–2811.

(50) Kroke, E.; Schwarz, M. Novel group 14 nitrides. *Coord. Chem. Rev.* **2004**, *248* (5), 493–532. DOI: 10.1016/j.ccr.2004.02.001.

(51) Lotsch, B. V.; Schnick, W. Thermal Conversion of Guanylurea Dicyanamide into Graphitic Carbon Nitride via Prototype CNx Precursors. *Chem. Mater.* **2005**, *17* (15), 3976–3982. DOI: 10.1021/cm050350q.

(52) Lotsch, B. V.; Schnick, W. From Triazines to Heptazines: Novel Nonmetal Tricyanomelaminates as Precursors for Graphitic Carbon Nitride Materials. *Chem. Mater.* **2006**, *18* (7), 1891–1900. DOI: 10.1021/cm052342f.

(53) Lotsch, B. V.; Schnick, W. Crystal Structure and Thermal Solid-State Reactivity of Ammonium Cyanoureate $NH_4[H_2NC(=O)NCN]$. *Z. Naturforsch.* **2004** (59b), 1229–1240.

(54) Lotsch, B. V.; Senker, J.; Kockelmann, W.; Schnick, W. Investigation of structural and dynamic properties of $NH_4[N(CN)_2]$ by means of X-ray and neutron powder diffraction as well as vibrational and solid-state NMR spectroscopy. *J. Solid State Chem.* **2003**, *176* (1), 180–191. DOI: 10.1016/S0022-4596(03)00388-8.

(55) Bettina Valeska Lotsch. From Molecular Building Blocks to From Molecular Building Blocks to Condensed Carbon Nitride Networks: Structure and Reactivity, Doctoral Thesis, University of Munich (LMU) **2006**.

(56) Savateev, A.; Dontsova, D.; Kurpil, B.; Antonietti, M. Highly crystalline poly(heptazine imides) by mechanochemical synthesis for photooxidation of various organic substrates using an intriguing electron acceptor – Elemental sulfur. *J. Catal.* **2017**, *350*, 203–211. DOI: 10.1016/j.jcat.2017.02.029.

(57) Savateev, A.; Pronkin, S.; Epping, J. D.; Willinger, M. G.; Wolff, C.; Neher, D.; Antonietti, M.; Dontsova, D. Potassium Poly(heptazine imides) from Aminotetrazoles: Shifting Band Gaps of Carbon Nitride-like Materials for More Efficient Solar Hydrogen and Oxygen Evolution. *ChemCatChem* **2017**, *9* (1), 167–174. DOI: 10.1002/cctc.201601165.

(58) Lesnikovich, A. I.; Ivashkevich, O. A.; Levchik, S. V.; Balabanovich, A. I.; Gaponik, P. N.; Kulak, A. A. Thermal decomposition of aminotetrazoles. *Thermochim. Acta* **2002**, *388* (1), 233–251. DOI: 10.1016/S0040-6031(02)00027-8.

(59) Larsen, F. K.; Hasen Mamakhel, A.; Overgaard, J.; Jørgensen, J.-E.; Kato, K.; Brummerstedt Iversen, B. Accessing the rich carbon nitride materials chemistry by heat treatments of ammonium thiocyanate, NH_4SCN. *Acta Crystallogr. B Struct. Cryst. Cryst. Chem.* **2019**, *75* (4), 621–633. DOI: 10.1107/S2052520619005791.

(60) Algara-Siller, G.; Severin, N.; Chong, S. Y.; Björkman, T.; Palgrave, R. G.; Laybourn, A.; Antonietti, M.; Khimyak, Y. Z.; Krasheninnikov, A. V.; Rabe, J. P.; Kaiser, U.; Cooper, A. I.; Thomas, A.; Bojdys, M. J. Triazine-Based Graphitic Carbon Nitride: a Two-Dimensional Semiconductor. *Angew. Chem. Int. Ed.* **2014**, *53* (29), 7450–7455. DOI: 10.1002/anie.201402191.

(61) Weidinger, A.; Waiblinger, M.; Pietzak, B.; Almeida Murphy, T. Atomic nitrogen in C_{60}:N@C_{60}. *Appl. Phys. A* **1998**, *66* (3), 287–292. DOI: 10.1007/s003390050668.

(62) Sato, T.; Narazaki, A.; Kawaguchi, Y.; Niino, H.; Bucher, G. Dicyanocarbodiimide and Trinitreno-s-triazine Generated by Consecutive Photolysis of Triazido-s-triazine in a Low-Temperature Nitrogen Matrix. *Angew. Chem. Int. Ed.* **2003**, *42* (42), 5206–5209. DOI: 10.1002/anie.200351879.

(63) Sattler, A.; Pagano, S.; Zeuner, M.; Zurawski, A.; Gunzelmann, D.; Senker, J.; Müller-Buschbaum, K.; Schnick, W. Melamine-melem adduct phases: investigating the thermal condensation of melamine. *Chemistry* **2009**, *15* (47), 13161–13170. DOI: 10.1002/chem.200901518.

(64) Kessler, F. K.; Burow, A. M.; Savasci, G.; Rosenthal, T.; Schultz, P.; Wirnhier, E.; Oeckler, O.; Ochsenfeld, C.; Schnick, W. Structure Elucidation of a Melam-Melem Adduct by a Combined Approach of Synchrotron X-ray Diffraction and DFT Calculations. *Chem. Eur. J.* **2019**, *25*, 8415. DOI: 10.1002/chem.201901391.

(65) Lotsch, B. V.; Döblinger, M.; Sehnert, J.; Seyfarth, L.; Senker, J.; Oeckler, O.; Schnick, W. Unmasking Melon by a Complementary Approach Employing Electron Diffraction, Solid-State NMR Spectroscopy, and Theoretical Calculations—Structural Characterization of a Carbon Nitride Polymer. *Chem. Eur. J.* **2007**, *13* (17), 4969–4980. DOI: 10.1002/chem.200601759.

(66) Komatsu, T. The First Synthesis and Characterization of Cyameluric High Polymers. *Macromol. Chem. Phys.* **2001**, *202* (1), 19–25. DOI: 10.1002/1521-3935(20010101)202:1<19:AID-MACP19>3.0.CO;2-G.

(67) Hu, Y.; Shim, Y.; Oh, J.; Park, S.; Park, S.; Ishii, Y. Synthesis of ^{13}C-, ^{15}N-Labeled Graphitic Carbon Nitrides and NMR-Based Evidence of Hydrogen-Bonding Assisted Two-Dimensional Assembly. *Chem. Mater.* **2017**, *29* (12), 5080–5089. DOI: 10.1021/acs.chemmater.7b00069.

(68) Schwarzer, A.; Saplinova, T.; Kroke, E. Tri-s-triazines (s-heptazines)—From a “mystery molecule” to industrially relevant carbon nitride materials. *Coord. Chem. Rev.* **2013**, *257* (13), 2032–2062. DOI: 10.1016/j.ccr.2012.12.006.

(69) Yang, J.; Gong, X.; Wang, G. Structure, aromaticity, stability, and energetic performance of the analogues and derivatives of s-heptazine. *J. Mol. Model.* **2014**, *20* (8), 2379. DOI: 10.1007/s00894-014-2379-1.

(70) Wirnhier, E.; Mesch, M. B.; Senker, J.; Schnick, W. Formation and Characterization of Melam, Melam Hydrate, and a Melam-Melem Adduct. *Chem. Eur. J.* **2013**, *19* (6), 2041–2049. DOI: 10.1002/chem.201203340.

(71) Cui, Y.; Ding, Z.; Fu, X.; Wang, X. Construction of Conjugated Carbon Nitride Nanoarchitectures in Solution at Low Temperatures for Photoredox Catalysis. *Angew. Chem. Int. Ed.* **2012**, *51* (47), 11814–11818. DOI: 10.1002/anie.201206534.

(72) Döblinger, M.; Lotsch, B. V.; Wack, J.; Thun, J.; Senker, J.; Schnick, W. Structure elucidation of polyheptazine imide by electron diffraction—a templated 2D carbon nitride network. *Chem. Commun.* **2009** (12), 1541. DOI: 10.1039/b820032g.

(73) Bojdys, M. J.; Müller, J.-O.; Antonietti, M.; Thomas, A. Ionothermal Synthesis of Crystalline, Condensed, Graphitic Carbon Nitride. *Chem. Eur. J.* **2008**, *14* (27), 8177–8182. DOI: 10.1002/chem.200800190.

(74) Rietveld, H. M. A profile refinement method for nuclear and magnetic structures. *J. Appl. Crystallogr.* **1969**, *2* (2), 65–71. DOI: 10.1107/S0021889869006558.

(75) Mesch, M. B.; Bärwinkel, K.; Krysiak, Y.; Martineau, C.; Taulelle, F.; Neder, R. B.; Kolb, U.; Senker, J. Solving the Hydrogen and Lithium Substructure of Poly(triazine imide)/LiCl Using NMR Crystallography. *Chem. Eur. J.* **2016**, *22* (47), 16878–16890. DOI: 10.1002/chem.201603726.

(76) Chong, S. Y.; Jones, J. T. A.; Khimyak, Y. Z.; Cooper, A. I.; Thomas, A.; Antonietti, M.; Bojdys, M. J. Tuning of gallery heights in a crystalline 2D carbon nitride network. *J. Mater. Chem. A* **2013**, *1* (4), 1102–1107. DOI: 10.1039/C2TA01068B.

(77) Bojdys, M. J.; Severin, N.; Rabe, J. P.; Cooper, A. I.; Thomas, A.; Antonietti, M. Exfoliation of Crystalline 2D Carbon Nitride: Thin Sheets, Scrolls and Bundles via Mechanical and Chemical Routes. *Macromol. Rapid Commun.* **2013**, *34* (10), 850–854. DOI: 10.1002/marc.201300086.

(78) Schwinghammer, K.; Mesch, M. B.; Duppel, V.; Ziegler, C.; Senker, J.; Lotsch, B. V. Crystalline Carbon Nitride Nanosheets for Improved Visible-Light Hydrogen Evolution. *J. Am. Chem. Soc.* **2014**, *136* (5), 1730–1733. DOI: 10.1021/ja411321s.

(79) Zhang, Z.; Leinenweber, K.; Bauer, M.; Garvie, Laurence A. J.; McMillan, P. F.; Wolf, G. H. High-Pressure Bulk Synthesis of Crystalline $C_6N_9H_3 \cdot HCl$: A Novel C_3N_4 Graphitic Derivative. *J. Am. Chem. Soc.* **2001**, *123* (32), 7788–7796. DOI: 10.1021/ja0103849.

(80) Horvath-Bordon, E.; Kroke, E.; Svoboda, I.; Fuess, H.; Riedel, R. Potassium melonate, $K_3[C_6N_7(NCN)_3]\cdot 5H_2O$, and its potential use for the synthesis of graphite-like C_3N_4 materials. *New J. Chem.* **2005**, *29* (5), 693. DOI: 10.1039/b416390g.

(81) Sattler, A.; Schnick, W. On the Formation and Decomposition of the Melonate Ion in Cyanate and Thiocyanate Melts and the Crystal Structure of Potassium Melonate, $K_3[C_6N_7(NCN)_3]$. *Eur. J. Inorg. Chem.* **2009** (33), 4972–4981. DOI: 10.1002/ejic.200900585.

(82) Qiu, C.; Xu, Y.; Fan, X.; Xu, D.; Tandiana, R.; Ling, X.; Jiang, Y.; Liu, C.; Yu, L.; Chen, W.; Su, C. Highly Crystalline K-Intercalated Polymeric Carbon Nitride for Visible-Light Photocatalytic Alkenes and Alkynes Deuterations. *Adv. Sci.* **2019**, *6* (1), 1801403. DOI: 10.1002/advs.201801403.

(83) Wu, M.; Yan, J.-M.; Tang, X.-n.; Zhao, M.; Jiang, Q. Synthesis of Potassium-Modified Graphitic Carbon Nitride with High Photocatalytic Activity for Hydrogen Evolution. *ChemSusChem* **2014**, *7* (9), 2654–2658. DOI: 10.1002/cssc.201402180.

(84) Lin, L.; Ou, H.; Zhang, Y.; Wang, X. Tri- s -triazine-Based Crystalline Graphitic Carbon Nitrides for Highly Efficient Hydrogen Evolution Photocatalysis. *ACS Catal.* **2016**, *6* (6), 3921–3931. DOI: 10.1021/acscatal.6b00922.

(85) Markushyna, Y.; Lamagni, P.; Teutloff, C.; Catalano, J.; Lock, N.; Zhang, G.; Antonietti, M.; Savateev, A. Green radicals of potassium poly(heptazine imide) using light and benzylamine. *J. Mater. Chem. A* **2019**, *7* (43), 24771–24775. DOI: 10.1039/C9TA09500D.

(86) Lin, L.; Ren, W.; Wang, C.; Asiri, A. M.; Zhang, J.; Wang, X. Crystalline carbon nitride semiconductors prepared at different temperatures for photocatalytic hydrogen production. *Appl. Catal. B* **2018**, *231*, 234–241. DOI: 10.1016/j.apcatb.2018.03.009.

(87) Komatsu, T. Prototype carbon nitrides similar to the symmetric triangular form of melon. *J. Mater. Chem.* **2001**, *11* (3), 802–803. DOI: 10.1039/b007165j.

(88) Kessler, F. K.; Schnick, W. From Heptazines to Triazines - On the Formation of Poly(triazine imide). *Z. anorg. allg. Chem.* **2019**, *645* (12), 857–862. DOI: 10.1002/zaac.201900043.

(89) Kroke, E.; Schwarz, M.; Horath-Bordon, E.; Kroll, P.; Noll, B.; Norman, A. D. Tri-s-triazine derivatives. Part I. From trichloro-tri-s-triazine to graphitic C_3N_4 structures. *New J. Chem.* **2002**, *26* (5), 508–512. DOI: 10.1039/B111062B.

(90) Sehnert, J.; Baerwinkel, K.; Senker, J. Ab Initio Calculation of Solid-State NMR Spectra for Different Triazine and Heptazine Based Structure Proposals of g-C_3N_4. *J. Phys. Chem. B* **2007**, *111* (36), 10671–10680. DOI: 10.1021/jp072001k.

(91) Jürgens, B.; Irran, E.; Senker, J.; Kroll, P.; Müller, H.; Schnick, W. Melem (2,5,8-Triamino-tri- s -triazine), an Important Intermediate during Condensation of Melamine Rings to Graphitic Carbon Nitride: Synthesis, Structure Determination by X-ray Powder Diffractometry, Solid-State NMR, and Theoretical Studies. *J. Am. Chem. Soc.* **2003**, *125* (34), 10288–10300. DOI: 10.1021/ja0357689.

(92) Arazoe, H.; Miyajima, D.; Akaike, K.; Araoka, F.; Sato, E.; Hikima, T.; Kawamoto, M.; Aida, T. An autonomous actuator driven by fluctuations in ambient humidity. *Nat. Mater.* **2016**, *15* (10), 1084–1089. DOI: 10.1038/nmat4693.

(93) Qin, J.; Barrio, J.; Peng, G.; Tzadikov, J.; Abisdris, L.; Volokh, M.; Shalom, M. Direct growth of uniform carbon nitride layers with extended optical absorption towards efficient water-splitting photoanodes. *Nat. Commun.* **2020**, *11* (1), 4701. DOI: 10.1038/s41467-020-18535-0.

(94) Xu, J.; Brenner, T. J. K.; Chabanne, L.; Neher, D.; Antonietti, M.; Shalom, M. Liquid-Based Growth of Polymeric Carbon Nitride Layers and Their Use in a Mesostructured Polymer Solar Cell with V_{oc} Exceeding 1 V. *J. Am. Chem. Soc.* **2014**, *136* (39), 13486–13489. DOI: 10.1021/ja508329c.

(95) Haase, F.; Lotsch, B. V. Solving the COF trilemma: towards crystalline, stable and functional covalent organic frameworks. *Chem. Soc. Rev.* **2020**, *49* (23), 8469–8500. DOI: 10.1039/D0CS01027H.

(96) Wang, L.; Sahabudeen, H.; Zhang, T.; Dong, R. Liquid-interface-assisted synthesis of covalent-organic and metal-organic two-dimensional crystalline polymers. *npj 2D Mater. Appl.* **2018**, *2* (1), 26. DOI: 10.1038/s41699-018-0071-5.

(97) Lau, V. W.-h.; Yu, V. W.-z.; Ehrat, F.; Botari, T.; Moudrakovski, I.; Simon, T.; Duppel, V.; Medina, E.; Stolarczyk, J.; Feldmann, J.; Blum, V.; Lotsch, B. V. Urea-Modified Carbon Nitrides: Enhancing Photocatalytic Hydrogen Evolution by Rational Defect Engineering. *Adv. Energy Mater.* **2017**, 1602251. DOI: 10.1002/aenm.201602251.

(98) Wang, W.; Zhang, H.; Zhang, S.; Liu, Y.; Wang, G.; Sun, C.; Zhao, H. Potassium-Ion-Assisted Regeneration of Active Cyano Groups in Carbon Nitride Nanoribbons: Visible-Light-Driven Photocatalytic Nitrogen Reduction. *Angew. Chem. Int. Ed.* **2019**, *58* (46), 16644–16650. DOI: 10.1002/anie.201908640.

(99) Hu, S.; Li, F.; Fan, Z.; Wang, F.; Zhao, Y.; Lv, Z. Band gap-tunable potassium doped graphitic carbon nitride with enhanced mineralization ability. *Dalton Trans.* **2015**, *44* (3), 1084–1092. DOI: 10.1039/C4DT02658F.

(100) Wang, Y.; Zhao, S.; Zhang, Y.; Fang, J.; Zhou, Y.; Yuan, S.; Zhang, C.; Chen, W. One-pot synthesis of K-doped g-C_3N_4 nanosheets with enhanced photocatalytic hydrogen production under visible-light irradiation. *Appl. Surf. Sci.* **2018**, *440*, 258–265. DOI: 10.1016/j.apsusc.2018.01.091.

(101) Chen, L.; Zhu, D.; Li, J.; Wang, X.; Zhu, J.; Francis, P. S.; Zheng, Y. Sulfur and potassium co-doped graphitic carbon nitride for highly enhanced photocatalytic hydrogen evolution. *Appl. Catal. B* **2020**, *273*, 119050. DOI: 10.1016/j.apcatb.2020.119050.

(102) Thomas, A.; Fischer, A.; Goettmann, F.; Antonietti, M.; Müller, J.-O.; Schlögl, R.; Carlsson, J. M. Graphitic carbon nitride materials: variation of structure and morphology and their use as metal-free catalysts. *J. Mater. Chem.* **2008**, *18* (41), 4893. DOI: 10.1039/b800274f.

(103) Grimmer, A.-R.; Blümich, B. Introduction to Solid-State NMR. In *Solid-State NMR I Methods*; Blümich, B., Ed.; Springer Berlin Heidelberg: Berlin, Heidelberg, 1994; pp 1–62.

(104) Takanabe, K. Photocatalytic Water Splitting: Quantitative Approaches toward Photocatalyst by Design. *ACS Catal.* **2017**, *7* (11), 8006–8022. DOI: 10.1021/acscatal.7b02662.

(105) Chen, S.; Takata, T.; Domen, K. Particulate photocatalysts for overall water splitting. *Nat. Rev. Mater.* **2017**, *2* (10), 17050. DOI: 10.1038/natrevmats.2017.50.

(106) Walter, M. G.; Warren, E. L.; McKone, J. R.; Boettcher, S. W.; Mi, Q.; Santori, E. A.; Lewis, N. S. Solar Water Splitting Cells. *Chem. Rev.* **2010**, *110* (11), 6446–6473. DOI: 10.1021/cr1002326.

(107) Osterloh, F. E. Photocatalysis versus Photosynthesis: A Sensitivity Analysis of Devices for Solar Energy Conversion and Chemical Transformations. *ACS Energy Lett.* **2017**, *2* (2), 445–453. DOI: 10.1021/acsenergylett.6b00665.

(108) Zhu, S.; Wang, D. Photocatalysis: Basic Principles, Diverse Forms of Implementations and Emerging Scientific Opportunities. *Adv. Energy Mater.* **2017**, *7* (23), 1700841. DOI: 10.1002/aenm.201700841.

(109) de Levie, R. The electrolysis of water. *J. Electroanal. Chem.* **1999**, *476* (1), 92–93. DOI: 10.1016/S0022-0728(99)00365-4.

(110) Fujishima, A.; Honda, K. Electrochemical Photolysis of Water at a Semiconductor Electrode. *Nature* **1972**, *238* (5358), 37–38. DOI: 10.1038/238037a0.

(111) Yoshikawa, K.; Kawasaki, H.; Yoshida, W.; Irie, T.; Konishi, K.; Nakano, K.; Uto, T.; Adachi, D.; Kanematsu, M.; Uzu, H.; Yamamoto, K. Silicon heterojunction solar cell with interdigitated back contacts for a photoconversion efficiency over 26%. *Nat. Energy* **2017**, *2* (5), 17032. DOI: 10.1038/nenergy.2017.32.

(112) Wang, X.; Blechert, S.; Antonietti, M. Polymeric Graphitic Carbon Nitride for Heterogeneous Photocatalysis. *ACS Catal.* **2012**, *2* (8), 1596–1606. DOI: 10.1021/cs300240x.

(113) Section 10 - Solar. In *Handbook of Energy*; Cutler J. Cleveland, Christopher Morris, Eds.; Elsevier, 2013; pp 405–450. DOI: 10.1016/B978-0-08-046405-3.00010-3.

(114) Guijarro, N.; Prévot, M. S.; Sivula, K. Surface modification of semiconductor photoelectrodes. *Phys. Chem. Chem. Phys.* **2015**, *17* (24), 15655–15674. DOI: 10.1039/C5CP01992C.

(115) Zelewski, S. J.; Nawrot, K. C.; Zak, A.; Gladysiewicz, M.; Nyk, M.; Kudrawiec, R. Exciton Binding Energy of Two-Dimensional Highly Luminescent Colloidal Nanostructures Determined

from Combined Optical and Photoacoustic Spectroscopies. *J. Phys. Chem. Lett.* **2019**, *10* (12), 3459–3464. DOI: 10.1021/acs.jpclett.9b00591.

(116) Zhang, J.; Zhang, M.; Sun, R.-Q.; Wang, X. A Facile Band Alignment of Polymeric Carbon Nitride Semiconductors to Construct Isotype Heterojunctions. *Angew. Chem. Int. Ed.* **2012**, *51* (40), 10145–10149. DOI: 10.1002/anie.201205333.

(117) Piliego, C.; Loi, M. A. Charge transfer state in highly efficient polymer–fullerene bulk heterojunction solar cells. *J. Mater. Chem.* **2012**, *22* (10), 4141–4150. DOI: 10.1039/C2JM15027A.

(118) Zhang, M.; Wang, X. Two dimensional conjugated polymers with enhanced optical absorption and charge separation for photocatalytic hydrogen evolution. *Energy Environ. Sci.* **2014**, *7* (6), 1902–1906. DOI: 10.1039/C3EE44189J.

(119) Wei, W.; Jacob, T. Strong excitonic effects in the optical properties of graphitic carbon nitride g-C_3N_4 from first principles. *Phys. Rev. B* **2013**, *87* (8), 85202. DOI: 10.1103/PhysRevB.87.085202.

(120) Simon, T.; Carlson, M. T.; Stolarczyk, J. K.; Feldmann, J. Electron Transfer Rate vs Recombination Losses in Photocatalytic H_2 Generation on Pt-Decorated CdS Nanorods. *ACS Energy Lett.* **2016**, *1* (6), 1137–1142. DOI: 10.1021/acsenergylett.6b00468.

(121) Weiss, T. P.; Bissig, B.; Feurer, T.; Carron, R.; Buecheler, S.; Tiwari, A. N. Bulk and surface recombination properties in thin film semiconductors with different surface treatments from time-resolved photoluminescence measurements. *Sci. Rep.* **2019**, *9* (1), 5385. DOI: 10.1038/s41598-019-41716-x.

(122) Osterloh, F. E. Inorganic nanostructures for photoelectrochemical and photocatalytic water splitting. *Chem. Soc. Rev.* **2013**, *42* (6), 2294–2320. DOI: 10.1039/C2CS35266D.

(123) Gershon, T.; Shin, B.; Bojarczuk, N.; Hopstaken, M.; Mitzi, D. B.; Guha, S. The Role of Sodium as a Surfactant and Suppressor of Non-Radiative Recombination at Internal Surfaces in Cu_2ZnSnS_4. *Adv. Energy Mater.* **2015**, *5* (2), 1400849. DOI: 10.1002/aenm.201400849.

(124) Ong, W.-J.; Tan, L.-L.; Ng, Y. H.; Yong, S.-T.; Chai, S.-P. Graphitic Carbon Nitride (g-C_3N_4)-Based Photocatalysts for Artificial Photosynthesis and Environmental Remediation: Are We a Step Closer To Achieving Sustainability? *Chem. Rev.* **2016**, *116* (12), 7159–7329. DOI: 10.1021/acs.chemrev.6b00075.

(125) Jang, J. S.; Kim, H. G.; Lee, J. S. Heterojunction semiconductors: A strategy to develop efficient photocatalytic materials for visible light water splitting. *Catal. Today* **2012**, *185* (1), 270–277. DOI: 10.1016/j.cattod.2011.07.008.

(126) Tung, R. T. The physics and chemistry of the Schottky barrier height. *Appl. Phys. Rev.* **2014**, *1* (1), 11304. DOI: 10.1063/1.4858400.

(127) Li, J.; Wu, N. Semiconductor-based photocatalysts and photoelectrochemical cells for solar fuel generation: a review. *Catal. Sci. Technol.* **2015**, *5* (3), 1360–1384. DOI: 10.1039/C4CY00974F.

(128) Morales-Guio, C. G.; Stern, L.-A.; Hu, X. Nanostructured hydrotreating catalysts for electrochemical hydrogen evolution. *Chem. Soc. Rev.* **2014**, *43* (18), 6555–6569. DOI: 10.1039/C3CS60468C.

(129) Trasatti, S. Work function, electronegativity, and electrochemical behaviour of metals: III. Electrolytic hydrogen evolution in acid solutions. *J. Electroanal. Chem. Interf. Electrochem.* **1972**, *39* (1), 163–184. DOI: 10.1016/S0022-0728(72)80485-6.

(130) Man, I. C.; Su, H.-Y.; Calle-Vallejo, F.; Hansen, H. A.; Martínez, J. I.; Inoglu, N. G.; Kitchin, J.; Jaramillo, T. F.; Nørskov, J. K.; Rossmeisl, J. Universality in Oxygen Evolution Electrocatalysis on Oxide Surfaces. *ChemCatChem* **2011**, *3* (7), 1159–1165. DOI: 10.1002/cctc.201000397.

(131) Quaino, P.; Juarez, F.; Santos, E.; Schmickler, W. Volcano plots in hydrogen electrocatalysis - uses and abuses. *Beilstein J. Nanotechnol.* **2014**, *5*, 846–854. DOI: 10.3762/bjnano.5.96.

(132) Kato, H.; Asakura, K.; Kudo, A. Highly Efficient Water Splitting into H_2 and O_2 over Lanthanum-Doped $NaTaO_3$ Photocatalysts with High Crystallinity and Surface Nanostructure. *J. Am. Chem. Soc.* **2003**, *125* (10), 3082–3089. DOI: 10.1021/ja027751g.

(133) Bard, A. J. Photoelectrochemistry. *Science* **1980**, *207* (4427), 139–144. DOI: 10.1126/science.207.4427.139.

(134) Moniz, S. J. A.; Shevlin, S. A.; Martin, D. J.; Guo, Z.-X.; Tang, J. Visible-light driven heterojunction photocatalysts for water splitting – a critical review. *Energy Environ. Sci.* **2015**, *8* (3), 731–759. DOI: 10.1039/C4EE03271C.

(135) Yang, J.; Wang, D.; Han, H.; Li, C. Roles of Cocatalysts in Photocatalysis and Photoelectrocatalysis. *Acc. Chem. Res.* **2013**, *46* (8), 1900–1909. DOI: 10.1021/ar300227e.

(136) Haschke, S.; Mader, M.; Schlicht, S.; Roberts, A. M.; Angeles-Boza, A. M.; Barth, J. A. C.; Bachmann, J. Direct oxygen isotope effect identifies the rate-determining step of electrocatalytic OER at an oxidic surface. *Nat. Commun.* **2018**, *9* (1), 4565. DOI: 10.1038/s41467-018-07031-1.

(137) Chen, X.; Shen, S.; Guo, L.; Mao, S. S. Semiconductor-based photocatalytic hydrogen generation. *Chem. Rev.* **2010**, *110* (11), 6503–6570. DOI: 10.1021/cr1001645.

(138) Kröger, J.; Jiménez-Solano, A.; Savasci, G.; Rovó, P.; Moudrakovski, I.; Küster, K.; Schlomberg, H.; Vignolo-González, H. A.; Duppel, V.; Grunenberg, L.; Dayan, C. B.; Sitti, M.; Podjaski, F.; Ochsenfeld, C.; Lotsch, B. V. Interfacial Engineering for Improved Photocatalysis in a Charge Storing 2D Carbon Nitride: Melamine Functionalized Poly(heptazine imide). *Adv. Energy Mater.* **2021**, *11*, 2003016. DOI: 10.1002/aenm.202003016.

(139) Schneider, J.; Bahnemann, D. W. Undesired Role of Sacrificial Reagents in Photocatalysis. *J. Phys. Chem. Lett.* **2013**, *4* (20), 3479–3483. DOI: 10.1021/jz4018199.

(140) Mesa, C. A.; Kafizas, A.; Francàs, L.; Pendlebury, S. R.; Pastor, E.; Ma, Y.; Le Formal, F.; Mayer, M. T.; Grätzel, M.; Durrant, J. R. Kinetics of Photoelectrochemical Oxidation of Methanol on Hematite Photoanodes. *J. Am. Chem. Soc.* **2017**, *139* (33), 11537–11543. DOI: 10.1021/jacs.7b05184.

(141) Kasap, H.; Caputo, C. A.; Martindale, Benjamin C. M.; Godin, R.; Lau, V. W.-h.; Lotsch, B. V.; Durrant, J. R.; Reisner, E. Solar-Driven Reduction of Aqueous Protons Coupled to Selective Alcohol Oxidation with a Carbon Nitride–Molecular Ni Catalyst System. *J. Am. Chem. Soc.* **2016**, *138* (29), 9183–9192. DOI: 10.1021/jacs.6b04325.

(142) Pellegrin, Y.; Odobel, F. Sacrificial electron donor reagents for solar fuel production. *C. R. Chimie* **2017**, *20* (3), 283–295. DOI: 10.1016/j.crci.2015.11.026.

(143) Savateev, A.; Kurpil, B.; Mishchenko, A.; Zhang, G.; Antonietti, M. A "waiting" carbon nitride radical anion:A charge storage material and key intermediate in direct C-H thiolation of methylarenes using elemental sulfur as the "S"-source. *Chem. Sci.* **2018**, *9* (14), 3584–3591. DOI: 10.1039/c8sc00745d.

(144) Farràs, P.; Di Giovanni, C.; Clifford, J. N.; Palomares, E.; Llobet, A. H_2 generation and sulfide to sulfoxide oxidation with H_2O and sunlight with a model photoelectrosynthesis cell. *Coord. Chem. Rev.* **2015**, *304-305*, 202–208. DOI: 10.1016/j.ccr.2014.10.007.

(145) Bajada, M. A.; Vijeta, A.; Savateev, A.; Zhang, G.; Howe, D.; Reisner, E. Visible-Light Flow Reactor Packed with Porous Carbon Nitride for Aerobic Substrate Oxidations. *ACS Appl. Mater. Interfaces* **2020**, *12* (7), 8176–8182. DOI: 10.1021/acsami.9b19718.

(146) Uekert, T.; Kasap, H.; Reisner, E. Photoreforming of Nonrecyclable Plastic Waste over a Carbon Nitride/Nickel Phosphide Catalyst. *J. Am. Chem. Soc.* **2019**, *141* (38), 15201–15210. DOI: 10.1021/jacs.9b06872.

(147) Lin, L.; Wang, C.; Ren, W.; Ou, H.; Zhang, Y.; Wang, X. Photocatalytic overall water splitting by conjugated semiconductors with crystalline poly(triazine imide) frameworks. *Chem. Sci.* **2017**, *8* (8), 5506–5511. DOI: 10.1039/c7sc00900c.

(148) Zheng, D.; Cao, X.-N.; Wang, X. Precise Formation of a Hollow Carbon Nitride Structure with a Janus Surface To Promote Water Splitting by Photoredox Catalysis. *Angew. Chem. Int. Ed.* **2016**, *55* (38), 11512–11516. DOI: 10.1002/anie.201606102.

(149) Liu, J.; Liu, Y.; Liu, N.; Han, Y.; Zhang, X.; Huang, H.; Lifshitz, Y.; Lee, S.-T.; Zhong, J.; Kang, Z. Water splitting. Metal-free efficient photocatalyst for stable visible water splitting via a two-electron pathway. *Science* **2015**, *347* (6225), 970–974. DOI: 10.1126/science.aaa3145.

(150) Schröder, M.; Kailasam, K.; Borgmeyer, J.; Neumann, M.; Thomas, A.; Schomäcker, R.; Schwarze, M. Hydrogen Evolution Reaction in a Large-Scale Reactor using a Carbon Nitride Photocatalyst under Natural Sunlight Irradiation. *Energy Technol.* **2015**, *3* (10), 1014–1017. DOI: 10.1002/ente.201500142.

(151) Sagara, N.; Kamimura, S.; Tsubota, T.; Ohno, T. Photoelectrochemical CO_2 reduction by a p-type boron-doped g-C_3N_4 electrode under visible light. *Appl. Catal. B* **2016**, *192*, 193–198. DOI: 10.1016/j.apcatb.2016.03.055.

(152) Huang, Z.-F.; Song, J.; Pan, L.; Wang, Z.; Zhang, X.; Zou, J.-J.; Mi, W.; Zhang, X.; Wang, L. Carbon nitride with simultaneous porous network and O-doping for efficient solar-energy-driven hydrogen evolution. *Nano Energy* **2015**, *12*, 646–656. DOI: 10.1016/j.nanoen.2015.01.043.

(153) Wang, Y.; Di, Y.; Antonietti, M.; Li, H.; Chen, X.; Wang, X. Excellent Visible-Light Photocatalysis of Fluorinated Polymeric Carbon Nitride Solids. *Chem. Mater.* **2010**, *22* (18), 5119–5121. DOI: 10.1021/cm1019102.

(154) Guo, S.; Deng, Z.; Li, M.; Jiang, B.; Tian, C.; Pan, Q.; Fu, H. Phosphorus-Doped Carbon Nitride Tubes with a Layered Micro-nanostructure for Enhanced Visible-Light Photocatalytic Hydrogen Evolution. *Angew. Chem. Int. Ed.* **2016**, *55* (5), 1830–1834. DOI: 10.1002/anie.201508505.

(155) Zhang, J.; Sun, J.; Maeda, K.; Domen, K.; Liu, P.; Antonietti, M.; Fu, X.; Wang, X. Sulfur-mediated synthesis of carbon nitride: Band-gap engineering and improved functions for photocatalysis. *Energy Environ. Sci.* **2011**, *4* (3), 675–678. DOI: 10.1039/C0EE00418A.

(156) Zhou, L.; Zhang, H.; Sun, H.; Liu, S.; Tade, M. O.; Wang, S.; Jin, W. Recent advances in non-metal modification of graphitic carbon nitride for photocatalysis: a historic review. *Catal. Sci. Technol.* **2016**, *6* (19), 7002–7023. DOI: 10.1039/C6CY01195K.

(157) Niu, P.; Zhang, L.; Liu, G.; Cheng, H.-M. Graphene-Like Carbon Nitride Nanosheets for Improved Photocatalytic Activities. *Adv. Funct. Mater.* **2012**, *22* (22), 4763–4770. DOI: 10.1002/adfm.201200922.

(158) Corp, K. L.; Schlenker, C. W. Ultrafast Spectroscopy Reveals Electron-Transfer Cascade That Improves Hydrogen Evolution with Carbon Nitride Photocatalysts. *J. Am. Chem. Soc.* **2017**, *139* (23), 7904–7912. DOI: 10.1021/jacs.7b02869.

(159) Jiang, L.; Yuan, X.; Zeng, G.; Liang, J.; Wu, Z.; Wang, H. Construction of an all-solid-state Z-scheme photocatalyst based on graphite carbon nitride and its enhancement to catalytic activity. *Environ. Sci. Nano* **2018**, *5* (3), 599–615. DOI: 10.1039/C7EN01031A.

(160) Takanabe, K.; Kamata, K.; Wang, X.; Antonietti, M.; Kubota, J.; Domen, K. Photocatalytic hydrogen evolution on dye-sensitized mesoporous carbon nitride photocatalyst with magnesium phthalocyanine. *Phys. Chem. Chem. Phys.* **2010**, *12* (40), 13020–13025. DOI: 10.1039/C0CP00611D.

(161) Zhang, G.; Lan, Z.-A.; Wang, X. Surface engineering of graphitic carbon nitride polymers with cocatalysts for photocatalytic overall water splitting. *Chem. Sci.* **2017**, *8* (8), 5261–5274. DOI: 10.1039/C7SC01747B.

(162) Zhao, H.; Wang, J.; Dong, Y.; Jiang, P. Noble-Metal-Free Iron Phosphide Cocatalyst Loaded Graphitic Carbon Nitride as an Efficient and Robust Photocatalyst for Hydrogen Evolution under Visible Light Irradiation. *ACS Sustain. Chem. Eng.* **2017**, *5* (9), 8053–8060. DOI: 10.1021/acssuschemeng.7b01665.

(163) Schwinghammer, K.; Hug, S.; Mesch, M. B.; Senker, J.; Lotsch, B. V. Phenyl-Triazine Oligomers for Light-Driven Hydrogen Evolution. *Energy Environ. Sci.* **2015.** DOI: 10.1039/C5EE02574E.

(164) Wu, H.-Z.; Liu, L.-M.; Zhao, S.-J. The effect of water on the structural, electronic and photocatalytic properties of graphitic carbon nitride. *Phys. Chem. Chem. Phys.* **2014**, *16* (7), 3299–3304. DOI: 10.1039/C3CP54333A.

(165) Zuluaga, S.; Liu, L.-H.; Shafiq, N.; Rupich, S. M.; Veyan, J.-F.; Chabal, Y. J.; Thonhauser, T. Structural band-gap tuning in g-C_3N_4. *Phys. Chem. Chem. Phys.* **2015**, *17* (2), 957–962. DOI: 10.1039/C4CP05164E.

(166) Zhu, B.; Cheng, B.; Zhang, L.; Yu, J. Review on DFT calculation of s-triazine-based carbon nitride. *Carbon Energy* **2019**, *1* (1), 32–56. DOI: 10.1002/cey2.1.

(167) Katharina Schwinghammer. Synthesis and Characterization of Triazine-Based Frameworks for Light-Driven Hydrogen Evolution, Doctoral Thesis, University of Munich (LMU) **2016**.

(168) Lau, V. W.-h.; Klose, D.; Kasap, H.; Podjaski, F.; Pignié, M.-C.; Reisner, E.; Jeschke, G.; Lotsch, B. V. Dark Photocatalysis: Storage of Solar Energy in Carbon Nitride for Time-Delayed Hydrogen Generation. *Angew. Chem. Int. Ed.* **2017**, *56* (2), 510–514. DOI: 10.1002/anie.201608553.

(169) Podjaski, F.; Kröger, J.; Lotsch, B. V. Toward an Aqueous Solar Battery:Direct Electrochemical Storage of Solar Energy in Carbon Nitrides. *Adv. Mater.* **2018**, *30* (9), 1705477. DOI: 10.1002/adma.201705477.

2 Structural Insights into Poly(Heptazine Imides): A Light-Storing Carbon Nitride Material for Dark Photocatalysis

Hendrik Schlomberg, Julia Kröger, Gökcen Savasci, Maxwell W. Terban, Sebastian Bette, Igor Moudrakovski, Viola Duppel, Filip Podjaski, Renée Siegel, Jürgen Senker, Robert E. Dinnebier, Christian Ochsenfeld and Bettina V. Lotsch

Published in: Chem. Mater. **2019**, *31* (18), 7478–7486.
DOI: https://pubs.acs.org/doi/10.1021/acs.chemmater.9b02199
Formatting and number of figures were changed.
Adapted with permission from The American Chemical Society

Abstract

Solving the structure of carbon nitrides has been a long-standing challenge due to the low crystallinity and complex structures observed within this class of earth-abundant photocatalysts. Herein, we report on two-dimensional layered potassium poly(heptazine imide) (K-PHI) and its proton-exchanged counterpart (H-PHI), obtained by ionothermal synthesis using a molecular precursor route. We present a comprehensive analysis of the in-plane and three-dimensional structure of PHI. Transmission electron microscopy and solid-state NMR spectroscopy, supported by quantum-chemical calculations, suggest a planar, imide-bridged heptazine backbone with trigonal symmetry in both K-PHI and H-PHI, whereas pair distribution function analyses and X-ray powder diffraction using recursive-like simulations of planar defects point to a structure-directing function of the pore content. While the out-of-plane structure of K-PHI exhibits a unidirectional layer offset, mediated by hydrated potassium ions, H-PHI is characterized by a high degree of stacking faults due to the weaker structure directing influence of pore water. Structure–property relationships in PHI reveal that a loss of in-plane coherence, materializing in smaller lateral platelet dimensions and increased terminal cyanamide groups, correlates with improved photocatalytic performance. Size-optimized H-PHI is highly active toward photocatalytic hydrogen evolution, with a rate of 3363 μmol/gh H_2 placing it on par with the most active carbon nitrides. K- and H-PHI adopt a uniquely long-lived photoreduced polaronic state in which light-induced electrons are stored for more than 6 h in the dark and released upon addition of a Pt cocatalyst. This work highlights the importance of structure–property relationships in carbon nitrides for the rational design of highly active hydrogen evolution photocatalysts.

2.1 Introduction

A new class of (semi)crystalline two-dimensional (2D) carbon nitrides has emerged over the past few years, which exhibits outstanding photocatalytic performance[1–3] along with intriguing photophysical properties, such as the potential for time-delayed fuel production ("dark photocatalysis"),[4] which also make them attractive candidate materials for solar batteries.[5] A hallmark of this carbon nitride family is its ability to store electrons in the form of a long-lived photoreduced state,[4,6,7] which allows for the separation of light absorption (the light reaction) and catalytic conversion (the dark reaction) akin to natural photosynthesis. This material has been postulated to exhibit a 2D poly(heptazine imide) (PHI)-based structure, but so far a comprehensive elucidation of its local and long-range structure is lacking. PHI has been synthesized by both, molecular precursor approaches[8,9] as well as top down strategies starting from the well-known melon polymer.[2,10] And yet, even though the synthesis procedures may vary widely, the use of salt melts, i.e., ionothermal synthesis, seems to be vital to all of these approaches.[2,8–10]

Ionothermal synthesis routes often yield fundamentally different products as compared to high-temperature solid-state approaches. A prominent example is the synthesis of melon, which is often referred to as graphitic carbon nitride, g-C_3N_4. Although the solid-state synthesis of melon yields a one-dimensional heptazine-based polymer, 2D networks are typically formed by a salt-melt approach using the same types of precursors. Under these conditions, the ionic flux and its components, typically alkali metal halides, serve as a high-temperature solvent and structure-directing agent at the same time.[11–13] The structure-directing influence of alkali ions has been observed by Savateev et al. and is also known to be the governing factor during the formation of secondary building units in zeolites.[9,14] Interestingly, the composition of the melt also seems to have a profound influence on the type of carbon nitride backbone—triazine or heptazine-based—that is formed during the reaction.[8]

Herein, we have used a molecular building block approach to synthesize highly crystalline potassium containing PHI terminated by cyanamide(NCN^-)-functional groups, abbreviated as potassium PHI (K-PHI), and its metal-free counterpart H-PHI. A comprehensive investigation of their local and long-range structures has been carried out through a combination of electron diffraction (ED) and transmission electron microscopy (TEM) imaging, solid-state nuclear magnetic resonance (ssNMR) spectroscopy, supported by quantum-chemical calculations, X-ray powder diffraction (XRPD), and pair distribution function analysis (PDF). We show that both materials feature an extended 2D network constituted by tri-s-triazine (heptazine) units connected via imide bridges. These layers assemble in either ordered or disordered long-range stacking relationships driven by interactions with the pore content, resulting in hitherto unknown structural modifications in this PHI family.

2.2 Results and Discussion

The ionothermal bottom-up synthesis of PHI starts from the molecular precursors potassium melonate, dicyandiamide, and potassium thiocyanate (KSCN), which are heated under their autogenous pressure in an ampoule to yield highly crystalline potassium poly(heptazine imide) (K-PHI), terminated with NCN-functional groups. In contrast to other PHI-derived materials (mainly synthesized from LiCl/KCl eutectics), the herein discussed synthesis is based on KSCN as the salt component and hence flux. When K-PHI is treated with dilute acid, it is converted into the proton-bearing H-PHI, thus pointing to the Brønsted acid–base character of the polymer.[9] Note that the reaction is insensitive to which acid (e.g., HCl, H_3PO_4, H_2SO_4, or $HClO_4$) is used for the transformation (Figure A 50-52). In the following text, we elucidate the local structure of K-PHI and H-PHI by solid-state NMR spectroscopy and characterize the 2D projection of the structure by means of TEM, whereas XRPD, PDF analyses, and recursive-like simulations of planar defects lead to the classification of the material in the third dimension.

TEM Analysis

The TEM image in Figure 2.1a reveals the sheetlike morphology of the crystallites and high crystallinity of the carbon nitride backbone over a large area of up to several 100 nm (for overview TEM images see Supporting Information Figure A 1 and A3). The lattice fringes correspond to an interval of 11 Å within the layer planes, illustrated by the high-resolution (HR) TEM image in Figure 2.1a. The good agreement between the measured (Figure 2.1b) and simulated (1c) selected area electron diffraction (SAED) patterns along the [001] zone axis based on the structural model shown in Figure 2.1d indicates trigonal layer symmetry of the PHI backbone in H-PHI. The fast Fourier transformation (FFT) obtained from large crystallites (Figure 2.1a, inset) also fits the depicted SAED pattern. The 100 lattice spacing of 11 Å corresponds to the pore-to-pore distance of 12.8 Å and is consistent with a hexagonal arrangement of trigonal pores and a 2D network topology, similar to that found in the triazine analogue poly(triazine imide) (PTI).[11,12] The TEM data suggest that ideal H-PHI layers crystallize with trigonal symmetry, forming a "graphitic" 2D framework of imide-bridged heptazine building units akin to melamine-intercalated PHI, which crystallizes in the space group *P*31*m*.[15] Particularly in the H-PHI case, slight intensity deviations from the perfect hexagonal distribution of the electron diffraction spots (Figure 2.1b) and the fact that the diffraction data of H-PHI are relatively tolerant against tilting of the specimen for up to ±10° indicate structural disorder along the [001] zone axis. Intensity deviations might also arise from losing pore content (i.e., water) in ultra high vacuum and local heating through the electron beam, which may induce on-spot incipient degradation and enable the layers to shift to the

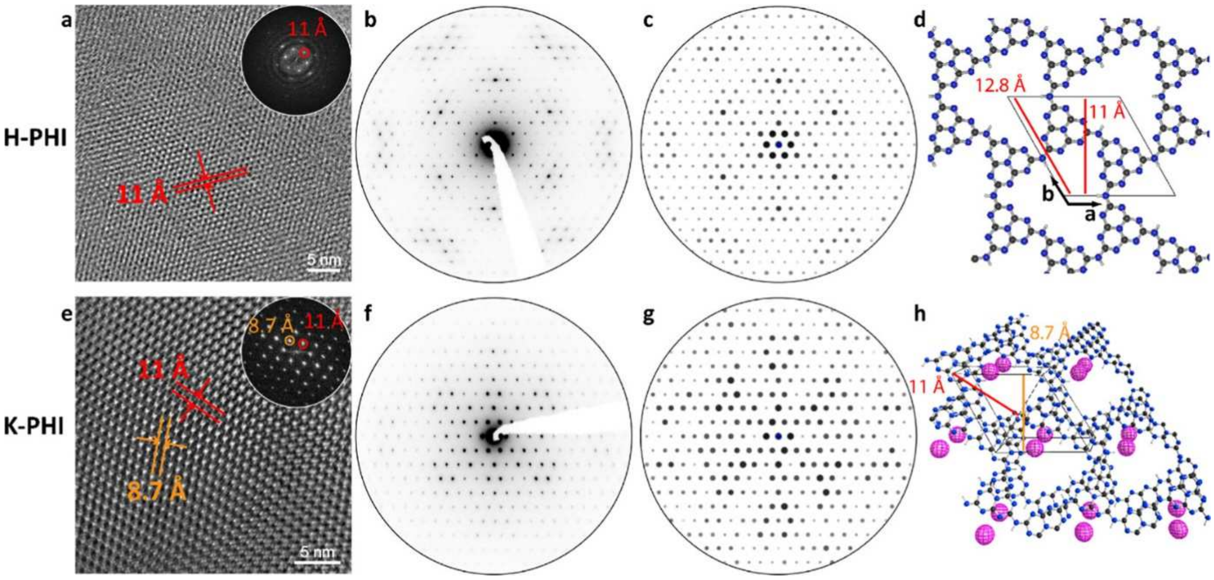

Figure 2.1. (a) High-resolution TEM image of H-PHI clearly revealing lattice fringes over extended areas; (b) SAED pattern and (c) simulated SAED pattern of the [001] zone axis of H-PHI, based on a theoretical trigonal cell model depicted in (d). (e–g) cover the corresponding figures for K-PHI. Insets show the FFT confirming the 6-fold symmetry of the diffraction pattern for H-PHI and the reduced monoclinic layer symmetry for K-PHI, respectively. (h) Structural model obtained from Rietveld refinement for K-PHI (see Figure 2.3b); water molecules inside the pores were omitted for better visibility.

eclipsed case, as also seen in thermogravimetric XRPD experiments in Figure A 27. The diffraction spots of K-PHI (Figure 2.1f, [001] zone axis) imply that the material exhibits monoclinic layer symmetry. The SAED pattern can be reproduced by ED simulation with corresponding distances of 11 Å for the $\bar{1}10$ and 8.7 Å for the 100 reflection (Figure 2.1g). The HR-TEM image (Figure 2.1e) also points toward the existence of large crystalline domains, with the FFT (inset) reproducing the pattern obtained from the simulation in Figure 2.1g. The difference in symmetry suggests an altered stacking behavior of the PHI backbones in K-PHI and H-PHI, likely driven by the pore constituents (water in H-PHI or potassium ions in K-PHI). Note that the water content nearly doubles from 10 wt% for K-PHI to 20 wt% for H-PHI, determined by combustion analysis and inductively coupled plasma (Table A 8 and A9).

Solid-State NMR Spectroscopy

To probe the local structure of PHI, especially the intralayer connectivity and the distribution of cations within the pores, ^{13}C, ^{15}N, ^{14}N, and ^{1}H ssNMR spectra were recorded for K-PHI and compared with those of H-PHI. Figure 2.2a-i shows the ^{13}C direct excitation, ^{15}N cross-polarization (CP) and ^{1}H ssNMR spectra of K-PHI (top row) and H-PHI (middle row), as well as the ^{13}C–^{15}N 2D heteronuclear correlation (HETCOR)[16] spectrum of K-PHI, the ^{1}H–^{14}N 2D HETCOR, and 2D 1H double-quantum–single-quantum (DQ–SQ)[17] spectra of H-PHI (bottom row). Various model systems of single PHI pores with different substitution patterns and positions were designed and optimized on the PBE0-D3/def2-TZVP[18–21] level of theory to then calculate NMR chemical shifts

on the B97-2/pcsSeg-2[22,23] level of theory on optimized pore geometries (Figure A 18-A24) to develop a better understanding of the experimental data and to support the assignment.

The direct excitation ^{13}C NMR experiment shows five distinct signals for K-PHI, which can be assigned according to the inset in Figure 2.2a. Like in melem,[24] the central carbon atom (C1) in the heptazine unit exhibits a chemical shift of 157 ppm. The signal at 164 ppm is attributed to a peripheral carbon atom next to a NH group (C2) as its signal is the most intense in the ^{13}C cross-polarization experiment confirming its proximity to a proton (Figure A 12). Additionally, the ^{13}C–^{15}N 2D HETCOR spectrum shows distinctly that C2 correlates with the NH group at −242 ppm (Figure 2.2g), identifying this NH as the connecting bridge between two heptazine units. The ^{13}C NMR signal at 168 ppm arises from a carbon atom next to a deprotonated imide bridge (C3). Indeed, this C3 is only connected to nitrogen atoms with a chemical shift at −173 ppm (Figure 2.2g), a typical value for nonprotonated nitrogen. In the case of an attached NCN moiety, the neighboring heptazine carbon atom (C4) is shifted downfield to 172 ppm whereas the carbon atom of the terminal NCN group (C5) is found at 120 ppm, which is likewise observed for cyanamide in molecular potassium melonate.[25] However, according to the integrated intensities in NMR spectra, these cyanamide groups are only present in about every second to fifth (batch variations) heptazine ring in K-PHI. Assuming only terminating cyanamide groups at the edges of the crystallites, especially for large crystals in the range of 100 nm, the expected NCN content would be lower than the observed amount. However, additional cyanamide could have been introduced as point defects within the PHI sheet. Such a point defect is equivalent to a missing heptazine unit, leveraging additional internal NCN termini, since the former NH bridges become

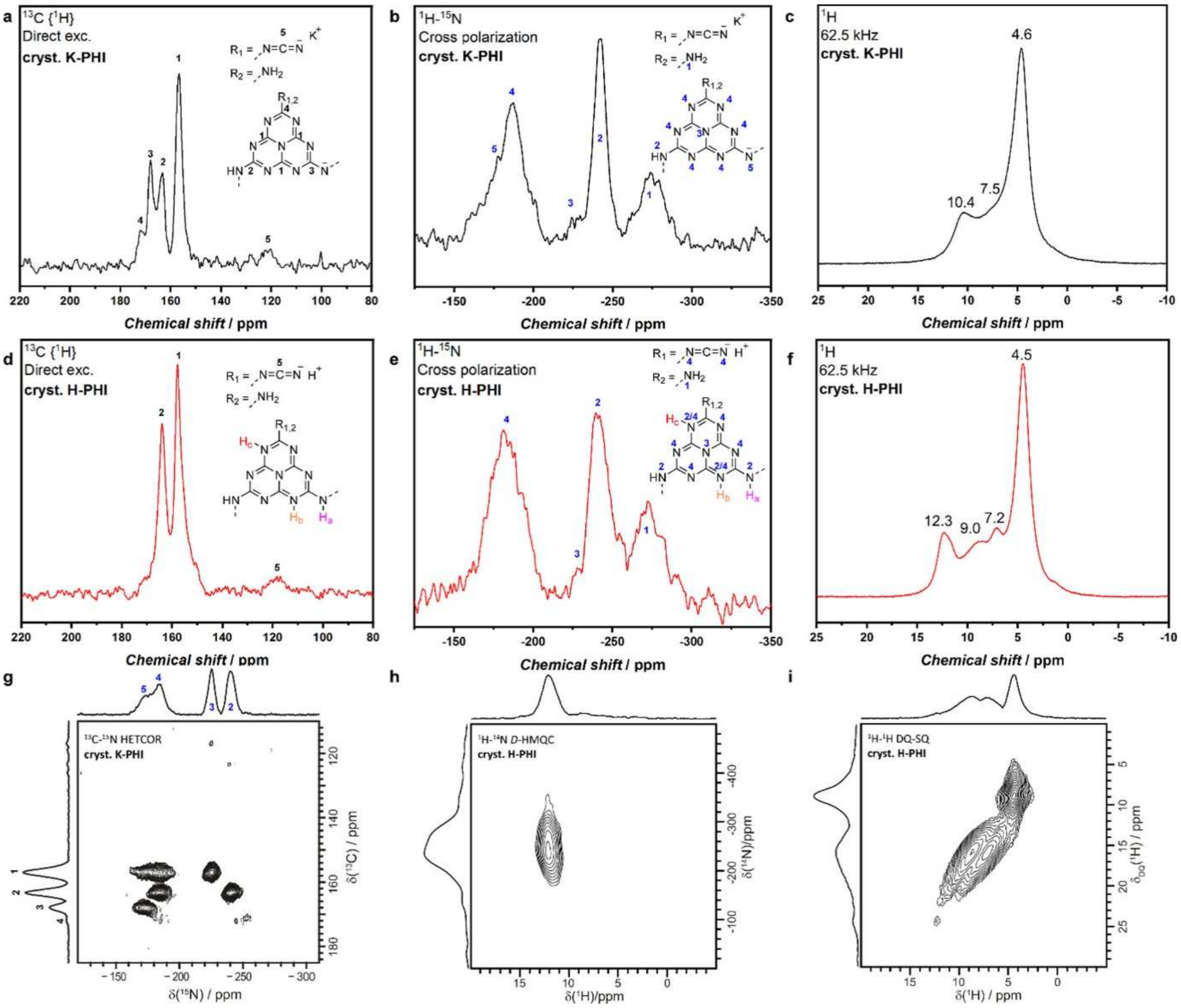

Figure 2.2. (a, d) ^{13}C direct and (b, e) ^{15}N cross-polarization and (c, f) ultrafast ^{1}H magic angle spinning (MAS) solid-state NMR spectra of K-PHI and H-PHI. The contact times of CP ^{15}N NMR spectra were both set to 4 ms. Insets show the proposed structures and their NMR assignments in black for carbon atoms and in blue for nitrogen atoms. In the case of H-PHI, the different possible protonation sites are labeled H_a, H_b, H_c; however, coexistence of several different tautomers is possible with the majority of NH groups still located at bridges. (g) ^{13}C–^{15}N dynamic nuclear polarization (DNP) HETCOR NMR spectrum of K-PHI, ^{1}H–^{14}N dipolar heteronuclear multiple-quantum coherence, and ^{1}H–^{1}H DQ–SQ spectra of H-PHI (h, i).

terminating NCN groups inside the PHI layer. As discussed in more detail in the Supporting Information (SI) (Figure A 9), the concentration of these defects has been estimated to be approx. 5–12%. The number of NCN groups seems to be reduced upon the transformation to H-PHI, which can be attributed to partial hydrolysis of the functional group, resulting in an increased number of terminal NH_2 groups or urea terminations.

^{15}N CP MAS NMR of K-PHI confirms the presence of NH groups at −242 ppm (N2, inset Figure 2.2b) bridging the heptazine units, as well as a small amount of terminal NH_2 groups at −273 ppm (N1) (note that the intensity of the NH_2 CP signal is grossly overestimated). The ^{15}N direct excitation spectra (Figure A 11) show negligible (below detection limit) amounts of these NH_2 groups. The central nitrogen atom at −229 ppm (N3) has a very low intensity in the CP experiments, as the polarization transfer is very poor. This assignment is confirmed by the ^{13}C–^{15}N 2D correlation experiment (Figure 2.2g) in which the central nitrogen is only connected to the carbon at 157 ppm (C1). The peripheral nitrogen atoms at −160 to −200 ppm (N4) lie in the typical range of shifts known from heptazine-derived molecules.[24] Interestingly, the best agreement with our quantum-chemical models is found by assuming the "naked" anionic N-bridge to be screened by a potassium ion (Figure A 23). In this case, calculations suggest that the signal of the anionic bridge (N5) lies at −173 ppm and is thus beneath the shifts of the heptazine core. Placing the potassium ion in the center of the pore (Figure A 24), a shift at >−140 ppm is calculated for the bridging nitrogen atom, which is not found in our measurements. Thus, our data suggest that K^+, presumably with a partial hydration shell, is located off-center and moved toward the polymeric backbone.

Although the structure of the acid-treated polymer H-PHI is largely similar, some distinct changes in the NMR spectra accompany the transformation. The NMR data of H-PHI support the assumption that protonation occurs predominantly at formerly negatively charged bridging nitrogen atoms (H_a, inset Figure 2.2d). Due to the conjugated charge in the network, however, protonation may also occur directly at the heptazine ring. Quantum-chemical calculations have identified H_b and H_c (inset Figure 2.2d) as potential protonation sites. The corresponding calculated chemical shift of these ring protonations are −247 and −261 ppm, respectively, which is in agreement with the upfield shift of the NH-group signal in Figure 2.2e. Molecular heptazine-based compounds such as cyameluric acid or protonated calcium melonate support this possibility, as they also bear the proton at the heptazine ring.[26,27] However, the overall low absolute amount of NH sites at the ring, along with the coexistence of different protonation sites and expected similar chemical shifts (see calculated pore models in Figure A 18, A 19 and A 22) for this group compared with the bridging NH, does not allow for an unambiguous resolution of the protonation sites.

In direct excitation ^{13}C NMR of protonated samples (H-PHI), the previously visible signal C3 next to a deprotonated bridge now disappears, hinting that this nitrogen has been protonated, which would result in a chemical shift similar to that of C2. Indeed, the relative intensity of C2 increases for H-PHI in the directly detected ^{13}C spectrum. The resonance of C5 at 120 ppm slightly shifts upfield to 117 ppm as compared to that of K-PHI, which is also mapped by our calculations (Figure A 18). The carbon atom next to the protonated NCN group is now located beneath the signal of C2. The ^{15}N CP MAS experiment yields a picture for H-PHI very similar to that for K-PHI. However, the NH group at −242 ppm is broadened toward higher fields in H-PHI and the central nitrogen in the heptazine unit is slightly upfield-shifted to −233 ppm as well. Additionally, a shoulder of the carbon signal at 157 ppm toward higher fields is also observed. These small changes could be related to interactions with protons of water in close proximity to nitrogen atoms on the *s*-heptazine ring and the possibility of NH located at the ring.

The ^{1}H NMR measurements of K-PHI and H-PHI (Figure 2.2c, f) help to give a clearer picture on the role of water and protons within those networks. Both spectra exhibit an intense signal at about 4.5 ppm, which is assigned to relatively free water inside the pores. Several additional overlapping peaks can be observed between 5 and 12.3 ppm for H-PHI. From the ^{1}H–^{14}N 2D correlation spectra, the proton of the bridging NH can be assigned to a chemical shift of about 10.4 ppm for K-PHI (Figure A 14b) and 12.3 ppm for H-PHI (Figure 2.2h), confirming that the majority of the bridging nitrogen atoms are protonated. Note that this low-field shifted resonance varies with the amount of water present in the sample. For a "dry" H-PHI sample (vacuum-dried at 120 °C for 2 days), this peak shifts upfield to about 7 ppm, as shown by its ^{1}H–^{14}N 2D HETCOR spectrum (Figure A 14a). This is in agreement with the calculations, hinting at water as a factor that significantly influences the proton NMR shifts. A calculated model pore with one water molecule interacting with an imide bridge leads to a shift of the NH proton from 8 ppm (without water) to roughly 11 ppm (with water), which is close to the experimental results (cf. Figure A 19 and A 20). In H-PHI, this proton signal is downfield-shifted to 12.3 ppm compared to that of the potassium-containing anionic network (10.4 ppm), thus indicating more acidic protons for H-PHI. The ^{1}H NMR resonances between the free water and the NH-bridging peaks (between 5 and 12 ppm for H-PHI) reveal no strong bonding to the network and consequently show no correlation with any nitrogen in the ^{1}H–^{14}N 2D HETCOR spectrum and hence are assigned to additional water inside the pore. The ^{1}H–^{1}H 2D DQ–SQ spectrum of H-PHI (Figure 2.2i) provides both a higher resolution for ^{1}H and information on proximity between these protons. On the diagonal we observe the self-correlation peak of free water at 4.5 ppm and also the bridging NH self-correlation, although this second one is less intense due to a large distance between the NH units. In addition, we observe a quite intense correlation between one ^{1}H at 7.2 and one at 9.0 ppm. From the DQ–SQ experiment acquired with different recoupling times (Figure A 15), these two protons are close to each other (their distance is similar to the ^{1}H–^{1}H distance in water). This would hint at a water molecule with each of its two protons creating hydrogen bonds to nitrogen atoms on the heptazine ring. Similar protons are also observed in the case of K-PHI (Figure A 16), i.e., also in close contact to the network. In general, ssNMR spectroscopy, in combination with our calculated pore models, corroborates the existence of a heptazine-based interconnected 2D network for K-PHI and H-PHI partially functionalized by NCN groups. In both materials, the network strongly interacts with water and hydrated potassium, respectively. This interplay represents a key factor for explaining the three-dimensional (3D) structure, as presented in the following sections.

X-Ray Powder Diffraction and PDF Analysis

XRPD patterns show significant peak broadening for H-PHI, whereas K-PHI exhibits higher crystallinity and was therefore used as the starting point for modeling (Figure 2.3a). In line with the TEM data, the Bragg peaks could be indexed with a triclinic unit cell, which was confirmed by Pawley refinement[28] to be pseudohexagonal with $a = b = 12.78$ Å, $c = 4.31$ Å, $\alpha = \beta = 109.63°$ and $\gamma = 120°$, $R_{\mathrm{wp}} = 3.87\%$. The structure model for the Rietveld refinement[29] (Figure 2.3b) was based upon the previously solved structure of PTI, reimagined for PHI sheets.[11,12] The cell metric indicates a single layer per cell, which is stacked in a slip-stacked fashion, given the non-90° α/β angles. A planar heptazine dimer was defined as a rigid body and oriented in the *ab*-plane, forming large triangular pores with two heptazine units on each side and an interlayer distance of approximately 3.2 Å, in agreement with the prominent 001 stacking reflection at ca. 28° 2θ. Reasonable relative peak intensities could only be obtained by including K and O atoms (i.e., water molecules) representing the pore content, indicating that the pores are indeed filled. Further details on Pawley and Rietveld analyses can be found in Figure A 28–A 31.

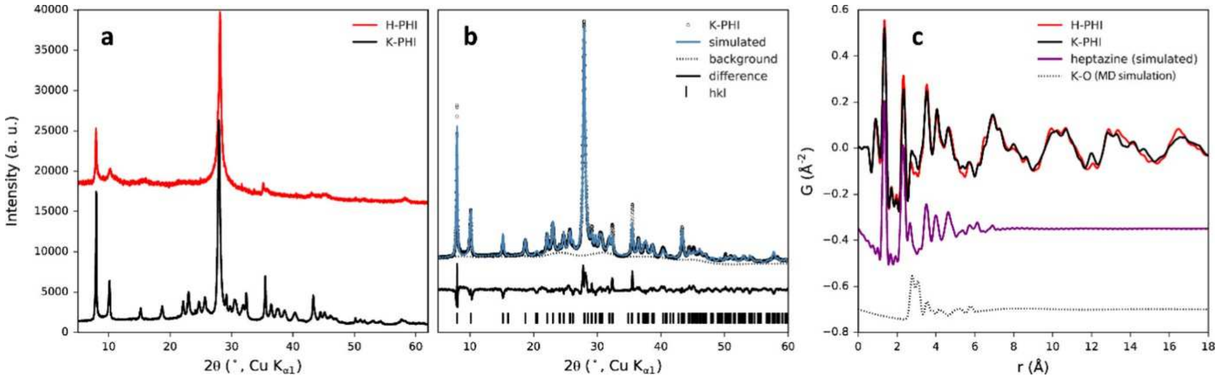

Figure 2.3. (a) XRPD patterns of H-PHI and K-PHI measured using Cu Kα_1 radiation, (b) Rietveld refinement for K-PHI, and (c) experimental PDFs for K-PHI and H-PHI, and simulated ones from a single heptazine molecule and from a model of potassium–oxygen distances derived from molecular dynamics (MD) simulations.

H-PHI appears to be structurally related through well-defined 1$\bar{1}$0, 010/100, 001, and 32$\bar{1}$/23$\bar{1}$ reflections and could be indexed by Pawley refinement with a similar cell (Figure A 29). However, a suitable Rietveld refinement for H-PHI was not possible due to significant peak broadening. Since NMR and TEM data suggest an intact layer constitution of H-PHI, this broadening is attributed to planar defects occurring as stacking fault disorder that developed during K^+ removal, which is discussed in the next section.

To gain further insights into the local structure, PDFs (Figure A 32 and A 33) were obtained from synchrotron X-ray total scattering data for H-PHI and K-PHI, in Figure 2.3c. A direct comparison shows highly similar local structures in both compounds. The heptazine units are present and conformationally rigid. Broad, interlayer peaks repeating with a wavelength of ~3.19 Å for K-PHI and ~3.17 Å for H-PHI indicate that the sheets are stacked with high fidelity, on the order of at least several hundred Angstroms, shown in Figure A 32 and A 33. The lack of longer wavelength modulations expected from periodic porous channels indicates that the pores are populated by uncorrelated electron density. Small differences in medium-range, low-amplitude features indicate possible differences in local ordering of pore content and neighboring layers, whereas more drastic long-range deviation in the behavior of the interlayer peaks provides additional evidence of differences in the stacking behavior. Model refinements to the K-PHI and H-PHI PDFs (Figure A 34–A 36) were consistent with the results from Rietveld refinements, as shown in Figure A 30 and A 31. In terms of short-range ordering, the most notable difference between H-PHI and K-PHI is the increase in peak intensity around 2.7–3.3 Å, which correlates with an increase in K^+ (Figure A 37) concentration. This feature is connected to potassium–oxygen distances found in water-solvated potassium ions observed via MD simulations (Figure A 25), providing direct evidence of water–K^+ coordination within the pores. Notably, in all Rietveld and PDF refinements, K^+ ions consistently moved off center, in-plane, toward one corner of the triangular pore. Complexation of K^+ ions with azines has previously been shown favorable (planar orientation/similar bond distances).[30] It is reasonable that K^+ could occupy both fully water-coordinated and partial nitrogen-coordinated positions.

Both TEM and XRPD data are consistent with the comparably high crystallinity of the carbon nitride backbone. The overall high in-plane order likely results from the use of molecular precursors that have a higher mobility in the salt melt, which serves as a source for error correction during bond formation. The fact that the reflections in the XRPD pattern of H-PHI are particularly broadened will be discussed in the next section.

Stacking Fault Simulations

Information on the 3D structure of the bulk PHI is difficult to extract from electron diffraction patterns due to the local nature of the method and the pronounced 2D morphology of the crystallites. The structural coherence of the PHI materials in the third dimension is governed by the stacking order of the layers and in the case of H-PHI is vastly affected by planar defects occurring as stacking faults. Thus, systematic simulations[31] of distinct faulting scenarios have been performed and compared qualitatively to the measured XRPD pattern, which yields information on all three dimensions of the bulk material. H-PHI in Figure 2.4a shows significant peak broadening and triangular, Warren-type line shapes,[32] which are indicative of planar defects in the crystal structure. We therefore conclude that H-PHI has a higher degree of out-of-plane disorder compared with K-PHI.

In Figure 2.4b, possible interactions of pore water with the poly(heptazine imide) backbone of H-PHI are depicted. These interactions direct the stacking of the layers and induce a layer offset; i.e., a layer is shifted toward the pore of the preceding layer. Due to the intrinsic trigonal symmetry of the heptazine subunit, this type of stacking exhibits three equivalent directions (Figure 2.4c). The eclipsed case was also considered for the simulations, i.e., layers stacked directly atop each other. Different faulting scenarios were developed using these four stacking relationships and used for qualitative simulations on the diffractional effect of structural disorder (detailed information is given in chapter 12 of the Appendix A). The faulting scenario ("Faulting scenario IV", Figure A 47–A 49) that was evaluated as the most suitable based on the match between simulated and measured patterns describes completely random transitions between all three

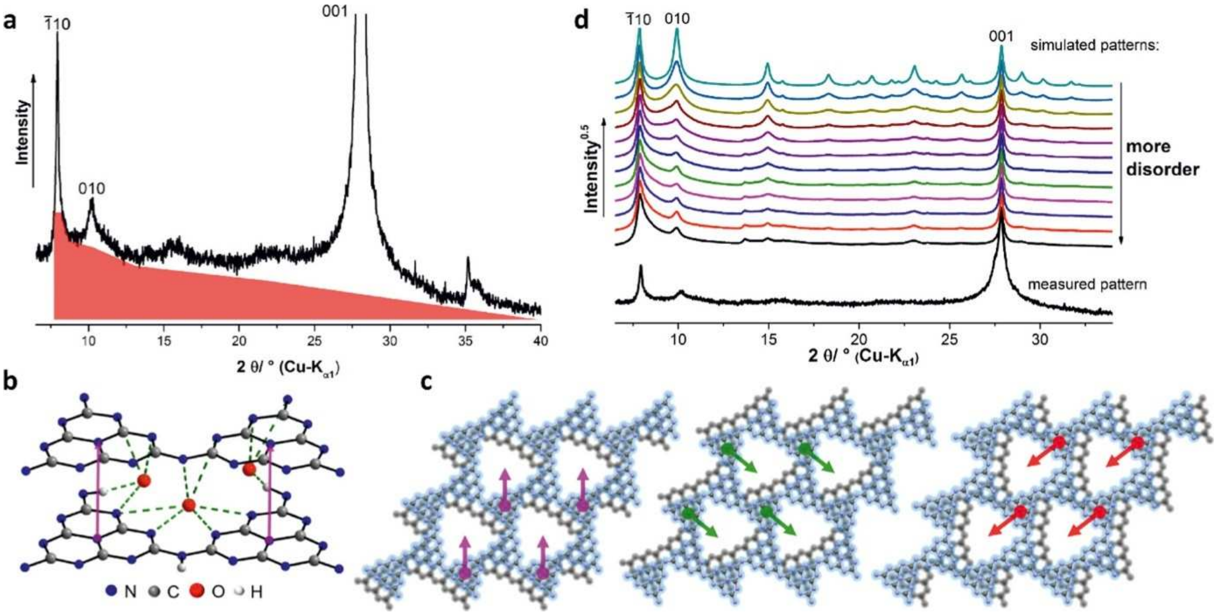

Figure 2.4. (a) XRPD of H-PHI showing the triangular peak shape. (b) Model with suggested influence of pore material (in this case, water, Figure A 40), leading to indirect interactions between the layers as well as different stacking variants with respective colored stacking vectors. (c) Possible equivalent stacking vectors for sheets of PHI; (d) simulation for faulting scenario IV (see chapter 12 of the Appendix A and Figure A 47–A 49).

pore directed stackings. This leads to a loss in the orientational coherence perpendicular to the layer planes and therefore to vast broadening of most reflections in the XRPD pattern in Figure 2.4d. Small sections of homogenously stacked layers are, however, still apparent, as indicated by the presence of the remaining 010 reflection.

The combined approach of PDF and XRPD along with stacking fault simulations reveals the overall 3D structures of H-PHI and K-PHI. It has been shown that the stacking of the pores is governed by rather weak pore–water interactions in the case of H-PHI, resulting in highly defective stacking. Nevertheless, pore water clearly mediates interlayer interaction. When the water molecules are removed by heating H-PHI up to 400 °C under an inert, dynamic atmosphere in a TG-experiment, an ex situ XRPD analysis of the residue (Figure A 27) reveals a significant decrease in the crystallite size perpendicular to the layer planes. The complete removal of pore water also shifts the layer arrangement toward an eclipsed stacking order. The presence of potassium within the pores leads to a more ordered stacking, which is indicated by much sharper reflections in the corresponding XRPD pattern (see Figure 2.3a). Therefore, the range of the interlayer interaction is much larger in K-PHI than in H-PHI. This can be attributed both to the large ionic radius of the potassium cation and its more isolated positive charge. As potassium is located off-center in the pores, it interacts with the PHI framework. In addition, a partial hydration sphere is formed around the cation by the pore water molecules (Figure A 25), which may indirectly mediate interactions to further distant layers.

Photocatalysis

Knowledge of the structure–property relationships in this class of carbon nitrides is key for the rational design of photocatalysts with improved properties. We therefore investigated the photocatalytic activity of H-PHI and K-PHI, obtained from ampoule synthesis, for the hydrogen evolution reaction (HER) with a focus on carving out those structural features that affect the activity the most. We find that H-PHI, like K-PHI, is active toward HER in the presence of a Pt cocatalyst and methanol as the sacrificial electron donor but shows only moderate activity (H-PHI: 88 µmol/gh, K-PHI: 193 µmol/gh). This can be directly traced back to the large crystallites that tend to form aggregates that disperse only weakly in aqueous solution, thus having less accessible surface area and a reduced number of edge sites available. The latter seems to be vital for the catalytic activity[33] for cocatalyst-supported systems through the presence of cyanamide terminations at the edges of the platelets. These terminations can bind more efficiently to the Pt cocatalyst and provide a higher degree of ionicity and thus colloidal stability.[2]

To test this hypothesis, we synthesized variants of H-PHI and K-PHI with smaller crystallite sizes (~20 nm) and an increased amount of external cyanamide groups accordingly, by using a mixture of melon and KSCN as precursors at ambient pressure under an argon flow, followed by treatment in diluted HCl. For the as-obtained, optimized K-PHI, we recorded a 3-fold increased activity of 600 µmol/gh compared to that of the highly crystalline sample, whereas we registered a 38-time increase in activity for H-PHI (3364 µmol/gh, Figure 2.5b). This is well beyond the activity of the prototypical carbon nitride melon with an activity of just 25 µmol/gh measured under the same conditions. Note, however, that a quantitative comparison of the intrinsic photocatalytic activities

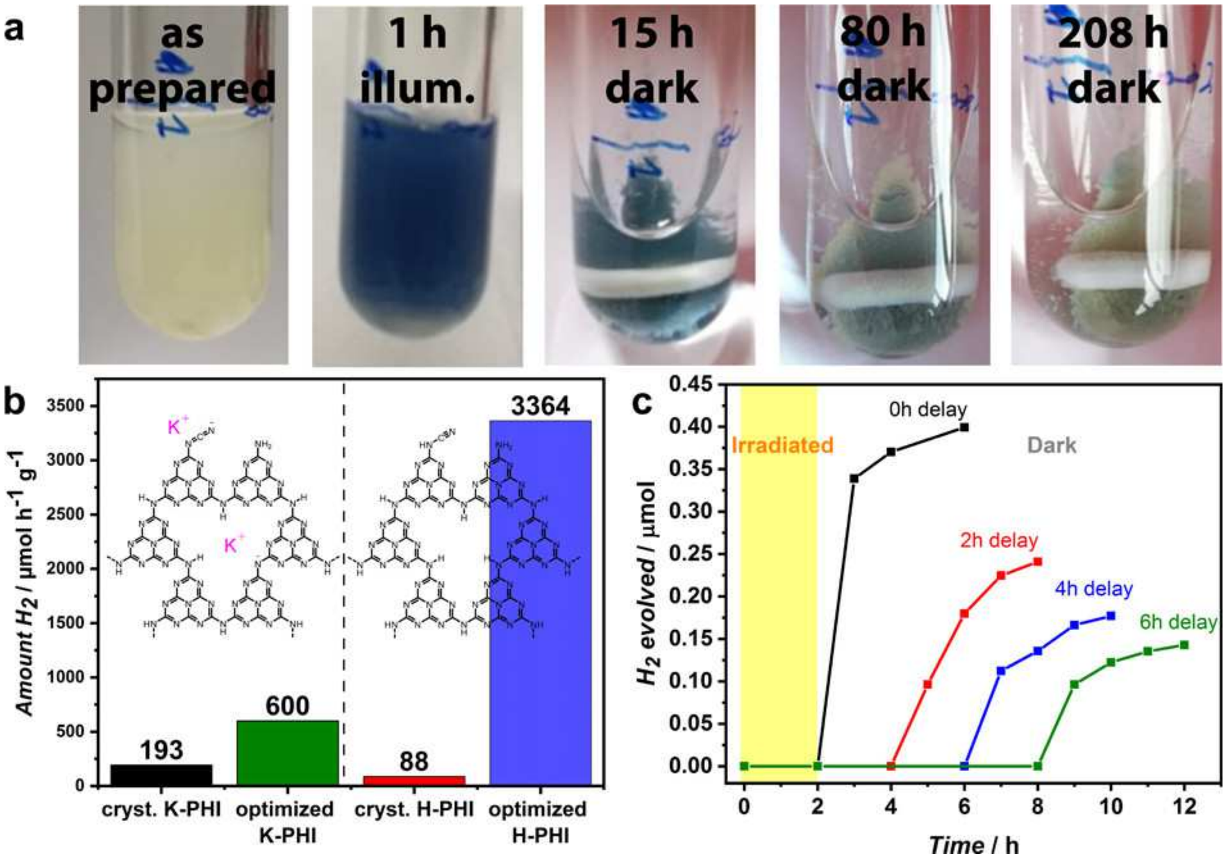

Figure 2.5. (a) H-PHI before and after 1 h of illumination and after storing the material in the stable, photoreduced "blue" state up to 208 h in the dark. A shade toward green is likely due to small amounts of oxygen leaking into the vessel. (b) Comparison of photocatalytic rates for hydrogen evolution for K-PHI and H-PHI, respectively. (c) Dark photocatalysis in phosphate buffer with various delay times for addition of platinum cocatalyst, i.e., 0, 2, 4, or 6 h.

of K-PHI and H-PHI is difficult since the observed hydrogen evolution rates depend on a complex interplay between various parameters, which, in addition, may scale differently with the particle size. These include exfoliation and agglomeration of the crystallites, the nature and amount of defects, or the amount of cocatalyst incorporated in the sample.

For a more detailed structural characterization of these optimized compounds, see Figure A 7 and A 8. It is apparent that the optimized materials exhibit lower long-range in-plane order, as indicated by broad, diffuse reflections. In particular, both $1\bar{1}0$ and the 010 reflections are vastly broadened, which is attributed to a loss of coherence within the layer plane, i.e., smaller platelets (Figure A 5). By using the Scherrer equation from the XRPD data in Figure A 8, the crystallite sizes in the lateral dimension have been estimated to be about 20 nm for the optimized samples and up to 100 nm (Table A 1) for the most crystalline samples. The extension in *c*-direction remains fairly similar for all samples at approx. 20 nm. Small crystallites have a higher amount of accessible cyanamide groups at their surface and are suspended more easily in water, enabling them to participate more efficiently in the photocatalytic reaction.

While the HER activity observed for H-PHI puts it on par with the best carbon nitride photocatalysts,[34–39] it bears another intriguing property, which has previously been documented for K-PHI;[4,6] under illumination and in the presence of an electron donor, H-PHI also forms a photoreduced state that is exceptionally long-living, clearly visible by its blue color. Figure 2.5a depicts the suspension during photoreduction, which is yellow initially and then turns dark blue upon irradiation in the presence of 4-methyl benzylalcohol as the electron donor. Under an argon atmosphere, the photoexcited photocatalyst is reduced by the electron donor and remains in the photoreduced state for over 200 h. The diminishing of the blue color is due to quenching of the anion radical by oxygen, which slowly diffuses into the solution over time (Figure 2.5a, right). The photoreduced radical state was also monitored by electron magnetic resonance spectroscopy (EPR), which shows a photoinduced paramagnetic signal for both K-PHI and H-PHI with g-factors of ≈2.003 (Figure A 10), indicative of a heptazine-centered π radical.[4,36,40,41] To test whether photoreduced H-PHI is able to store the trapped electrons and release them upon addition of a hydrogen evolution catalyst after a time delay, 15 mg of the sample was irradiated under a Xenon lamp (100 mW/cm^2, AM 1.5 G) in phosphate buffer with 4-methylbenzyl alcohol as an electron donor for 2 h. Then, a colloidal platinum suspension was added in the dark (Figure 2.5c) either directly or 2, 4, or 6 h after illumination. Indeed, hydrogen was evolved for several hours (27 µmol/g, direct addition), which shows the ability of the system to separate the light (photoexcitation) from the dark reaction (catalysis) akin to the biological model of photosynthesis. Even after waiting for 6 h, 37% of the initial amount of H_2 could still be registered.

2.3 Conclusions

In conclusion, we have synthesized a 2D poly(heptazine imide) (PHI) polymer, which is comparable with PTI · LiCl[11,12] in terms of crystallinity but by far exceeds its photocatalytic performance.[13,42] Characterization of K-PHI and H-PHI provides insights into the structure–property–activity relationship of this new class of high-performance photocatalysts. By combining a suite of analytical techniques, including TEM, NMR spectroscopy, XRPD, PDF analysis, and quantum-chemical calculations, we were able to confirm the in-plane PHI-based 2D structure and derive a detailed picture of the out-of-plane structure. Our analysis not only suggests that ionothermal synthesis conditions likely support error correction, thus leading to extended crystallites of over 100 nm in lateral dimension, but also that metal ions can act as out-of-plane structure-directing agents, leading to a pronounced long-range order in the *c*-direction. Furthermore, water inside the pores has been found to have a major influence on the 3D stacking structure of PHI networks. Our work thus adds another structurally characterized member to the large yet ill-defined class of carbon nitrides, which is notoriously difficult to characterize. As such, this study provides synthetic and analytical tools that are crucial for the rational design of better photocatalysts and helps to carve out the structural features that are essential for observing an unusually long-lived charge separated state, enabling time-delayed photocatalysis in the dark.

2.4 Experimental Section

Crystalline Ampoule Synthesis of Potassium Poly(Heptazine Imide), K-PHI

Dicyandiamide (97 mg, 1.14 mmol, Sigma-Aldrich >98%), KSCN (18 mg, 0.19 mmol, Gruessing 99%), and potassium melonate penta-hydrate (79 mg, 0.16 mmol) were ground in a mortar and transferred into a Duran glas ampoule, which was subsequently purged four times with argon and then dried under high vacuum. The ampoule was then sealed and placed into a tube furnace (6 °C/min, 500 °C, 6 h, 1 °C/min, rt). The bright yellow solid was washed four times with deionized (DI) water and then dried at 60 °C.

Crystalline Ampoule Synthesis of Protonated Poly(Heptazine Imide), H-PHI

Finely ground cryst. K-PHI (100 mg) was treated with 100 mL of 2 M HCl and stirred for 15 min. The suspension was filtered and the residue washed four times with DI water to yield H-PHI.

Further details on the synthesis of optimized samples for photocatalysis, melon, and potassium melonate can be found in Supporting Information.

2.5 Associated Content

The Supporting Information is available free of charge on the ACS Publications website at DOI: 10.1021/acs.chemmater.9b02199.

- Further experimental details, instrumental details, additional characterization (TEM, IR, Raman, XRPD (XLSX), TG-XRPD (XLSX), crystallite size estimations, EPR, ssNMR, TGA, PDF analysis, quantum-chemical calculations and methods (XLSX), recursive-type stacking simulations, EA and water sorption) (PDF)
- Structural model for K-PHI from Rietveld refinement (CIF)
- Structural model for H-PHI from PDF refinement (CIF)

2.6 Author Information

Corresponding author:
E-mail: b.lotsch@fkf.mpg.de

Author contributions:
H.S. and J.K. contributed equally to this work.

Funding sources:
Financial support is gratefully acknowledged from the Max Planck Society, the ERC Starting Grant (project COFLeaf, grant number 639233), the Center for NanoScience (CeNS), the German Research Foundation (SFB 840), and the BASF.

2.7 Acknowledgments

Financial support by the ERC Starting Grant (project COF Leaf, grant number 639233), the Max Planck Society, the DFG cluster of excellence “e-conversion”, and the Center for NanoScience (CeNS) is gratefully acknowledged. C.O. acknowledges financial support as a Max Planck Fellow at the Max Planck Institute for Solid State Research, Stuttgart. M.W.T. acknowledges support from BASF. This research used beamline 28-ID-2 of the National Synchrotron Light Source II, a U.S. Department of Energy (DOE) Office of the Science User Facility operated for the DOE Office of Science by Brookhaven National Laboratory under Contract no. DE-SC0012704. The authors thank Agnieszka Poulain for assistance with experiments performed on beamline ID-31 at the European Synchrotron Radiation Facility (ESRF), Grenoble, France. R.S. and J.S. gratefully acknowledge financial support from the German Research Foundation (SFB 840). We thank Torsten Gutmann for support with the DNP NMR measurements and Prof. Gerd Buntkowsky (TU Darmstadt) for generous allocation of measurement time at his Bruker Avance III 400 DNP spectrometer. The authors further thank Stefan Trenker and Alberto von Mankowski for water sorption measurements as well as Armin Schulz for Raman spectra.

2.8 References

(1) Savateev, A.; Dontsova, D.; Kurpil, B.; Antonietti, M. Highly crystalline poly(heptazine imides) by mechanochemical synthesis for photooxidation of various organic substrates using an intriguing electron acceptor – Elemental sulfur. *J. Catal.* **2017**, *350*, 203–211. DOI: 10.1016/j.jcat.2017.02.029.

(2) Lau, V. W.-h.; Moudrakovski, I.; Botari, T.; Weinberger, S.; Mesch, M. B.; Duppel, V.; Senker, J.; Blum, V.; Lotsch, B. V. Rational design of carbon nitride photocatalysts by identification of cyanamide defects as catalytically relevant sites. *Nat. Commun.* **2016**, *7*, 12165. DOI: 10.1038/ncomms12165.

(3) Ou, H.; Lin, L.; Zheng, Y.; Yang, P.; Fang, Y.; Wang, X. Tri- s -triazine-Based Crystalline Carbon Nitride Nanosheets for an Improved Hydrogen Evolution. *Adv. Mater.* **2017**, *29* (22), 1700008. DOI: 10.1002/adma.201700008.

(4) Lau, V. W.-h.; Klose, D.; Kasap, H.; Podjaski, F.; Pignié, M.-C.; Reisner, E.; Jeschke, G.; Lotsch, B. V. Dark Photocatalysis: Storage of Solar Energy in Carbon Nitride for Time-Delayed Hydrogen Generation. *Angew. Chem. Int. Ed.* **2017**, *56* (2), 510–514. DOI: 10.1002/anie.201608553.

(5) Podjaski, F.; Kröger, J.; Lotsch, B. V. Toward an Aqueous Solar Battery:Direct Electrochemical Storage of Solar Energy in Carbon Nitrides. *Adv. Mater.* **2018**, *30* (9), 1705477. DOI: 10.1002/adma.201705477.

(6) Zeng, Z.; Quan, X.; Yu, H.; Chen, S.; Zhang, Y.; Zhao, H.; Zhang, S. Carbon nitride with electron storage property:Enhanced exciton dissociation for high-efficient photocatalysis. *Appl. Catal. B* **2018**, *236*, 99–106. DOI: 10.1016/j.apcatb.2018.05.003.

(7) Savateev, A.; Kurpil, B.; Mishchenko, A.; Zhang, G.; Antonietti, M. A "waiting" carbon nitride radical anion:A charge storage material and key intermediate in direct C-H thiolation of methylarenes using elemental sulfur as the "S"-source. *Chem. Sci.* **2018**, *9* (14), 3584–3591. DOI: 10.1039/c8sc00745d.

(8) Chen, Z.; Savateev, A.; Pronkin, S.; Papaefthimiou, V.; Wolff, C.; Willinger, M. G.; Willinger, E.; Neher, D.; Antonietti, M.; Dontsova, D. "The Easier the Better" Preparation of Efficient Photocatalysts-Metastable Poly(heptazine imide) Salts. *Adv. Mater.* **2017**, *8*, 1700555. DOI: 10.1002/adma.201700555.

(9) Savateev, A.; Pronkin, S.; Willinger, M. G.; Antonietti, M.; Dontsova, D. Towards Organic Zeolites and Inclusion Catalysts: Heptazine Imide Salts Can Exchange Metal Cations in the Solid State. *Chem. Asian J.* **2017**, *15*, 783. DOI: 10.1002/asia.201700209.

(10) Lin, L.; Ren, W.; Wang, C.; Asiri, A. M.; Zhang, J.; Wang, X. Crystalline carbon nitride semiconductors prepared at different temperatures for photocatalytic hydrogen production. *Appl. Catal. B* **2018**, *231*, 234–241. DOI: 10.1016/j.apcatb.2018.03.009.

(11) Wirnhier, E.; Döblinger, M.; Gunzelmann, D.; Senker, J.; Lotsch, B. V.; Schnick, W. Poly(triazine imide) with Intercalation of Lithium and Chloride Ions [$(C_3N_3)_2(NH_xLi_{1-x})_3\cdot LiCl$]: A Crystalline 2D Carbon Nitride Network. *Chem. Eur. J.* **2011**, *17* (11), 3213–3221. DOI: 10.1002/chem.201002462.

(12) Mesch, M. B.; Bärwinkel, K.; Krysiak, Y.; Martineau, C.; Taulelle, F.; Neder, R. B.; Kolb, U.; Senker, J. Solving the Hydrogen and Lithium Substructure of Poly(triazine imide)/LiCl Using NMR Crystallography. *Chem. Eur. J.* **2016**, *22* (47), 16878–16890. DOI: 10.1002/chem.201603726.

(13) Ham, Y.; Maeda, K.; Cha, D.; Takanabe, K.; Domen, K. Synthesis and Photocatalytic Activity of Poly(triazine imide). *Chem. Asian J.* **2013**, *8* (1), 218–224. DOI: 10.1002/asia.201200781.

(14) Iwama, M.; Suzuki, Y.; Plévert, J.; Itabashi, K.; Ogura, M.; Okubo, T. Location of Alkali Ions and their Relevance to Crystallization of Low Silica X Zeolite. *Cryst. Growth Des.* **2010**, *10* (8), 3471–3479. DOI: 10.1021/cg100289p.

(15) Döblinger, M.; Lotsch, B. V.; Wack, J.; Thun, J.; Senker, J.; Schnick, W. Structure elucidation of polyheptazine imide by electron diffraction—a templated 2D carbon nitride network. *Chem. Commun.* **2009** (12), 1541. DOI: 10.1039/b820032g.

(16) Schaefer, J.; McKay, R.A.; Stejskal, E.O. Double-cross-polarization NMR of solids. *J. Magn. Reson.* **1979**, *34* (2), 443–447. DOI: 10.1016/0022-2364(79)90022-2.

(17) Levitt, M. H. Symmetry-Based Pulse Sequences in Magic-Angle Spinning Solid-State NMR. In *eMagRes*; R. K. Harris, R. L. Wasylishen, Eds.; Wiley, 2007.

(18) Adamo, C.; Barone, V. Toward reliable density functional methods without adjustable parameters:The PBE0 model. *J. Chem. Phys.* **1999**, *110* (13), 6158–6170. DOI: 10.1063/1.478522.

(19) Ernzerhof, M.; Scuseria, G. E. Assessment of the Perdew–Burke–Ernzerhof exchange-correlation functional. *J. Chem. Phys.* **1999**, *110* (11), 5029–5036. DOI: 10.1063/1.478401.

(20) Grimme, S.; Antony, J.; Ehrlich, S.; Krieg, H. A consistent and accurate ab initio parametrization of density functional dispersion correction (DFT-D) for the 94 elements H-Pu. *J. Chem. Phys.* **2010**, *132* (15), 154104. DOI: 10.1063/1.3382344.

(21) Schäfer, A.; Huber, C.; Ahlrichs, R. Fully optimized contracted Gaussian basis sets of triple zeta valence quality for atoms Li to Kr. *J. Chem. Phys.* **1994**, *100* (8), 5829–5835. DOI: 10.1063/1.467146.

(22) Wilson, P. J.; Bradley, T. J.; Tozer, D. J. Hybrid exchange-correlation functional determined from thermochemical data and ab initio potentials. *J. Chem. Phys.* **2001**, *115* (20), 9233–9242. DOI: 10.1063/1.1412605.

(23) Jensen, F. Segmented contracted basis sets optimized for nuclear magnetic shielding. *J. Chem. Theory Comput.* **2015**, *11* (1), 132–138. DOI: 10.1021/ct5009526.

(24) Jürgens, B.; Irran, E.; Senker, J.; Kroll, P.; Müller, H.; Schnick, W. Melem (2,5,8-Triamino-tri- s -triazine), an Important Intermediate during Condensation of Melamine Rings to Graphitic Carbon Nitride: Synthesis, Structure Determination by X-ray Powder Diffractometry, Solid-State NMR, and Theoretical Studies. *J. Am. Chem. Soc.* **2003**, *125* (34), 10288–10300. DOI: 10.1021/ja0357689.

(25) Horvath-Bordon, E.; Kroke, E.; Svoboda, I.; Fuess, H.; Riedel, R. Potassium melonate, $K_3[C_6N_7(NCN)_3]\cdot5H_2O$, and its potential use for the synthesis of graphite-like C_3N_4 materials. *New J. Chem.* **2005**, *29* (5), 693. DOI: 10.1039/b416390g.

(26) Sattler, A.; Schnick, W. Zur Frage der Tautomerie von Cyamelursäure im Kristall. *Z. anorg. allg. Chem.* **2006**, *632* (8-9), 1518–1523. DOI: 10.1002/zaac.200600099.

(27) Makowski, S. J.; Gunzelmann, D.; Senker, J.; Schnick, W. Protonated Melonate $Ca[HC_6N_7(NCN)_3] \cdot 7\ H_2O$ - Synthesis, Crystal Structure, and Thermal Properties. *Z. anorg. allg. Chem.* **2009**, 2434–2439. DOI: 10.1002/zaac.200900231.

(28) Pawley, G. S. Unit-cell refinement from powder diffraction scans. *J. Appl. Crystallogr.* **1981**, *14* (6), 357–361. DOI: 10.1107/S0021889881009618.

(29) Rietveld, H. M. A profile refinement method for nuclear and magnetic structures. *J. Appl. Crystallogr.* **1969**, *2* (2), 65–71. DOI: 10.1107/S0021889869006558.

(30) Amunugama, R.; Rodgers, M.T. Absolute alkali metal ion binding affinities of several azines determined by threshold collision-induced dissociation and ab initio theory. *Int. J. Mass Spectrom.* **2000**, *195-196*, 439–457. DOI: 10.1016/S1387-3806(99)00145-1.

(31) Coelho, A. A.; Evans, J. S. O.; Lewis, J. W. Averaging the intensity of many-layered structures for accurate stacking-fault analysis using Rietveld refinement. *J. Appl. Crystallogr.* **2016**, *49* (5), 1740–1749. DOI: 10.1107/S1600576716013066.

(32) Warren, B. E. X-Ray Diffraction in Random Layer Lattices. *Phys. Rev.* **1941**, *59* (9), 693–698. DOI: 10.1103/PhysRev.59.693.

(33) Haiber, D. M.; Crozier, P. A. Nanoscale Probing of Local Hydrogen Heterogeneity in Disordered Carbon Nitrides with Vibrational Electron Energy-Loss Spectroscopy. *ACS Nano* **2018**, *12* (6), 5463–5472. DOI: 10.1021/acsnano.8b00884.

(34) Liu, G.; Wang, T.; Zhang, H.; Meng, X.; Hao, D.; Chang, K.; Li, P.; Kako, T.; Ye, J. Nature-Inspired Environmental "Phosphorylation" Boosts Photocatalytic H_2 Production over Carbon Nitride Nanosheets under Visible-Light Irradiation. *Angew. Chem. Int. Ed.* **2015**, *54* (46), 13561–13565. DOI: 10.1002/anie.201505802.

(35) Martin, D. J.; Qiu, K.; Shevlin, S. A.; Handoko, A. D.; Chen, X.; Guo, Z.; Tang, J. Highly Efficient Photocatalytic H_2 Evolution from Water using Visible Light and Structure-Controlled Graphitic Carbon Nitride. *Angew. Chem. Int. Ed.* **2014**, *53* (35), 9240–9245. DOI: 10.1002/anie.201403375.

(36) Sun, J.; Zhang, J.; Zhang, M.; Antonietti, M.; Fu, X.; Wang, X. Bioinspired hollow semiconductor nanospheres as photosynthetic nanoparticles. *Nat. Commun.* **2012**, *3* (1), 711. DOI: 10.1038/ncomms2152.

(37) Kurpil, B.; Savateev, A.; Papaefthimiou, V.; Zafeiratos, S.; Heil, T.; Özenler, S.; Dontsova, D.; Antonietti, M. Hexaazatriphenylene doped carbon nitrides—Biomimetic photocatalyst with superior oxidation power. *Appl. Catal. B* **2017**, *217*, 622–628. DOI: 10.1016/j.apcatb.2017.06.036.

(38) Lau, V. W.-h.; Yu, V. W.-z.; Ehrat, F.; Botari, T.; Moudrakovski, I.; Simon, T.; Duppel, V.; Medina, E.; Stolarczyk, J.; Feldmann, J.; Blum, V.; Lotsch, B. V. Urea-Modified Carbon Nitrides: Enhancing Photocatalytic Hydrogen Evolution by Rational Defect Engineering. *Adv. Energy Mater.* **2017**, 1602251. DOI: 10.1002/aenm.201602251.

(39) Cui, L.; Song, J.; McGuire, A. F.; Kang, S.; Fang, X.; Wang, J.; Yin, C.; Li, X.; Wang, Y.; Cui, B. Constructing Highly Uniform Onion-Ring-like Graphitic Carbon Nitride for Efficient Visible-Light-Driven Photocatalytic Hydrogen Evolution. *ACS Nano* **2018**, *12* (6), 5551–5558. DOI: 10.1021/acsnano.8b01271.

(40) Dvoranová, D.; Mazúr, M.; Papailias, I.; Giannakopoulou, T.; Trapalis, C.; Brezová, V. EPR Investigations of g-C_3N_4/TiO_2 Nanocomposites. *Catalysts* **2018**, *8* (2), 47. DOI: 10.3390/catal8020047.

(41) Rodríguez, N. A.; Savateev, A.; Grela, M. A.; Dontsova, D. Facile Synthesis of Potassium Poly(heptazine imide) (PHIK)/Ti-Based Metal-Organic Framework (MIL-125-NH2) Composites for Photocatalytic Applications. *ACS Appl. Mater. Interfaces* **2017**, *9* (27), 22941–22949. DOI: 10.1021/acsami.7b04745.

(42) Schwinghammer, K.; Tuffy, B.; Mesch, M. B.; Wirnhier, E.; Martineau, C.; Taulelle, F.; Schnick, W.; Senker, J.; Lotsch, B. V. Triazine-based Carbon Nitrides for Visible-Light-Driven Hydrogen Evolution. *Angew. Chem. Int. Ed.* **2013**, *52* (9), 2435–2439. DOI: 10.1002/anie.201206817.

3 K-CN-Phase – Autogenous pressure influences polymorphism in potassium poly(heptazine imides) affecting "dark photocatalysis"

3.1 Introduction

Carbon nitrides show remarkable light-harvesting properties rendering them interesting as semiconducting materials for the energy sector. In this context, they could replace cost-intensive or toxic inorganic materials, due to their composition based on the abundant elements carbon and nitrogen. However, the exact identification of the chemical structure remains a major challenge for carbon nitrides, owing to their dominantly amorphous nature. Structural modifications have a significant impact on e.g. improving the photocatalytic activity.[1–3] This process, however, can only be deliberately planned and implemented with accurate knowledge of the parental structure. By analogy, from inorganic semiconductors like silicon it is well known that precise information on its purity is vital to reach specific doping levels, which in turn, tune the properties of the final electronic device.

Recent studies have shown that the use of salt melts is essential for yielding highly crystalline carbon nitrides.[4–7] We and others attributed this to the structure directing influence of the alkali ions leading to an enhanced ordering of building units, more than is typically observed for simple condensation routes of carbon nitride precursors.[5,8] Another vital, yet often underestimated reaction parameter is the autogenous ammonia pressure, which is seldomly discussed, because of its inherent difficulty to control.[9]

Herein, by combining both strategies, salt melt and autogenous ammonia pressure, we have discovered a new carbon nitride material that is closely related to two-dimensional potassium poly(heptazine imide) (K-PHI, cf. chapter 2). It likewise contains potassium, but in contrast to K-PHI, its structure is composed of 1D strands of condensed heptazine units linked via imide bridges, thus being closer to the archetype CN-material: melon.[9] Owing to the salt melt assisted synthetic conditions, the imide bridge is deprotonated and coordinated by potassium cations. This phase, denoted as K-CN-phase[b], can also be protonated by treatment with diluted acid (H-CN-phase), which however goes hand in hand with a significant loss of long-range order. Finally, we discuss how the deviating structural arrangement in the K-CN-phase has a detrimental effect on the charge-storing property, thus preventing dark photocatalysis (cf. chapter 2) in this system.

---

[b] A note concerning the nomenclature of the compounds presented in this chapter: To the reader the name, "K-CN-phase" or "H-CN-phase" may seem somewhat generic and indeed she or he is correct in this assessment. However, these names have been chosen with care in order to avoid too much structural information placed into them, and thus bias the reader. The misapprehension that lead to numerous publications naming melon erroneously g-C_3N_4 (cf. chapter 1) has emphasized to act carefully when it comes to naming new CN-compounds (and probably valid for other areas). Anticipatory, the same cautiousness applies to the naming of Ni-CN_x, discussed in the subsequent chapter 4.

3.2 Results and Discussion

Preparation and elemental composition

Dicyandiamide (97 mg, 1.14 mmol, Sigma-Aldrich >98%), KSCN (18 mg, 0.19 mmol, Gruessing 99%) and potassium melonate penta-hydrate (79 mg, 0.16 mmol) were ground in a mortar and transferred into a Duran glass ampoule, which was subsequently purged four times with argon and then dried under high-vacuum. The ampoule was then flame-sealed and placed into a tube furnace (6 °C/min, 500 °C, 6 h, 1 °C/min, rt). In a final step the yellow solid was washed four times with DI water and then dried at 60 °C.

The procedure is the same as for the material presented in chapter 2. But the main difference could only be observed after the heating process. It turned out that in some cases K-PHI could not be obtained, but a similar looking material with different properties formed. This new product, which also contains potassium, is called K-CN-phase. A close inspection of what could cause the different products lead to the discovery of fine cracks that could only be found for K-PHI syntheses. These cracks were not present in ampoules leading to the K-CN-phase (Figure 3.1). Therefore, it is likely that during a typical K-PHI synthesis, evolved gases can – at least partially – escape the reaction vessel. In turn, the autogenous pressure is retained for the K-CN-phase samples.

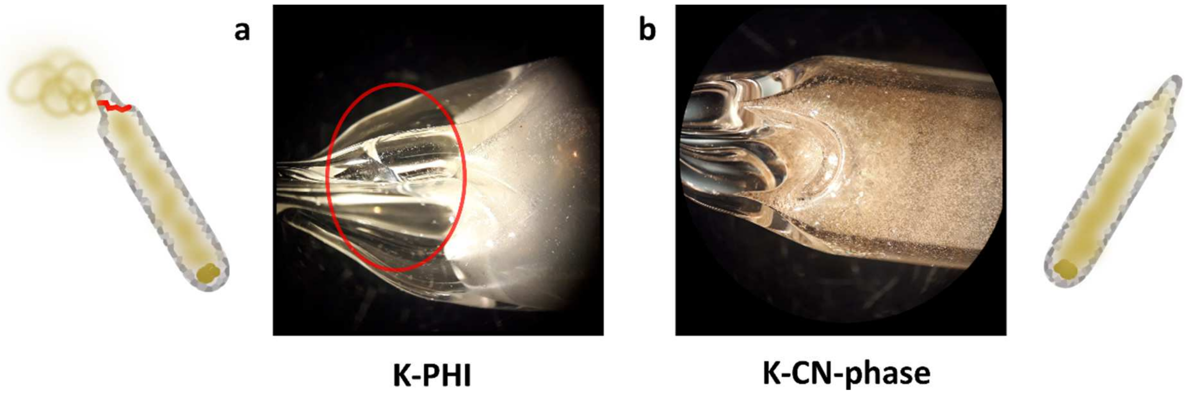

Figure 3.1. Photographs under a light microscope of (a) a K-PHI ampoule and (b) K-CN-phase ampoule. In (a) a tiny crack is visible (red circle), which causes the pressure to be released over the course of the synthesis as is illustrated in the drawings.

For the K-CN-phase synthesis, the upper part of the ampoule also contained a small amount of colorless, rhombus-shaped crystals, which could be successfully identified by single-crystal analysis to be a melem-melamine adduct phase, previously reported by *Sattler et al.*[10] However, the XRD pattern of this phase is not found as a contaminant in the K-CN-phase. The finding of these crystals only signifies a continuous exchange of volatile CN-species in the gas phase over the course of the reaction. It thus becomes apparent that not only the presence of the salt melt is important for the formation of the K-CN-phase, but also its sustained exposure to the vapors within the ampoule. The vapors could be composed of a mixture of elementary CN-precursors such as ammonia, melamine, dicyanamide, cyanamide etc. Generally, one would expect oligomeric or less condensed structures for higher reaction pressures.[11,12]

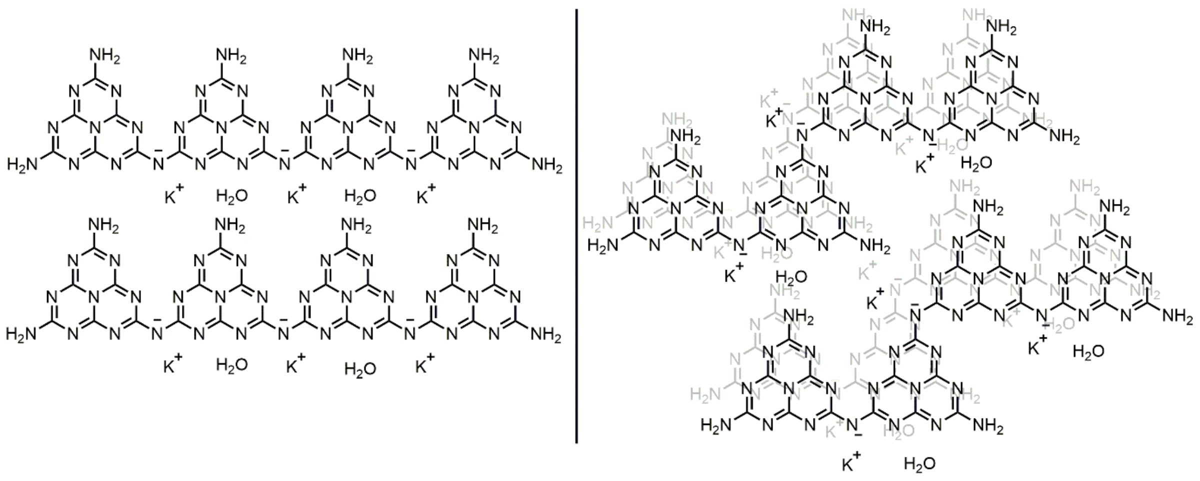

Figure 3.2. (Left) Schematic representation of the possible chemical structure, consistent with elemental analyses. (Right) The same strands arranged in a zigzag fashion as found in melon.

Table 3.1 shows the elemental composition obtained by combustion analyses and ICP/AE spectroscopy of the K-CN-phase and the H-CN-phase, respectively. While the K-CN-phase contains a substantial amount of potassium in a similar range as reported for K-PHI in chapter 2, no potassium could be detected in the case of the H-CN-phase, which indicates a complete exchange after the treatment in diluted acid. The higher oxygen content in the H-CN-phase suggests that potassium has been replaced by water molecules. It is noteworthy that the N/C ratio is close to 1.5, which is exactly the stoichiometry observed in melon. Further similarities between the K/H-CN-phase and melon will be discussed later.

Table 3.1. Elemental analysis obtained from combustion analysis and ICP/AE spectroscopy for K-CN-phase and H-CN-phase, respectively. For the H-CN-phase no potassium could be detected by ICP/AE spectroscopy.

	K-CN-phase		H-CN-phase	
	wt%	mol%	wt%	mol%
C	29.6	30.2	30.8	25.1
N	52.2	45.6	52.8	37.8
K	13.0	4.1	-	-
H	1.4	17.4	2.8	28.0
O	3.8	2.8	13.6	9.0
Total	100.0	100.0	100.0	100.0
N/C	**1.51**	**$C_6N_9H_{2.5}K_{0.8} \cdot 0.5\ H_2O$**	**1.47**	**$C_6N_9H_{2.5} \cdot 2\ H_2O$**

Transmission Electron Microscopy and X-Ray Diffraction

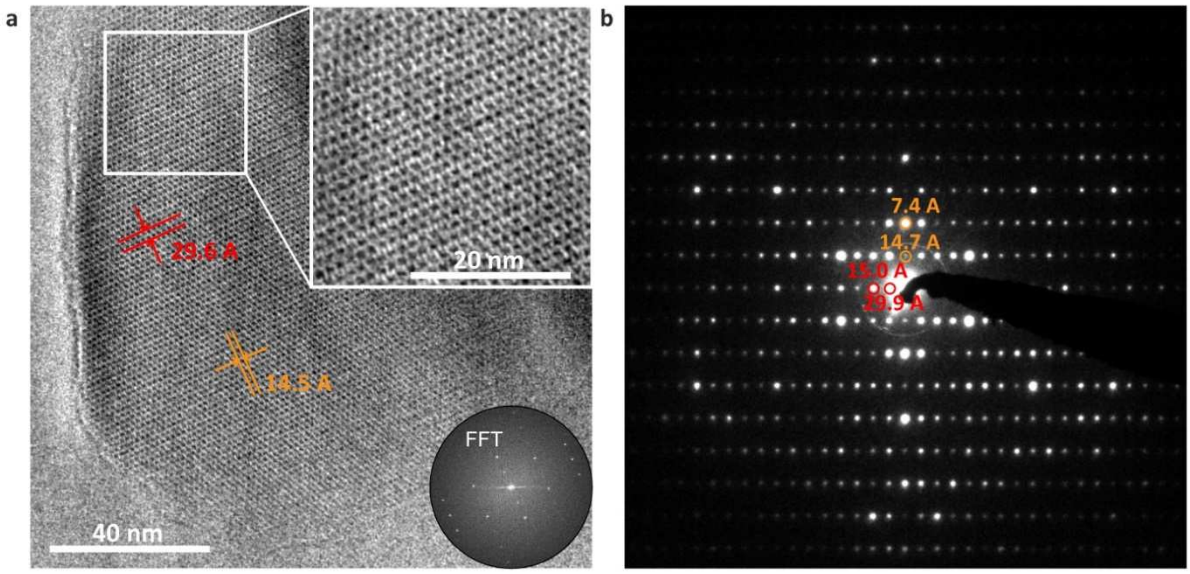

Figure 3.3. (a) High resolution TEM micrograph of K-CN-phase; inset shows the magnified image. The lattice fringes with the corresponding distances of 29.6 Å (010) and 14.5 Å (100) are marked in red and orange, respectively. (b) SAED pattern of [001] zone axis with the 100, 200, 010 and 020 reflections highlighted.

TEM selected area electron diffraction (SAED) images provide data on the probable unit cell of the new carbon nitride phase. The high-resolution image in Figure 3.3a obtained from a free-standing crystallite confirms the highly crystalline nature of this new K-CN-phase. Discrete lattice fringes can be observed, which correspond to the main lattice orientations observed in electron diffraction mode. The Fast-Fourier-Transformation (FFT) (inset Figure 3.3a) of this real space information well fits the diffraction pattern in Figure 3.3b. This degree of crystallinity is especially remarkable considering that carbon nitrides are prone to rapid degradation in the electron beam,[13] due to their light element composition. From previous studies on carbon nitride systems, we assume that the image shown in Figure 3.3b represents the diffraction pattern of the [001] zone axis.[5] Often these compounds tend to form 2D extended macroscopic structures that have a very high aspect ratio, which can cause a preferential arrangement of the crystallites on the TEM grid,[5,7,14] with the [001] zone axis exposed perpendicularly to the electron beam. This is supported by the brightfield images (Figure 3.3a), showing a sheet-like crystallite. Hence, the two observed perpendicular lattice vectors of 29.9 Å and the other of 14.7 Å, as extracted from the HR-TEM image and SAED pattern (Figure 3.3), correspond to unit cell axes *a* and *b*, respectively. This finding is corroborated by a Pawley refinement[15] of the X-ray powder diffraction data in Figure 3.4a (Pawley fit) resulting in a monoclinic unit cell ($P2_1$) with a = 14.6 Å, b = 29.6 Å, c = 3.9 Å, $\alpha = \gamma$ = 90° and β = 91°, R_{wp} = 4.7%. Notably, the *c* parameter is slightly larger than usual for a 2D carbon nitride structure, in which typically stacking distances of 3.1-3.3 Å are observed.[1,16–18] Potassium ions, incorporated into the structure, might lead to a widening of the carbon nitride backbone in *c*-direction. It can also be assumed that the structure is not as condensed as the 2D poly(heptazine imides), as will be analyzed in more detail by means of ssNMR spectroscopy. Therefore, the out-of-plane orientation might be more complex for the K-CN-phase than the previously studied case of K-PHI and could include twisting and distortions of the structural motifs out of the basal plane. Disordered intensity modulation in the pair distribution function

(PDF) (Figure 3.4b) above r > 18 Å – with respect to the data observed for two-dimensional K-PHI[5] – also implies such a more diverse stacking behavior. The streaking of electron diffraction spots along the *c**-axis (Figure B 1) also fits well to the assumption of disorder in the stacking direction.

The general appearance of the pair distribution function of K/H-CN-phase in Figure 3.4b follows the shape of typical representatives for heptazine-based polymers like K-PHI and melon, respectively. Triazine-based structures would lead to a different pattern for distances below 5 Å, illustrated in Figure B 2 in the appendix. The peak at the dashed line at approx. 2.8 Å is related to the potassium coordination distance for potassium ions to the network or to water molecules, and is therefore slightly more intense for the CN-materials containing potassium cations. Quantum-chemical calculations have indeed shown that the water coordination shell of potassium corresponds to this distance.[5] Thus, it can be expected that potassium is coordinated to the negatively charged network, while being additionally surrounded by water. Water can also have an influence in the arrangement of heptazine units via hydrogen bonds. However, the influence is presumably weaker as the XRPD pattern of the protonated H-CN-phase in Figure B 3 in the appendix suggests a significant loss of crystallinity by the extraction of potassium and replacement by water.

Overall a close relationship between the new K-CN-phase and melon[17] can be identified, based on the similarities in the electron diffraction images. This is further supported by PDF analysis, pointing to heptazine as the primary building unit, identical to melon. One difference is of course the presence of potassium within the structure of the K-CN-phase. Likely, this new structural element causes the changes in symmetry, but at the same time increases the degree of crystallinity, due to stronger interaction of the building blocks. Melon crystallizes in space group $P2_12_12$, thus with orthogonal axes. In the K-CN-phase the β-angle of 91° is very close to the right angle, nearly matching the metric of melon. Furthermore, the unit cell lengths a and b deviate from melon (a_{melon} = 16.8 Å, b_{melon} = 12.1 Å), but one axes is nearly doubled in the K-CN-phase

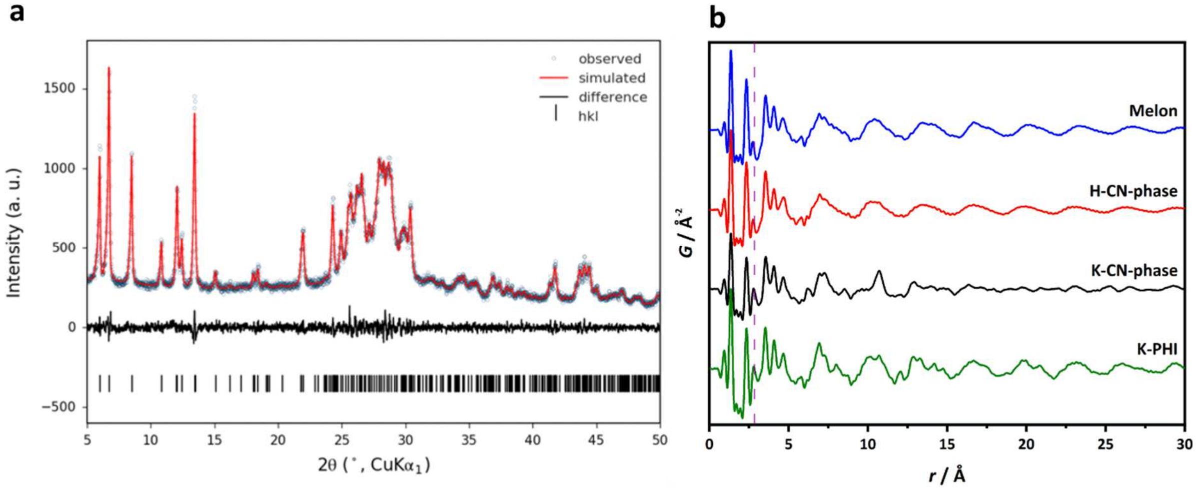

Figure 3.4. (a) X-ray powder diffraction data with Pawley-fit of the K-CN-phase. (b) PDF analysis of melon, H-CN-phase, K-CN-phase and K-PHI up to 30 Å. The PDFs of melon and the protonated H-CN-phase contain similar features as well as the corresponding PDFs of the K-CN-phase and K-PHI have matching maxima. Note that though generally very similar, the dashed purple line indicates differences between potassium containing samples in the low distance regime. In K-PHI this distance could be assigned to the K-N/O-distances between the network and potassium or potassium and water.

(b = 29.6 Å). This can be explained by longer heptazine chains constituting the structural motifs, requiring a larger unit cell due to the additional structural element of potassium. Of course, the comparison of both compounds in terms of their crystalline structure has to be taken with a grain of salt, because actually firm statements from this evaluation would demand for a structural solution. Unfortunately, this remains a major challenge from powder- and electron diffraction data alone. A structure solution via a simulated annealing approach (with prebuilt heptazine unit blocks) has been attempted, but yielded no satisfactory results.

Morphology

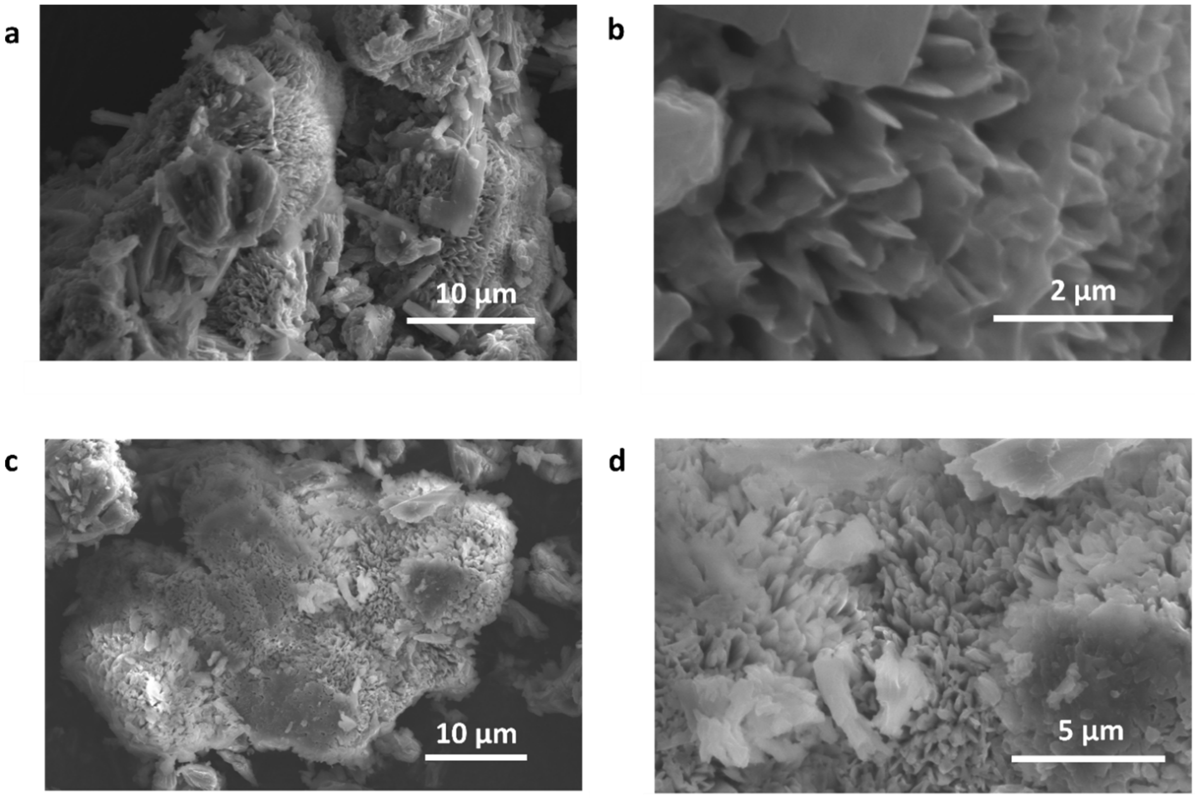

Figure 3.5. SEM micrographs of (a-b) K-CN-phase and (c-d) the protonated H-CN-phase. The morphology is retained after the acidic treatment.

The K-CN-phase crystallites have a macroscopic platelet-like morphology as the scanning electron images in Figure 3.5a–b reveal. This habitus is not significantly changed after acidic treatment (Figure 3.5c–d). Thus, on the one hand the crystals lose long-range order to a certain degree, which is apparent from the XRD data (Figure B 3) and is likely caused by the extraction of the structure directing potassium cations. On the other hand, this process does not involve dissolution or obvious other forms of degradation of the crystallites.

Solid-state nuclear magnetic resonance spectroscopy

Already disclosing the similarities to melon by scattering techniques, in the following section a more thorough analysis of the local structure is given, utilizing ssNMR spectroscopy. Here, special emphasis has been put on the comparison of the pristine (K-CN-phase) and protonated variant (H-CN-phase).

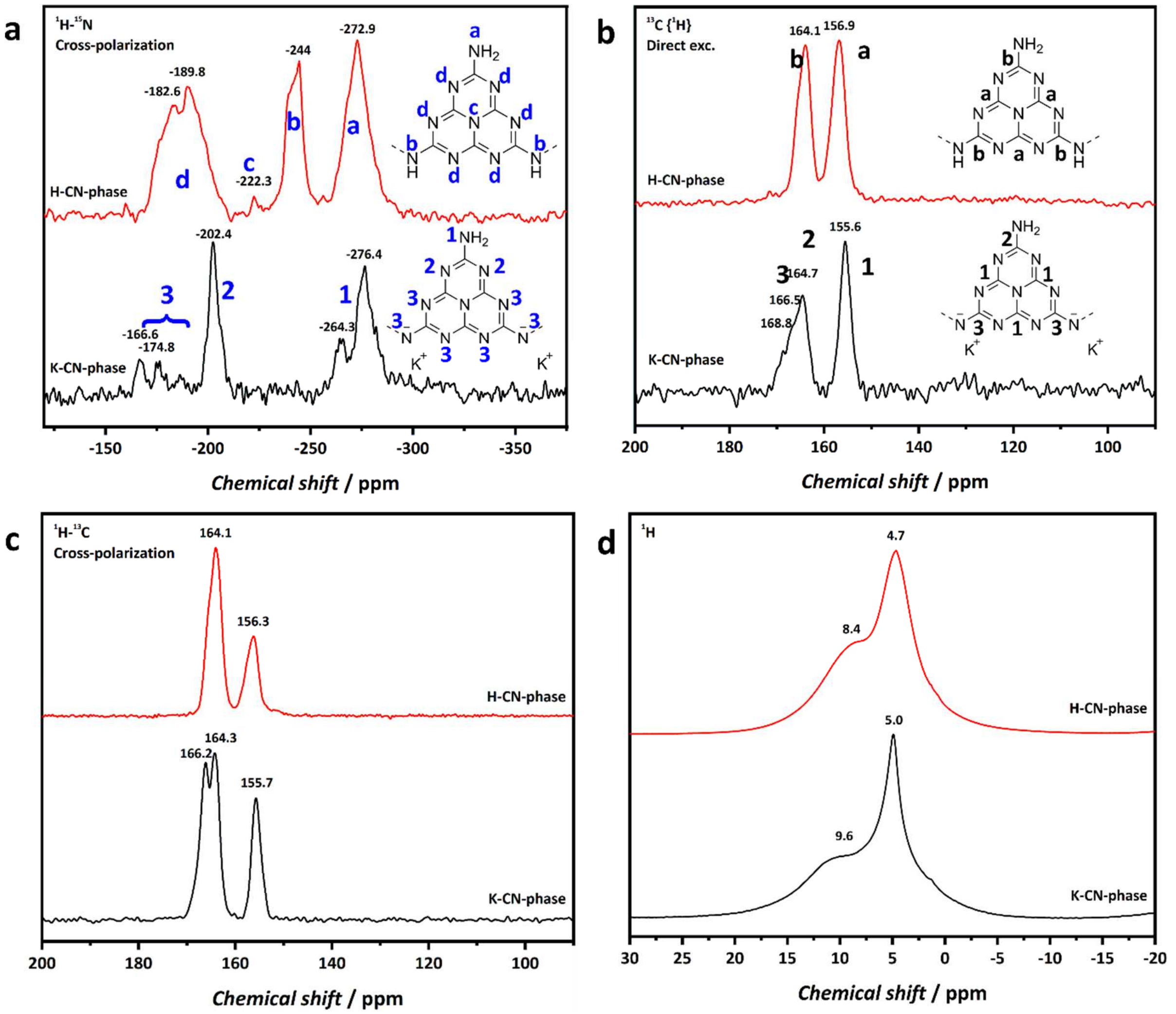

Figure 3.6. (a) ^{15}N cross-polarization, (b) direct excitation ^{13}C, (c) ^{13}C cross-polarization (CP) and (d) ^{1}H magic angle spinning (MAS) solid-state NMR of K-CN-phase (black curves) and H-CN-phase (red curves). The contact times for both CP measurements were set to 4 ms. The insets contain the structural assignment of NMR signals for carbon atoms (black) and nitrogen atoms (blue). To distinguish more easily between the K-CN-phase and H-CN-phase, the assignments were chosen to be digits and letters, respectively.

^{15}N NMR

The ^{15}N cross-polarization (CP) experiment in Figure 3.6a shows signals at chemical shifts of -167 and -175 ppm (N3), which can be attributed to the nitrogen atoms in close vicinity to potassium, which has been shown before by quantum-chemical calculations.[5] In addition, the compound exhibits such a degree of order that these signals are even better resolved than in the previously reported K-PHI structure. The rather small intensity of these signals originates from the increased distance to protons under cross-polarization conditions. The signal at -202 ppm (N2) is typical for tertiary nitrogen atoms located in the heptazine core near the NH_2-moiety, given the relatively high intensity. The last group of signals, located from -260 to -284 ppm (N1), belongs to NH_2-groups, terminating heptazine units. These chemical shifts are typical for a tri-*s*-triazine connected amino group in comparison to a connection to triazine compounds such as in melam or melamine, where higher field shifts between ca. -280–(-300) ppm would be expected.[19,20]

Comparing the ^{15}N CP ssNMR spectrum for the K-CN-phase with the corresponding spectrum for K-PHI – both recorded with the same contact times – offers insights into the interconnectivity of the building blocks. Since NH_2-groups terminate the carbon nitride backbone, a surplus of these groups indicates a less condensed polymer. Figure 3.7 illustrates that the relative quantity of NH_2-groups in K-CN-phase is higher, when normalized to the heptazine core nitrogen signals (>-200 ppm), which is also a tendency observed in the infrared spectrum (see Figure 3.10). Therefore, we conclude the local structure to consist of strands of heptazine units like in the archetypical carbon nitride melon instead of the more condensed, two-dimensional arrangement observed in K-PHI, where NH_2-signals are barely visible. Of course, it should be noted that we simplified in ways that the integral of the tertiary nitrogen atoms in the K-CN-phase is presumably slightly underestimated. It is known that a significant quantity of NH-bridges is present in K-PHI, hence leading to an increased transfer of magnetization of this proton to the tertiary nitrogen group. Ultimately, it would need an isotopically labelled sample and a direct excitation ^{15}N NMR experiment to resolve this issue.

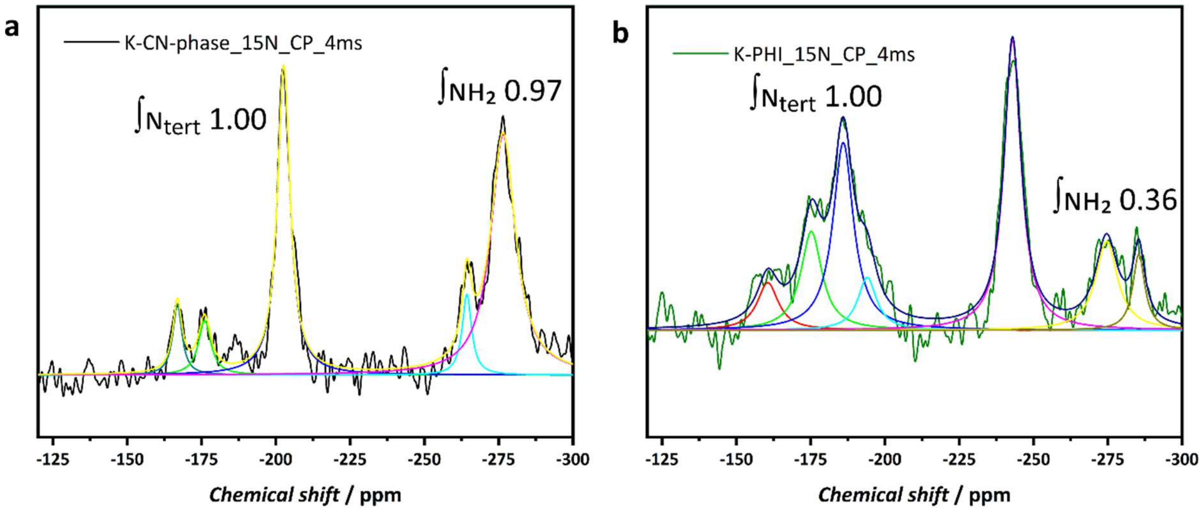

Figure 3.7. ^{15}N CP ssNMR spectra of (a) K-CN-phase and (b) K-PHI recorded with equal contact times of 4 ms. In both spectra the integral under the tertiary nitrogen signals have been arbitrarily chosen to be 1.00. The signals belonging to NH_2 groups in the K-CN-phase have a much larger area relative to the corresponding signals in K-PHI. The peak-integrals and fitting parameters may be found in appendix B.

When the compound is protonated in diluted acid (H-CN-phase, Figure 3.6a), we observe a spectrum that strongly resembles the one of melon (see comparison to melon in Figure 3.8b), in which all bridging nitrogen atoms are protonated.[21] The introduced proton has three effects on the ^{15}N-CP spectrum. Firstly and most strikingly, a new signal arises at 244 ppm (N_b) with a shoulder at 240 ppm, attributed to the newly formed NH-moiety. Second, the central nitrogen atom in the heptazine unit is responsible for the low intensity signal at 222 ppm (N_c). Although this atom should have been also present in the K-CN-phase, the higher concentration of protons in the acid treated compound enables its visibility, due to higher transfer of magnetization to the nitrogen nucleus in the CP setup. Third, the signal at >-200 ppm (N_d) becomes significantly broader, which is expected for two reasons: On the one hand the newly introduced proton may enhance also the visibility of these nuclei. On the other hand, the loss of potassium from between the strands of carbon nitride polymer likely has a disordering impact, resulting in overall broadened signals. The effect of the structuring influence of potassium ions – and also the loss thereof, when treated in acid, thus leading to a more random orientation of the polymer backbone – has been discussed in detail in the study on potassium poly(heptazine imide) in chapter 2.[5]

^{13}C NMR

The observation of two clearly separated groups of signals, 156 ppm (C1) and >164 ppm (C2,3), in the direct excitation ^{13}C NMR experiment (Figure 3.6b) is usually associated with the presence of heptazine building blocks. The inner carbon atoms of the heptazine unit resonate at a chemical shift of 155.6 ppm (C1).[19] Comparing that to a triazine-based polymer such as PTI · LiCl (Figure B 5) with a chemical shift of 158–168 ppm, the signal in the K-CN-phase for the inner carbon atoms is shifted upfield by a few ppm, which correlates to increased distance from protons.[20,22] This also explains why this signal exhibits reduced intensities in a cross-polarization experiment (Figure 3.6c). The second group of signals is overlapping with each other, but can be further divided into two signals at 165 (C2), 167 (C3) with a shoulder to lower field. The first of these is associated with the carbon atom next to a terminating NH_2-group, and is corroborated by the increased intensity of this signal in the ^{13}C cross-polarization NMR experiment (Figure 3.6c).[20] The resonance at approx. 167 ppm (C3) can be attributed to carbon atoms next to the deprotonated bridging nitrogen atom. As quantum-chemical calculations have shown, the potassium ion is not centrally facing the deprotonated bridge, but is slightly moved to one side.[5] This explains that the signal exhibits a shoulder corresponding to the carbon atom in closer vicinity to the potassium ion. Additionally, intermolecular water is interacting with the outer carbon atom C2, which is revealed by a ^{13}C-^{1}H-HETCOR MAS spectrum (Figure B 8) with short contact times of 0.25 ms. Here, a correlation to the proton signal at 4.9 ppm can be extracted, a reminder that also intermolecular magnetization transfer can occur in these structures. This close interaction of water with the polymer can potentially explain the increased signal intensity of C3-group in the CP spectrum.

After protonation, the H-CN-phase exhibits only two major signals, which correspond to the inner carbon atoms (CN_3) and the outer nuclei. The signals of the outer nuclei ($N_2\underline{C}NH_2$ and $N_2\underline{C}NH$) have a too similar shift to be distinguishable. The spectrum is however very similar to the one of melon (cf. Figure 3.8a), from which we infer that the compounds must be closely related in the first place. It is likely that potassium serves as a structure directing unit. Hence, the crystallinity is reduced after removal of the alkali ion, but compared to the as-synthesized melon still exhibits a higher degree of order.

In comparison to the closely related 2D potassium poly(heptazine imide) system, no signal for cyanamide groups (usually observable at approx. 120 ppm) is found in the K-CN-phase, nor in its protonated counterpart, implying that there is, at most, only a low level of cyanamide terminations/defects within this structure. The low amount of those defects can also be one of the reasons for the observed high degree of order in the K-CN-phase.

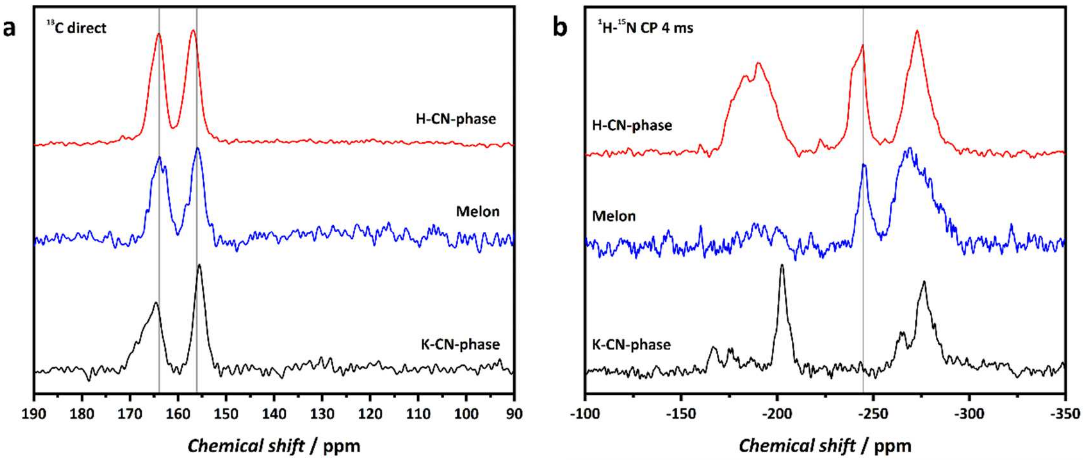

Figure 3.8 ssNMR spectra as a direct comparison between the K/H-CN-phase and the 1D polymer melon, showing the similarities between the acid treated H-CN-phase and melon. (a) ^{13}C direct excitation ssNMR spectrum (b) ^{15}N cross-polarization ssNMR spectrum. Grey lines for orientation.

^{1}H NMR

The proton NMR spectrum (Figure 3.6d) for the K-CN-phase features two broad signals with maxima at approx. 9.6 ppm and 5.0 ppm. The assignment of these signals is not unambiguous, due to the likelihood of complex hydrogen bridges that may form between NH_2-groups and the tri-s-triazine backbone. The signal at 9.6 ppm likely stems from NH_2-group protons with a shoulder to higher chemical shifts, which may be attributed to the deshielding effects of hydrogen bonding of these protons. The signal at 5.0 ppm is attributed to water molecules in the vicinity of the CN-network. In hydrogen bond accepting systems, the presence of closely bound water can have a profound influence on chemical shifts of the surrounding polymer, as quantum-chemical calculations, presented in chapter 2, have shown.[5]

Treatment with acid leads to an emerging peak at ca. 8.4 ppm, which is in the typical range of an imido proton of the now protonated nitrogen bridge. The signal of the NH_2-group at lower field is only visible as a shoulder. A ^{15}N-^{1}H HETCOR NMR spectrum (Figure B 9) supports the finding that the signals of NH (N_b) and NH_2 (N_a) correlate roughly with the same, relatively broad proton signal between 7-9 ppm. The proton signal at ca. 4.7 ppm, belonging to water, is only mildly affected by the protonation.

In conclusion, the ssNMR spectra supports a heptazine-based structure. While the emerging NH-groups upon protonation point toward an interconnected, hence polymeric backbone, the high amount of NH_2-groups rather suggest the presence of oligomers.[23] The exceptionally high local order of the K-CN-phase could be indicative of rigid hydrogen bonding between those oligomeric strands, as commonly observed in both molecular and polymeric CN-compounds.[10,12,17,21] In the case of the new K-CN-phase, additional coulombic interactions prevail between the negatively charged backbone and the potassium cations, leading to the rigid and stable network as shown in the following.

Thermal analysis

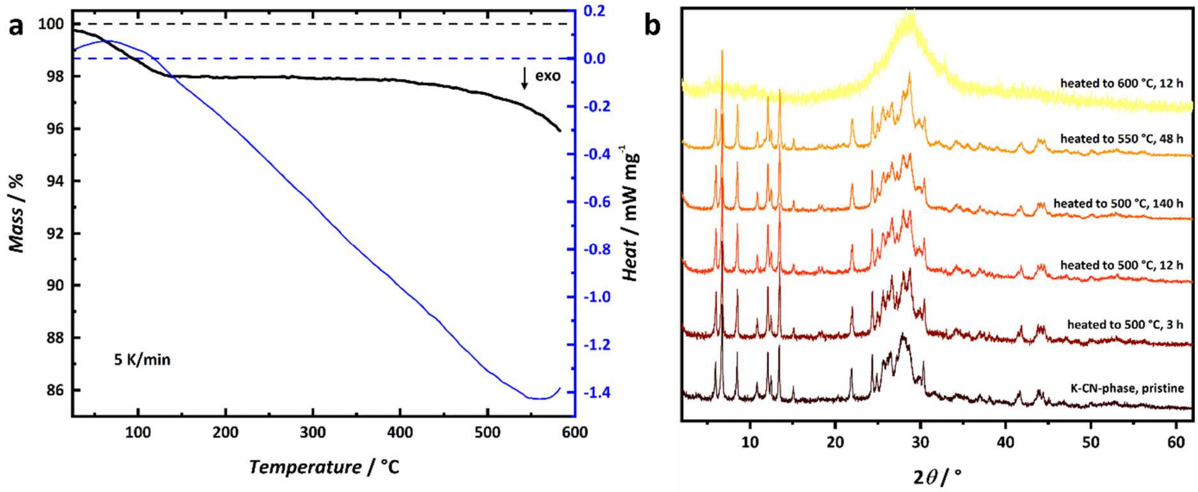

Figure 3.9. (a) Thermogravimetry and differential scanning calorimetry curves for K-CN-phase. The sample was heated in a corundum crucible from r.t. to 600 °C at a rate of 5 K/min under argon flow. (b) Ex-situ temperature dependent XRD patterns of K-CN-phase at various temperatures from 500–600 °C and different lengths of time.

In the thermogravimetry curve in Figure 3.9a, there is only one distinct mass loss observable, beginning at temperatures below 50 °C and reaching a plateau at ca. 150 °C. The mass loss equals 2-3 wt% and is likely related to the loss of adhesive water, and fits the estimated amount from elemental analysis. A second, more continuous mass loss sets in beyond 450 °C, which can be related to a beginning decomposition. Moreover, the heat flow in the DSC curve shows no evident signal that could be referred to a phase transition or decomposition reaction.

In a second set of experiments the thermal stability was investigated by heating small amounts of the sample (ca. 25 mg) in a dried, evacuated and flame-sealed glass ampoule for various times at temperatures ranging from 500–600 °C (Figure 3.9b). It is remarkable that the K-CN-phase remains stable and crystalline at a temperature of 550 °C for an extended period of 48 h, which is even higher than the synthesis temperature of 500 °C. Small changes in the diffraction patterns may occur due to the already discussed loss of water or small shifts of mobile species like potassium cations. Especially, in the range of 25-30° 2θ, more pronounced changes are observable, which may be attributed to a flexibility in the vertical arrangement of the poly(heptazine imide) strands. Prolonged heating at 600 °C leads to a loss in crystallinity, owing to the decomposition and carbonization of the CN-network.

Infrared Spectroscopy

The infrared (IR) spectrum (Figure 3.10) of the potassium containing polymer shows the out-of-plane bending mode of the heptazine unit at 795 $\mathrm{cm^{-1}}$, which is slightly lower than the usual ~805 $\mathrm{cm^{-1}}$ for heptazine systems.[17,24] A negative charge on the heptazine unit could cause such a red-shift and is for instance observed for the negatively charged nucleus of potassium melonate.[25,26] After protonation this vibration indeed shifts to 805 $\mathrm{cm^{-1}}$, once more implying the structural similarity of the local building unit to the one in melon (804 $\mathrm{cm^{-1}}$). Additionally, after protonation a peak emerges at 880 cm^{-1} (dashed line), which can be found in melon as well. The peak at 985 cm^{-1} is associated with the deprotonated bridging CNC-group coordinated by the alkali metal ion.[27] This signature is missing in the protonated case, but is present in K-PHI, underscoring the similar potassium coordination in both potassium containing CN-polymers.

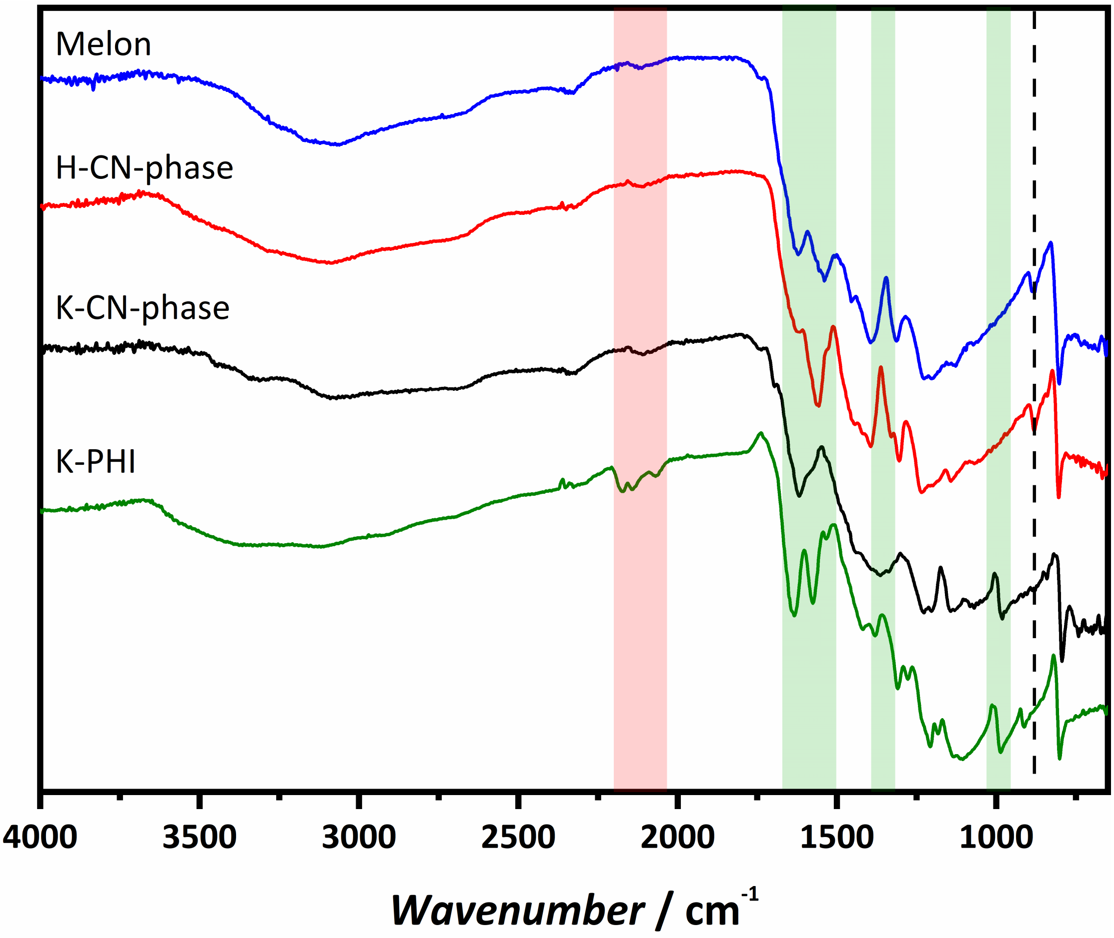

Figure 3.10. Infrared spectra of the K-CN-phase (black) and the protonated substance (red). For comparison the spectra of melon (blue) and K-PHI (green) are shown. The light-green areas mark key differences in the spectra that may be attributed to a loss of the potassium ions and hence a changed vibronic structure. The red marked area marks the position of potential cyanamide functionalities, hardly present in the samples. The dashed black line shows the close connection between melon and the protonated H-CN-phase.

The very small peak at 1700–1750 cm^{-1} stems from C=O double bonds likely terminating the surface of the oligomers and can be ascribed to terminating defects. Interestingly, the signal of cyanamide groups that has been identified before in the related K-PHI, at approx. 2150 cm^{-1} (highlighted red) has only very low intensity. Hence, the K-CN-phase is mostly free of those groups, which is an important factor for the discussion of the structure–property relationships, when exposed to light as will be discussed later in this chapter. A very broad signal is observed for OH- and NH_2-vibrations (2600-3500 cm^{-1}) presumably owing to the wide distribution of hydrogen bonding networks between oligomeric strands as well as from intermolecular water molecules.[28] Formation of imido bridges after protonation may explain the marginally increased intensity in this region. Overall the IR-spectrum supports the idea of a close connection between the protonated H-CN-phase and the 1D heptazine-based polymer melon.

Optical properties, photocatalysis and charge storage

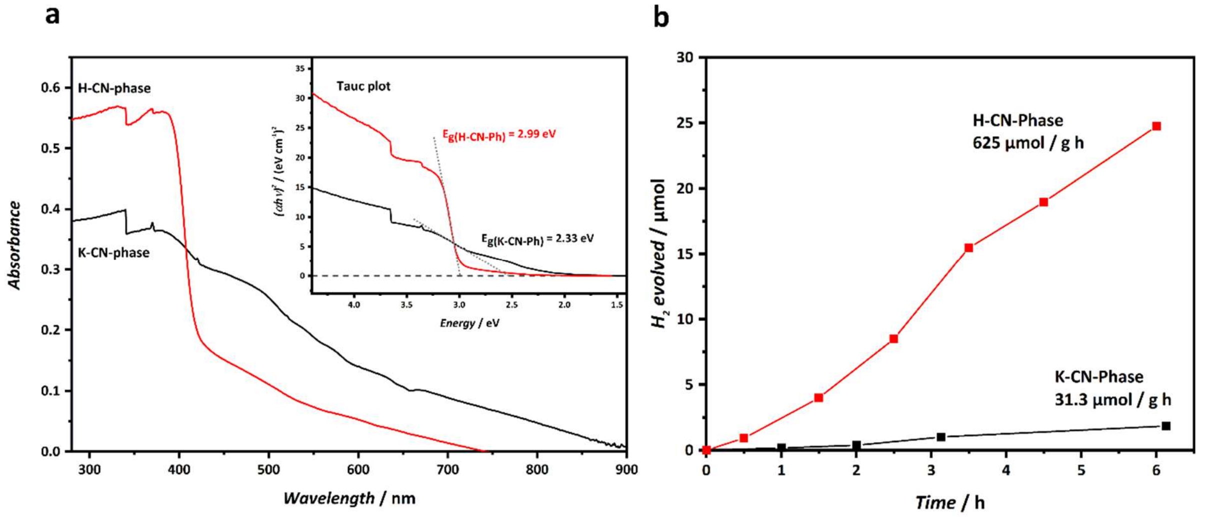

Figure 3.11. (a) UV/Vis Absorption spectra of K-CN-phase (black) and H-CN-phase (red) and the corresponding Tauc plots assuming a direct band gap[7] for both materials. At 340 nm the change of the light source causes a measurement artefact. (b) Photocatalytic hydrogen evolution experiments of K-CN-phase and H-CN-phase measured at 100 mW/cm^2 and methanol as a sacrificial electron donor and *in-situ* photodeposited platinum as a cocatalyst.

Figure 3.11a displays the absorption spectra of the K-CN-phase and its protonated counterpart. The inset shows the corresponding Tauc plots, assuming a direct band gap. The broad tail in the spectrum of the K-CN-phase is not found for the H-CN-phase with a clear-cut absorption edge and could therefore be explained by potassium ions, giving access to intraband states.[29] This is also reflected in the appearance of the powder by a brownish color of the potassium variant opposed to the white/beige color of the protonated compound. The calculated band gap from these spectra is 2.33 eV for the potassium compound and a significantly higher 2.99 eV for the protonated compound. Note however, that the calculation of the band gap for the K-CN-phase is difficult due to the large Urbach-tail obscuring a clear absorption band edge. However, the same trend of a larger band gap for the protonated compound can be observed for the related structures K-PHI and H-PHI.[1,5,30]

Many carbon nitrides synthesized from salt melts show increased photocatalytic activity due to either increased surface area and/or defective structure elements such as terminal groups.[1,2,5,29,31] We were intrigued by the question how the new K-CN-phase would perform in the photocatalytic hydrogen evolution test, since the synthesis yields a very crystalline material with supposedly only a low proportion of defects, as evidenced from XRD, IR and NMR spectra. Figure 3.11b shows the photocatalytic activity for the K-CN-phase and its protonated H-CN-phase counterpart, respectively. The HER rate with methanol as an electron donor for the K-CN-phase amounts to 31.3 µmol/gh, which is significantly less than observed for crystalline K-PHI (~193 µmol/gh), presented in the previous chapter.[5] The K-CN-phase rather has a comparable rate to the prototypical carbon nitride melon, often referred to as g-C_3N_4. Melon is a material consisting of linearly connected heptazine units, which in turn form layered arrangements by strong hydrogen bonds to the adjacent strand.[17] It exhibits a H_2-production rate of only about 25 µmol/gh of hydrogen under the same conditions. The similarly close-packed arrangement in both the

K-CN-phase and melon, and hence a low accessible reaction surface for water reduction, could explain the relatively low photocatalytic activity.

With a hydrogen evolution rate of 625 µmol/gh, the H-CN-phase is surpassing that of the potassium variant by far. The same trend is observed for the transformation of K-PHI to H-PHI (cf. chapter 2), where also a drastic increased HER rate is reported for the acid treated sample.[30] The increased band gap of H-CN-phase may explain this boost in activity, assuming a widening of the energy gap at approximately equally shifted valence/conduction band positions. Although the amount of usable light is reduced by a larger band gap, the augmented driving force (overpotential) compensates for this effect and the overall reduction rate is increased. In a recent study, *Stolarczyk* and co-workers reported that the protonation of the photocatalyst supports a fast charge transfer to protons, causing an overall increase in the hydrogen evolution rate.[32] In a similar fashion, the acid treated backbone of the H-CN-phase could supply protons in the vicinity of the employed cocatalyst, thus augmenting the rate. Furthermore, it has been shown that modifying the surface of carbon nitrides has a strong influence on how the catalyst disperses in the aqueous reaction solution, and hence its interaction with i.e. the hole scavenger.[2] Additionally, the rather low rate for the K-CN-phase may also stem from a larger recombination rate, due to the discussed presence of intraband states, which could lead to a competing recombination of excitons and extraction of electrons from the catalytic cycle within trap states. However, the very low intensity of the electron paramagnetic resonance signal (Figure 3.12a) in presence of 4-methyl benzyl alcohol (4-MBA) as a sacrificial electron donor is a hint that these traps may not be as long-lived as is the case for K-PHI, which is shown for a comparison in the same figure. All spectra yield a g-factor of ca. 2.003, indicative of a free electron, typical for CN-systems.[33] In general, one must critically note that the magnitude of the signal (K-CN-phase) is so low, that it should not be overinterpreted and the observed signal can also derive from small impurities of K-PHI, which may be present, due to the similar synthetic route.

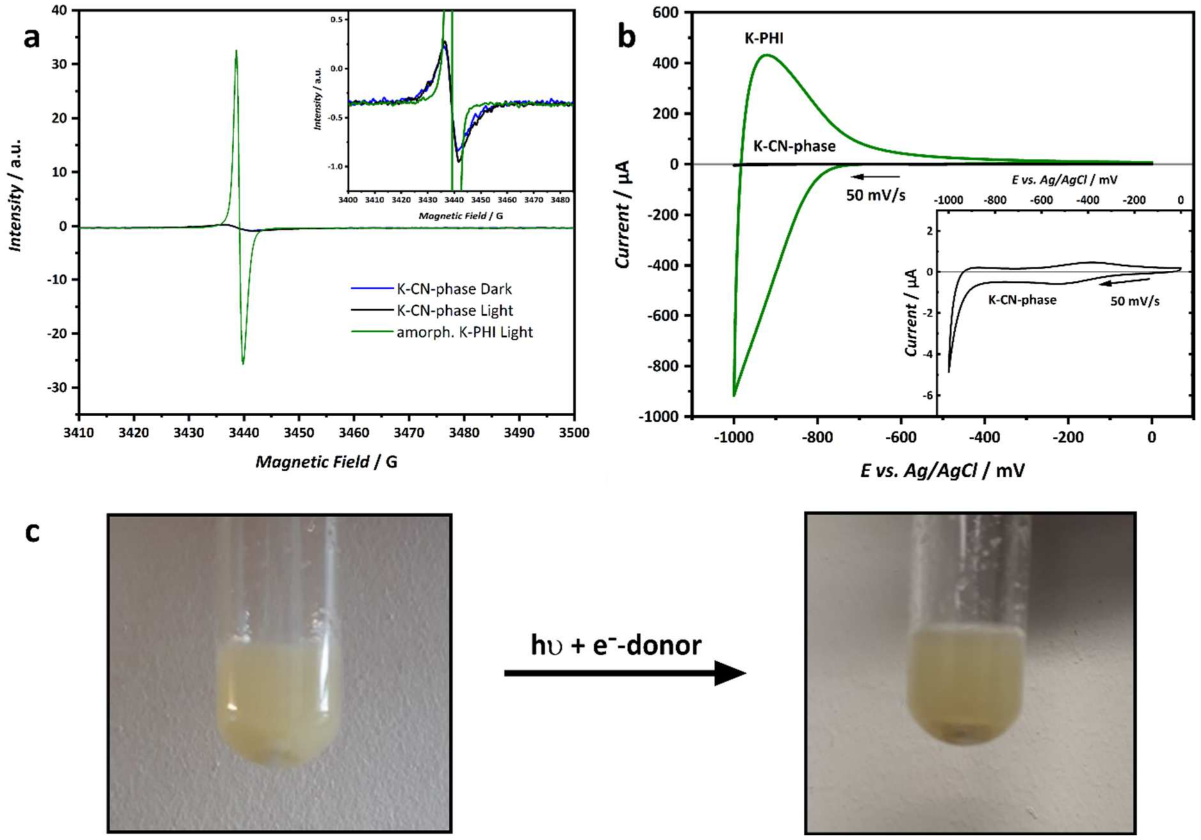

Figure 3.12. (a) EPR spectrum with inset of K-CN-phase before (blue) and after (black) irradiation in presence of 4-MBA as sacrificial donor. There is no increase in intensity, in dependence of illumination. The green graph belongs to an irradiated K-PHI sample with much higher intensity. (b) Cyclic voltammogram of K-PHI (green) and K-CN-phase (black) both recorded at 50 mV/s scan rate in 1 M KCl electrolyte. The inset shows the drastically decreased current for the K-CN-phase, which is comparable to the blank FTO electrode Figure B 12. The redox event at -500 mV is a negligible background effect also present for the blanc FTO. (c) K-CN-phase suspension in a mixture of dest. water and 4-MBA as a sacrificial electron donor before (left) and after (right) irradiation with a Xe-lamp. The slightly darker hue in the right photograph is an effect from a different lighting situation and a beginning segregation of the solid at the bottom of the flask.

In K/H-PHI (cf. chapter 2), a fascinating long-lived photoreduced state can be observed, when the sample is irradiated in presence of an electron donor. This transformation is accompanied by a color change from yellow to blue.[34] The donor quickly extracts the holes, leaving the photocatalyst with stored electrons that cannot undergo excitonic recombination.[34–37] For the K-CN-phase a similar long-lived photoreduced state cannot be observed under comparable conditions; neither the color change (Figure 3.12c) nor a significant EPR signal can be obtained (Figure 3.12a).

In a recent study, *Podjaski et al*. could show that the charged state can also be achieved electrochemically for K-PHI, thus yielding the blue state through a pseudocapacitive behavior.[37] Here, alkali metal cations from the electrolyte act as stabilizing agents for the negative charge on the carbon nitride backbone. The same process has been investigated by cyclic voltammetry for the new K-CN-phase depicted in Figure 3.12b. However, in comparison to K-PHI, only a very low current can be observed during sweeping to negative potentials of -1000 mV (vs. Ag/AgCl), which should thermodynamically enable crossing of electrons from the conductive FTO substrate to the conduction band of the carbon nitride. The current at -1000 mV (vs. Ag/AgCl) does not even exceed -5 µA for the K-CN-phase, which is in the range of the blank FTO electrode (cf. Figure B **12**).

K-PHI with a comparable electrode area shows a current two orders of magnitude higher with values up to -900 µA. Moreover, for the K-CN-phase, the discharge curve (positive current) is non-existent on the reverse scan, which indicates that the previously obtained negative current probably stems from beginning electrolyte decomposition (i.e. electrolysis). This is corroborated by the fact that scanning to even more negative potentials (-1400 mV) results in higher, non-reversible hydrogen evolution currents.

Since the material consists of heptazine units and deprotonated imide bridges very similar to K-PHI, it stands to reason that the assembly of the polymeric backbone is a key factor for the observed color change. While the K-PHI network is connected two-dimensionally, we have found a one-dimensional connectivity for the K-CN-phase, similar to the architecture found in melon. From this discrepancy, we infer that the observation of the long-lived photoreduced state may either depend on the 2D structure of the polymer backbone or can be explained by the presence of cyanamide functionalities in K-PHI, or both. The latter have been discussed as stabilizing moieties for the blue state,[34,37–39] but are not found in the K-CN-phase, evidenced by infrared- and direct exc. ^{13}C NMR-spectra. The third component which is necessary to stabilize the reduced state comprises alkali ions, which are provided in both K-PHI and the K-CN-phase. One thing that needs to be taken into account is the mobility of the potassium ions. These are mobile in the case of K-PHI,[37] but might not be in the K-CN-phase and hence not able to stabilize the blue state. On the other hand, the possibility to extract the potassium ions during acid treatment at least suggests a certain mobility of the cations. Therefore, we can conclude that the mere presence of alkali ions is a necessary criterion for the charge stabilization, yet cannot be exclusively responsible for the phenomenon.

By synthesizing the new K-CN-phase, we were able to obtain a material exquisitely suited for comparison with K-PHI with regards to the origin of the long-lived excited state. Major features, like the heptazine building units and potassium coordination to deprotonated imide bridges, are closely related, while the K-CN-phase lacks the cyanamide functionalities and being less interconnected (linear), due to the increased ammonia back pressure during the ampoule synthesis. It can thus be assumed that either of those features (or both) is a prerequisite for the electron storage behavior.

Although the disentanglement of these last factors cannot be unambiguously solved in this work, a peculiarity, observed in the K-PHI study in chapter 2, may be worth revisiting here: Direct excitation ^{13}C ssNMR spectroscopy of crystalline K-PHI and optimized amorphous samples has revealed a higher content of cyanamide functionalities for the crystalline species. However, when put to the test for the photoreduced state, the crystalline K-PHI sample exhibits less intense blue suspensions compared to the amorphous K-PHI (Figure B 11), indicative of lower concentration of photoreduced states. At first glance, the missing proportional relation between cyanamide concentration and intensity of the excited state could suggest that the cyanamide groups are not the decisive factor. Unfortunately, this observation does not yet produce an irrefutable proof, because the entanglement of other parameters like crystallite size and surface located cyanamide functionalities is not considered. Nonetheless, our finding of a potassium containing linear, yet not photo-chargeable, heptazine based polymer is another puzzle piece that will help to elucidate this intriguing property. If a method was capable of selectively cleaving the cyanamide groups in 2D interconnected K-PHI sample, a subsequent test for the photoreduced state could yield the proof, whether the 2D arrangement, the cyanamide groups or both are the necessary components for facilitating the photoreduced state.

An important step in this direction have been undertaken by *Kröger et al.*, who took K-PHI and transformed the cyanamide functional groups into melamine moieties, while preserving the 2D poly(heptazine imide) backbone.[2] This material, called Mel-PHI, does not show the signature of cyanamide groups in the IR- and ssNMR spectrum, respectively. Yet, Mel-PHI has shown the potential to perform dark photocatalysis, therefore indicating the presence of the photoreduced state. Technically, the replacement of the NCN-moiety by melamine does not deliver a final proof, as this new functional group could theoretically have the same effect as cyanamide. Yet, by combining these findings with the above presented results, we can tentatively conclude that indeed the 2D architecture of the heptazine backbone is likely the governing factor for the emergence of a photoreduced state.

3.3 Conclusion

The synthesis and characterization of a new highly crystalline ionic carbon nitride and its protonated counterpart has been presented. While the synthetic approach is closely related to the one discussed in chapter 2 for K-PHI, it could be shown that the delicate equilibrium of reaction gases has a profound influence on the obtained product.

The electron diffraction pattern resembles the archetypical carbon nitride, melon. The Bragg reflections in powder X-ray diffraction, however, are resolved significantly better compared to the largely amorphous character of melon. The unit cell, derived from Pawley refinement, is corroborated by electron diffraction and is considerably larger than melon's, which can be attributed to the likelihood of more space-consuming oligomeric structural motifs. The PDF of the H-CN-phase yields comparable results to melon, while the correlation function of the K-CN-phase especially deviates for greater correlation distances, which is indicative of a more complex three-dimensional arrangement of the subunits. Hence, analogous to the observation in chapter 2, the potassium ions play an important structure-directing role, inducing a rigid connection between the CN-backbone, which is then partially lost upon protonation. Solid-state NMR spectroscopy further supports an oligomeric, linear arrangement of heptazine units. Especially, the spectral features of the protonated H-CN-phase compare exceptionally well to melon.

Both the pristine and the protonated compounds are photocatalytically active for hydrogen evolution. The latter exceeds its ionic counterpart nearly twentyfold, hence following the same trend as observed for the transition from K-PHI to H-PHI. Intriguingly, and contrary to the closely related K-PHI material, we could show that the K-CN-phase does not produce a photoreduced state; neither upon irradiation in presence of an electron donor nor by charging the compound electrochemically. Since both, K-PHI and the K-CN-phase, exhibit a deprotonated imide bridged heptazine-backbone, balanced by potassium ions, we consequently infer that the ionic nature of a CN-network cannot be responsible for the reduced state on its own. With the help of previous work on melamine functionalized poly(heptazine imide), featuring a material with no NCN-functionalities yet an existing photoreduced state, we can tentatively deduce that the 2D arrangement within K-PHI constitutes the crucial feature enabling the photocharging effect. We thereby add valuable experimental evidence for solving this ongoing debate.

3.4 Acknowledgments

I would like to thank Leo Diehl for critical discussions, M. W. Terban for the total scattering experiments, Sascha Harm for his help and numerous crystallographic discussions, Viola Duppel for TEM images, Jakob Blahusch for TG-measurements and Igor Moudrakovski and Christian Minke for ssNMR experiments. Further, I would like to thank A. Gouder, F. Podjaski for electrochemical guidance and J. Kröger for helpful discussions.

Experimental contributions

Hendrik Schlomberg designed this study, synthesized, characterized the K/H-CN-phase and interpreted the data if not state otherwise. H.S. also collected photocatalytic and electrochemical measurements. Maxwell W. Terban performed pair distribution function analysis and created the Pawley fit with X-ray powder diffraction data. Igor Moudrakovski performed solid-state NMR spectroscopy. Viola Duppel collected electron microscopy images and electron diffraction data. TGA samples were measured by Jakob Blahusch. Christian Minke supplied SEM images and EDX spectra.

3.5 References

(1) Lau, V. W.-h.; Moudrakovski, I.; Botari, T.; Weinberger, S.; Mesch, M. B.; Duppel, V.; Senker, J.; Blum, V.; Lotsch, B. V. Rational design of carbon nitride photocatalysts by identification of cyanamide defects as catalytically relevant sites. *Nat. Commun.* **2016**, *7*, 12165. DOI: 10.1038/ncomms12165.

(2) Kröger, J.; Jiménez-Solano, A.; Savasci, G.; Rovó, P.; Moudrakovski, I.; Küster, K.; Schlomberg, H.; Vignolo-González, H. A.; Duppel, V.; Grunenberg, L.; Dayan, C. B.; Sitti, M.; Podjaski, F.; Ochsenfeld, C.; Lotsch, B. V. Interfacial Engineering for Improved Photocatalysis in a Charge Storing 2D Carbon Nitride: Melamine Functionalized Poly(heptazine imide). *Adv. Energy Mater.* **2021**, *11*, 2003016. DOI: 10.1002/aenm.202003016.

(3) Kurpil, B.; Savateev, A.; Papaefthimiou, V.; Zafeiratos, S.; Heil, T.; Özenler, S.; Dontsova, D.; Antonietti, M. Hexaazatriphenylene doped carbon nitrides—Biomimetic photocatalyst with superior oxidation power. *Appl. Catal. B* **2017**, *217*, 622–628. DOI: 10.1016/j.apcatb.2017.06.036.

(4) Wirnhier, E.; Döblinger, M.; Gunzelmann, D.; Senker, J.; Lotsch, B. V.; Schnick, W. Poly(triazine imide) with Intercalation of Lithium and Chloride Ions [$(C_3N_3)_2(NH_xLi_{1-x})_3{\cdot}LiCl$]: A Crystalline 2D Carbon Nitride Network. *Chem. Eur. J.* **2011**, *17* (11), 3213–3221. DOI: 10.1002/chem.201002462.

(5) Schlomberg, H.; Kröger, J.; Savasci, G.; Terban, M. W.; Bette, S.; Moudrakovski, I.; Duppel, V.; Podjaski, F.; Siegel, R.; Senker, J.; Dinnebier, R. E.; Ochsenfeld, C.; Lotsch, B. V. Structural Insights into Poly(Heptazine Imides): A Light-Storing Carbon Nitride Material for Dark Photocatalysis. *Chem. Mater.* **2019**, *31* (18), 7478–7486. DOI: 10.1021/acs.chemmater.9b02199.

(6) Savateev, A.; Pronkin, S.; Epping, J. D.; Willinger, M. G.; Wolff, C.; Neher, D.; Antonietti, M.; Dontsova, D. Potassium Poly(heptazine imides) from Aminotetrazoles: Shifting Band Gaps of Carbon Nitride-like Materials for More Efficient Solar Hydrogen and Oxygen Evolution. *ChemCatChem* **2017**, *9* (1), 167–174. DOI: 10.1002/cctc.201601165.

(7) Chen, Z.; Savateev, A.; Pronkin, S.; Papaefthimiou, V.; Wolff, C.; Willinger, M. G.; Willinger, E.; Neher, D.; Antonietti, M.; Dontsova, D. "The Easier the Better" Preparation of Efficient Photocatalysts-Metastable Poly(heptazine imide) Salts. *Adv. Mater.* **2017**, *8*, 1700555. DOI: 10.1002/adma.201700555.

(8) Savateev, A.; Pronkin, S.; Willinger, M. G.; Antonietti, M.; Dontsova, D. Towards Organic Zeolites and Inclusion Catalysts: Heptazine Imide Salts Can Exchange Metal Cations in the Solid State. *Chem. Asian J.* **2017**, *15*, 783. DOI: 10.1002/asia.201700209.

(9) Döblinger, M.; Lotsch, B. V.; Wack, J.; Thun, J.; Senker, J.; Schnick, W. Structure elucidation of polyheptazine imide by electron diffraction—a templated 2D carbon nitride network. *Chem. Commun.* **2009** (12), 1541. DOI: 10.1039/b820032g.

(10) Sattler, A.; Pagano, S.; Zeuner, M.; Zurawski, A.; Gunzelmann, D.; Senker, J.; Müller-Buschbaum, K.; Schnick, W. Melamine-melem adduct phases: investigating the thermal condensation of melamine. *Chemistry* **2009**, *15* (47), 13161–13170. DOI: 10.1002/chem.200901518.

(11) Botari, T.; Huhn, W. P.; Lau, V. W.-h.; Lotsch, B. V.; Blum, V. Thermodynamic Equilibria in Carbon Nitride Photocatalyst Materials and Conditions for the Existence of Graphitic Carbon Nitride g-C_3N_4. *Chem. Mater.* **2017**, *29* (10), 4445–4453. DOI: 10.1021/acs.chemmater.7b00965.

(12) Kessler, F. K.; Burow, A. M.; Savasci, G.; Rosenthal, T.; Schultz, P.; Wirnhier, E.; Oeckler, O.; Ochsenfeld, C.; Schnick, W. Structure Elucidation of a Melam-Melem Adduct by a Combined Approach of Synchrotron X-ray Diffraction and DFT Calculations. *Chem. Eur. J.* **2019**, *25*, 8415. DOI: 10.1002/chem.201901391.

(13) Haiber, D. M.; Crozier, P. A. Nanoscale Probing of Local Hydrogen Heterogeneity in Disordered Carbon Nitrides with Vibrational Electron Energy-Loss Spectroscopy. *ACS Nano* **2018**, *12* (6), 5463–5472. DOI: 10.1021/acsnano.8b00884.

(14) Suter, T. M.; Miller, T. S.; Cockcroft, J. K.; Aliev, A. E.; Wilding, M. C.; Sella, A.; Corà, F.; Howard, C. A.; McMillan, P. F. Formation of an ion-free crystalline carbon nitride and its reversible intercalation with ionic species and molecular water. *Chem. Sci.* **2019**, *10* (8), 2519–2528. DOI: 10.1039/c8sc05232h.

(15) Pawley, G. S. Unit-cell refinement from powder diffraction scans. *J. Appl. Crystallogr.* **1981**, *14* (6), 357–361. DOI: 10.1107/S0021889881009618.

(16) Bojdys, M. J.; Severin, N.; Rabe, J. P.; Cooper, A. I.; Thomas, A.; Antonietti, M. Exfoliation of Crystalline 2D Carbon Nitride: Thin Sheets, Scrolls and Bundles via Mechanical and Chemical Routes. *Macromol. Rapid Commun.* **2013**, *34* (10), 850–854. DOI: 10.1002/marc.201300086.

(17) Lotsch, B. V.; Döblinger, M.; Sehnert, J.; Seyfarth, L.; Senker, J.; Oeckler, O.; Schnick, W. Unmasking Melon by a Complementary Approach Employing Electron Diffraction, Solid-State NMR Spectroscopy, and Theoretical Calculations—Structural Characterization of a Carbon Nitride Polymer. *Chem. Eur. J.* **2007**, *13* (17), 4969–4980. DOI: 10.1002/chem.200601759.

(18) Giusto, P.; Cruz, D.; Heil, T.; Arazoe, H.; Lova, P.; Aida, T.; Comoretto, D.; Patrini, M.; Antonietti, M. Shine Bright Like a Diamond: New Light on an Old Polymeric Semiconductor. *Adv. Mater.* **2020**, *32* (10), e1908140. DOI: 10.1002/adma.201908140.

(19) Wirnhier, E.; Mesch, M. B.; Senker, J.; Schnick, W. Formation and Characterization of Melam, Melam Hydrate, and a Melam-Melem Adduct. *Chem. Eur. J.* **2013**, *19* (6), 2041–2049. DOI: 10.1002/chem.201203340.

(20) Jürgens, B.; Irran, E.; Senker, J.; Kroll, P.; Müller, H.; Schnick, W. Melem (2,5,8-Triamino-tri- s -triazine), an Important Intermediate during Condensation of Melamine Rings to Graphitic Carbon Nitride: Synthesis, Structure Determination by X-ray Powder Diffractometry, Solid-State NMR, and Theoretical Studies. *J. Am. Chem. Soc.* **2003**, *125* (34), 10288–10300. DOI: 10.1021/ja0357689.

(21) Seyfarth, L.; Seyfarth, J.; Lotsch, B. V.; Schnick, W.; Senker, J. Tackling the stacking disorder of melon--structure elucidation in a semicrystalline material. *Phys. Chem. Chem. Phys.* **2010**, *12* (9), 2227–2237. DOI: 10.1039/b919918g.

(22) Mesch, M. B.; Bärwinkel, K.; Krysiak, Y.; Martineau, C.; Taulelle, F.; Neder, R. B.; Kolb, U.; Senker, J. Solving the Hydrogen and Lithium Substructure of Poly(triazine imide)/LiCl Using NMR Crystallography. *Chem. Eur. J.* **2016**, *22* (47), 16878–16890. DOI: 10.1002/chem.201603726.

(23) Lau, V. W.-h.; Mesch, M. B.; Duppel, V.; Blum, V.; Senker, J.; Lotsch, B. V. Low-Molecular-Weight Carbon Nitrides for Solar Hydrogen Evolution. *J. Am. Chem. Soc.* **2015**, *137* (3), 1064–1072. DOI: 10.1021/ja511802c.

(24) Savateev, A.; Dontsova, D.; Kurpil, B.; Antonietti, M. Highly crystalline poly(heptazine imides) by mechanochemical synthesis for photooxidation of various organic substrates using an intriguing electron acceptor – Elemental sulfur. *J. Catal.* **2017**, *350*, 203–211. DOI: 10.1016/j.jcat.2017.02.029.

(25) Sattler, A.; Schnick, W. On the Formation and Decomposition of the Melonate Ion in Cyanate and Thiocyanate Melts and the Crystal Structure of Potassium Melonate, $K_3[C_6N_7(NCN)_3]$. *Eur. J. Inorg. Chem.* **2009** (33), 4972–4981. DOI: 10.1002/ejic.200900585.

(26) Horvath-Bordon, E.; Kroke, E.; Svoboda, I.; Fuess, H.; Riedel, R. Potassium melonate, $K_3[C_6N_7(NCN)_3]\cdot 5H_2O$, and its potential use for the synthesis of graphite-like C_3N_4 materials. *New J. Chem.* **2005**, *29* (5), 693. DOI: 10.1039/b416390g.

(27) Markushyna, Y.; Lamagni, P.; Teutloff, C.; Catalano, J.; Lock, N.; Zhang, G.; Antonietti, M.; Savateev, A. Green radicals of potassium poly(heptazine imide) using light and benzylamine. *J. Mater. Chem. A* **2019**, *7* (43), 24771–24775. DOI: 10.1039/C9TA09500D.

(28) Hesse, M.; Meier, H.; Zeeh, B.; Bienz, S.; Bigler, L.; Fox, T. *Spektroskopische Methoden in der organischen Chemie*, 9., überarbeitete und erweiterte Auflage; Georg Thieme Verlag, 2016. DOI: 10.1055/b-004-129729.

(29) Savateev, A.; Tarakina, N. V.; Strauss, V.; Hussain, T.; Brummelhuis, K. ten; Sánchez Vadillo, J. M.; Markushyna, Y.; Mazzanti, S.; Tyutyunnik, A. P.; Walczak, R.; Oschatz, M.; Guldi, D. M.; Karton, A.; Antonietti, M. Potassium Poly(Heptazine Imide): Transition Metal-Free Solid-State Triplet Sensitizer in Cascade Energy Transfer and [3+2]-cycloadditions. *Angew. Chem. Int. Ed.* **2020**, *59* (35), 15061–15068. DOI: 10.1002/anie.202004747.

(30) Lau, V. W.-h.; Yu, V. W.-z.; Ehrat, F.; Botari, T.; Moudrakovski, I.; Simon, T.; Duppel, V.; Medina, E.; Stolarczyk, J.; Feldmann, J.; Blum, V.; Lotsch, B. V. Urea-Modified Carbon Nitrides: Enhancing Photocatalytic Hydrogen Evolution by Rational Defect Engineering. *Adv. Energy Mater.* **2017**, 1602251. DOI: 10.1002/aenm.201602251.

(31) Kröger, J.; Jiménez-Solano, A.; Savasci, G.; Lau, V. W. h.; Duppel, V.; Moudrakovski, I.; Küster, K.; Scholz, T.; Gouder, A.; Schreiber, M.-L.; Podjaski, F.; Ochsenfeld, C.; Lotsch, B. V. Morphology Control in 2D Carbon Nitrides: Impact of Particle Size on Optoelectronic Properties and Photocatalysis. *Adv. Funct. Mater.* **2021**, *31*, 2102468. DOI: 10.1002/adfm.202102468.

(32) Fang, J.; Debnath, T.; Bhattacharyya, S.; Döblinger, M.; Feldmann, J.; Stolarczyk, J. K. Photobase effect for just-in-time delivery in photocatalytic hydrogen generation. *Nat. Commun.* **2020**, *11* (1), 5179. DOI: 10.1038/s41467-020-18583-6.

(33) Dvoranová, D.; Mazúr, M.; Papailias, I.; Giannakopoulou, T.; Trapalis, C.; Brezová, V. EPR Investigations of g-C_3N_4/TiO_2 Nanocomposites. *Catalysts* **2018**, *8* (2), 47. DOI: 10.3390/catal8020047.

(34) Lau, V. W.-h.; Klose, D.; Kasap, H.; Podjaski, F.; Pignié, M.-C.; Reisner, E.; Jeschke, G.; Lotsch, B. V. Dark Photocatalysis: Storage of Solar Energy in Carbon Nitride for Time-Delayed Hydrogen Generation. *Angew. Chem. Int. Ed.* **2017**, *56* (2), 510–514. DOI: 10.1002/anie.201608553.

(35) Yang, W.; Godin, R.; Kasap, H.; Moss, B.; Dong, Y.; Hillman, S. A. J.; Steier, L.; Reisner, E.; Durrant, J. R. Electron Accumulation Induces Efficiency Bottleneck for Hydrogen Production in Carbon Nitride Photocatalysts. *J. Am. Chem. Soc.* **2019**, *141* (28), 11219–11229. DOI: 10.1021/jacs.9b04556.

(36) Savateev, A.; Kurpil, B.; Mishchenko, A.; Zhang, G.; Antonietti, M. A "waiting" carbon nitride radical anion:A charge storage material and key intermediate in direct C-H thiolation of methylarenes using elemental sulfur as the "S"-source. *Chem. Sci.* **2018**, *9* (14), 3584–3591. DOI: 10.1039/c8sc00745d.

(37) Podjaski, F.; Kröger, J.; Lotsch, B. V. Toward an Aqueous Solar Battery:Direct Electrochemical Storage of Solar Energy in Carbon Nitrides. *Adv. Mater.* **2018**, *30* (9), 1705477. DOI: 10.1002/adma.201705477.

(38) Zeng, Z.; Quan, X.; Yu, H.; Chen, S.; Zhang, Y.; Zhao, H.; Zhang, S. Carbon nitride with electron storage property:Enhanced exciton dissociation for high-efficient photocatalysis. *Appl. Catal. B* **2018**, *236*, 99–106. DOI: 10.1016/j.apcatb.2018.05.003.

(39) Ou, H.; Tang, C.; Chen, X.; Zhou, M.; Wang, X. Solvated Electrons for Photochemistry Syntheses Using Conjugated Carbon Nitride Polymers. *ACS Catal.* **2019**, *9* (4), 2949–2955. DOI: 10.1021/acscatal.9b00314.

4 Ni-CN_x – An ionic carbon nitride storing and converting CO_2 by photothermal catalysis

4.1 Introduction

Thus far, in terms of applications, this thesis has dealt with photocatalytic water splitting, which will surely be an important corner stone for a future sustainable society, albeit, the capture and reduction of CO_2 – a major contributor to greenhouse gases – will be an equally important factor. Not only will the reduction of CO_2 help to prevent global warming, but it will also be the first step in the creation of higher hydrocarbons with the help of syngas (CO and H_2). This has two major advantages: Firstly, it would enable the utilization of H_2 generated at times of high energy availability (intermittency of renewable sources) and thereby add to a better storable energy carrier (e.g. methanol, methane, ammonia).[1] Secondly, CO_2 could directly be used as a cheap carbon feedstock, hence reducing the harmful greenhouse gas emissions.[2] Furthermore, this approach would allow for a better connection between chemical industry and energy sector, which is one of the key challenges of future production flows.[3]

The highly stable carbon dioxide molecule requires a catalyst for the activation of the strong double bond. The element nickel has proven its potential to reduce carbon dioxide in numerous experimental and theoretical studies.[4–9] Unlike reduction catalysts like palladium,[10] platinum,[11] rhodium[12] and ruthenium,[13] nickel is more abundant and thus far more cost-efficient.[14] It has been shown that Ni- or NiO- agglomerates favor the full reduction to methane.[15,16] On the other hand single-site catalysts show better selectivity towards CO, which is mechanistically associated with a faster desorption of the intermediate.[17]

In this study, we employed a photothermal setup for the catalytic tests, which promotes easier dissociation of the product from the catalyst at the working temperatures above 150 °C. Typically, the hydrogenation of CO_2 is conducted at much higher temperatures of 300-500 °C.[13,14] Lowering this temperature would allow for a more environmentally benign process.[18] In the photothermal approach, the additional light irradiation is locally heating the catalytic centers through vibronic relaxation, thus supplying energy directly, where the reaction occurs.[19,20] Herein, following an ionothermal approach, a carbon nitride with incorporated nickel centers, henceforth referred to as Ni-CN_x, has been synthesized and characterized by X-ray and electron diffraction alongside pair distribution function analysis, electron microscopy, IR-, UV-Vis-, photoelectron- and ssNMR-spectroscopy. We followed the rationale that the atomically dispersed nickel sites could prove suitable for an efficient CO_2 reduction to CO. At the same time the inherent Lewis basic functionalities (e.g. -NH_2) in carbon nitrides could facilitate an effective extraction of CO_2 from the gas phase, thus killing two birds with one stone.

In the following paragraph, we briefly comment on some peculiarities encountered in this part opposed to chapters 2 and 3, in which heptazine-based polymers were examined. Ni-CN_x, however, could also be constituted of triazine units. Regarding the synthetic conditions, this is not totally unexpected, because the ratio of the salt melt medium to the amount of CN-precursor is much higher as compared to the heptazine based variants. Similar observations have been made in ampoule syntheses of poly(triazine imide), PTI · LiCl (see chapter 1.2).[21,22] The amount of salt melt and the resulting dilution of precursor seems to favor the formation of the triazine based 2D polymer. What remains highly challenging is, however, the unambiguous structural characterization, because of several issues related to the presence of nickel cations. On the one hand the paramagnetism of the nickel cation (Ni^{2+}) for many coordination environments (except for quadratic planar coordination) interferes with techniques that rely on a homogeneous magnetic field such as NMR spectroscopy. Due to the paramagnetic centers, the chemical shifts for the nuclei of interest (^{13}C,^{15}N, ^{1}H) will be shifted and broadened to a great extent so that a clear assignment is ultimately not possible. The other factor that can influence these measurements are traces of metallic nickel, which would likewise adversely affect the spectrum, due to its ferromagnetic properties. As has been extensively shown in the previous two chapters, the structural assessment of carbon nitrides – in the absence of suitable single-crystals – remains difficult to say the least and may be further complicated, forfeiting the powerful ssNMR spectroscopy.

4.2 Results

Preparation

Ni-CN_x was prepared similarly to the protocol of the PTI · LiCl synthesis. Dicyandiamide (190 mg, 2.25 mmol) and an eutectic melt of $NiCl_2$ (394 mg, 3.05 mmol) and KCl (605 mg, 8.11 mmol) was ground and transferred into a Duran glass ampoule, which was purged three times with argon. The powder was further dried in vacuo and subsequently flame sealed and subjected to the following temperature program in a tube furnace (6 °C/min, 500 °C, 6 h, 1 °C/min, rt). The eutectic of $NiCl_2$/KCl melts at 502 °C so that at the synthesis temperature at least a partial melting should be expected. The ratio of CN-precursor to salt melt is similar to the protocol of PTI · LiCl. The obtained solid was washed five times with DI water and then dried at 60 °C overnight.

X-ray and electron diffraction

In contrast to other polymeric type carbon nitrides, Ni-CN_x exhibits an exceptionally high crystallinity, expressed by sharp Bragg reflections in the XRPD pattern paired with very high intensities (Figure 4.1a) through the incorporation of Ni. The synthetic conditions in terms of temperature program, ampoule geometry, starting pressure as well as the amount of CN-precursor, are very much the same compared to the synthesis of crystalline version of K-PHI (cf. chapter 2). Apart from using a different salt mixture, the key difference between this synthesis and those discussed in previous chapters lies in the amount of the salt melt. Opposed to the ratio of salt to CN-precusor (ca. 1:2 by weight) for the PHI-based compounds presented in chapters 2 and 3, the herein applied ratio (ca. 5:1 by weight) of salt to dicyandiamide has been significantly higher.

The degree of crystallinity is atypical for polymeric carbon nitrides except for the examples introduced in chapters 2 and 3, and PTI · LiCl,[21] which has been introduced in chapter 1. Most

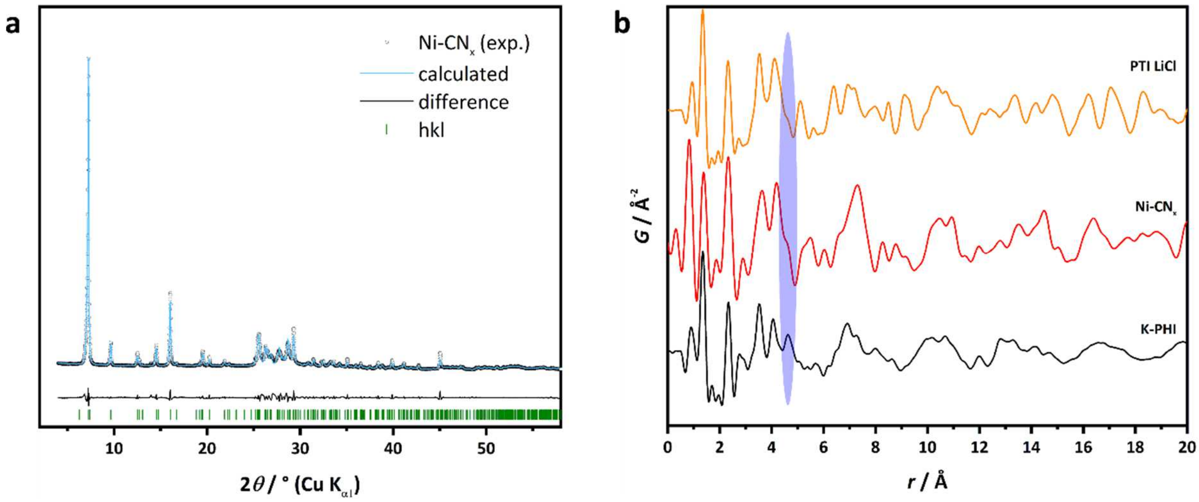

Figure 4.1. (a) Experimental X-ray powder diffraction pattern (black dots) and corresponding Pawley fit (blue) of Ni-CN_x using Cu $K_{\alpha1}$ radiation. The green tick marks correspond to the Miller indices of the resulting space group $P2_1/c$. (b) Pair distribution functions (PDFs) of PTI · LiCl (orange), Ni-CN_x (red) and K-PHI (black). PTI · LiCl and K-PHI serve as model compounds for either triazine- or heptazine-based carbon nitrides. The blue area marks the key deviation between triazine- and heptazine-based structures. Note that the peak at approx. 0.8 Å is an artefact and corresponds to no actual interatomic distance.

other examples of highly crystalline carbon nitride materials comprise molecular compounds composed of monomers of melem, melamine and melam and their derivatives or respective salts.[23–25] In general, the synthesis temperatures giving access to those molecular species are usually lower than the herein applied 500 °C. Although the applied procedure suggests a polymeric type carbon nitride, we cannot exclude the formation of a stable monomeric phase. Of course the influence of the coordinating cation – in this case nickel – must not be neglected, as cations have proven to be a key factor for the structural arrangement of the carbon nitride (cf. chapters 2 and 3).[26] However, it may well be that nickel employed in the synthesis as a divalent transition metal acts differently compared to alkali ions. Furthermore, nickel is a stronger scatterer than i.e. potassium, which may explain the very pronounced reflections observed for Ni-CN_x.

A Pawley[27] refinement (Figure 4.1a) resulted in an eligible unit cell within the monoclinic space group $P2_1/c$ and a = 23.27 Å, b = 23.97 Å, c = 3.64 Å, $\alpha = \gamma$ = 90° and β =37.38°, R_{wp} = 6.6%. The overlap of the calculated intensities matches the experimental pattern reasonably well. Even in the range (25-30° 2θ), where usually the stacking reflection is allocated, the match is acceptable. Imagining that here the stacking behavior of the CN-backbone may vary over each crystallite by a bit, it is not unusual to expect some deviations in this region. In 2D or quasi-2D arrangements of carbon nitrides, the weaker van-der-Waals- and π–π-interactions – as opposed to intraplanar covalent or hydrogen bonded constellation – create a certain softness of the structural arrangement in the c-direction. The unit cell is strongly tilted, due to the acute β-angle. However, this may just point towards a sheet-like arrangement of the atoms within the unit cell that are stacked with an offset with respect to the underlying layer.

Figure 4.1b displays the pair distribution function (PDF) of Ni-CN_x in comparison to data of a triazine-based (PTI · LiCl) and a heptazine-based (K-PHI) carbon nitride, respectively. For low distances r < 4 Å, the functions have similar shape, which is expected due to the close similarity of

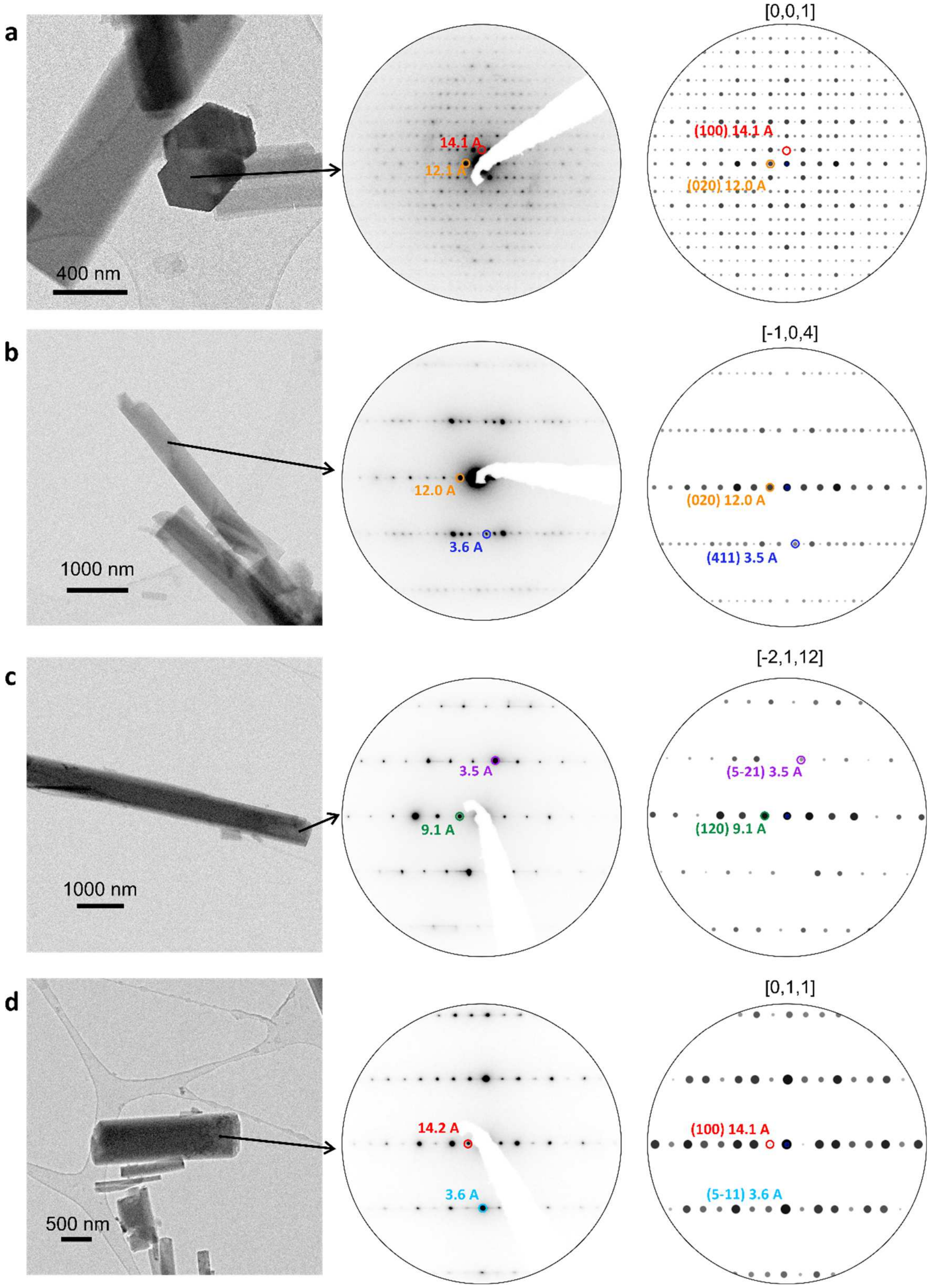

Figure 4.2. (a-d) TEM micrographs (left), electron diffraction images (middle) and simulations of electron diffraction patterns (right) of corresponding zone axes. Note that the intensities of simulations are not representing correct electron densities (cf. main text). The arrows indicate the approximate location of the diffraction aperture. Colored circles mark indexed reflections in each zone axis.

the CN-building blocks and fairly rigid C-N bonding distances. (The peak at 0.8 Å is an artefact and belongs to no meaningful atomic distance.) A major difference is highlighted in the blue marked region, though. While the PDF of K-PHI exhibits a "triplet", Ni-CN$_x$ and PTI · LiCl only have two pronounced maxima, thus Ni-CN$_x$ is likely to be also triazine-based. Furthermore, in K-PHI a long-range periodicity of ca. 3.2 Å over at least several tens of Angstroms can be observed. In the real structure, this effect can be related to the periodic AA-stacking of PHI sheets as has been discussed in chapter 2. However, both Ni-CN$_x$ and PTI · LiCl lack this periodicity, indicative of a more complicated arrangement of the structural motifs. In the case of PTI · LiCl, it is known that the

poly(triazine imide) sheets follow an AB-type stacking, causing this variance in the PDF.[28] Note that this does not necessarily imply a similar structural arrangement for Ni-CN$_x$. For instance, also a monomeric form could have larger variations in interatomic distances and therefore causing more overlap of signals in the region above $r > 6$ Å.

The derived unit cell from the Pawley refinement could be corroborated by electron diffraction. The needle-shaped crystallites are mostly oriented horizontally, causing the probed zone axes observed in the electron diffraction to lie dominantly perpendicular to the growing direction. In very few cases the crystallites were so small that a top irradiation by the electron beam was possible, as depicted in Figure 4.2a, thus presumably yielding the [001] zone axis. In the same figure the electron diffraction image was compared to a simulated pattern, based on a model unit cell using the parameters of the Pawley refinement from above. It must be noted that this model cell contains dummy atoms that generate some electron density to permit the simulation, but that this arrangement is by no means related to real electron density map for Ni-CN$_x$. Therefore, the metric and extinctions of the diffraction spots can be compared, but not their intensities. In the electron diffraction of the [001] zone axis an extinction along the $(0k0)$ can be observed, owed to the 2_1 screw axis along b. The 90° angle between the diffraction spots is clearly visible, corresponding to γ of the monoclinic lattice. The other pictures (b–d) show zone axes pointing outwards from the oblong side of the crystallites. They could be matched with simulated patterns, but here it is even more difficult to deduce which facet is looked upon, because a slight rotation of the crystallite as well as deviations from the horizontal plane can change the zone axis. The overall decent match between electron diffraction and the obtained unit cell based on X-ray diffraction indicates that the structural classification is plausible, although a crystal structure solution is yet to be accomplished.

The TEM measurement also revealed a minority phase with similar elemental composition (EDX), but alternate lattice distances (Figure C 2). These crystallites differentiate from the bulk of needles by a more compact, diamond-shape. The crystallites are more stable in the electron beam and their edges are more defined as can be seen in high-resolution TEM images (Figure C 2e), suggesting that these crystallites indeed stem from a different minority phase. In contrast, decent high-resolution images of the needle-shaped crystals could not be obtained, suggesting that the beam stability of the majority phase is relatively low, as can be recognized from the apparent beam damage in brightfield images (Figure C 3) before and after attempting diffraction/high-resolution imaging of Ni-CN$_x$.

The morphology of Ni-CN$_x$ is largely dominated by needle-shaped crystals as observed by SEM and TEM imaging (Figure 4.2 and Figure 4.3). The high aspect ratio and overall small size (several hundred nanometers × several micrometers) of the crystals increase the difficulty for single-crystal analysis. The remarkable uniformity of the crystals could point towards a molecular arrangement similar to that observed in metal organic frameworks (MOFs), in which the molecular organic building blocks are linked by metal clusters and usually yield clean-cut crystal shapes. In the studied case this could encompass a negatively charged CN-unit bridged by nickel cations, additionally coordinated by chloride ligands. Often, carbon nitride structures occur in planar structural arrangements (both polymeric and molecular).[29,30] This typical tendency likely infers from the different types of interactions that are either governed by stronger covalent or hydrogen-bonds within the plane and are set apart from weaker π-stacking- or van-der-Waals interactions perpendicular to the plane.[26,31] However, these sheet-like arrangements do not necessarily imply that the habitus of the crystals always finds expression in platelets, as show the examples of PTI · LiCl,[21] potassium melonate,[32] or diamincopper cyamelurate ($[Cu(NH_3)_2]_3(C_6N_7O_3)_2 \cdot 2H_2O$),[33] which contain quasi planar arrangements of the CN-species and yet form needle-shaped crystals. Hence, for Ni-CN$_x$ the electron microscopy data neither allows for a decision whether a planar arrangement of structural motifs is present nor whether these take on a polymeric or monomeric form.

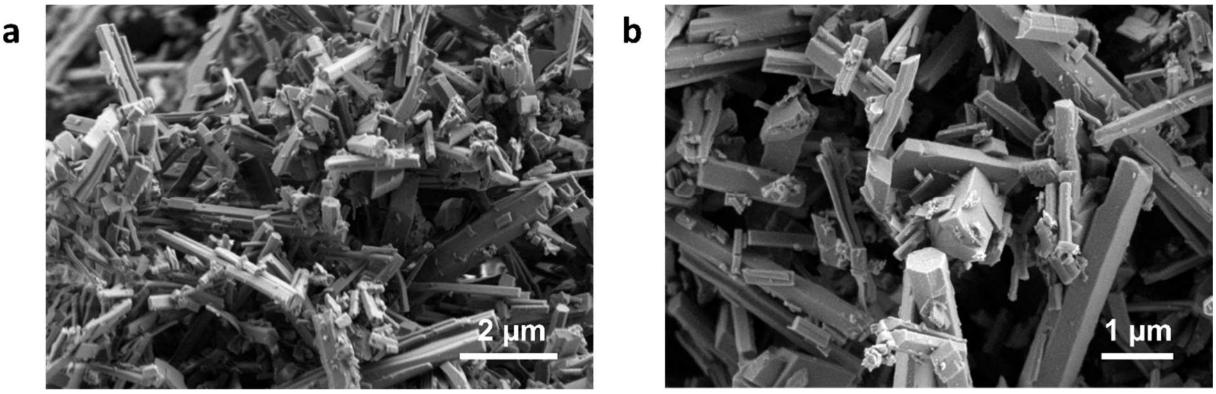

Figure 4.3. (a-b) SEM images of Ni-CN$_x$ showing the needle-shaped crystallites with sizes of several microns in length and a few hundred nanometers in width. The needles appear to have hexagonal facets. Assuming a non-hexagonal crystal structure, these could occur either due to intergrowth of crystallites (twinning) or even only appear to be hexagonal but in truth are monoclinic and the facets e.g. of needles only appears to be (pseudo)hexagonal at the ends, as for instance in the case of the mineral epidote.

Solid-state NMR spectroscopy

As mentioned in the beginning, ssNMR spectroscopy has the major disadvantage of being influenced by the nickel species within the sample. Although the quality of the spectra is certainly not adequate for assigning signals, it may be argued that at least the maxima of the extremely broadened signal (Figure 4.4a) is in the range, which one would expect for carbon nitride materials. The ^{13}C-peak maxima at 180, 156 and 125 ppm may be shifted significantly, but the measurement could indicate that there are at least three distinct carbon atoms within the structure of Ni-CN$_x$.

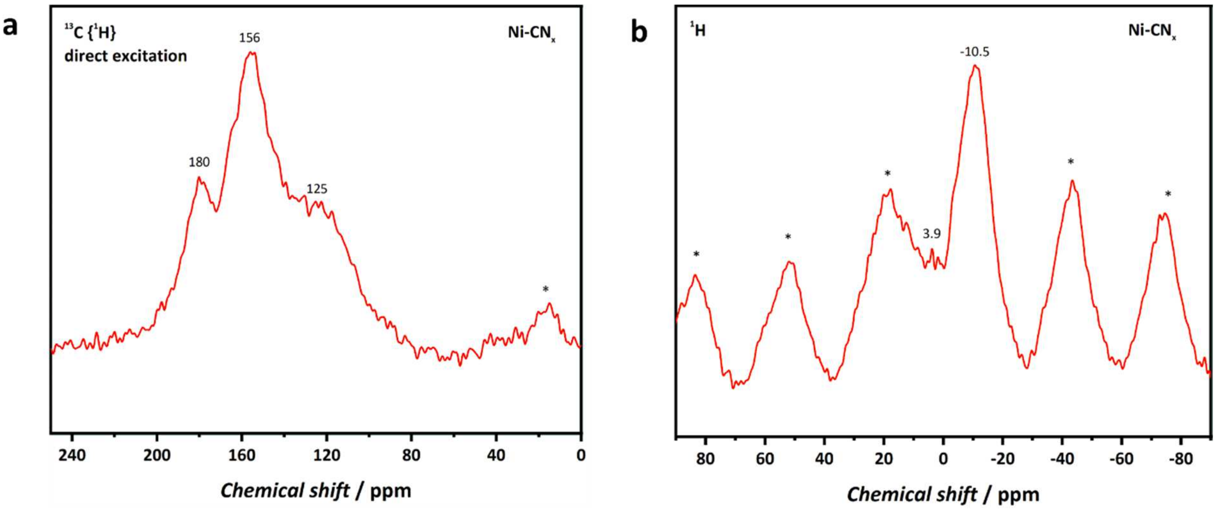

Figure 4.4. (a) ^{13}C ssNMR direct excitation NMR spectrum of Ni-CN$_x$ and (b) corresponding proton spectrum. The asterisks mark spinning side bands. Note that the signals are drastically broadened due to the inherent presence of paramagnetic nickel cations in the sample.

The proton ssNMR spectrum (Figure 4.4b) is equally ambiguous and it can just be concluded that protons are present within the structure. The naturally already narrow range for proton shifts (-10–20 ppm) does not allow for more precise classification of the signals. From the synthetic conditions and the stability in air, it is highly improbable that the major signal at -10 ppm could correspond to a hydridic species, which can be typically encountered at this high field.[34]

Vibrational spectroscopy and acidic treatment

The Fourier-transformed infrared spectrum (FT-IR), depicted in Figure 4.5, can offer insights into the constituting functional moieties of Ni-CN$_x$, which is especially relevant since no conclusive NMR data could be collected. For a carbon nitride compound, it is remarkable that the absorption bands are exceptionally well resolved, which may be attributed to the high crystallinity. Usually, such distinct peaks are only observed for molecular carbon nitride compounds so that here again the mere quality of the spectrum hints in this direction. The highlighted blue region contains NH_2-/NH- bending vibrations and shows that presumably the CN-species are terminated by amino groups or are bound via imide bridges as in i.e. melam or in condensation products such as oligomers. Additionally, OH-termination, hydroxyl and adsorbed water, respectively, could give

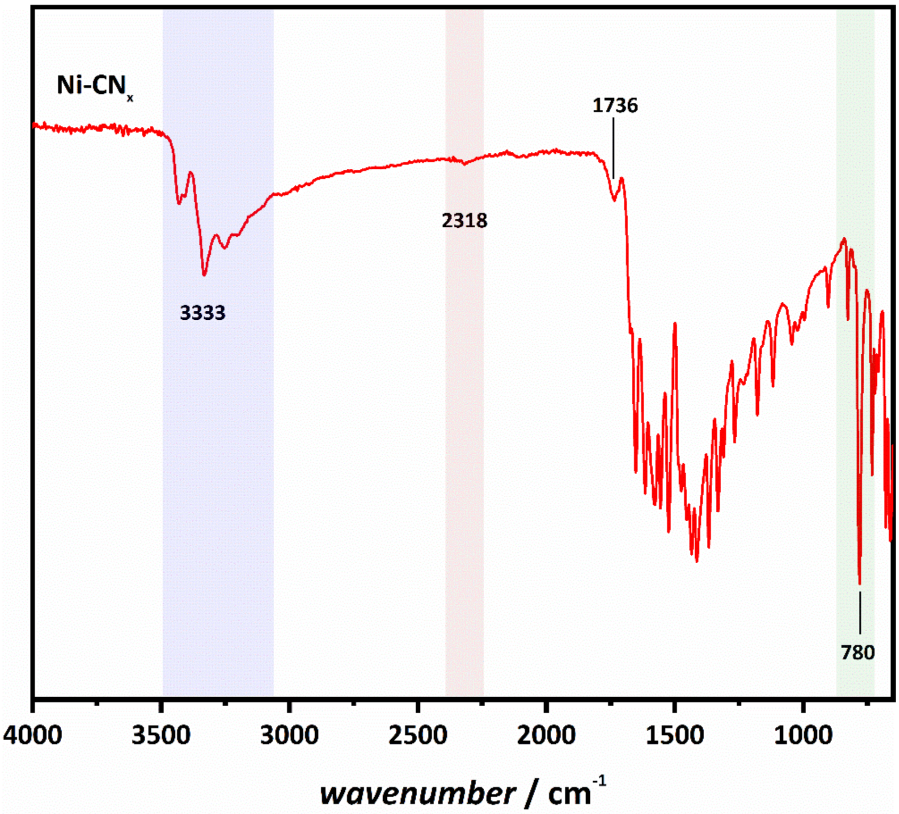

Figure 4.5. FT-IR spectrum of Ni-CN$_x$. The blue area marks vibration related to NH/NH$_2$ moieties while the green area marks the typical ring-sextant out-of-plane bending vibration observed for many heptazine-/triazine- derivatives.[35–37] In the red area a small peak is visible, which could stem from adsorbed CO$_2$.

rise to vibrational bands at even higher wavenumbers (>3400 cm^{-1}) in this region, although thermogravimetry suggest rather low amounts of water species (cf. Figure 4.7a). Potentially, also small amounts of nickel hydroxide species might be present, if a reaction of trace water with the salt melt occurred during the synthesis and could not subsequently be washed out. However, these nickel oxide/hydroxide minority species would most likely be covered beneath peaks of the carbon nitride. At 1736 cm^{-1} a weak vibration can be identified, which in principle could stem from an oxygen containing group such as a carbonyl group. Such a functional group is present in metal cyamelurates, whose absorption is typically slightly red-shifted from 1600–1700 cm^{-1}, though.[38,39] A more blue-shifted vibration (>1700 cm^{-1}) can be found in ammeline or ammelinium salts, thus suggesting the presence of a protonated triazine core, partially terminated by oxygen.[23,40] A likewise shifted C=O-vibration may also be found for instance in graphene oxide.[41] This could be an indication that similar functional groups may be present in the carbon nitride material, which may be rationalized by the chemical similarity of CN- and pure carbon compounds, respectively. However, the overall low intensity and relatively broad peak shape with respect to the remainder of bands rather hints at an impurity or as discussed a termination effect.

The ring-sextant out-of-plane bending vibration at 780 cm^{-1}, which is characteristic of both heptazine- and triazine-based CN materials, is red-shifted by 15-30 cm^{-1} compared to many molecular CN-compounds such as metal cyamelurates (796–810 cm^{-1}),[38,39] metal melonates (794–802 cm^{-1}),[32,36] melamine (810 cm^{-1}),[42] melam (810 cm^{-1}),[43] melem (798 cm^{-1})[43] as well as polymeric forms such as melon (810 cm^{-1}),[29] K/H-PHI (~800 cm^{-1})[26] and PTI · LiCl (810 cm^{-1}),[21]

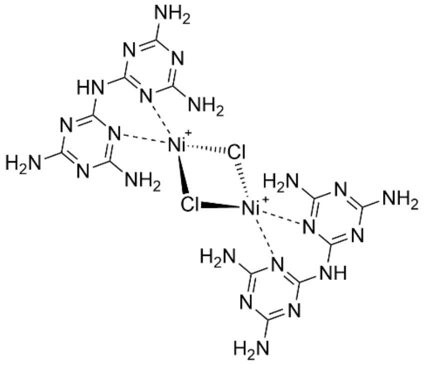

Scheme 4.1. Potential coordination environment of a nickel cation with melam as bidentate ligand. Nickel is sharing two chlorid ligands, thus formally exhibiting the oxidation state +1.

respectively. A shifted band towards lower frequencies is typical for protonated triazine units like in cyanuric acid (771 cm^{-1}),[23] ammelinium salts (764–774 cm^{-1})[23,40] and also protonated heptazine cores like in cyamelurate (784 cm^{-1}),[44] or protonated calcium melonate (790 cm^{-1}).[45] However, this revelation seems to be a bit counterintuitive, if nickel were to be in oxidation state +2, thus requiring a negative balancing charge at the CN-molecule. Since the elemental ratio of Ni:Cl is approx. 1:1 as obtained from EDX analysis, ICP/AES and potentiometric titration, respectively, one would indeed assume a negatively charged CN-network or molecule. The other conclusion may be that nickel ions were in oxidation state +1 and therefore solely balanced by the chloride anion. In the configuration depicted in Scheme 4.1, the carbon nitride would act as a neutral bidentate ligand instead of a ionic bonding partner, as similarily observed in a $ZnCl_2$-melam complex studied by *Lotsch et al.*[46]

Cyanamide vibrations, usually located at 2100–2200 cm^{-1}, do not appear in the Ni-CN$_x$ spectrum. Besides the cyamelurate- or cyanurate-building blocks, cyanamide moieties could have been a potential candidate for providing a negative charge at the carbon nitride. In a stability test, during which Ni-CN$_x$ was treated in concentrated HCl, the subsequently obtained FTIR spectrum (Figure C 5b) revealed a moderate band at 2116 cm^{-1}, indicative of a cyanamide (or nitrile) functionality. It is known that the protonation state (i.e. in the transformation of K-PHI → H-PHI → K-PHI) can reversibly affect the intensity of this IR-band.[26] Possibly, this vibrational mode is suppressed in pristine Ni-CN$_x$. The EDX spectrum after acid treatment still shows a ratio of Ni:Cl close to unity, but it may be that the former NCN$^-$ bound [NiCl]$^+$ has been washed out yielding just the neutrally coordinated Ni-compound and a NCNH moiety.

The filtrate of the acid treated sample (using conc. DCl in D_2O) has been analyzed by liquid NMR spectroscopy to track any soluble degradation product. However, the spectrum yielded no detectable species, which infers that either no soluble product has formed or the soluble product's concentration stays beneath the detection threshold (see Figure C 6). In order to detect also tiny amounts of dissolved species, mass spectrometry of an acid treated Ni-CN$_x$ sample was performed. Due to technical limitations these tests have been carried out with formic acid instead of hydrochloric acid. However, the spectra in Figure C 7 reveal no detectable species, except for the background signal of formic acid. Remarkably, this suggests that the network is fairly insensitive to hydrolysis. In contrast to that, the mass spectrum of polymeric K-PHI under the same conditions shows a signal at m/z=219, corresponding to a protonated melem unit, which proves the method's potential of tracking dissolved (rather large) CN-molecules in the liquid phase. It remains unclear, whether K-PHI hydrolyses under these conditions or melem impurities were still present in K-PHI and were just accessed by suspending it in acid. It has been shown that the transformation of K-PHI to H-PHI is accompanied by a structural rearrangement,[26] which could lead to a shifting of the layers and release previously unaccessible melem.

The degradation of crystallinity after hydrochloric acid treatment is apparent from the loss of Bragg reflections and strong broadening of the only two remaining reflections at 7° and 25° 2θ (Figure C 5a). The latter could be attributed to the stacking periodicity within the sample. The broadening could indicate that this stacking is strongly affected by the acid treatment. The SEM micrograph (Figure 4.6a) shows that a certain structural rearrangement is observed because the morphology is changed from needle-shaped crystallites to more clotted structures.

CO_2 sorption

The final interesting observation with regard to a CO_2 hydrogenation catalyst is the small peak at ca. 2318 cm^{-1}, which may be attributed to adsorbed CO_2.[47] It remains unclear whether the gas is physi- or chemisorbed, nevertheless, it is a hint that the material can interact with carbon dioxide, which is a beneficial factor for the conversion of CO_2. Due to the low intensity, we performed a CO_2-sorption experiment to further proof the ability to adsorb CO_2.

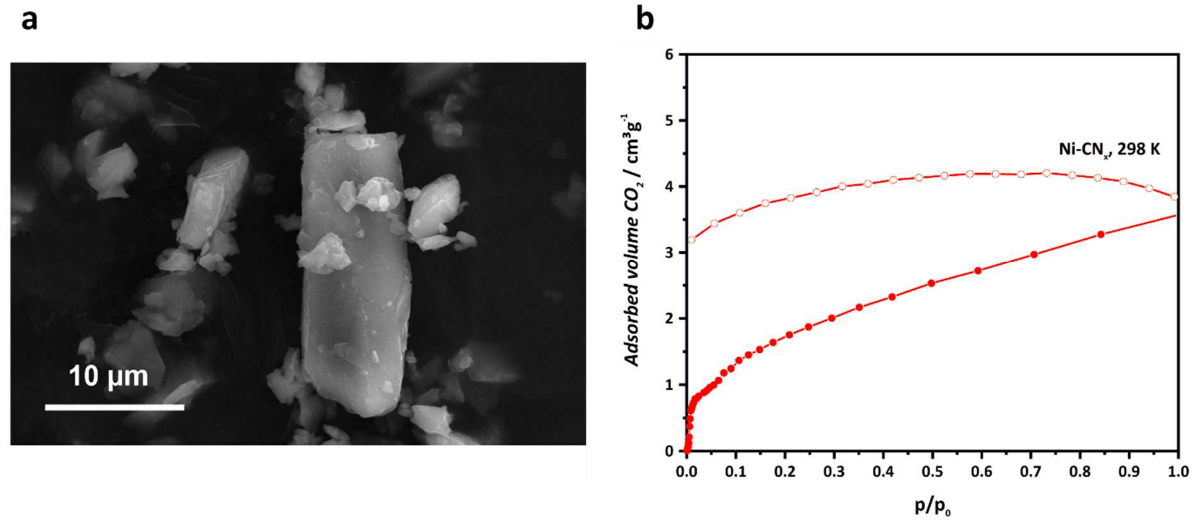

Figure 4.6. (a) SEM micrograph of hydrochloric acid treated Ni-CN$_x$. The morphology resembles stacked sheets in contrast to the needle-shaped crystallites of the pristine material. (b) Carbon dioxide adsorption (filled circles) and desorption (empty circles) isotherms of Ni-CN$_x$ measured at 298 K.

The CO_2-isotherm (Figure 4.6b) at 298 K yielded a moderate uptake of CO_2 of 3.9 cm^3/g (0.16 mmol/g), but in relation to the very low BET surface area of only ca. 20 m^2/g, the amount of adsorbed CO_2 is comparably high. A material which is known for its good CO_2 sorption capacity is e.g. the microporous network bipyridine-CTF (Covalent Triazine Framework) with uptakes of 45 cm^3/g (1.8 mmol/g) with a respective BET surface area of approx. 750 m^2/g.[48] Ni-CN$_x$ is non-porous and therefore the overall uptake is expectedly low. Normalized to the accessible surface area, the capacity would theoretically be roughly three times better for the carbon nitride, though. The terminating amine groups and N-heterocycles are known to facilitate the absorption process for CO_2.[49,50] In principle, the Lewis basic oxygen of CO_2 could also be coordinated to the nickel cations. Additionally, the isotherm in Figure 4.6b shows a hysteresis, which indicates that a certain amount of CO_2 remains absorbed on Ni-CN$_x$ or at least is not desorbed, when evacuated without further heating.

Elemental analysis

Table 4.1. Elemental composition of Ni-CN_x as obtained from combustion analysis and ICP/AES.

Ni-CN_x	C	N	H	Ni	Cl	Sum	N/C
wt%	19.0	38.0	1.6	28.3	14.1	101	1.71
mol%	23.3	40.0	23.3	6.7	6.7	100	-
Possible chemical formula			$C_7N_{12}H_7Ni_2Cl_2$				

Within the measurement errors and bearing in mind that three complementary analyses had to be utilized (C,N,H by combustion analysis, Cl by titration and Ni by ICP/AES), the sum of all relative weight percentages adding up to 101% is acceptable. Since the sum of all values is near unity, it can be assumed that no additional components in significant amounts are present. There might be only small amounts of water present, which is indicated by a small mass loss (<2 wt%) in the TG curve at moderate temperatures (<150 °C), at which one would not expect decomposition or condensation of CN-precursors. In turn this means that not much water is expected to be structurally bound or adsorbed within the sample and therefore the presented elemental composition is providing a liable representation of the constituting elements.

Thermal analysis and mass spectrometry

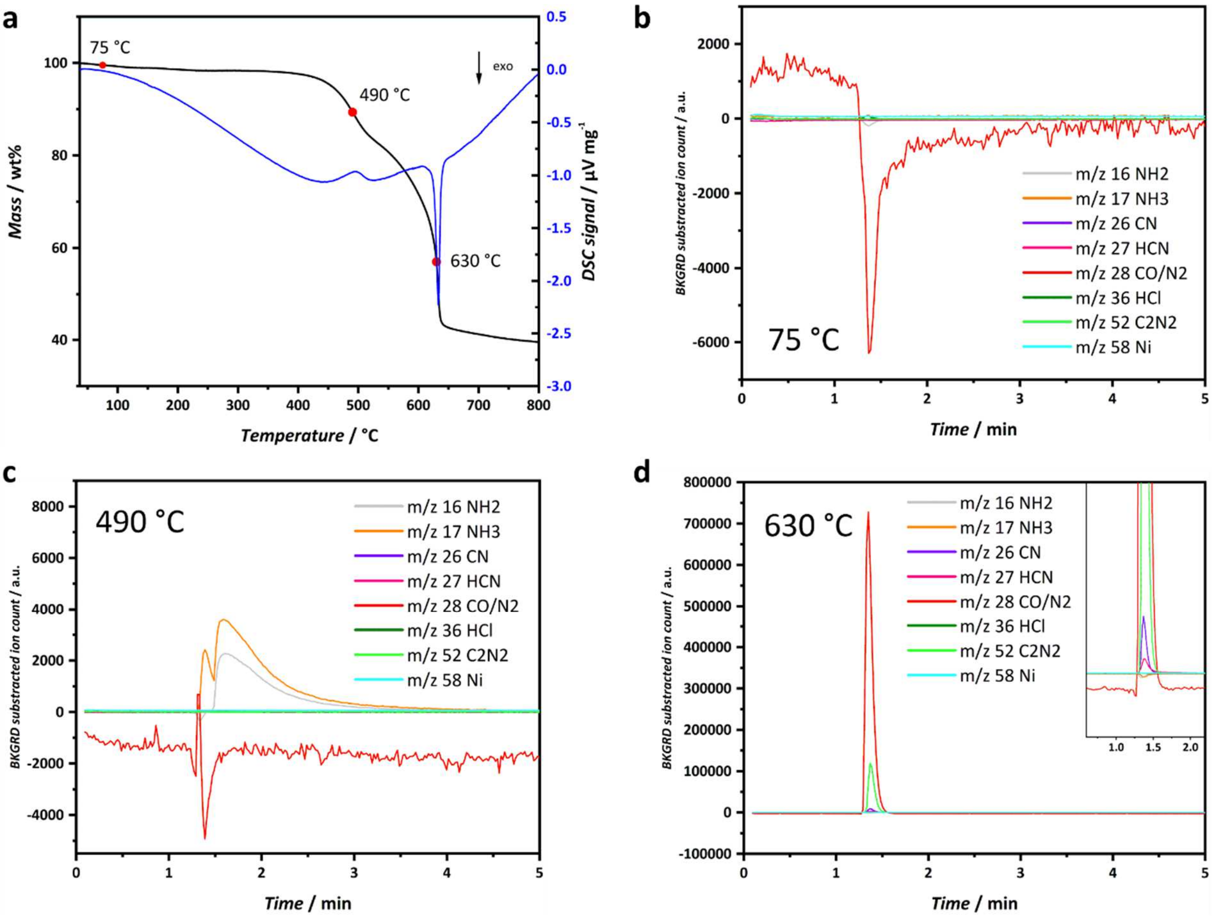

Figure 4.7. (a) TG and DSC curves for Ni-CN$_x$. The sample was heated in a corundum crucible from r.t. to 800 °C at a rate of 5 K/min under helium flow. The red dots mark the points in time, upon which a volume of the gas phase was injected into a GC-MS. The continuous creeping DSC signal is an artefact due to a mismatch between the heat capacities of the sample and the empty reference crucible. (b–d) Selection of background subtracted mass spectra for various small molecules taken at the various temperatures highlighted in (a). Note that due to leakage, especially the spectrum for CO/N2 is not totally reliable, visible by the negative value after background subtraction. However, in (d), the strong increase is real and reveals decomposition of Ni-CN$_x$. Further not that the column could not separate the evolved gases very well.

The thermal behavior of Ni-CN$_x$ has been investigated by thermogravimetry and differential scanning calorimetry, presented in Figure 4.7a. Upon heating under argon atmosphere at a heating rate of 5 K/min, the compound remains unchanged over a large temperature range, just accompanied by a small mass loss of <2 wt%, likely corresponding to adsorbed species like water. A more drastic mass loss is observed beginning at ~450 °C and could be caused by beginning decomposition of the material and the release of gaseous products. The decomposition sets in slightly earlier as compared to polymeric products such as K-PHI (>500 °C),[26] melon (>500 °C)[51] or PTI · LiCl (>500 °C),[52] but the thermal stability is nonetheless decent and the presence of a polymeric phase cannot be excluded outright by this method.

The DSC signal begins to decrease until 250 °C, which can be attributed to a difference in heat capacity with respect to the reference rather than to any actual thermal event occurring in Ni-CN$_x$. The first injection of the exhaust gas stream into the gas chromatograph at 75 °C (Figure 4.7b) into the mass spectrometer shows nearly no specific increase in the traced ions. Note that, due to leakage of N_2 from the atmosphere, the signal m/z=28 (red graph) is not reliable in measurements at 75 °C and 490 °C. In the temperature regime above 450 °C a weak endothermic event can be observed, followed by a small exothermic signal. While the first feature might be attributed to a conversion of material into the gas phase, the subsequent peak could indicate an energy releasing condensation reaction, reasoned by an increase of NH_3 (m/z=17) and NH_2 (m/z=16) in the corresponding mass spectrum taken at 490 °C (cf. Figure 4.7c). The fact that a condensation reaction can occur in Ni-CN_x, points towards a not fully condensed composition, in which the constituting species can further react with each other. Finally, a strong exothermic event can be observed at ca. 630 °C, which likely correspond to the decomposition of the material and the release of thermodynamically more stable products such as molecular nitrogen/carbon monoxide (m/z=28), dicyan (m/z=52), hydrogen cyanide (m/z 27), cyanide (m/z=26), which is corroborated by the ion currents in Figure 4.7d. At this temperature the very high signal of the N_2/CO curve is most likely real and only weakly affected by leaking N_2 from the laboratory.

Optical properties

The light absorption is a fundamental parameter for every photocatalyst. In a conventional photocatalyst the band gap, extracted from the absorption spectrum, indicates the maximum potential energy the photocatalyst can provide. However, as Ni-CN_x is employed in a photothermal setup, the materials light absorption, enabling a photochemical reaction, is less important compared to a conventional photocatalyst. It still holds that a high absorption profile over large parts of the visible spectrum may lead to higher local temperatures that benefit the catalyzed reaction.[19] With respect to these considerations, it is desirable to additionally harvest low energy visible or even IR frequencies that would not allow for a direct use as photoinduced electrochemical potential, but still account for over 50% of the incident solar power.[53]

The absorption spectrum (Figure 4.8a) may also reveal structural information on Ni-CN_x. The fact that two distinct bands at 450 and 550 nm are present in the visible region suggests that there could be two coordinating environments of nickel cations giving rise to these absorption energies. This explanation is corroborated by the Ni-photoelectron spectrum (XPS) (Figure C 9), which

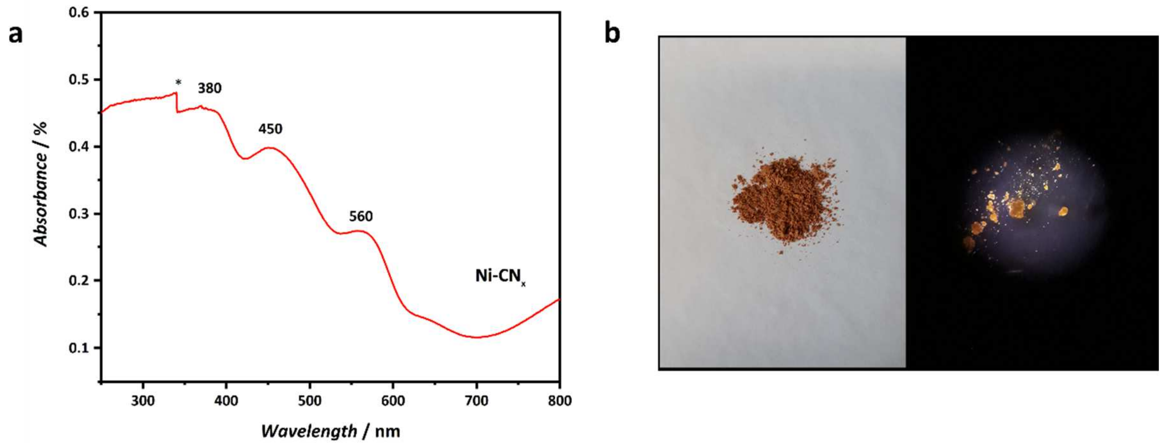

Figure 4.8. (a) Optical absorption spectrum for Ni-CN_x. In the overall broad absorption range, two absorption bands are distinctly visible, caused by the nickel centers. At higher energies a third absorption may be observed potentially stemming from the carbon nitride species. The asterisk marks an artefact due to the lamp change from tungsten halogen to deuterium arc. (b) Photograph and micrograph with 10× magnification of Ni-CN_x sample. The powder is not completely opaque, but does not contain larger single-crystals under the polarization filter.

shows two nickel species corresponding to binding energies of 855.1 eV and 856.3 eV, respectively. The relatively high binding energies (>855 eV) could indicate a high oxidation state (2+/3+) or that the nickel cations are octahedrally coordinated, possibly both. Tetrahedral and quadratic planar arrangements are usually located at lower binding energies (~852-854 eV).[54] Owing to the rich redox chemistry of nickel (+3, +2, +1, 0) – which gave rise to the notation "NiO$_x$" in various papers – an unambiguous assignment of the peaks remains challenging.[55]

The third region in the UV/Vis spectrum <450 nm could stem from the coordinating CN-species. These transitions can either originate from a polymeric CN-material, in which case this would correspond to the absorption of the band gap, to intramolecular transitions within CN-monomers (e.g. π–π^*, n–σ^*)[56,57] or to metal ligand charge-transfer (ML/LMCT) states.[58] In the measurement we may assume another transition to occur in the region above 800 nm, because the signal is rising again. It is known that, for instance, nickel (II) cations with octahedral coordination environment may exhibit three allowed transitions, approximately between ~900–1200 nm, ~540–720 nm and 330–500 nm, respectively.[57] Taking into account the three reported bands in Figure 4.8a (450 nm, 550 nm and >800 nm), an octahedrally coordinated Ni^{2+} species seems to be a viable possibility, although it is not yet clarified whether a second coordination environment and/or oxidation state comes into play as well. From evidence thus far (e.g. low symmetry space-group, XPS spectra) it is unlikely that only one Ni-environment is present within the sample. Therefore, it remains challenging to extract an unambiguous coordination number from the UV/Vis spectrum without further knowledge of the crystal structure.

In general, the overall high absorption profile in the visible and presumably near IR range may enhance the above discussed effects for a photothermal application of Ni-CN$_x$, which will be further discussed in the next section.

Photothermal CO_2 conversion

The underlying idea of this project has been to test a cost-efficient CN material for its application towards the CO_2 reduction reaction. The measurements have been conducted by Dr. L. Diehl in the lab of Prof. G. A. Ozin at the University of Toronto. We chose a photothermal setup, using a thermally activated catalyst. The catalyst was dispersed on a silicate filter and transferred into a pressure chamber (Figure C 10), which was then purged and filled with one atmosphere of hydrogen gas and one atmosphere of isotopically labelled $^{13}CO_2$. The experiment was conducted in a batch setup, during which the reactor was irradiated by a Xe-lamp (ca. 30 mW/cm^2) and heated simultaneously on a heating block at adjustable temperatures (150–190 °C). The gas in the headspace of the reactor was subsequently analyzed by gas chromatography combined with a mass spectrometer, which enabled separate detection of ^{13}CO and naturally abundant ^{12}CO, coming from leaks or even decomposition of the catalyst itself. Since the first run yielded significant amounts of ^{12}CO alongside the desired ^{13}CO product, it made sense to discard this measurement, because it could have been affected by $^{12}CO_2$ adsorbed prior to loading or small impurities on the catalyst's surface. For the consecutive runs, the loaded sample has not been removed from the reactor, but merely reloaded with the respective gases.

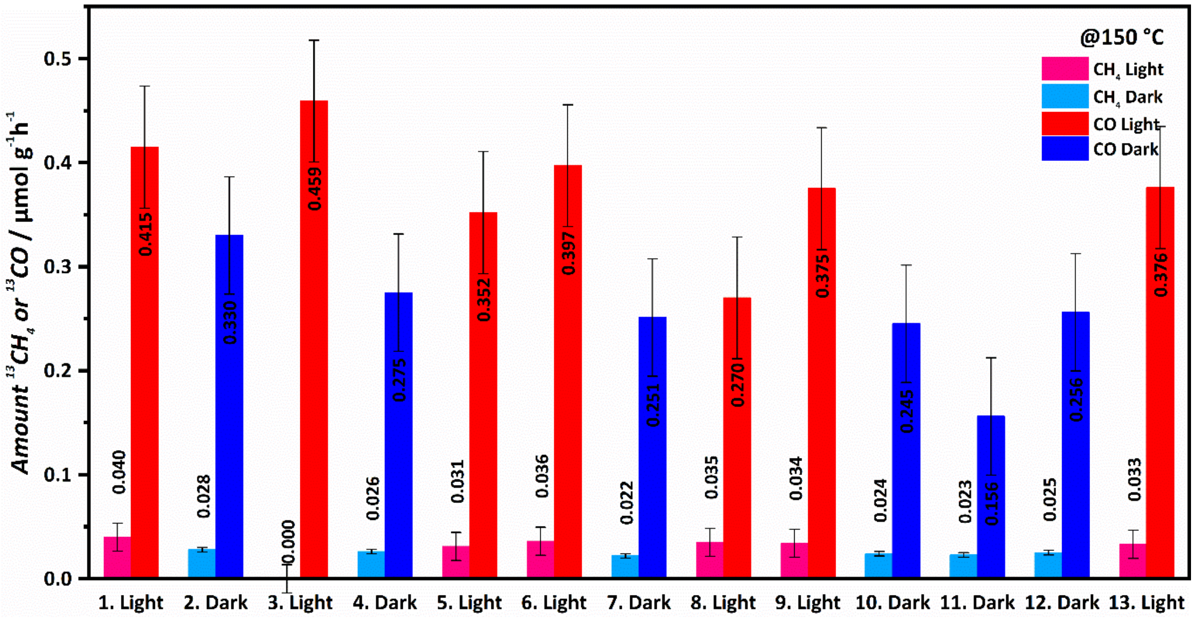

Figure 4.9. Photothermal batch experiments at 150 °C with one atm. H_2 and one atm. $^{13}CO_2$. The loaded catalyst is the same in each run. The pink ($^{13}CH_4$) and red (^{13}CO) columns symbolize runs with irradiation (30 mW/cm^2), while light blue ($^{13}CH_4$) and blue (^{13}CO) show the experiments in the dark. The first run was omitted, due to an increased amount of ^{12}CO, that stems from impurities or carbon dioxide absorbed prior to loading of the chamber. An error of about 15-20% can be expected from these measurements.

In a first set of experiments (Figure 4.9) a standard procedure known from other materials has been followed, which utilized a heating block temperature of 150 °C.[59] First of all the data proves that Ni-CN$_x$ is indeed able to convert $^{13}CO_2$ to ^{13}CO under the given conditions. The selectivity over methane of over 90% is already relatively high, but can be further increased as will be shown later. Despite methane being a valuable product itself, many branches of chemical industry rely on a mixture of CO/H_2 (syngas) as a C1-feedstock, which is why a high conversion selectivity to carbon monoxide may prove beneficial based on the existing infrastructure. The production rate of CO for Ni-CN$_x$ amounts to 0.38 ± 0.06 µmol/gh (light) and 0.25 ± 0.05 µmol/gh (dark) averaged over the corresponding runs. Every batch experiment takes approx. 6 h, it thus may be concluded that the catalyst retains stable activity for at least 78 h.

In all irradiated runs, the rates for CO/CH_4 surpass those obtained in darkness. However, it is likewise obvious that a substantial rate persists in the dark, thus suggesting a thermally activated process, which is only enhanced by the radiative power of the lamp. In other words, we can exclude that the light itself acts as a driving force lowering the activation barrier, e.g. by providing excited electronic states as in conventional photocatalysis (cf. chapter 1.3).

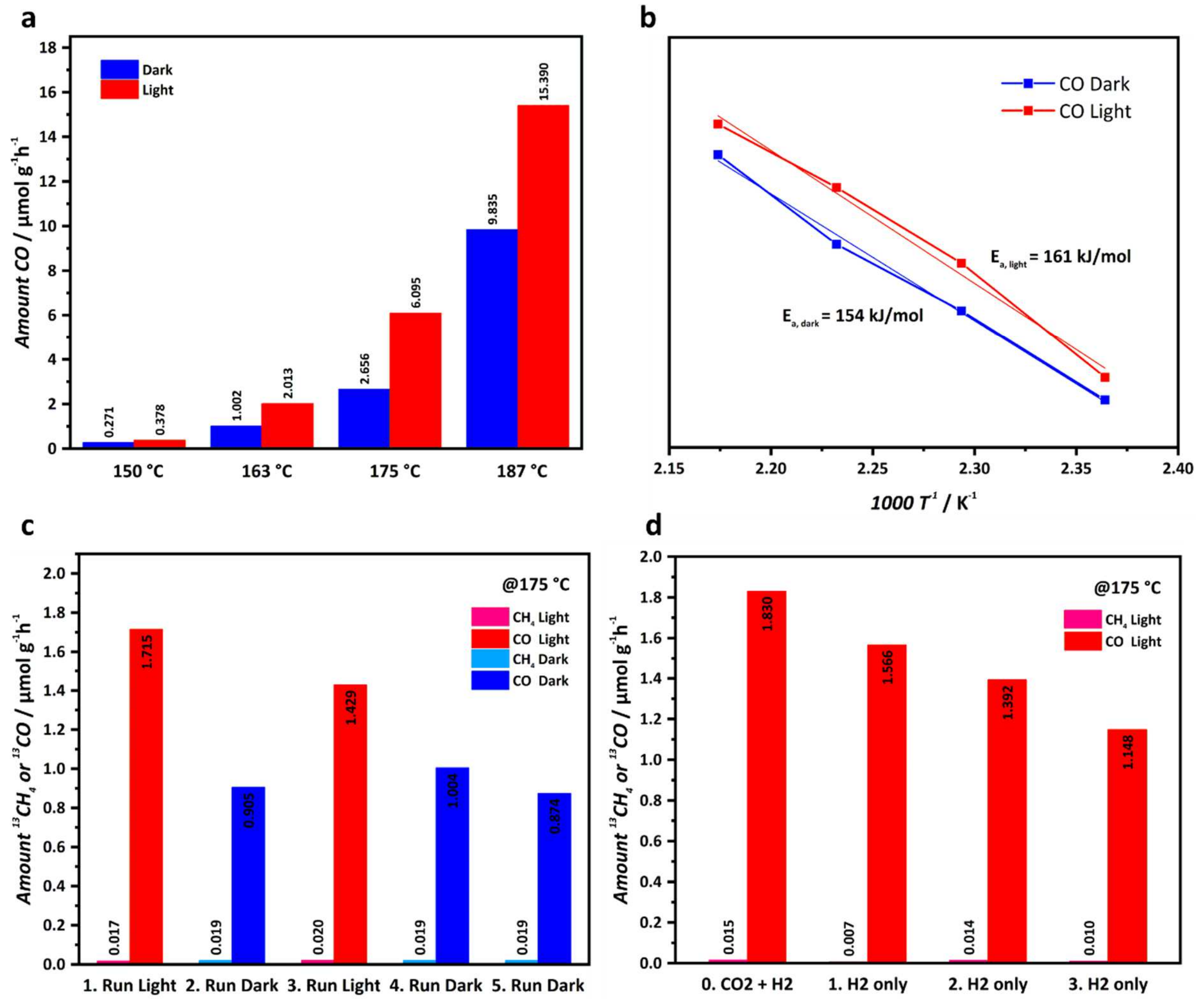

Figure 4.10. Catalytic production rates of ^{13}CO and $^{13}CH_4$, respectively, obtained in photothermal measurements in a pressure reactor filled with 1 bar of $^{13}CO_2$ and H_2, if not stated otherwise. Please note that after each change of the catalyst an initial run has been performed to clean the catalyst surface from potentially absorbed natural $^{12}CO_2$, which would lead to higher intensity in ^{12}CO signal, obscuring the ^{13}CO signal. (a) Temperature dependence controlled by the heating element. The blue columns represent the ^{13}CO evolution rates in the dark, while the red columns are obtained with radiation from a Xe-lamp (ca. 30 mW/cm^2). In (a) the arithmetic mean from several measurements is shown. (b) Linearized Arrhenius plots for CO generation under irradiation and in the dark. (c) Five subsequent runs of the same catalyst-loading at 175 °C and the corresponding rates for $^{13}CH_4$ and ^{13}CO, respectively. The selectivity of carbon monoxide over methane is >98%. Note that the absolute rates are rel. low for a 175 °C run, which is likely related to a leaking of this reactor thereby reducing the overall yield of detected products. (d) Experiment at 175 °C, taking the same catalyst, with an initial loading of $^{13}CO_2$ and H_2, while in the continuous runs only H_2 was replenished (p = 2 bar). The selectivity stayed constantly >98%. Although registering a decrease in produced CO, the material is capable of storing CO_2, hence producing a substantial amount even in the third run with H_2 only (approx. 24 h after initial loading).

To further disentangle the influence of the temperature on the evolution rates, experiments at different temperatures have been conducted. Figure 4.10a presents the CO rates for experiments performed at 150 °C, 163 °C, 175 °C and 187 °C, respectively. An exponential correlation between the reactor's temperature and the production rate of carbon monoxide can be determined. From the slope of the linearized Arrhenius plot (Figure 4.10b) activation energies of 154 kJ/mol for the dark reaction and 161 kJ/mol for the light reaction could be derived. Within the error, no lowering of the activation barrier is observed for the light reaction, thus favoring a photothermal mechanism over a photocatalytic type reaction (Figure 4.11). The temperature dependent measurements also show that the rate at 150 °C is comparably low, meaning the reaction is only very sluggish and stays just above detection threshold. Hence, the following experiments were performed at a temperature of 175 °C in order to avoid interference with baseline issues.

Figure 4.10c shows five consecutive runs at 175 °C alternating between irradiation (red columns) and darkness (blue columns). The rates for CO are significantly increased over the 150 °C set of experiments and amounts to approx. 1.6 µmol/gh (light) and 0.9 µmol/gh (dark). Additionally, at these higher temperatures, the selectivity over methane is increased to >98%. In general, the low generation of methane speaks for a single-site mechanism.[17] A control experiment (Figure C 11) with nickel nanoparticles at 190 °C with otherwise identical conditions yielded a rate of 22.4 µmol/gh (light) ^{13}CO, though with inverse selectivity over $^{13}CH_4$ (50.1 µmol/gh). We attribute the enhanced production of methane to the active surface of the nickel particles that favor successive complete reduction of carbon dioxide.[17,60] Additionally, the total amount of loaded metal catalyst is comparably higher and the metal centers are not individually distributed over the sample, thus requiring a greater amount of more expensive nickel. In fact, compared to the 187 °C experiment for Ni-CN_x, the CO evolution even excels for the carbon nitride compound, taking into consideration the lower nickel content of only 27 wt%. Due to the high crystallinity as well as the lack of apparent nickel particles in TEM micrographs, it can be indirectly derived that nickel is presumably atomically dispersed. In consequence, by increasing the surface area of the particles, e.g. by downsizing of the Ni-CN_x material, the catalytic rates should increase considerably.

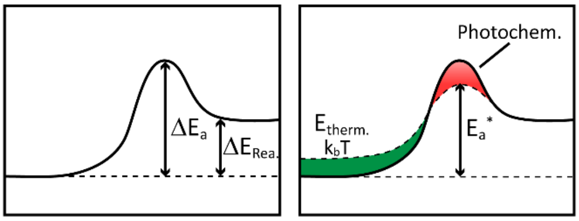

Figure 4.11. Comparison of the energy profile between a conventional (left) and a thermally/photochemically affected reaction. The green area represents the increased accessible energy at elevated temperatures, while a photochemical influence would lower the activation barrier (red area).

The mechanism of the CO_2 reduction cannot be assessed here, in particular, because the local structure is not yet resolved. However, a single-site mechanism seems likely, as e.g. UV/Vis spectroscopy suggests coordination centers and powder diffraction points to a very ordered system. Additionally, the above introduced concept of local heating of the catalyst's surface (cf. optical property section) is particularly of interest regarding the desorption of the product, which is created during a catalytic cycle.[19,61] During a catalytic cycle, CO and water as a byproduct need to be released into the gas phase, thus resupplying fresh active sites. In the Mond-process[62], the decomposition of nickel carbonyl (e.g. $Ni(CO)_4$) commences at elevated temperatures (>180 °C),[63] which may likely be a required step for the herein presented photothermal reduction of carbon dioxide. Although the structure deviates from a nickel tetracarbonyl, the structural feature of an intermediate Ni-CO bond is highly probable and therefore the high temperature for cleaving the product from the catalytic center could be necessary. In this case, irradiation of the catalyst acts as an additional source of energy to this aim, as illustrated in Figure 4.11.

Evidence has been provided that Ni-CN_x physically stores carbon dioxide on its surface or even chemically at surface functionalities. Hence, a final experiment (Figure 4.10d) was designed to test whether this carbon dioxide can be accessed under reaction conditions. To this end, after an initial standard loading with $^{13}CO_2$ and H_2, successive runs were conducted, supplying only fresh H_2 (2 bar). Indeed, it showed that in the first run with H_2-only, 85% of the initial rate could be retained. In consecutive runs the rate is reduced by another 10-20%. This finding proves that, in principle, it is possible to decouple the carbon dioxide adsorption and later conversion to carbon monoxide by hydrogen addition at elevated temperatures. Hence, one could envision a scenario, in which CO_2 is captured – potentially from exhaust gases when the energy demand is high – and then reacted with green hydrogen at times with high energy availability.

4.3 Discussion and conclusion

Ni-CN_x is presented as a new member of the carbon nitride family, synthesized ionothermally from an eutectic mixture of $NiCl_2$ and KCl in a closed reaction vessel. While the high crystallinity rather points to a monomeric form, a polymeric carbon nitride backbone cannot be ruled out completely, due the lack of clear evidence for monomers (e.g. by liq. NMR or mass spectrometry). In the case of a monomeric arrangement the structure could be constituted similarly to metal organic frameworks, in which the carbon nitride bridges metal clusters. It is known that a metal cation can be coordinated by a negatively charged carbon nitride both in monomeric and polymeric form.[26,32,33,64,65] Unfortunately, the Ni-content rendered the local structural assessment by NMR techniques impossible. On the other hand, the good crystallinity allowed for the extraction of a potential unit cell based on X-ray powder diffraction and could be corroborated by electron diffraction, which could lend a good basis for further attempts to solve the structure.

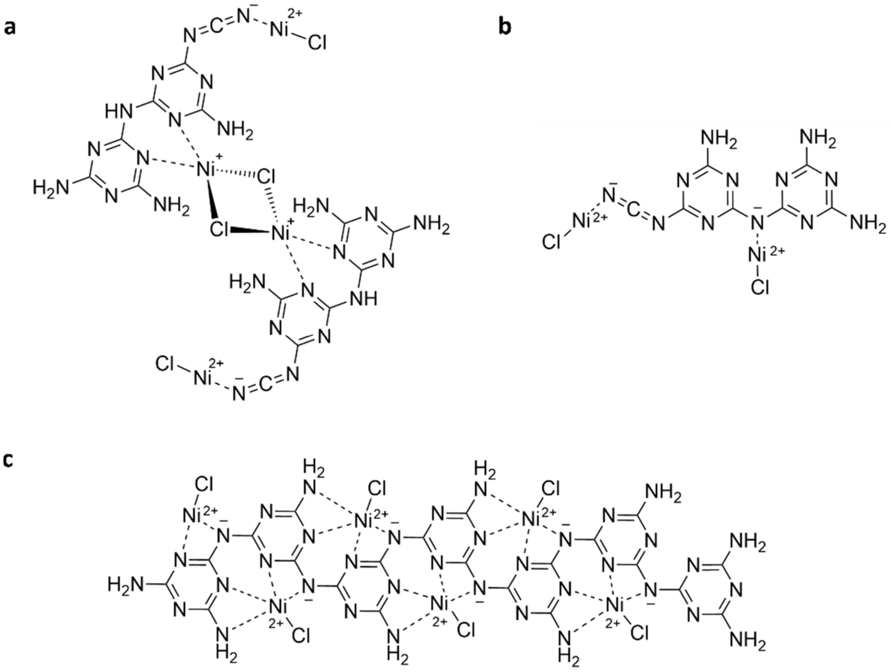

Figure 4.12. Hypothetical structures of Ni-CN_x, assuming a molecular (a-b) and an oligomeric (c) arrangement of subunits. The melam units in (a) feature a coordinative and ionic bond towards nickel with oxidation states of +1 and +2, respectively. In (b) the melam is negatively charged featuring only ionic bonds and ox. state +2. (c) In the oligomeric form only ionic bonds persist; with nickel in ox. state +2.

Nevertheless, it lies in the chemist's nature to long for a structural representation. Well knowing that solid ground is partially left behind, Figure 4.12 depicts potential building elements, that are largely in accordance with the observed analytical data. However, as the range of analytical techniques is limited, especially given the problematic nature of the NMR data, these suggestions paint by no means an exhaustive picture of possible solutions. For instance, if adduct phases with different, yet structurally similar subunits (e.g. melamine, melam and melem and derivatives) were formed, the potential window of opportunities would be even larger. All shown models take into account the relatively high N/C ratio of approx. 1.7, paired with a high content of nickel and chlorine, while featuring multiple NH_2 groups as indicated by IR vibrations. Moreover, all models are triazine based, which presumably match the PDF of Ni-CN_x best. The structure in Figure 4.12a contains nickel in varied oxidation states (+1, +2), whereas those in Figure 4.12b–c have a formal oxidation state of +2 balanced by a negatively charged carbon nitride and chloride ions. Regarding the insolubility of Ni-CN_x and the synthetic conditions close to those of PTI · LiCl, the oligomeric structure could indeed prove to be a valid candidate, combining features that would favor a polymeric and monomeric form, respectively. It is striking that each of the presented models comprise building blocks that would allow for the construction of a poly(triazine imide) polymer, hence foreshadowing a certain relationship.

Ni-CN_x possesses the mutual properties of storing and on the other hand reducing CO_2 to CO with very high selectivity under suitable conditions, rendering it a promising material for effectively using energy from renewable sources. The herein applied photothermal approach has the advantage of readily desorbing the reaction product upon formation. In a purely photocatalytic CO_2 reduction approach, as has been shown i.e. for Ni@TiO_2 under UV irradiation, the catalytic rate may suffer from deactivation, due to accumulating products on the surface.[66] Ni-CN_x acts as a photothermal catalyst. Hence, the high absorption profile throughout the visible range supports the catalysis in a sense of local heating at the active sites, thus substantially increasing the rates for CO during illumination. With a stable rate of ca. 2 µmol/gh @175 °C, Ni-CN_x performs comparably to photocatalytic CO_2 reduction catalysts.[67] There are reports on photothermal CO_2 reduction e.g. with Fe-based catalysts that reach conversion rates within the mmol-range. However, the utilized temperatures (~300 °C) and irradiation powers (2 W/cm^2 vs. 30 mW/cm^2) are significantly higher than achievable by natural incident sunlight.[68] In a more comparable study with a photothermal reaction setup at 150 °C (~100 mW/cm^2) using Ni-particles on a carbon nitride support, CH_4 rates of 28 µmol/gh are reached, though with a selectivity favoring the production of CH_4.[18] Additionally, Ni-CN_x has not yet been optimized, e.g. by increasing the surface area. In the presented measurements, the selectivity over methane reaches near unity. Creating CO from CO_2 with high selectivity and thus syngas in consequence, has the great economic advantage that an enormous infrastructure is already installed for its further use, e.g. the Fischer-Tropsch-process (10^6 L a^{-1}, Nordic Blue Crude, Norway).[69] Ni-CN_x exhibits the major advantage that it can capture carbon dioxide and subsequently use this stored CO_2 under a hydrogen atmosphere for the conversion to carbon monoxide, allowing for the temporal separation of both processes.

4.4 Acknowledgments

First and foremost, I would like to thank Leo Diehl, who performed the photothermal CO_2-reduction measurements with Ni-CN_x at Prof. Ozin's lab at the University of Toronto; also, for the many inspiring discussions around this project! I thank Maxwell W. Terban for collecting the PDF data and V. Duppel for TEM data. I would like to thank my colleagues Stefan Trenker, for sorption experiments, Lars Grunenberg for conducting mass spectrometry, Jakob Blahusch and Christian Schneider for TG/DSC analyses and Kathrin Küster for XPS measurements. Further thanks go to Igor Moudrakovski for trying his best with the Ni-species at the NMR spectrometer.

Experimental contributions

Hendrik Schlomberg, in collaboration with Leo Diehl, designed this study. Hendrik Schlomberg synthesized and characterized the Ni-CN_x compound, if not stated otherwise. Leo Diehl performed the photothermal catalytic experiments at Prof. G. A. Ozin's lab at the University of Toronto. Maxwell W. Terban collected pair distribution function analysis data. Viola Duppel collected TEM images and electron diffraction data. XPS was performed and analyzed by Kathrin Küster. Stefan Trenker measured CO_2 sorption data. Lars Grunenberg performed LCMS measurements. Jakob Blahusch and Christian Schneider conducted TGA and TG-MS measurements, respectively. Igor Moudrakovski gathered ssNMR data. Christian Minke collected SEM images and EDX spectra.

4.5 References

(1) Vogt, C.; Monai, M.; Sterk, E. B.; Palle, J.; Melcherts, A. E. M.; Zijlstra, B.; Groeneveld, E.; Berben, P. H.; Boereboom, J. M.; Hensen, E. J. M.; Meirer, F.; Filot, I. A. W.; Weckhuysen, B. M. Understanding carbon dioxide activation and carbon–carbon coupling over nickel. *Nat. Commun.* **2019**, *10* (1), 5330. DOI: 10.1038/s41467-019-12858-3.

(2) Schlögl, R. E-Mobility and the Energy Transition. *Angew. Chem. Int. Ed.* **2017**, *56* (37), 11019–11022. DOI: 10.1002/anie.201701633.

(3) Schlögl, R. The Revolution Continues: Energiewende 2.0. *Angew. Chem. Int. Ed.* **2015**, *54* (15), 4436–4439. DOI: 10.1002/anie.201405876.

(4) Roiaz, M.; Monachino, E.; Dri, C.; Greiner, M.; Knop-Gericke, A.; Schlögl, R.; Comelli, G.; Vesselli, E. Reverse Water–Gas Shift or Sabatier Methanation on Ni(110)? Stable Surface Species at Near-Ambient Pressure. *J. Am. Chem. Soc.* **2016**, *138* (12), 4146–4154. DOI: 10.1021/jacs.5b13366.

(5) Hong, D.; Kawanishi, T.; Tsukakoshi, Y.; Kotani, H.; Ishizuka, T.; Kojima, T. Efficient Photocatalytic CO_2 Reduction by a Ni(II) Complex Having Pyridine Pendants through Capturing a Mg^{2+} Ion as a Lewis-Acid Cocatalyst. *J. Am. Chem. Soc.* **2019**, *141* (51), 20309–20317. DOI: 10.1021/jacs.9b10597.

(6) Liu, S.; Yang, H. B.; Hung, S.-F.; Ding, J.; Cai, W.; Liu, L.; Gao, J.; Li, X.; Ren, X.; Kuang, Z.; Huang, Y.; Zhang, T.; Liu, B. Elucidating the Electrocatalytic CO_2 Reduction Reaction over a Model Single-Atom Nickel Catalyst. *Angew. Chem. Int. Ed.* **2020**, *59* (2), 798–803. DOI: 10.1002/anie.201911995.

(7) Tomiyama, S.; Takahashi, R.; Sato, S.; Sodesawa, T.; Yoshida, S. Preparation of Ni/SiO_2 catalyst with high thermal stability for CO_2-reforming of CH_4. *Appl. Catal. A: Gen.* **2003**, *241* (1), 349–361. DOI: 10.1016/S0926-860X(02)00493-3.

(8) Silaghi, M.-C.; Comas-Vives, A.; Copéret, C. CO_2 Activation on Ni/γ–Al_2O_3 Catalysts by First-Principles Calculations: From Ideal Surfaces to Supported Nanoparticles. *ACS Catal.* **2016**, *6* (7), 4501–4505. DOI: 10.1021/acscatal.6b00822.

(9) Lin, W.; Stocker, K. M.; Schatz, G. C. Mechanisms of Hydrogen-Assisted CO_2 Reduction on Nickel. *J. Am. Chem. Soc.* **2017**, *139* (13), 4663–4666. DOI: 10.1021/jacs.7b01538.

(10) Park, J.-N.; McFarland, E. W. A highly dispersed Pd–Mg/SiO_2 catalyst active for methanation of CO_2. *J. Catal.* **2009**, *266* (1), 92–97. DOI: 10.1016/j.jcat.2009.05.018.

(11) Yu, K.-P.; Yu, W.-Y.; Kuo, M.-C.; Liou, Y.-C.; Chien, S.-H. Pt/titania-nanotube: A potential catalyst for CO_2 adsorption and hydrogenation. *Appl. Catal. B* **2008**, *84* (1), 112–118. DOI: 10.1016/j.apcatb.2008.03.009.

(12) Beuls, A.; Swalus, C.; Jacquemin, M.; Heyen, G.; Karelovic, A.; Ruiz, P. Methanation of CO_2: Further insight into the mechanism over Rh/γ-Al_2O_3 catalyst. *Appl. Catal. B* **2012**, *113-114*, 2–10. DOI: 10.1016/j.apcatb.2011.02.033.

(13) Sharma, S.; Hu, Z.; Zhang, P.; McFarland, E. W.; Metiu, H. CO_2 methanation on Ru-doped ceria. *J. Catal.* **2011**, *278* (2), 297–309. DOI: 10.1016/j.jcat.2010.12.015.

(14) Aziz, M.A.A.; Jalil, A. A.; Triwahyono, S.; Mukti, R. R.; Taufiq-Yap, Y. H.; Sazegar, M. R. Highly active Ni-promoted mesostructured silica nanoparticles for CO_2 methanation. *Appl. Catal. B* **2014**, *147*, 359–368. DOI: 10.1016/j.apcatb.2013.09.015.

(15) Chen, C.-S.; Budi, C. S.; Wu, H.-C.; Saikia, D.; Kao, H.-M. Size-Tunable Ni Nanoparticles Supported on Surface-Modified, Cage-Type Mesoporous Silica as Highly Active Catalysts for CO_2 Hydrogenation. *ACS Catal.* **2017**, *7* (12), 8367–8381. DOI: 10.1021/acscatal.7b02310.

(16) Lu, B.; Kawamoto, K. Preparation of mesoporous CeO_2 and monodispersed NiO particles in CeO_2, and enhanced selectivity of NiO/CeO_2 for reverse water gas shift reaction. *Mater. Res. Bull.* **2014**, *53*, 70–78. DOI: 10.1016/j.materresbull.2014.01.043.

(17) Millet, M.-M.; Algara-Siller, G.; Wrabetz, S.; Mazheika, A.; Girgsdies, F.; Teschner, D.; Seitz, F.; Tarasov, A.; Levchenko, S. V.; Schlögl, R.; Frei, E. Ni Single Atom Catalysts for CO_2 Activation. *J. Am. Chem. Soc.* **2019**, *141* (6), 2451–2461. DOI: 10.1021/jacs.8b11729.

(18) Barrio, J.; Mateo, D.; Albero, J.; García, H.; Shalom, M. A Heterogeneous Carbon Nitride–Nickel Photocatalyst for Efficient Low-Temperature CO_2 Methanation. *Adv. Energy Mater.* **2019**, *9* (44), 1902738. DOI: 10.1002/aenm.201902738.

(19) Ghoussoub, M.; Xia, M.; Duchesne, P. N.; Segal, D.; Ozin, G. Principles of photothermal gas-phase heterogeneous CO_2 catalysis. *Energy Environ. Sci.* **2019**, *12* (4), 1122–1142. DOI: 10.1039/C8EE02790K.

(20) O'Brien, P. G.; Sandhel, A.; Wood, T. E.; Jelle, A. A.; Hoch, L. B.; Perovic, D. D.; Mims, C. A.; Ozin, G. A. Photomethanation of Gaseous CO_2 over Ru/Silicon Nanowire Catalysts with Visible and Near-Infrared Photons. *Adv. Sci.* **2014**, *1* (1), 1400001. DOI: 10.1002/advs.201400001.

(21) Wirnhier, E.; Döblinger, M.; Gunzelmann, D.; Senker, J.; Lotsch, B. V.; Schnick, W. Poly(triazine imide) with Intercalation of Lithium and Chloride Ions [$(C_3N_3)_2(NH_xLi_{1-x})_3\cdot LiCl$]: A Crystalline 2D Carbon Nitride Network. *Chem. Eur. J.* **2011**, *17* (11), 3213–3221. DOI: 10.1002/chem.201002462.

(22) Kessler, F. K.; Schnick, W. From Heptazines to Triazines - On the Formation of Poly(triazine imide). *Z. anorg. allg. Chem.* **2019**, *645* (12), 857–862. DOI: 10.1002/zaac.201900043.

(23) Kessler, F. K.; Schnick, W. Ammelinium Sulfate Monohydrate and Ammelinium Sulfate Cyanuric Acid - Synthesis and Structural Characterization. *Z. anorg. allg. Chem.* **2019**, *645* (12), 848–856. DOI: 10.1002/zaac.201900042.

(24) Sattler, A.; Schönberger, S.; Schnick, W. Melemium Methylsulfonates $HC_6N_7(NH_2)_3$ $H_2C_6N_7(NH_2)_3$ $(SO_3Me)_3 \cdot H_2O$ and $H_2C_6N_7(NH_2)_3$ (SO_3Me) $2 \cdot H_2O$. *Z. anorg. allg. Chem.* **2010**, *636* (3-4), 476–482. DOI: 10.1002/zaac.200900433.

(25) Irran, E.; Jürgens, B.; Schnick, W. Synthesis, crystal structure determination from X-ray powder diffractometry and vibrational spectroscopy of the tricyanomelaminate monohydrates $M_3[C_6N_9]\cdot H_2O$ (M=K, Rb). *Solid State Sci.* **2002**, *4* (10), 1305–1311. DOI: 10.1016/S1293-2558(02)00012-2.

(26) Schlomberg, H.; Kröger, J.; Savasci, G.; Terban, M. W.; Bette, S.; Moudrakovski, I.; Duppel, V.; Podjaski, F.; Siegel, R.; Senker, J.; Dinnebier, R. E.; Ochsenfeld, C.; Lotsch, B. V. Structural Insights into Poly(Heptazine Imides): A Light-Storing Carbon Nitride Material for Dark Photocatalysis. *Chem. Mater.* **2019**, *31* (18), 7478–7486. DOI: 10.1021/acs.chemmater.9b02199.

(27) Pawley, G. S. Unit-cell refinement from powder diffraction scans. *J. Appl. Crystallogr.* **1981**, *14* (6), 357–361. DOI: 10.1107/S0021889881009618.

(28) Mesch, M. B.; Bärwinkel, K.; Krysiak, Y.; Martineau, C.; Taulelle, F.; Neder, R. B.; Kolb, U.; Senker, J. Solving the Hydrogen and Lithium Substructure of Poly(triazine imide)/LiCl Using NMR Crystallography. *Chem. Eur. J.* **2016**, *22* (47), 16878–16890. DOI: 10.1002/chem.201603726.

(29) Lotsch, B. V.; Döblinger, M.; Sehnert, J.; Seyfarth, L.; Senker, J.; Oeckler, O.; Schnick, W. Unmasking Melon by a Complementary Approach Employing Electron Diffraction, Solid-State NMR Spectroscopy, and Theoretical Calculations—Structural Characterization of a Carbon Nitride Polymer. *Chem. Eur. J.* **2007**, *13* (17), 4969–4980. DOI: 10.1002/chem.200601759.

(30) Sattler, A.; Seyfarth, L.; Senker, J.; Schnick, W. Synthesen, Kristallstrukturen und spektroskopische Eigenschaften des Melem-Adduktes $C_6N_7(NH_2)_3 \cdot H_3PO_4$ sowie der Melemium-Salze $(H_2C_6N_7(NH_2)_3)SO_4 \cdot 2\ H_2O$ und $(HC_6N_7(NH_2)_3)ClO_4 \cdot H_2O$. *Z. anorg. allg. Chem.* **2005**, *631* (13-14), 2545–2554. DOI: 10.1002/zaac.200500017.

(31) Seyfarth, L.; Seyfarth, J.; Lotsch, B. V.; Schnick, W.; Senker, J. Tackling the stacking disorder of melon--structure elucidation in a semicrystalline material. *Phys. Chem. Chem. Phys.* **2010**, *12* (9), 2227–2237. DOI: 10.1039/b919918g.

(32) Sattler, A.; Schnick, W. On the Formation and Decomposition of the Melonate Ion in Cyanate and Thiocyanate Melts and the Crystal Structure of Potassium Melonate, $K_3[C_6N_7(NCN)_3]$. *Eur. J. Inorg. Chem.* **2009** (33), 4972–4981. DOI: 10.1002/ejic.200900585.

(33) Sattler, A.; Budde, M. R.; Schnick, W. Metal(II) Cyamelurates Prepared from Aqueous Ammonia. *Z. anorg. allg. Chem.* **2009**, *635* (12), 1933–1939. DOI: 10.1002/zaac.200900130.

(34) Ruiz-Morales, Y.; Schreckenbach, G.; Ziegler, T. Origin of the Hydridic ^1H NMR Chemical Shift in Low-Valent Transition-Metal Hydrides. *Organometallics* **1996**, *15* (19), 3920–3923. DOI: 10.1021/om960218n.

(35) Bettina Valeska Lotsch. From Molecular Building Blocks to From Molecular Building Blocks to Condensed Carbon Nitride Networks: Structure and Reactivity, Doctoral Thesis, University of Munich (LMU) **2006**.

(36) Elisabeta Horvath-Bordon. Synthese und Eigenschaften von Kohlenstoffnitriden, Doctoral Thesis, TU Darmstadt **2004**.

(37) Larkin, P. J.; Makowski, M. P.; Colthup, N. B.; Flood, L. A. Vibrational analysis of some important group frequencies of melamine derivatives containing methoxymethyl, and carbamate substituents: mechanical coupling of substituent vibrations with triazine ring modes. *Vib. Spectrosc.* **1998**, *17* (1), 53–72. DOI: 10.1016/S0924-2031(98)00015-0.

(38) Horvath-Bordon, E.; Kroke, E.; Svoboda, I.; Fue, H.; Riedel, R.; Neeraj, S.; Cheetham, A. K. Alkalicyamelurates, $M_3[C_6N_7O_3]xH_2O$, M = Li, Na, K, Rb, Cs: UV-luminescent and thermally very stable ionic tri-s-triazine derivatives. *Dalton Trans.* **2004** (22), 3900. DOI: 10.1039/b412517g.

(39) El-Gamel, N. E. A.; Seyfarth, L.; Wagler, J.; Ehrenberg, H.; Schwarz, M.; Senker, J.; Kroke, E. The Tautomeric Forms of Cyameluric Acid Derivatives. *Chem. Eur. J.* **2007**, *13* (4), 1158–1173. DOI: 10.1002/chem.200600435.

(40) Lotsch, B. V.; Schnick, W. Synthesis and Structural Characterization of the Ammelinium Salts $[C_3H_6N_5O]Cl$, $[C_3H_6N_5O]Br$, and $[C_3H_6N_5O]NO_3$. *Z. anorg. allg. Chem.* **2006**, *632* (8-9), 1457–1464. DOI: 10.1002/zaac.200600012.

(41) He, D.; Peng, Z.; Gong, W.; Luo, Y.; Zhao, P.; Kong, L. Mechanism of a green graphene oxide reduction with reusable potassium carbonate. *RSC Adv.* **2015**, *5* (16), 11966–11972. DOI: 10.1039/C4RA14511A.

(42) Jürgens, B.; Irran, E.; Senker, J.; Kroll, P.; Müller, H.; Schnick, W. Melem (2,5,8-Triamino-tri- s -triazine), an Important Intermediate during Condensation of Melamine Rings to Graphitic Carbon

Nitride: Synthesis, Structure Determination by X-ray Powder Diffractometry, Solid-State NMR, and Theoretical Studies. *J. Am. Chem. Soc.* **2003**, *125* (34), 10288–10300. DOI: 10.1021/ja0357689.

(43) Wirnhier, E.; Mesch, M. B.; Senker, J.; Schnick, W. Formation and Characterization of Melam, Melam Hydrate, and a Melam-Melem Adduct. *Chem. Eur. J.* **2013**, *19* (6), 2041–2049. DOI: 10.1002/chem.201203340.

(44) Sattler, A.; Schnick, W. Zur Frage der Tautomerie von Cyamelursäure im Kristall. *Z. anorg. allg. Chem.* **2006**, *632* (8-9), 1518–1523. DOI: 10.1002/zaac.200600099.

(45) Makowski, S. J.; Gunzelmann, D.; Senker, J.; Schnick, W. Protonated Melonate $Ca[HC_6N_7(NCN)_3] \cdot 7\ H_2O$ - Synthesis, Crystal Structure, and Thermal Properties. *Z. anorg. allg. Chem.* **2009**, 2434–2439. DOI: 10.1002/zaac.200900231.

(46) Lotsch, B. V.; Schnick, W. New Light on an Old Story: Formation of Melam during Thermal Condensation of Melamine. *Chem. Eur. J.* **2007**, *13* (17), 4956–4968. DOI: 10.1002/chem.200601291.

(47) Kauffman, K. L.; Culp, J. T.; Goodman, A.; Matranga, C. FT-IR Study of CO_2 Adsorption in a Dynamic Copper(II) Benzoate–Pyrazine Host with CO_2–CO_2 Interactions in the Adsorbed State. *J. Phys. Chem. C* **2011**, *115* (5), 1857–1866. DOI: 10.1021/jp102273w.

(48) Hug, S.; Stegbauer, L.; Oh, H.; Hirscher, M.; Lotsch, B. V. Nitrogen-Rich Covalent Triazine Frameworks as High-Performance Platforms for Selective Carbon Capture and Storage. *Chem. Mater.* **2015**, *27* (23), 8001–8010. DOI: 10.1021/acs.chemmater.5b03330.

(49) Varghese, A. M.; Karanikolos, G. N. CO_2 capture adsorbents functionalized by amine – bearing polymers: A review. *Int. J. Greenh. Gas Control* **2020**, *96*, 103005. DOI: 10.1016/j.ijggc.2020.103005.

(50) Linus Stegbauer. Two-dimensional Covalent Organic Frameworks as Platforms for Renewable Energy and Environmental Applications, Doctoral Thesis, University of Munich (LMU) **2016**.

(51) Michael Janus Bojdys. On new allotropes and nanostructures of carbon nitrides, Doctoral Thesis, Universität Potsdam **2009**.

(52) Foglia, F.; Clancy, A. J.; Berry-Gair, J.; Lisowska, K.; Wilding, M. C.; Suter, T. M.; Miller, T. S.; Smith, K.; Demmel, F.; Appel, M.; Sakai, V. G.\'\i.; Sella, A.; Howard, C. A.; Tyagi, M.; Corà, F.; McMillan, P. F. Aquaporin-like water transport in nanoporous crystalline layered carbon nitride. *Sci. Adv.* **2020**, *6* (39). DOI: 10.1126/sciadv.abb6011.

(53) Zhu, L.; Gao, M.; Peh, C. K. N.; Ho, G. W. Solar-driven photothermal nanostructured materials designs and prerequisites for evaporation and catalysis applications. *Mater. Horiz.* **2018**, *5* (3), 323–343. DOI: 10.1039/C7MH01064H.

(54) Matienzo, J.; Lo Yin, I.; Grim, S. O.; Swartz, W. E. X-ray photoelectron spectroscopy of nickel compounds. *Inorg. Chem.* **1973**, *12* (12), 2762–2769. DOI: 10.1021/ic50130a005.

(55) Zhang, S.; Diehl, L.; Wrede, S.; Lotsch, B. V.; Scheu, C. Structural Evolution of Ni-Based Co-Catalysts on $[Ca_2Nb_3O_{10}]^-$ Nanosheets during Heating and Their Photocatalytic Properties. *Catalysts* **2020**, *10* (1), 13. DOI: 10.3390/catal10010013.

(56) Zambon, A.; Mouesca, J.-M.; Gheorghiu, C.; Bayle, P. A.; Pécaut, J.; Claeys-Bruno, M.; Gambarelli, S.; Dubois, L. s-Heptazine oligomers: promising structural models for graphitic carbon nitride. *Chem. Sci.* **2016**, *7* (2), 945–950. DOI: 10.1039/C5SC02992A.

(57) López Lago, E.; Seijas, J. A.; Pedro, I. de; Rodríguez Fernández, J.; Vázquez-Tato, M. P.; González, J. A.; Rilo, E.; Segade, L.; Cabeza, O.; Rodríguez Fernández, C. D.; Arosa, Y.; Algnamat, B. S.; Varela, L. M.; Troncoso, J.; La Fuente, R. de. Structural and physical properties of a new reversible and continuous thermochromic ionic liquid in a wide temperature interval: $[BMIM]_4[Ni(NCS)_6]$. *New J. Chem.* **2018**, *42* (19), 15561–15571. DOI: 10.1039/C8NJ03294G.

(58) Shields, B. J.; Kudisch, B.; Scholes, G. D.; Doyle, A. G. Long-Lived Charge-Transfer States of Nickel(II) Aryl Halide Complexes Facilitate Bimolecular Photoinduced Electron Transfer. *J. Am. Chem. Soc.* **2018**, *140* (8), 3035–3039. DOI: 10.1021/jacs.7b13281.

(59) O'Brien, P. G.; Ghuman, K. K.; Jelle, A. A.; Sandhel, A.; Wood, T. E.; Loh, J. Y. Y.; Jia, J.; Perovic, D.; Singh, C. V.; Kherani, N. P.; Mims, C. A.; Ozin, G. A. Enhanced photothermal reduction of gaseous CO_2 over silicon photonic crystal supported ruthenium at ambient temperature. *Energy Environ. Sci.* **2018**, *11* (12), 3443–3451. DOI: 10.1039/C8EE02347F.

(60) Mateo, D.; Morlanes, N.; Maity, P.; Shterk, G.; Mohammed, O. F.; Gascon, J. Efficient Visible-Light Driven Photothermal Conversion of CO_2 to Methane by Nickel Nanoparticles Supported on Barium Titanate. *Adv. Funct. Mater.* **2021**, *31* (8), 2008244. DOI: 10.1002/adfm.202008244.

(61) Mateo, D.; Albero, J.; García, H. Photoassisted methanation using Cu_2O nanoparticles supported on graphene as a photocatalyst. *Energy Environ. Sci.* **2017**, *10* (11), 2392–2400. DOI: 10.1039/C7EE02287E.

(62) Mond, L.; Langer, C.; Quincke, F. L.—Action of carbon monoxide on nickel. *J. Chem. Soc., Trans.* **1890**, *57* (0), 749–753. DOI: 10.1039/CT8905700749.

(63) Kerfoot, D. G. E. Nickel. In *Ullmann's Encyclopedia of Industrial Chemistry*; American Cancer Society, 2000. DOI: 10.1002/14356007.a17_157.

(64) Lau, V. W.-h.; Moudrakovski, I.; Botari, T.; Weinberger, S.; Mesch, M. B.; Duppel, V.; Senker, J.; Blum, V.; Lotsch, B. V. Rational design of carbon nitride photocatalysts by identification of cyanamide defects as catalytically relevant sites. *Nat. Commun.* **2016**, *7*, 12165. DOI: 10.1038/ncomms12165.

(65) Chen, Z.; Savateev, A.; Pronkin, S.; Papaefthimiou, V.; Wolff, C.; Willinger, M. G.; Willinger, E.; Neher, D.; Antonietti, M.; Dontsova, D. "The Easier the Better" Preparation of Efficient Photocatalysts-Metastable Poly(heptazine imide) Salts. *Adv. Mater.* **2017**, *8*, 1700555. DOI: 10.1002/adma.201700555.

(66) Shtyka, O.; Ciesielski, R.; Kedziora, A.; Maniukiewicz, W.; Dubkov, S.; Gromov, D.; Maniecki, T. Photocatalytic Reduction of CO_2 Over Me (Pt, Pd, Ni, Cu)/TiO_2 Catalysts. *Top. Catal.* **2020**, *63* (1), 113–120. DOI: 10.1007/s11244-020-01241-y.

(67) Habisreutinger, S. N.; Schmidt-Mende, L.; Stolarczyk, J. K. Photocatalytic reduction of CO_2 on TiO_2 and other semiconductors. *Angew. Chem. Int. Ed.* **2013**, *52* (29), 7372–7408. DOI: 10.1002/anie.201207199.

(68) Song, C.; Liu, X.; Xu, M.; Masi, D.; Wang, Y.; Deng, Y.; Zhang, M.; Qin, X.; Feng, K.; Yan, J.; Leng, J.; Wang, Z.; Xu, Y.; Yan, B.; Jin, S.; Xu, D.; Yin, Z.; Xiao, D.; Ma, D. Photothermal Conversion of CO_2

with Tunable Selectivity Using Fe-Based Catalysts: From Oxide to Carbide. *ACS Catal.* **2020**, *10* (18), 10364–10374. DOI: 10.1021/acscatal.0c02244.

(69) Homepage of Nordicblue. *https://nordicelectrofuel.no/, Accessed on May 20, 2021*.

5 Conclusion and outlook

This thesis shows that the structural elucidation of the important carbon nitrides K-PHI and H-PHI, respectively, could only be accomplished by a combination of multiple analytic techniques, hence solving a long-standing problem within the field.[1] The structural identification on a local level and its implications on the 3D structure of K-PHI could be disentangled, however, this remains an challenging process in need of a whole variety of analytical techniques and therefore, unfortunately, is out of scope for standard characterization. Salt melt assisted syntheses (in closed reaction systems) constitute the key reaction pathway followed in this thesis and we may still point out the significance this approach still holds for future enquiries. We illuminated how it is possible to yield a very crystalline material of the same local character opposed to an earlier more amorphous synthetic protocol and therefore were able to extract more structural information; especially with regard to the third dimension and the herewith associated role of intermolecular building elements such as potassium ions and water molecules, rigidly binding to the CN-network. The synthetic achievements in this work open new avenues towards more crystalline carbon nitrides, which ultimately aim at the growth of single-crystals suitable for X-ray structure solution. In particular, the crystallite size could be augmented from several tens of nanometers to the range of several hundreds, thus already accessing valuable electron diffraction patterns. The next key step would be the adjustment of the salt melt assisted syntheses to gain even larger crystallites. I believe that once the critical sizes with suitable defect levels are reached the potential use of single-crystal analysis will ultimately boost the entire field's progress, giving rise to even better deduction of structure–property–relationships.

As has been discussed in the introduction to this thesis (chapter 1.2), a potential way to further enhance crystallinity and crystallite size could involve using substrates to allow for the growth of more defined crystals, which until now has only been investigated superficially. While a (partially) closed reaction environment is necessary to enable healing of crystal imperfections and growth of larger crystals, the use of suitable surfaces/substrates may allow for better starting conditions for crystal seeds.

With regard to crystal growth another not much recognized reaction control parameter comes into play: the choice of a catalyst. While a good substrate permits growth of larger crystals in two dimensions, a mobile, e.g. gaseous, catalyst would allow for further improved growth in the third dimension. One could imagine a Lewis acidic catalyst that coordinates to amino groups and thus facilitates the imide bond formation step. Thereby crystals with preferable aspect ratios could be grown, which will be a key requirement for single-crystal analysis, given the sheet-like structure of many carbon nitride polymers. Partly this function has already been achieved by the salt melt, on the one hand acting as structure-directing agent and on the other hand enhancing the solubility of the CN-precursors/monomers. However, drawing a parallel to COF chemistry, one could imagine applying a catalyst that facilitates the bond formation of monomers directly by intervening in the reaction mechanism. For many COF syntheses this is realized by addition of small amounts of acid to the reaction mixture.[2,3] Using a catalyst aims at lowering the activation barrier, in turn benefitting the formation of thermodynamically stable species and in consequence growth of larger crystals. Furthermore, the implementation of mineralizers such as ammonium chloride, influence the crystallization process in e.g. ammono-, hydrothermal syntheses as well as pyrolyses.[4–6] Here, the mineralizer presumably can enhance solubility of educts or acts as a source of ammonia that affects the crystal growth.

Already, the potential of carbon nitrides as photo- and electrocatalysts, time-delayed photocatalyst, light-driven microswimmers and solar batteries has been presented, but it is still worthwhile to take a step back to further structurally analyze these compounds in order to better understand these fascinating properties.

By carefully reinvestigating the synthetic process of K-PHI formation, we could identify a new highly crystalline, heptazine based compound (K-CN-phase), which exists in close structural relation to K-PHI, yet takes on the form of a 1D connected, potassium coordinated polymer. The higher internal ampoule pressure delicately affects the product formation, thus favoring the 1D polymorph. Similar to K-PHI (chapter 2), it is highly likely that the potassium ions are responsible for the relatively high order among these chains.[1] However, this additional feature interconnecting the strands in three dimensions increases the difficulty for a structural solution from electron and X-ray diffraction data, because of an increased unit cell, which is nearly double the size of the closely related material melon.[7] Although the quality of the diffraction data is high compared to other polymeric carbon nitride materials, the data from powders are not yet resolved enough to determine the crystal structure. In this regard, it would be beneficial to find means of increasing the crystallite size to ultimately perform single-crystal X-ray analysis. Especially for the K-CN-phase, formed within a fully closed system, the deliberate control of pressure and reaction times may offer a way to grow unimpaired crystals. Within the field of carbon nitrides, advances in structure solution have also been made by techniques such as synchrotron microfocus diffraction,[8] circumventing the need for very large crystals.

We have seen that most carbon nitrides tend to form amorphous solids, incorporating a high level of defects. Besides tuning classical reaction parameters, the implementation of so-called modulators presents another strategy of yielding extended and intact structures, thus adapting a concept from MOF- and COF-chemistry.[9–11] Herein, the modulator slows the growth rate of the polymers by reversible capping and uncapping of the polymer terminations, thereby enhancing crystallinity and domain size of the resulting crystallites. The modulator must have the ability to be cleaved from the network with a comparable binding strength as the actual repeating units, but should exhibit a monotopic functionality to act as an impasse to the network formation.[2] This approach has lead to the first single-crystal analysis of a 3D imine COF.[12]

Another interesting structural aspect of carbon nitrides is the presence of water molecules bound to the CN-backbone.[1,5] Thus far, this pore water and its binding situation has not been studied extensively for other materials, but will certainly be an important feature to look out for in future studies. Tightly bound surface molecules can have a profound influence on the electronic structure of the polymer and likewise affect the availability of active sites for catalytic processes. In H-PHI, for instance, this effect can be observed with the naked eye by the removal of water, resulting in a color change from beige/white to yellow. Therefore, the focus on this issue is especially relevant for carbon nitrides, because of their inherently strong tendency to form hydrogen bonds (cf. melon structure, chapter 1.2).[7,13]

Both materials, K-PHI and K-CN-phase, have proven their potential for photocatalytic hydrogen evolution. For both compounds, we could show that the protonation to H-PHI and H-CN-phase, respectively, is accompanied by a drastic increase of the hydrogen evolution rate (38-fold for H-PHI and 20-fold for H-CN-phase). These values have been obtained by the same measurement protocol and thus are comparable to each other. However, as *Takanabe* is pointing out, a reliable assessment of photocatalytic data among different studies is often complicated by the prevailing inconsistencies for sample preparation and measurement methods.[14] In particular, there are frequent reports on the same material (e.g. melon) with various performances and it remains unclear whether these have a real structural cause or merely originate from the applied measurement procedure. It will be one of the key tasks of future research to further harmonize those procedures to allow for better comparability.

Concerning the photoreduced, blue state – shown by K/H-PHI,[1,15] but not by the H/K-CN-phase – the combined efforts undertaken in chapters 2 and 3 have demonstrated how a thorough characterization can help to extract structure–property–relationships. By comparing structural features of the K-CN-phase to K-PHI, it has been possible to tentatively attribute the charge storing property of K-PHI to the 2D arrangement of heptazine units. However, to shed light on this structure–property–relationship multiple different threads had to be picked up. This circumstance illustrates the underlying complexity and that properties are often governed by whole set of (interdependent) parameters. This, once more, reveals the importance of characterizing new CN-compounds very thoroughly to provide good groundwork for future generations to draw the most plausible conclusions for pending applications, concurrently underlining the fundamental science character of this work. Future studies should aim at the synthesis of a functional-group-free PHI system to further narrow down the structural elements, which could be responsible for the light storing ability.

Relating back to the introductory mentioned problems concerning the duck curve, the revelations on the light- or electricity-storing property of K-PHI, could impact the problems associated with the intermittency of sunlight during the diurnal cycle. If excess energy over periods of strong irradiation were properly stored within the CN-network, we would have the possibility of buffering the effects of high quantities of installed solar power plants, even without the need for storing the energy in conventional batteries or chemical bonds; ready to use in times of high demand.

It has been shown that the PHI network is versatile in terms of the post-synthetic ion exchange.[16] In chapter 4 of this thesis, we transferred this idea towards a synthetic procedure, using directly the desired cation species as part of the eutectic reaction mixture. In particular, we employed a $NiCl_2$/KCl eutectic melt in order to create a new CN-species. With nickel being the active component in many CO_2-reduction catalysts, the underlying idea was to create distinct atomic sites of the transition metal, at which CO_2 can bind and be converted into carbon monoxide, a highly valuable industrial product. Although the structure could not be unambiguously resolved,

the material itself proved its capability of selective CO_2 reduction to CO within a photothermal process. The inherent CO_2 sorption property renders this material even suitable for the decoupled process of CO_2 storage and subsequent conversion, adding a potential built-in solution to temporally decouple the energy consumption and storing of the substrate.
In future studies, it could also be possible to reduce CO_2 (photo)electrocatalytically,[17,18] if Ni-CN_x can be successfully coated as a thin film on a conductive substrate. In this configuration the very stable carbon nitride with atomically dispersed nickel centers could combine the aspects of CO_2 adsorption with the use of electricity by renewable sources, thus widening the scope of the application. Due to the problems associated with the incorporation of nickel on important analytic techniques such as ssNMR spectroscopy, in a parallel step more efforts should be made to obtain larger crystallites in order to determine the structure of Ni-CN_x by diffraction techniques.

In the end, I hope this work could shed some light on this fascinating class of materials, which will further foster the understanding of structure and properties. And as this work often times resembles detective work, it is only fair to close this thesis with a famous detective's words:

> *"Data! Data! Data!" he cried impatiently. "I can't make bricks without clay."*[c]

---

[c] Quote from Adventures of Sherlock Holmes – Arthur Conan Doyle, 1892.

5.1 References

(1) Schlomberg, H.; Kröger, J.; Savasci, G.; Terban, M. W.; Bette, S.; Moudrakovski, I.; Duppel, V.; Podjaski, F.; Siegel, R.; Senker, J.; Dinnebier, R. E.; Ochsenfeld, C.; Lotsch, B. V. Structural Insights into Poly(Heptazine Imides): A Light-Storing Carbon Nitride Material for Dark Photocatalysis. *Chem. Mater.* **2019**, *31* (18), 7478–7486. DOI: 10.1021/acs.chemmater.9b02199.

(2) Haase, F.; Lotsch, B. V. Solving the COF trilemma: towards crystalline, stable and functional covalent organic frameworks. *Chem. Soc. Rev.* **2020**, *49* (23), 8469–8500. DOI: 10.1039/D0CS01027H.

(3) Bagheri, A. R.; Aramesh, N. Towards the room-temperature synthesis of covalent organic frameworks: a mini-review. *J. Mater. Sci.* **2021**, *56* (2), 1116–1132. DOI: 10.1007/s10853-020-05308-9.

(4) Savateev, A.; Chen, Z. P.; Dontsova, D. Baking 'crumbly' carbon nitrides with improved photocatalytic properties using ammonium chloride. *RSC Adv.* **2016**, *6* (4), 2910–2913. DOI: 10.1039/C5RA22167F.

(5) Kröger, J.; Jiménez-Solano, A.; Savasci, G.; Rovó, P.; Moudrakovski, I.; Küster, K.; Schlomberg, H.; Vignolo-González, H. A.; Duppel, V.; Grunenberg, L.; Dayan, C. B.; Sitti, M.; Podjaski, F.; Ochsenfeld, C.; Lotsch, B. V. Interfacial Engineering for Improved Photocatalysis in a Charge Storing 2D Carbon Nitride: Melamine Functionalized Poly(heptazine imide). *Adv. Energy Mater.* **2021**, *11*, 2003016. DOI: 10.1002/aenm.202003016.

(6) Suihkonen, S.; Pimputkar, S.; Sintonen, S.; Tuomisto, F. Defects in Single Crystalline Ammonothermal Gallium Nitride. *Adv. Electron. Mater.* **2017**, *3* (6), 1600496. DOI: 10.1002/aelm.201600496.

(7) Lotsch, B. V.; Döblinger, M.; Sehnert, J.; Seyfarth, L.; Senker, J.; Oeckler, O.; Schnick, W. Unmasking Melon by a Complementary Approach Employing Electron Diffraction, Solid-State NMR Spectroscopy, and Theoretical Calculations—Structural Characterization of a Carbon Nitride Polymer. *Chem. Eur. J.* **2007**, *13* (17), 4969–4980. DOI: 10.1002/chem.200601759.

(8) Kessler, F. K.; Burow, A. M.; Savasci, G.; Rosenthal, T.; Schultz, P.; Wirnhier, E.; Oeckler, O.; Ochsenfeld, C.; Schnick, W. Structure Elucidation of a Melam-Melem Adduct by a Combined Approach of Synchrotron X-ray Diffraction and DFT Calculations. *Chem. Eur. J.* **2019**, *25*, 8415. DOI: 10.1002/chem.201901391.

(9) Calik, M.; Sick, T.; Dogru, M.; Döblinger, M.; Datz, S.; Budde, H.; Hartschuh, A.; Auras, F.; Bein, T. From Highly Crystalline to Outer Surface-Functionalized Covalent Organic Frameworks—A Modulation Approach. *J. Am. Chem. Soc.* **2016**, *138* (4), 1234–1239. DOI: 10.1021/jacs.5b10708.

(10) Forgan, R. S. Modulated self-assembly of metal–organic frameworks. *Chem. Sci.* **2020**, *11* (18), 4546–4562. DOI: 10.1039/D0SC01356K.

(11) Hermes, S.; Witte, T.; Hikov, T.; Zacher, D.; Bahnmüller, S.; Langstein, G.; Huber, K.; Fischer, R. A. Trapping Metal-Organic Framework Nanocrystals: An in-Situ Time-Resolved Light Scattering Study on the Crystal Growth of MOF-5 in Solution. *J. Am. Chem. Soc.* **2007**, *129* (17), 5324–5325. DOI: 10.1021/ja068835i.

(12) Ma, T.; Kapustin, E. A.; Yin, S. X.; Liang, L.; Zhou, Z.; Niu, J.; Li, L.-H.; Wang, Y.; Su, J.; Li, J.; Wang, X.; Wang, W. D.; Wang, W.; Sun, J.; Yaghi, O. M. Single-crystal x-ray diffraction structures of covalent organic frameworks. *Science* **2018**, *361* (6397), 48–52. DOI: 10.1126/science.aat7679.

(13) Arazoe, H.; Miyajima, D.; Akaike, K.; Araoka, F.; Sato, E.; Hikima, T.; Kawamoto, M.; Aida, T. An autonomous actuator driven by fluctuations in ambient humidity. *Nat. Mater.* **2016**, *15* (10), 1084–1089. DOI: 10.1038/nmat4693.

(14) Takanabe, K. Photocatalytic Water Splitting: Quantitative Approaches toward Photocatalyst by Design. *ACS Catal.* **2017**, *7* (11), 8006–8022. DOI: 10.1021/acscatal.7b02662.

(15) Lau, V. W.-h.; Klose, D.; Kasap, H.; Podjaski, F.; Pignié, M.-C.; Reisner, E.; Jeschke, G.; Lotsch, B. V. Dark Photocatalysis: Storage of Solar Energy in Carbon Nitride for Time-Delayed Hydrogen Generation. *Angew. Chem. Int. Ed.* **2017**, *56* (2), 510–514. DOI: 10.1002/anie.201608553.

(16) Savateev, A.; Pronkin, S.; Willinger, M. G.; Antonietti, M.; Dontsova, D. Towards Organic Zeolites and Inclusion Catalysts: Heptazine Imide Salts Can Exchange Metal Cations in the Solid State. *Chem. Asian J.* **2017**, *15*, 783. DOI: 10.1002/asia.201700209.

(17) Yang, H.; Lin, Q.; Zhang, C.; Yu, X.; Cheng, Z.; Li, G.; Hu, Q.; Ren, X.; Zhang, Q.; Liu, J.; He, C. Carbon dioxide electroreduction on single-atom nickel decorated carbon membranes with industry compatible current densities. *Nat. Commun.* **2020**, *11* (1), 593. DOI: 10.1038/s41467-020-14402-0.

(18) Sun, M.-J.; Gong, Z.-W.; Yi, J.-D.; Zhang, T.; Chen, X.; Cao, R. A highly efficient diatomic nickel electrocatalyst for CO_2 reduction. *Chem. Commun.* **2020**, *56* (62), 8798–8801. DOI: 10.1039/D0CC03410J.

6 Appendix A

Note: This appendix is published as the Supporting Information to reference https://pubs.acs.org/doi/10.1021/acs.chemmater.9b02199.

6.1 Experimental details

Melon:

Dicyandiamide (Sigma-Aldrich 99 %) was ground in a mortar and transferred into an open crucible which was heated in a muffle furnace (10 °C/min, 550 °C, 4 h, slow cooling to ambient temperature). The resulting pale, yellow solid was ground and washed four times with DI water.

Potassium Melonate:

Melon and potassium thiocyanate (Gruessing 99 %) were thoroughly ground in a mortar and transferred into a crucible covered with a lid which was placed in a preheated muffle furnace (550 °C, 4 h, slow cooling to ambient temperature). The resulting bright yellow solid was washed three times with DI water. The volume of the combined transparent filtrate was then reduced by rotary evaporation and potassium melonate penta-hydrate precipitated overnight. Filtration yielded a colorless needle shaped compound which was recrystallized from a mixture of water/acetone.

Crystalline ampoule synthesis of potassium poly(heptazine imide) (K-PHI):

Dicyandiamide (97 mg, 1.14 mmol, Sigma-Aldrich >98%), KSCN (18 mg, 0.19 mmol, Gruessing 99%) and potassium melonate penta-hydrate (79 mg, 0.16 mmol) were ground in a mortar and transferred into a Duran glas ampoule, which was subsequently purged four times with argon and then dried under high-vacuum. The ampoule was then sealed and placed into a tube furnace (6 °C/min, 500 °C, 6 h, 1 °C/min, rt). The bright yellow solid was washed four times with DI water and then dried at 60 °C.

Crystalline ampoule synthesis of protonated poly(heptazine) imide (H-PHI):

Finely ground cryst. K-PHI (100 mg) was treated with 100 mL of 2 M HCl and stirred for 15 min. The suspension was filtered and the residue washed four times with DI water to yield H-PHI.

Optimized crucible synthesis of potassium poly(heptazine imide):

KSCN was heated over night at 140 °C in vacuum to remove water. Melon (1.5 g) and potassium thiocyanate (3 g, 30.8 mmol, Carl Roth 99%) were thoroughly ground in a mortar and transferred into an Al_2O_3 crucible which was placed in a tube furnace. The sample was heated in Ar-flow at 400 °C for 1 h with a heating rate of 30 K/min and to 500 °C for 30 min with the same heating rate. After cooling to room temperature the material was washed with DI water six times by centrifugation. The resulting yellow solid was dried at 60 °C in vacuum overnight.

Optimized crucible synthesis of protonated poly(heptazine imide):

K-PHI (0.5 g) was stirred in 1 M HCl (100 mL) overnight at room temperature. The material was washed with DI water six times by centrifugation until the supernatant was neutral. The resulting yellow solid was dried at 60 °C in vacuum overnight.

Photocatalytic experiments

In a typical photocatalytic experiment 14-20 mg (note that rates (µmol/gh) were normalized according to the used amount of catalyst) carbon nitride material, 9 mL DI water, 10 vol% of methanol as sacrificial donor and 10 µL of dihydrogen hexachloroplatinate which forms the platinum co-catalyst *in-situ* were transferred into a glass reactor with a quartz window. The optimized platinum loading of each sample can be extracted from literature (8 wt% for K-PHI and 2 wt% for H-PHI).[1,2] The suspension (20 mL total volume) was stirred and sonicated prior to illumination. Additionally, the headspace was evacuated and backfilled with argon several times. A 300 Xenon arc-lamp (Newport, 300 W) equipped with a 1.5 Global AM filter illuminated the suspension with 100 mW/cm^2 and from the headspace samples were periodically taken and quantified by gas-chromatography (Thermo Scientific TRACE GC Ultra) equipped with a TCD detector using argon as the carrier gas. The reaction was thermostated at 25 °C during illumination as in previous works.[1,2]

Dark photocatalysis experiments

Prior to dark photocatalysis experiments the glass vessels were cleaned with *aqua regia*, to avoid contaminations of platinum of previous runs. 15 mg of optimized H-PHI was suspended in 20 mL 1 M sodium phosphate buffer (containing sodium hydrogen phosphate and sodium dihydrogen phosphate only) at a pH of 7. 4-Methylbenzyl alcohol (4-MBA) (35 mg) was added as a sacrificial donor and the headspace was evacuated and flooded with argon several times. The suspension was illuminated with a 300 Xenon arc-lamp (Newport, 300 W) equipped with an 1.5 Global AM filter illuminated the suspension with an intensity of 100 mW/cm^2 for 2 h. After illumination 50 µL Pt nanoparticle suspension (1000 ppm aqueous colloidal solution, Aldrich) was injected into the reactor by using a gas tight needle to start the hydrogen evolution reaction. This injection was delayed by 0, 2, 4, and 6 h after illumination had stopped. During the periods of darkness the reaction vessel was wrapped in aluminum foil to avoid stray light.[3]

6.2 Instrumental details

Solid state ^{13}C and ^{15}N magic angle spinning (MAS) NMR experiments (main text Figure 2 a, b and d, e) were performed on a Bruker Avance-III 400 MHz instrument at the frequencies of 400, 100.61 and 40.53 MHz, respectively (B_0 = 9.4 T). All ^{1}H and ^{13}C spectra are referenced indirectly with respect to tetramethylsilane (TMS) using adamantane as secondary reference and the ^{14}N and ^{15}N to nitromethane using glycine and/or NH_4Cl as a secondary reference. MAS frequencies were between 6.5-14.0 kHz in a 4 mm ZrO_2 rotor.

The 2D ^{13}C-^{15}N HETCOR spectra (main text Figure 2 g) was recorded on a Bruker Avance III 400 DNP spectrometer equipped with an Ascend 400 DNP magnet system and a low temperature 3.2 mm triple-resonance probe. DNP-enhanced spectra were measured with microwave irradiation. The DNP-enhanced spectrum was recorded at a field of 9.4 T corresponding to frequencies of 400.03 MHz for ^{1}H, 100.60 MHz for ^{13}C, and 40.54 MHz for ^{15}N, at nominally 110 K and at a spinning rate of 8.0 kHz. For DNP, approximately 25 mg of the sample was mixed with 15 µl of a 15 mM AMUPol in glycerol-d8/D2O/H2O (60:30:10, *v/v/v*) solution. This resulted in DNP enhancement of about 70. The HETCOR was performed using a double CP experiment. First, the ^{1}H magnetization was transferred to ^{13}C after a CP contact time of 8 ms (ramped cross-polarization experiment, where the nutation frequency ν_{nut} on the proton channel was varied linearly by 50%). Second, after a t1 evolution time, a ramped CP from ^{13}C to ^{15}N (ramp of 70% on ^{15}N) with a contact time of 1 ms was employed to transfer the magnetization to ^{15}N and with simultaneously strong continuous wave ^{1}H decoupling (105 kHz). Finally, ^{1}H decoupling was applied using a spinal-64 sequence with a radio-frequency field of 80 kHz during t1 and t2 acquisition times.

Additional ^{1}H one-pulse MAS, ^{13}C CP MAS, ^{1}H-^{14}N *D*-HMQC MAS and ^{1}H-^{1}H DQ-SQ MAS experiments were acquired on a Bruker Avance III HD spectrometer operating at a B_0 field of 14.1 T. High-speed MAS ^{1}H (600.15 MHz) one-pulse spectra were recorded after a 90° pulse of 1.2 µs at a spinning frequency of 62.5 kHz using a Bruker 1.3 mm double-resonance MAS probe. ^{13}C (150.91 MHz) CP experiments were acquired at a spinning rate of 62.5 kHz with a contact time of 3 ms and a ^{1}H Spinal-64 decoupling of 25 kHz during acquisition. ^{1}H-^{14}N *D*-HMQC experiment was performed at a spinning speed of 40.0 kHz using a triple-resonance 1.9 mm probe (^{14}N at 43.35 MHz). The super-cycled symmetry based $SR4_1^2$ sequence[4] was used for the ^{1}H-^{14}N dipolar recoupling which lasted 200 µs. For the ^{1}H-^{1}H DQ-SQ experiments the sample were spun at 62.5 kHz (1.3 mm rotors). The DQ excitation and reconversion was executed using the $R12_2^5$ symmetry based recoupling.[5]

The ^{13}C and ^{15}N direct excitation Figure A 11 were acquired on a Bruker Avance III HD spectrometer operating at a B_0 field of 9.4 T using a double-resonance 4 mm Bruker MAS probe and rotation frequencies of 12.5 kHz and 10.0 kHz, respectively. The ^{13}C (100.61 MHz) and ^{15}N (40.56 MHz) Bloch-decay experiments were performed using respective 90° pulses of 3.5 and 4.8 µs, and recycle delays of 600 s and 900 s. Acquisition was accompanied by high power proton decoupling using a spinal-64 sequence with a radio-frequency field of 70 kHz.

Laboratory X-ray powder diffraction (XRPD) patterns of H-PHI and K-PHI were collected using a STOE Stadi P diffractometer with CuKα1 radiation (λ = 1.540598 Å) equipped with a MYTHEN 1 K detector (Dectris Ltd.) and a curved Ge(111) monochromator.

X-ray total scattering measurements were performed on a separate set of samples using beamline 28-ID-2 (XPD) of the National Synchrotron Light Source II (NSLS-II) at Brookhaven National Laboratory. Powders were loaded into 1 mm ID Kapton capillaries and measured in rapid acquisition PDF mode[6] with an x-ray energy of 68.01 keV (λ = 0.1823 Å) using a Perkin-Elmer 2D detector (2048 x 2048 pixels and 200 x 200 μm pixel size) mounted orthogonal to the incident beam path with a sample-to-detector distance of 205.6443 mm for data collected to a high maximum value of momentum transfer $Q_{\max}$ (where $Q=4\pi\sin\theta/\lambda$ for elastic scattering) and 1421.219 mm for data with higher Q resolution. Calibration of the detector geometry was carried out using a standard Ni sample.

Additional total scattering measurements were performed at beamline ID31 at the ESRF using an incident energy of 68.54 keV (λ =0.1809 Å), sample-to-detector distance of 273.38 mm, DECTRIS Eiger2X 16M single photon counting detector, and calibration using NIST CeO2 674b.

Force field minimizations and dynamics were performed using the Amber16 program package.[7] Periodic boundary conditions and particle mesh Ewald summation (PME) with a cutoff value of 12 Å were employed. A single potassium ion placed in a solvent box of water was minimized using the conjugate gradient algorithm in 10000 steps. The system was then heated to 300 K in 30 picoseconds and equilibrated subsequently for 30 nanoseconds with time steps of 2 femtoseconds employing the SETTLE algorithm. Molecular dynamics calculations were performed using the NAMD program package.[8]

Diffuse reflectance UV-Vis spectra were collected on a Cary 5000 spectrometer referenced to PTFE or barium sulfate as reference.

Infrared (IR) spectra were recorded on a JASCO Fourier transform infrared spectrometer equipped with a diamond attenuated total reflectance (ATR) unit and a resolution of 4 cm^{-1}.

Transmission electron microscope: Powders, ground and suspended in butanol, were distributed onto a holey carbon/copper grid and studied with a Philips CM 30 ST microscope (300 kV, LaB6 cathode). Images were taken with a TVIPS TemCam-F216 CMOS Camera. Simulations of the selected area electron diffraction patterns were obtained with the JEMS software package.[9]

Thermogravimetric (TG) analyses were performed at using a STA 449 F5-Jupiter (Netzsch) device. The sample was heated up in a corundum crucible in a dynamic argon (50 mL/ min) atmosphere to 300, 350 or 400 °C with a heating rate of 10 K min^{-1}, respectively. An empty corundum crucible was used as a reference. Corrections of instrumental effects and the buoyancy were performed with Al_2O_3 as an inert reference material during a separate measurement.

Combustion analysis for detection of C, H, N, S was performed on a Elementar Analysensysteme GmbH – Vario micro elemental analyzer.

Inductively coupled plasma atomic emission spectroscopy (ICP-AES) data was obtained from a Varian Vista RL CCD simultaneous ICP-ACS device. The sample was dissolved in concentrated HNO_3 in the microwave oven at 150 °C, before injecting into the plasma.

Electron paramagnetic resonance (EPR) spectra were measured on a Bruker EMXnano X-band device operating at an excitation frequency of ~9.6 GHz and 100 mW microwave power.

Water sorption measurements were performed on a Autosorb-iQ surface analyzer with vapor option (Quantachrome Instruments, USA). To initially remove guest molecules the samples were outgassed in vacuum at 200 °C for 12 h. The measurements were performed at 273 K.

The Raman spectra were taken with a Jobin Yvon Typ V 010 labram single grating spectrometer equipped with a double super razor edge filter and a peltier cooled CCD camera. The spectra were recorded in quasi-backscattering geometry using the linearly polarized light of a 632.8 nm He/Ne Laser and a 532.0 nm diode laser, respectively with powers of approx. 1 mW. The beam was focused to a 2-5 µm spot through the 100 x objective of an microscope onto the sample within a glass capillary.

6.3 Transmission electron microscopy (TEM)

H-PHI:

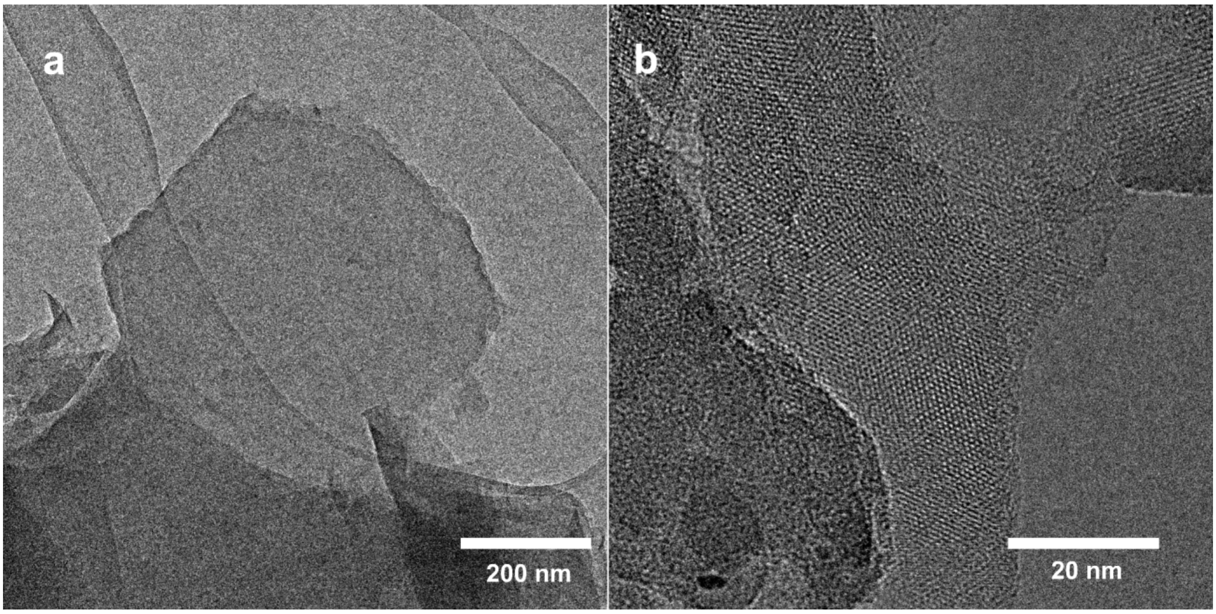

Figure A 1. (a) TEM overview image of H-PHI revealing the sheet-like morphology, (b) high-resolution TEM image of the same sample.

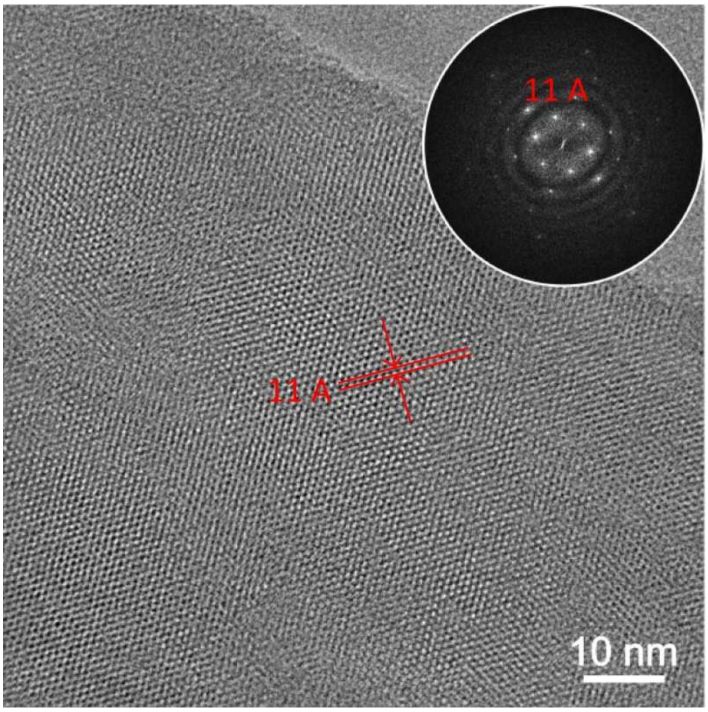

Figure A 2. HR-TEM image (Average Background Subtraction Filtered) of highly crystalline H-PHI, lattice planes could be determined at 11 Å in accordance with XRD results (picture in the main text is zoomed into the upper right part to enhance visibility of the lattice fringes). A clear hexagonal pattern is observable in the FFT, however weak powder rings indicate the presence of polycrystalline material.

K-PHI:

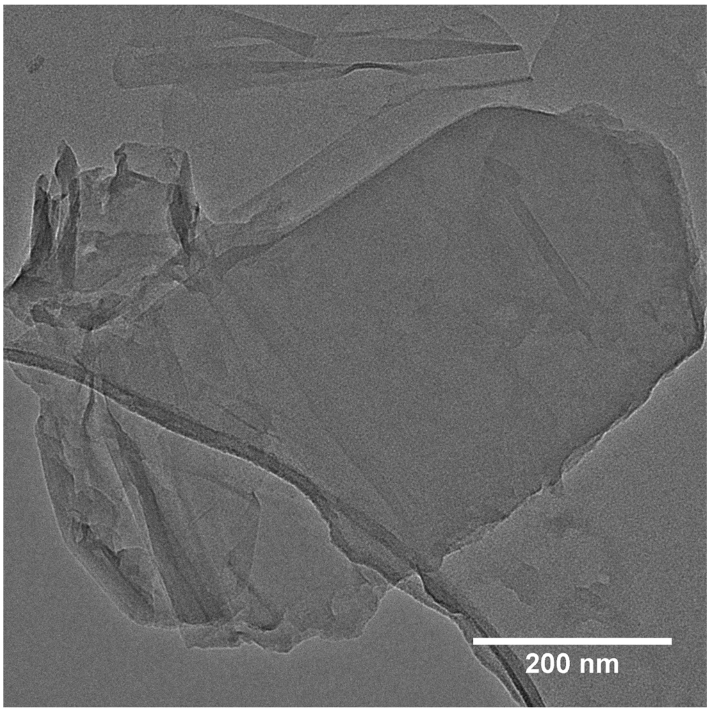

Figure A 3. TEM overview image of K-PHI revealing the sheet-like morphology and large lateral extension of the sheets. Large thin flakes exhibit wrinkles.

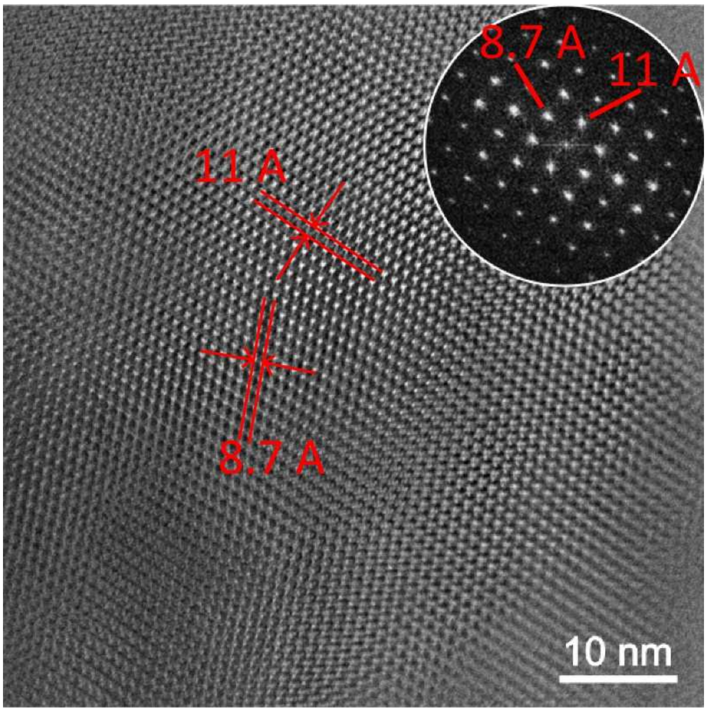

Figure A 4. HR-TEM image (Average Background Subtraction Filtered) of highly crystalline K-PHI, lattice planes could be determined at 11.1 Å and 8.7 Å in accordance with XRD results (picture in the main text is zoomed into upper right part to enhance visibility of the lattice fringes). The clean FFT in the inset suggests a single crystalline sheet.

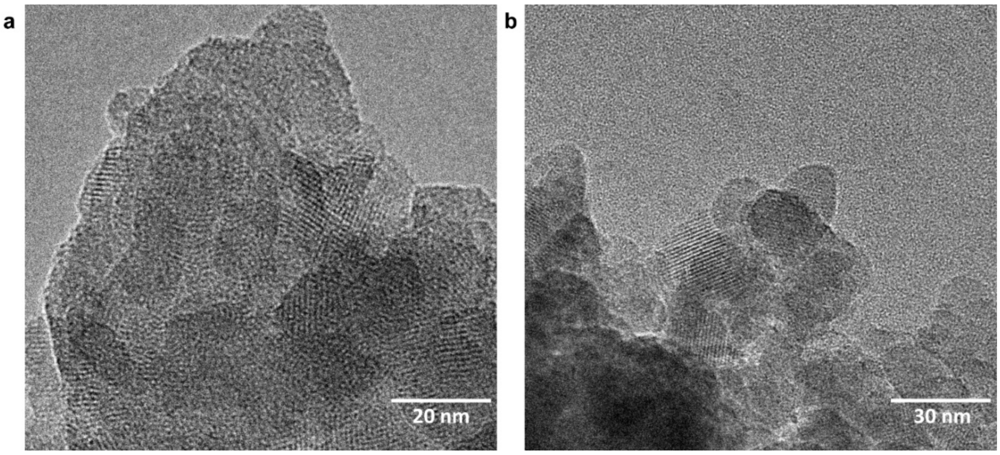

Figure A 5. In comparison to the crystalline sheets (e.g. in Figure A 3): two (a and b) TEM micrographs of an optimized K-PHI sample revealing much smaller crystallite sizes in the range of 20-30 nm. Please also see crystallite size estimation in Table A 1, section 5.

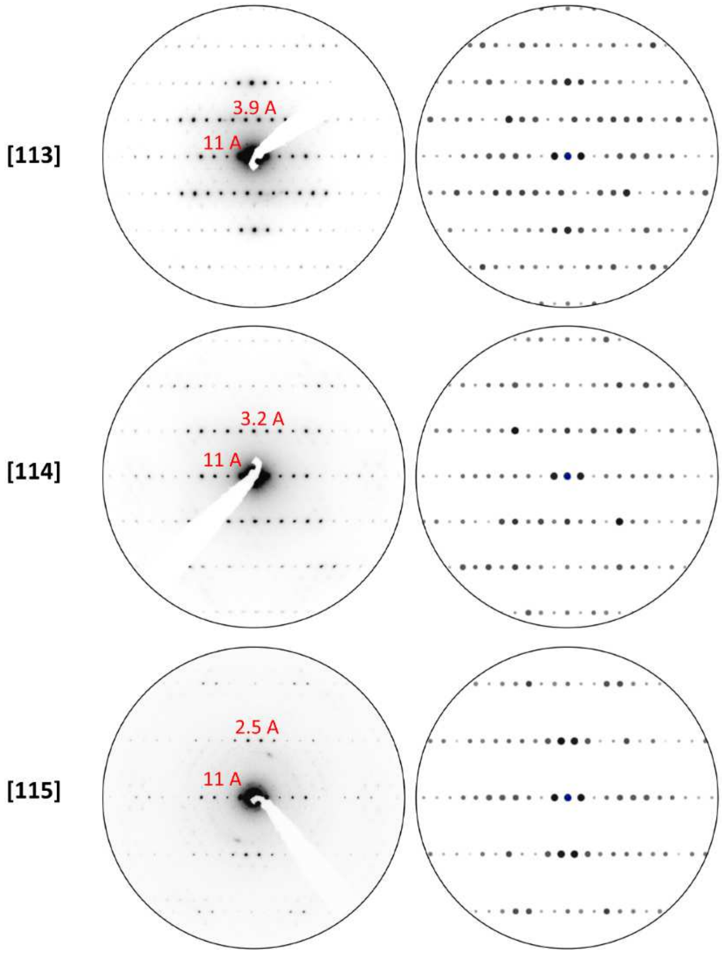

Figure A 6. (a. c, f) Experimental SAED patterns of ampoule-synthesized cryst. K-PHI and (b, d, f) ED-simulation from Rietveld refined model for zone axis [113], [114] and [115], respectively. The reasonable agreement for experimental and simulated patterns is rare for carbon nitrides. In some cases it was even possible to obtain the ED of multiple zone axes by tilting of the specimen. Usually carbon nitrides crystallites are prone to electron beam damage and amorphization upon too long exposures in the electron beam.

Tilting series of H-PHI:

Interestingly, the observed hexagonal diffraction pattern for H-PHI (Figure 2.1, main text) is relatively insensitive to the tilting angle of the specimen for up to ±10°. This "robustness" is not found in K-PHI where the crystallites need to be correctly aligned to obtain the pattern seen in Figure 1 f, main text). This effect may be influenced by several factors: Slightly distorted stacking distances in H-PHI can cause the reciprocal lattice points to elongate thus satisfying the Laue condition in a range of orientations of the TEM grid. This points towards a lesser degree of order in the H-PHI crystals. Additionally, buckling of very thin layers can also cause such a behavior as observed for 2D materials such as graphene or MoS_2.[10,11]

6.4 Fourier-transform infrared spectrum

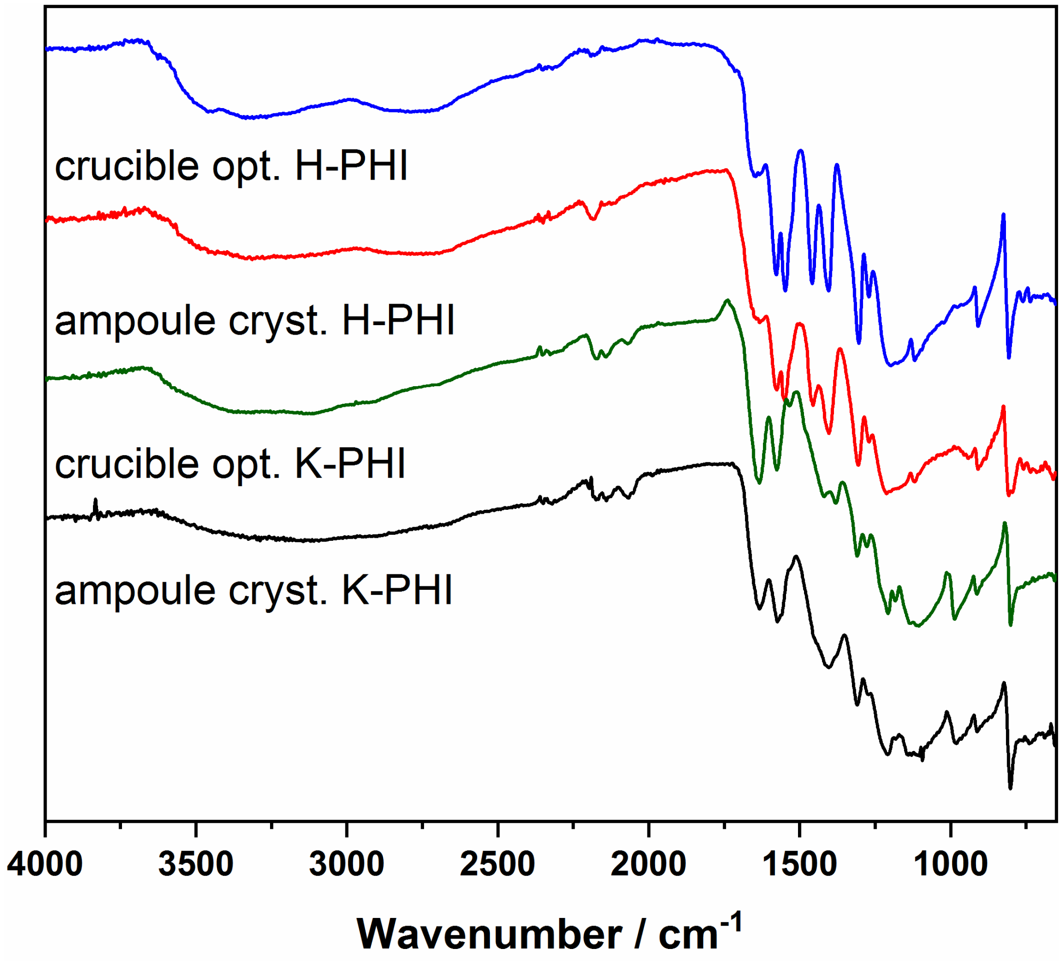

Figure A 7. FT-IR spectra of K/H-PHI from ampoule synthesis (crystalline) and optimized synthesis in a crucible. In terms of absorption bands the respective ampoule and crucible species do not differ significantly except for slightly higher water content (from elemental analysis) in the open crucible case, which causes higher intensity in the OH and hydrogen bond regime.

6.5 X-ray powder diffraction and size estimations

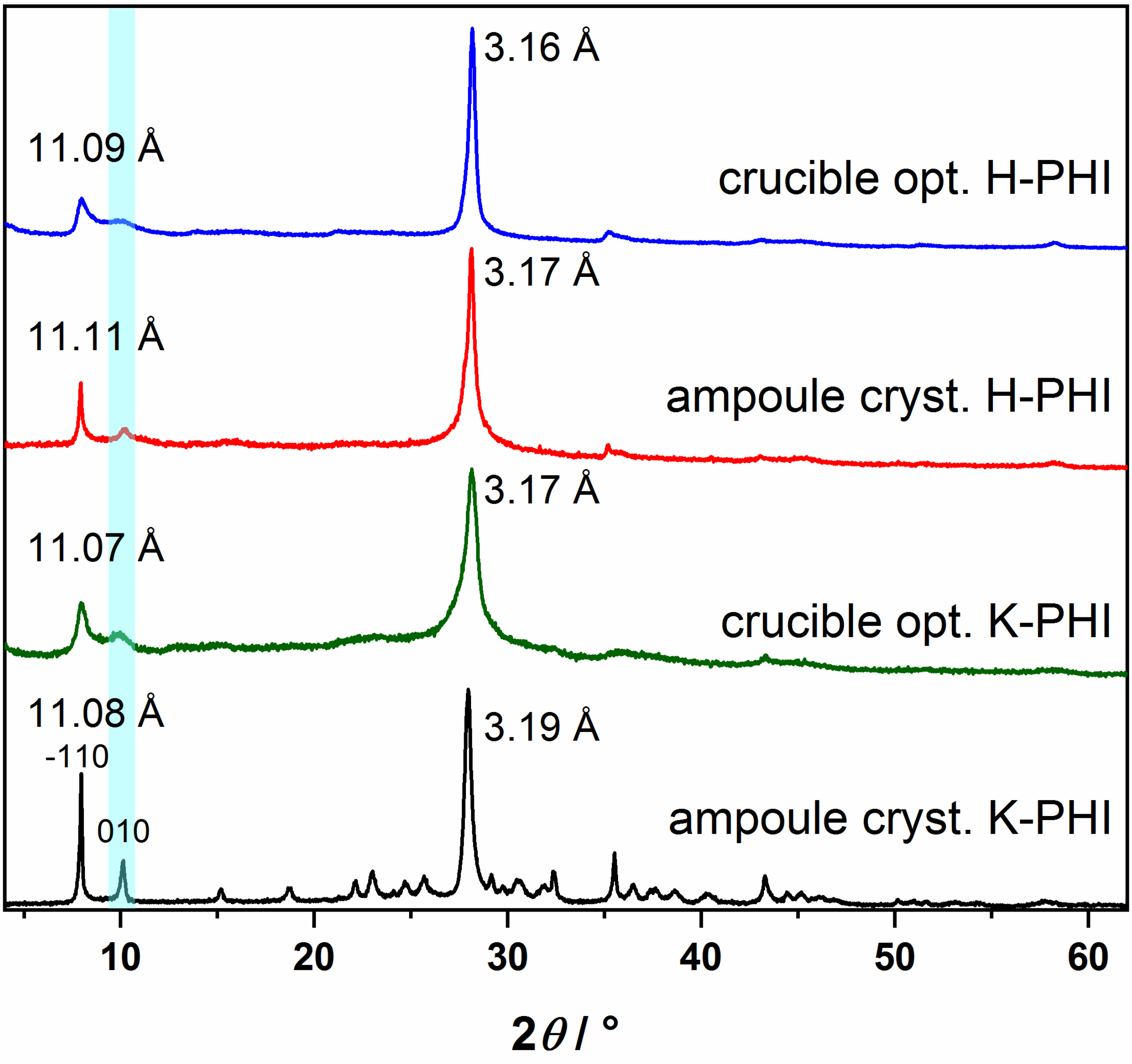

Figure A 8. XRPD of optimized crucible and ampoule synthesized K-PHI and H-PHI, respectively. Cyan marked area highlights the 010 reflection which is broadened in the optimized samples and in H-PHI.

Determination of crystallite size from XRPD:

The lateral and vertical sizes of the crystalline and optimized PHI-materials were determined from the powder patterns presented in Figure A 8 by using the Scherrer-equation[12]:

$$\tau = \frac{K\cdot\lambda}{\beta\cdot cos\theta}$$

where τ is the mean size of the ordered domains, K a dimensionless shape factor, λ is the wavelength of the diffractometer, β is the diffraction line broadening and θ is the Bragg angle. The instrumental profile was determined by refining the instrumental function, described by the fundamental parameter[13,14] approach using a diffraction pattern of the Si640D NIST standard and subtracted from the diffraction line profile. The lateral crystallite size was determined by a single line fit in a 2θ range of 6.0 to 12.5° of the $\bar{1}10$ reflection using the TOPAS[15] software. As the $\bar{1}10$ reflection overlaps with the anisotropically broadened 010 reflection a 2nd peak was included into the refinement and independently refined. The background was modeled with Chebychev polynomials of 2nd order. For the estimation of the vertical crystallite size a single line fit of the 001 reflection in a 2θ range of 26.5 to 29.5° was performed.

The estimated crystallite sizes of the crystalline and optimized PHI samples are presented in Table A 1. Due to the complex background of the diffraction patterns, that is governed by diffuse scattering and due to the overlap with anisotropically broadened reflections, a vastly increased analytical error (≈ 10 %) is given, that is far larger than the analytical error which is to be expected for a crystallite size determination using a high-resolution laboratory X-ray powder diffractometer (≈ 1-2 %). Despite the large analytical error it can be clearly seen that the crucible optimization procedure leads to a significantly smaller lateral crystallite size of both K- and H-PHI (Table A 1), whereas the vertical crystallite size is almost not affected. Hence, the crucible optimization leads to a decrease of the extension of the 2-dimensional layers, i.e. lateral crystallite size but the number of layers in a crystallite, i.e. vertical crystallite size remains the same.

Table A 1. Estimation of the lateral and the vertical crystallite sizes of ampoule crystalline and crucible optimized K- and H-PHI.

Sample	lateral size / nm	vertical size / nm
ampoule cryst. K-PHI	102 ± 10	25 ± 3
crucible opt. K-PHI	19 ± 2	19 ± 2
ampoule cryst. H-PHI	48 ± 5	18 ± 2
crucible opt. H-PHI	17 ± 2	23 ± 2

Effect of crystallite sizes on cyanamide groups and defects:

Depending on the batch, we observe one NCN group per 2-5 heptazine units as retrieved from quantitative (i.e. direct excitation) ^{13}C-ssNMR spectroscopy. However, this value is slightly higher than can be explained just by terminating cynamide at the edges of the sheets, given the lateral sizes found via PXRD analysis (see Table A 1). In order to account for the higher NCN content, especially for larger crystallites, defects in the form of missing heptazine building blocks may be present, which in turn increase the NCN terminations within the sheet. Note that in this context a point defect is defined as a missing heptazine unit. Hence, after removal of a heptazine unit, three additional NCN moieties are introduced into the PHI sheet. As the sheets are also terminated with NCN at the perimeter, the sheet size also influences the overall amount of NCN. A theoretical estimation of the level of these defects is made in Figure A 9 for a 100 nm and 20 nm sheet according to the values in Table A 1. For each size (100 nm or 20 nm) of the rectangular sheet the following boundary conditions are used for the mathematical function that yields the curves in Figure A 9:

<u>100 nm K-PHI rectangular sheet:</u>

- 100 nm is the diagonal of the model sheet, the distance from pore to pore is 12.8 Å
- The sheet consists of ~**7308 heptazine units** (before introduction of internal point defects)
- The sheet is terminated by ~**280 NCN** groups at edge sites (perimeter)
- Heptazine/NCN group = 26.1

<u>20 nm K-PHI rectangular sheet:</u>

- 20 nm is the diagonal of the model sheet, the distance from pore to pore is 12.8 Å
- The sheet consists of ~**420 heptazine units** (before introduction of internal point defects)
- The sheet is terminated by ~**74 NCN** groups at edge sites (perimeter)
- Heptazine/NCN group = 5.7

From the two examples above it is visible that the 20 nm sheet (without any defects) intrinsically contains more NCN groups per heptazine due to its larger perimeter to diagonal ratio. However, in the real samples the amount of cyanamide was found to be larger in the large crystallites. Therefore, point defects are introduced into the sheets, as described, above to yield a higher amount of cyanamide and to match the experimental NCN content for the respective sample.

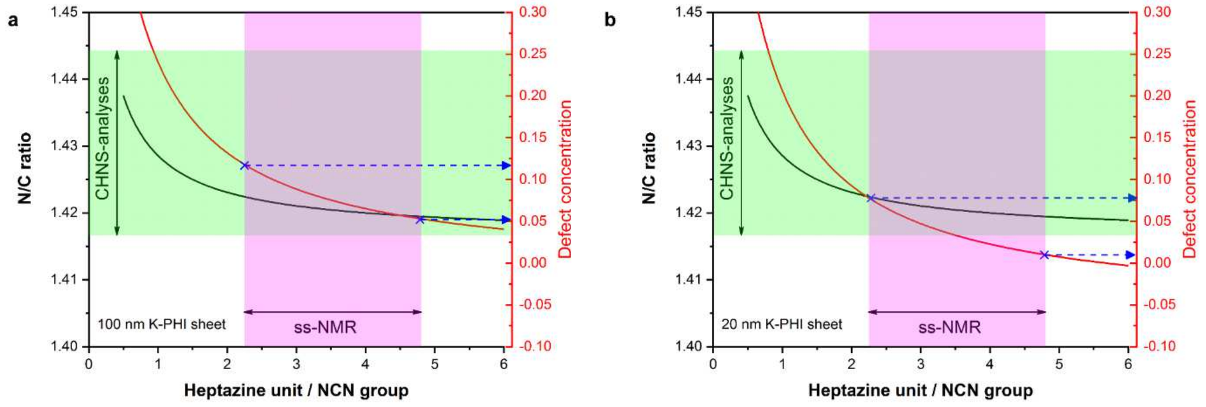

Figure A 9. Mathematical function of the N/C ratio (black line) and defect concentration (red line) for a 100 nm (left) and 20 nm (right) K-PHI sheet as a function of the heptazine unit/NCN ratio. The defect concentration is the ratio of the heptazine vacancies to the amount of heptazine units in the defectless sheet. The calculation of the defect concentration is taking the terminating NCN groups at edges into account. The extension of the green and magenta areas presents the batch to batch variation observed for synthesis of K-PHI. The green area represents values obtained from combustion analysis while the magenta area represents the integrated intensities of ^{13}C-ssNMR measurements (heptazine/cyanamide intensity) in different batches. The dashed blue lines show the minimal and maximal defect concentration based on the experimentally found range of heptazine/NCN group, respectively.

In Figure A 9a, the resulting defect concentration and the N/C ratio is theoretically calculated as a function of the ratio of heptazine units per NCN group for a 100 nm K-PHI sheet. The starting values for the calculations are the sheets without any defects as given in the boundary conditions above. As more and more heptazine units are replaced by NCN groups, the defect concentration is increased and also the N/C ratio is affected (going from right to left on the abscissa). The green area represents the experimentally observed distribution of the N/C ratio which is a relatively large span due to batch to batch variations and the uncertainty of the method. The magenta area represents the values for the heptazine/NCN-group ratio obtained from the integrated intensities of the direct ^{13}C-ssNMR spectroscopy. According to the 100 nm model, for a ratio on the abscissa of one NCN group in roughly every 2nd to 5th heptazine units, the concentration of point defects would have to range from 5-12%. This would mean that in a 100 nm sheet every 8th to 20th heptazine unit is missing and replaced by three internal NCN groups.

The N/C ratio for these x-values would range from 1.420-1.422 which correlates quite well with the measured N/C ratio of 1.416 for the batch whose data is presented in Figure A 8. Note that the N/C ratio should be taken with a grain of salt as there is significant variance in the combustion analyses even for the same batch, which does not allow for an exact determination of the experimental N/C ratio.

For the crucible optimized K-PHI sample (compare Table A 1) the lateral sheet size is approx. 20 nm (Figure A **9**b) and therefore the defect concentration (i.e. missing heptazine units) ranges from 1-9% for the same range of x-values (approx. 2 to 5). This shows that in order to yield the same experimental heptazine/NCN group ratio smaller crystallites have less point defects. This is related to the fact that the heptazine/edge NCN-terminations ratio (compare to the boundary conditions) is higher for those sheets. Although having less point defects, these crystallites are very small and therefore yield a significant broadening in the XRPD pattern. The N/C ratio for this span ranges from 1.422-1.419 accordingly, while the experimental value for this batch amounts to 1.422.

Overall the above estimations, implying a higher amount of point defects in the sheets for the larger sheets, yield a possible explanation for why a higher amount of NCN groups in the crystalline samples is observed in NMR spectroscopy. The higher nitrogen content for the crystalline ampoule material could, however, also originate from amorphous pore material which is blocked and cannot be removed during the washing procedure. Another explanation can be the different synthetic approach for the large crystallite samples. For the large crystalline sheets, we have used potassium melonate as a starting material, which intrinsically has NCN-moieties attached, while in the case of the 20 nm sheets, polymeric melon was used as a starting which bears no NCN-moities.

6.6 Electron paramagnetic resonance (EPR)

The g-factors of the paramagnetic compounds were determined with the following formula on a X-band device.

$$g = \frac{h\,v_{MW}}{\mu_B B_{res}}$$

where g is the g-factor, h the Planck constant, v_{MW} the microwave frequency, μ_{B} the Bohr magneton and B_{res} the magnetic field at resonance.

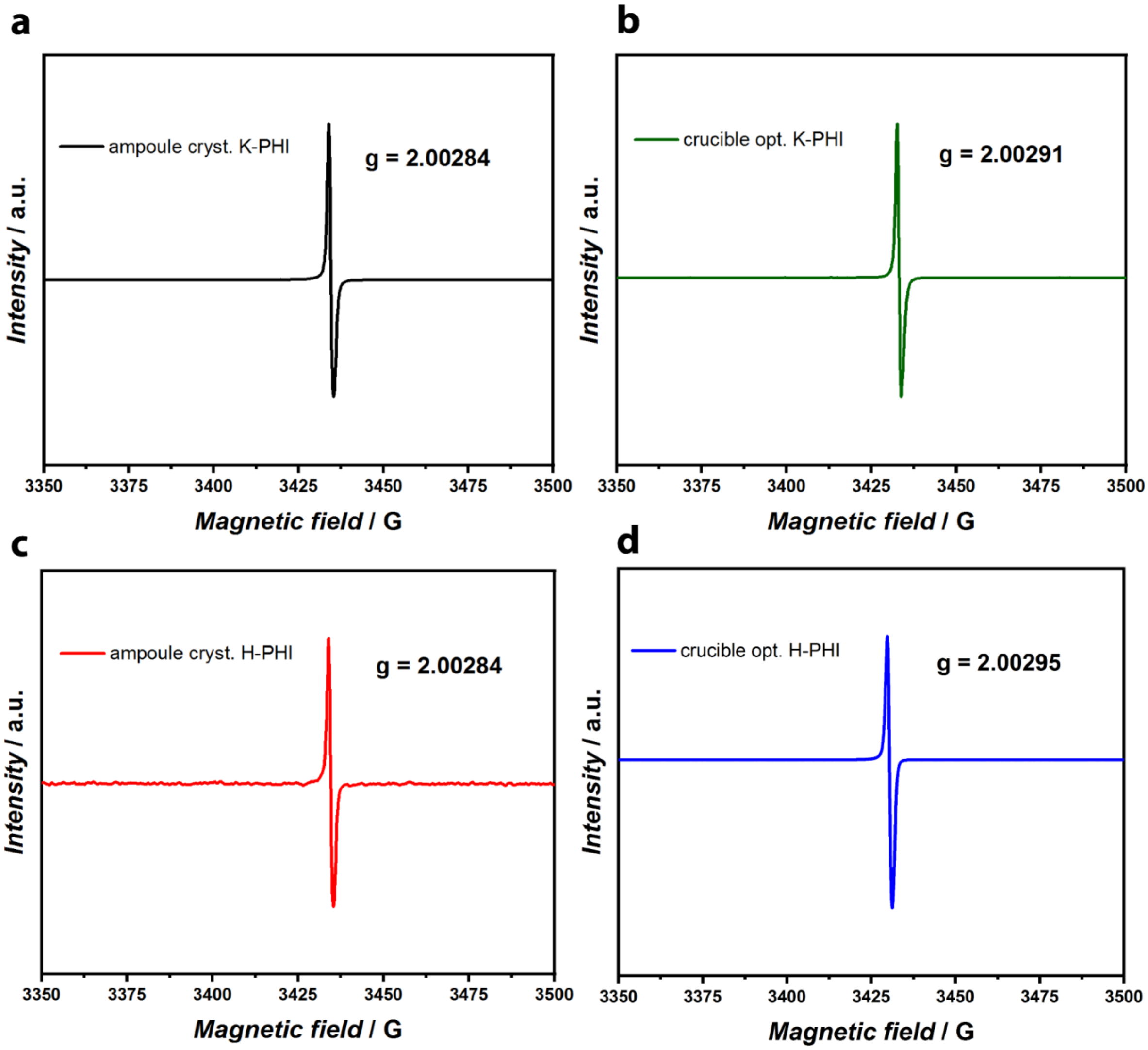

Figure A 10. Electron paramagnetic resonance (EPR) spectra of (a) crystalline (ampoule) and (b) optimized (crucible) K-PHI and (c) crystalline (ampoule) and (d) optimized (crucible) of H-PHI. g-factors values are very similar to the free electron with ca. 2.0028. The samples have been prepared with 4-MBA as an electron donor and flushed with argon. The samples were irradiated with a Xe-lamp (AM 1.5 G filter) prior to the measurement.

6.7 Solid-state nuclear magnetic resonance (ssNMR)

^{13}C and ^{15}N spectra:

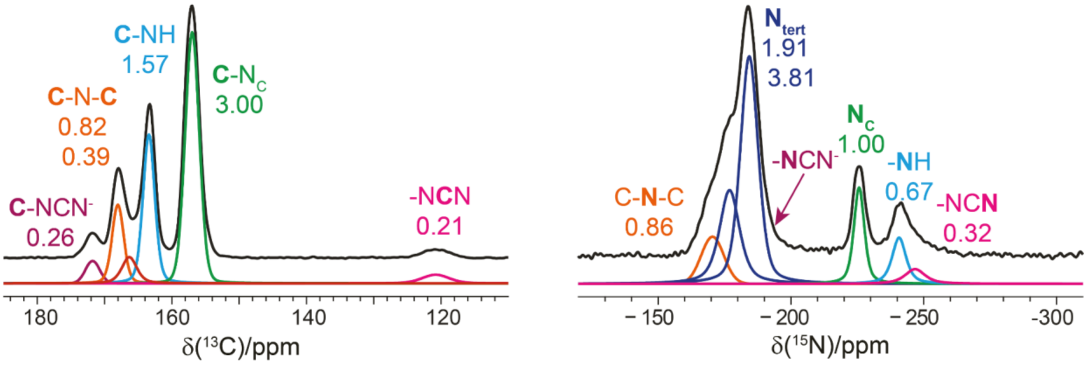

Figure A 11. One-pulse ^{13}C (left) and ^{15}N (right) ssNMR spectra of K-PHI along with their deconvolution. Area for each individual peak is given next to the peaks.

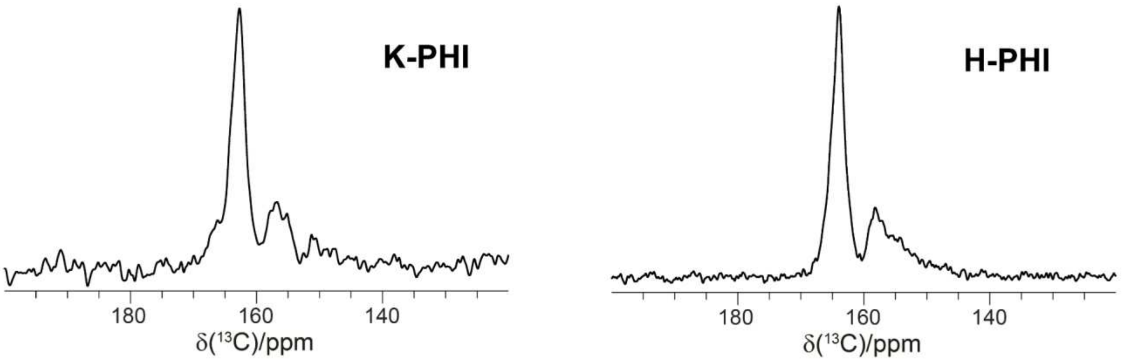

Figure A 12. ^{13}C CP MAS spectra of K-PHI (left) and H-PHI (right) acquired at a MAS of 62.5 kHz.

^{1}H-ssNMR spectra at high spinning frequencies of 62.5 kHz:

Unexpectedly, the range of proton shifts is rather large for only water and the bridging NH-group in the structure. However, this variety may be explained by water/NH-, water/heptazine-, water/water- and water/potassium- interactions within K-PHI and H-PHI. The more acidic character of H-PHI with leads further downfield shifted signals (12.3 ppm in H-PHI), thus an even broader distribution.

Drying the samples at 120 °C in vacuum for two days leads to changes in the peak intensities. On the one hand the loss of water causes the “naked” proton shift (7.0 ppm for K-PHI and 7.3 ppm for

H-PHI) of the imide bridge to emerge more strongly. DFT calculations show that the pore water is responsible for a broader distribution of this signal due to the described interactions named above (compare Figure A 19 and Figure A 20). In the calculated case the imide proton shifts from 7.8 ppm without water to 11.0 ppm with an attached water molecule. On the other hand not all water is removed by the drying step, also indicated by more than one step in the TG-experiments (compare Figure A 26) related to less strongly and strongly bound water, where the latter species are only removed at higher temperatures or in ultra-high vacuum.

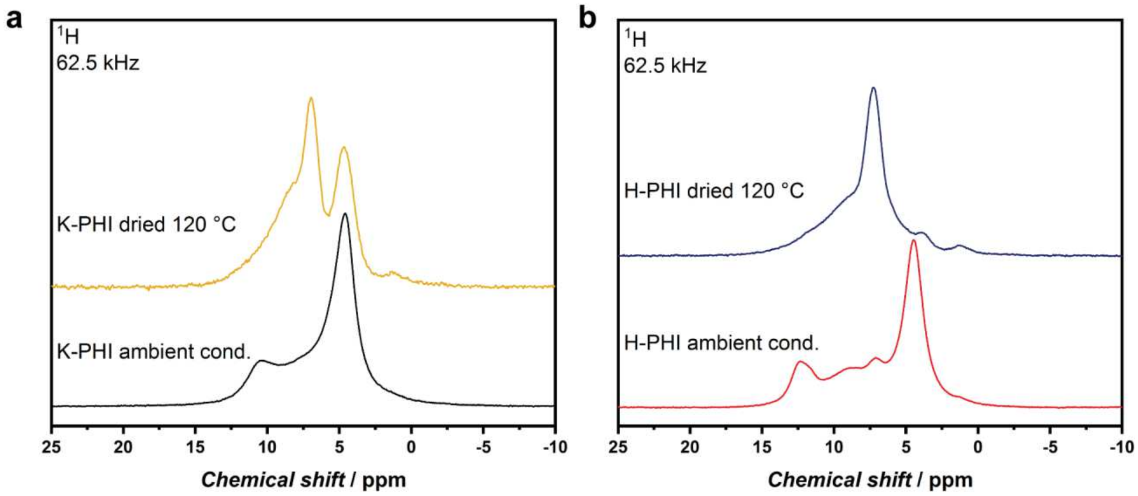

Figure A 13. ^{1}H ssNMR spectra of (a) ampoule cryst. K-PHI dried in vacuum at 120 °C for two days, and at ambient conditions, (b) corresponding spectra for H-PHI. Loss of water detectable by reduced intensity of the water peak at 5 ppm and changed intensities/positions for the NH-group upon drying, likely caused by water/network interactions and a loss thereof in dried state.

In summary, proton ssNMR first of all shows that chemically different water species are present within the pores of the poly(heptazine imide) backbone. The water interaction causes a broad distribution of ^{1}H-signals (at least five for H-PHI). Additionally, (partial) removal of water has a major effect as it changes the position of signals due to a loss of interaction while at the same time the amount of protons in the sample is reduced therefore increasing the difficulty of assignment. Nevertheless, ^{1}H-^{14}N-HMQC SR-4 experiments for the wet (Figure 2.2g, main text) and the dried H-PHI (Figure A 17) sample show that there is predominantly a correlation between a network nitrogen atom and the proton at 12.3 ppm, while the dry sample shows a major contribution from a network nitrogen atom with the proton at 7.3 ppm.

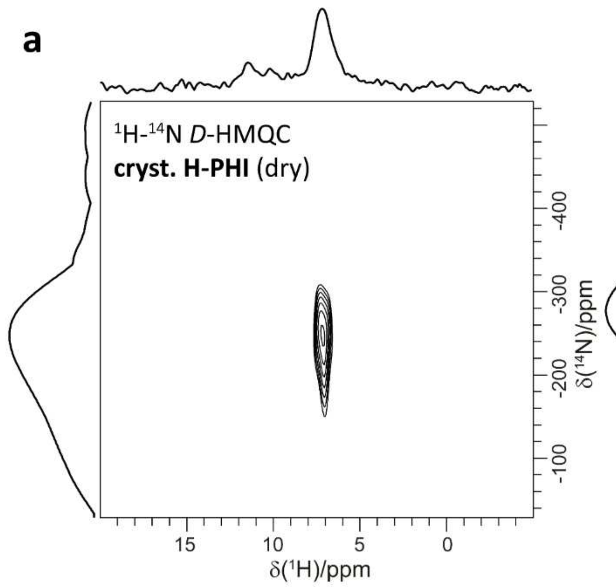

Figure A 14. (a) ^{1}H-^{14}N *D*-HMQC MAS spectrum of H-PHI dried at 120 °C and vacuum (10^{-2} mbar) as a comparison to the spectrum in Figure 2h at ambient conditions. It is well visible that compared to Figure 1h in the main text, the correlation signal is shifted upfield when dried. (b) ^{1}H-^{14}N *D*-HMQC MAS spectra of K-PHI under ambient conditions.

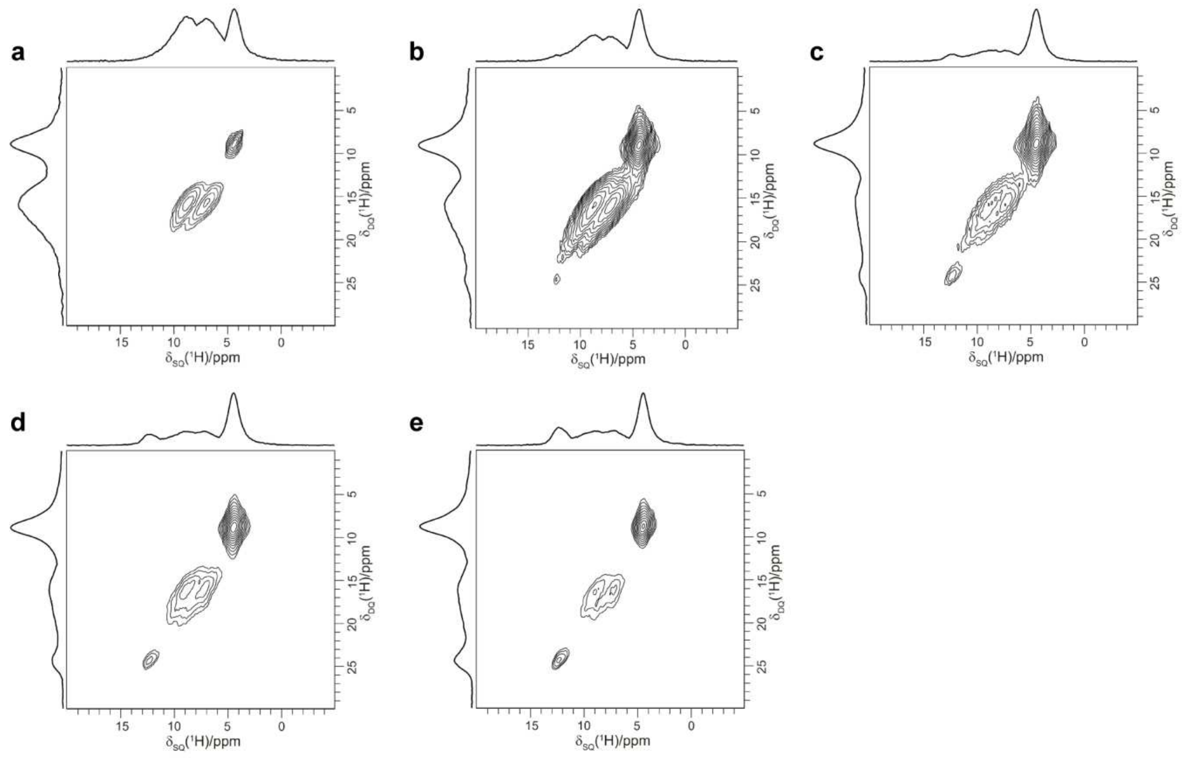

Figure A 15. ^{1}H-^{1}H DQ-SQ MAS spectra of H-PHI with increasing recoupling times of (a) 32 µs, (b) 64 µs, (c) 96 µs, (d) 128 µs and (e) 160 µs. Increasing recoupling times correspond to greater distances between coupling protons.

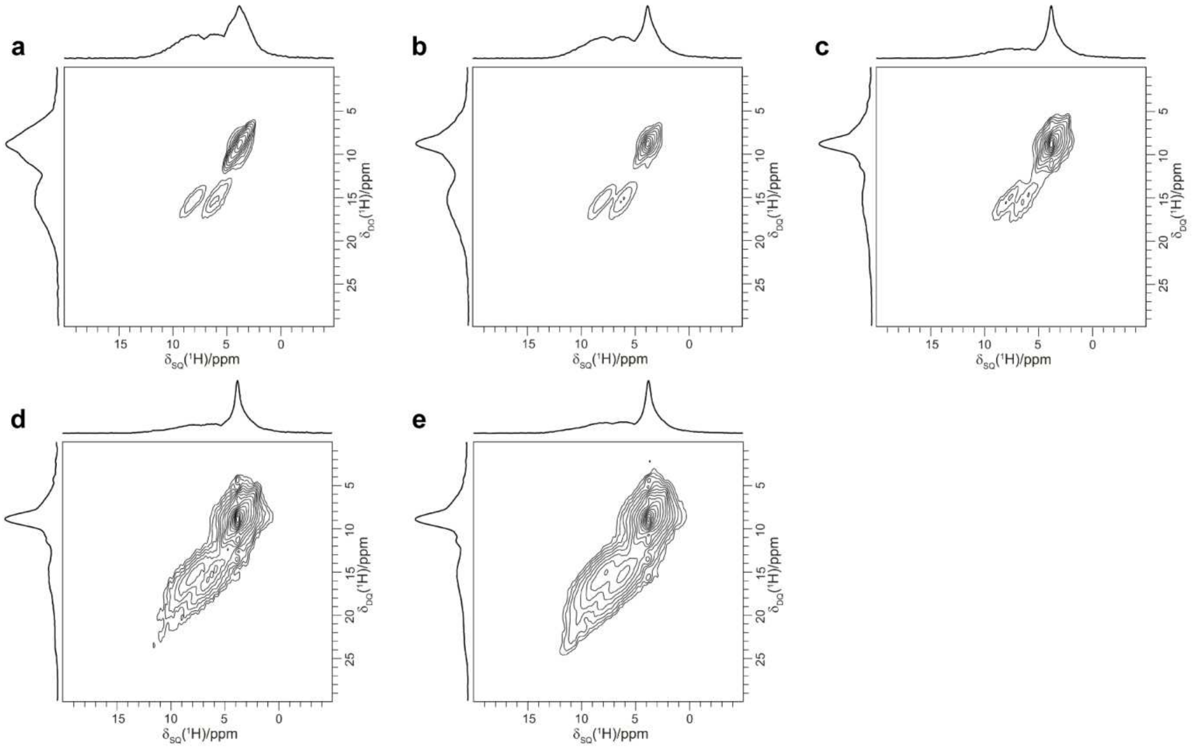

Figure A 16. ^{1}H-^{1}H DQ-SQ MAS spectra of K-PHI with increasing recoupling times of (a) 32 μs, (b) 64 μs, (c) 96 μs, (d) 128 μs and (e) 160 μs. Increasing recoupling times correspond to greater distances between coupling protons.

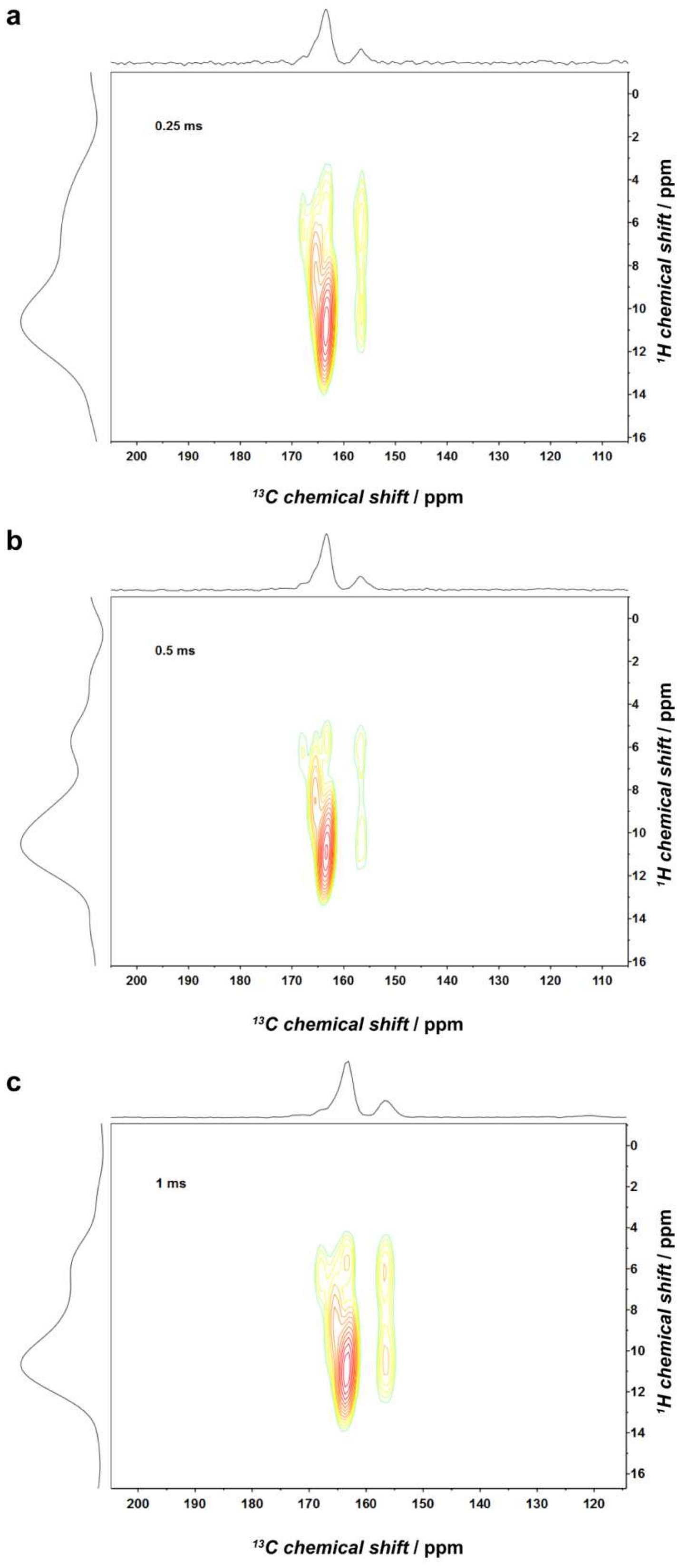

Figure A 17. Solid state ^{13}C-^{1}H MAS HETCOR NMR spectrum of K-PHI partially enriched via the use of KS^{13}C^{15}N as starting material. (a) 0.25 ms (b) 0.5 ms and (c) 1 ms contact time.

6.8 Quantum-chemical calculations

Methodology:

Structures for all investigated geometries were optimized at the PBE0-D3/def2-TZVP[16–19] level of theory. Monosolvated model systems were optimized by optimizing the PHI pore fragment and a single water molecule in separate calculations, optimizing the monosolvated PHI pore fragment complex afterwards with constraints on the PHI pore fragment.

NMR chemical shifts were obtained on B97-2/pcsSeg-2[20,21] level of theory using previously obtained geometries.

Geometry optimizations were performed using the Turbomole[22] program package in version 7.0.2, NMR chemical shifts were calculated using the FermiONs++[23,24] program package.

H-PHI

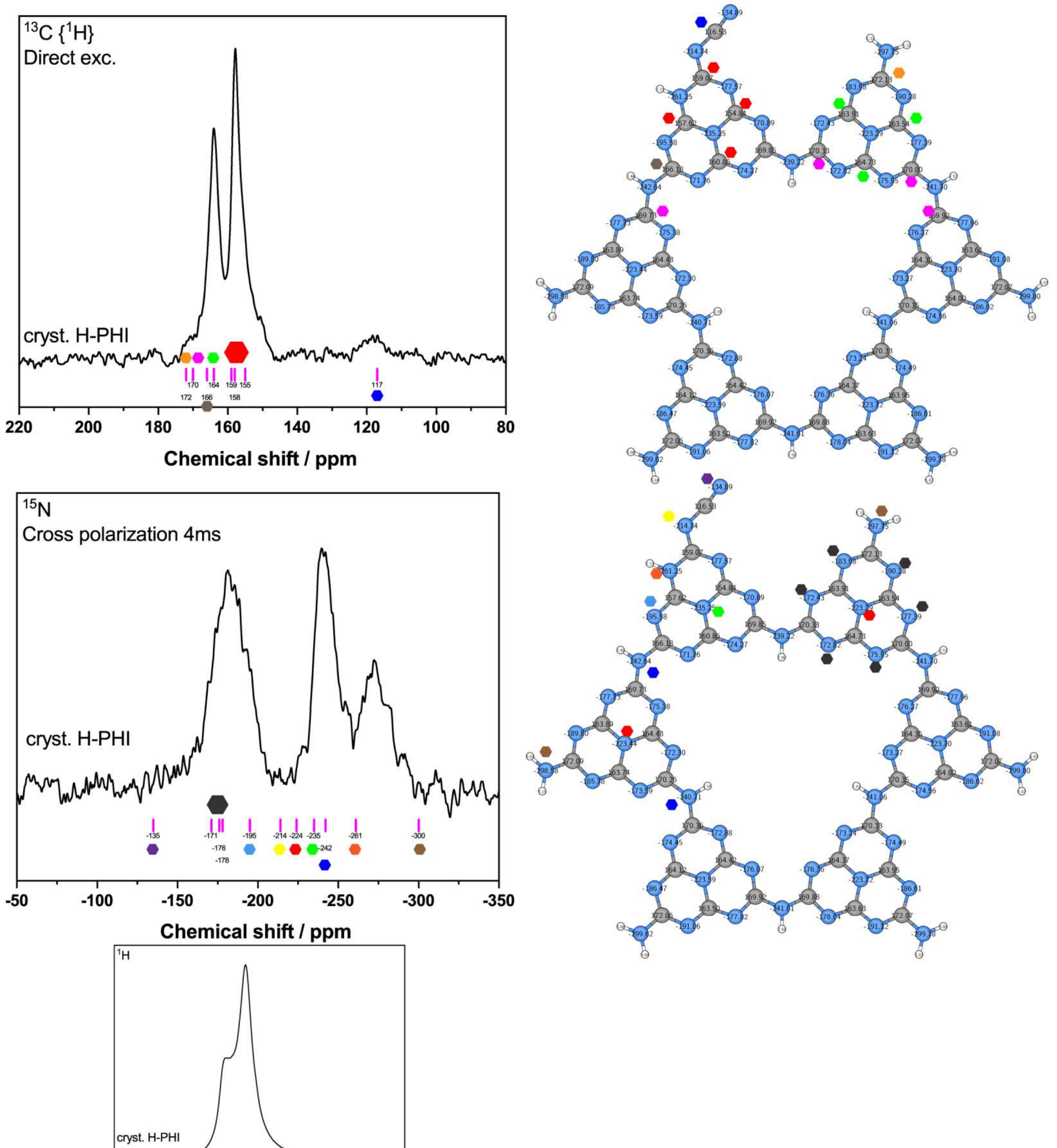

Figure A 18. ^{13}C- (direct exc.), ^{15}N-(CP) and ^{1}H- ssNMR spectra of protonated poly(heptazine imide) (H-PHI) and calculated NMR chemical shifts for a single protonated (neutral) heptazine pore, obtained on B97-2/pcsSeg-2//PBE0-D3/def2-TZVP level of theory. Protonation is located adjascent to the cyanamide group at the heptazine ring. This configuration fits the experimental results best. For better visualization, groups of atoms are marked with symbols in the corresponding pictures.

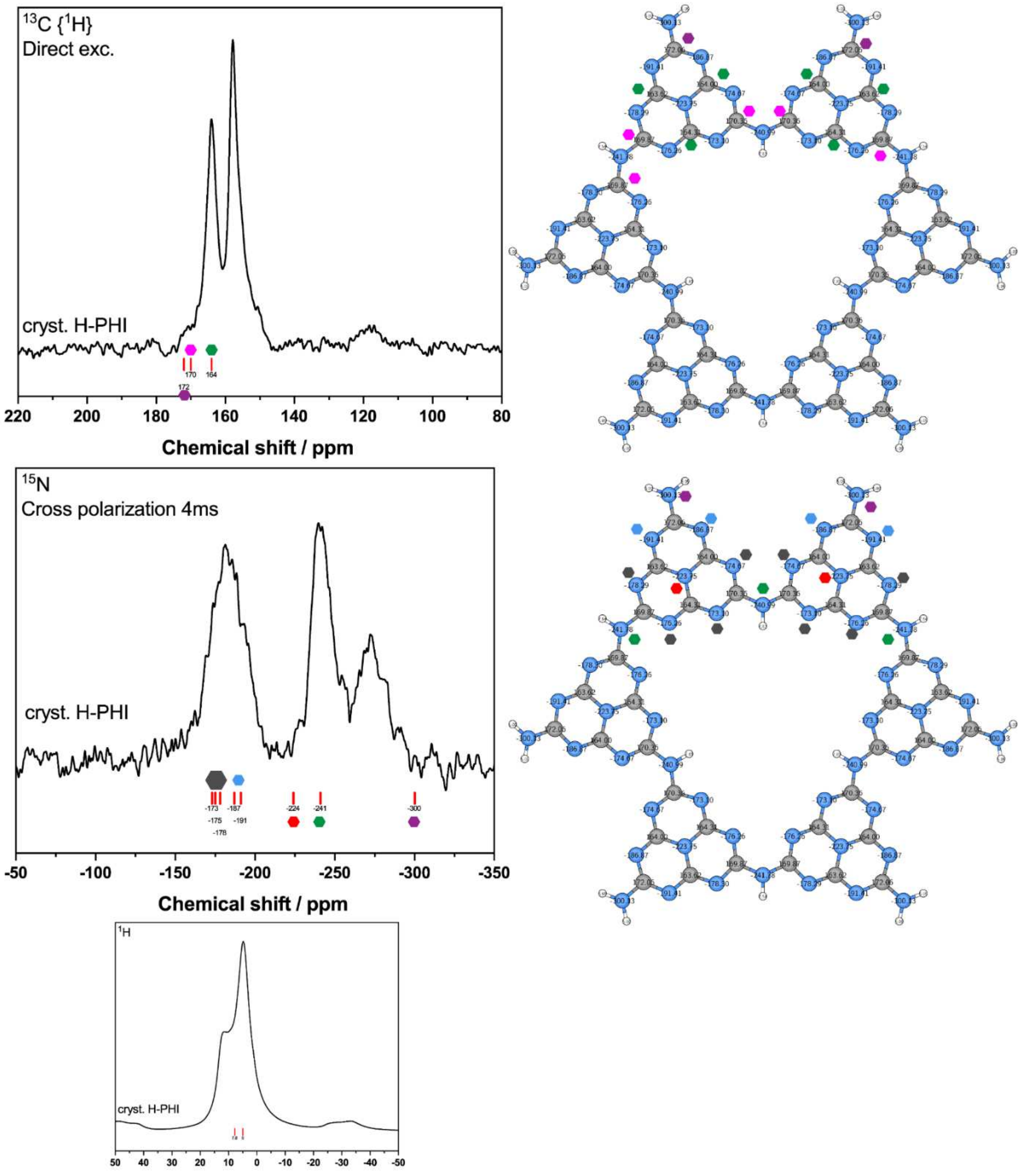

Figure A 19. ^{13}C- (direct exc.), ^{15}N-(CP) and ^{1}H- ssNMR spectra of protonated poly(heptazine imide) (H-PHI) and calculated NMR chemical shifts for a single protonated (neutral) heptazine pore, obtained on B97-2/pcsSeg-2//PBE0-D3/def2-TZVP level of theory. Protonation is located at the bridging nitrogen atom. For better visualization, groups of atoms are marked with symbols in the corresponding pictures.

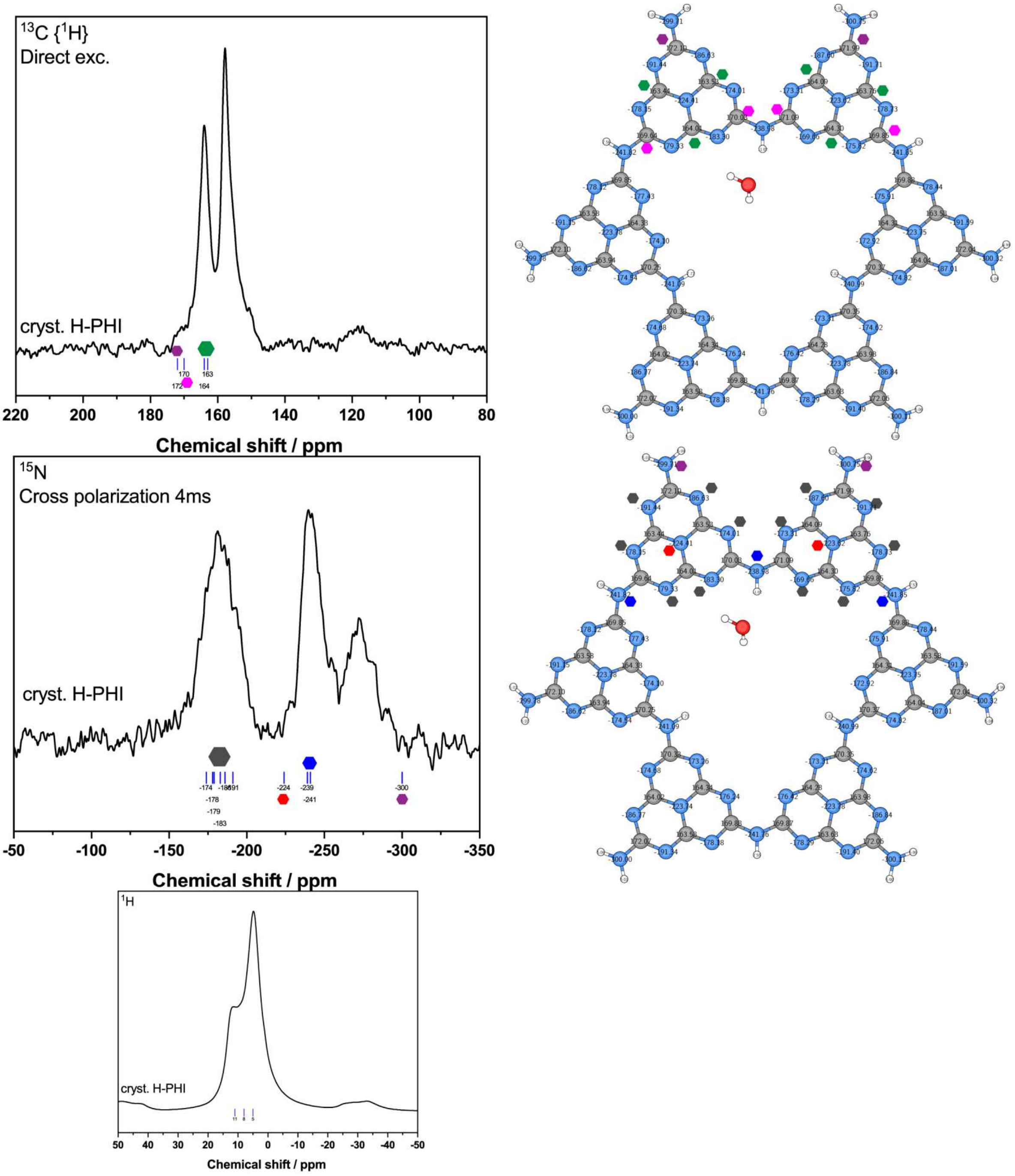

Figure A 20. ^{13}C- (direct exc.), ^{15}N-(CP) and ^{1}H- ssNMR spectra of protonated poly(heptazine imide) (H-PHI) and calculated NMR chemical shifts for a single protonated (neutral) heptazine pore, obtained on B97-2/pcsSeg-2//PBE0-D3/def2-TZVP level of theory. Protonation is located at the bridging nitrogen atom. Additionally, this simulation shows the influence of a water molecule within the pore on the chemical shifts. Especially the proton spectrum is simulated far better than without the influence of water. This is also in line with elemental analysis which shows a varying water content depending on synthesis conditions. For better visualization, groups of atoms are marked with symbols in the corresponding pictures.

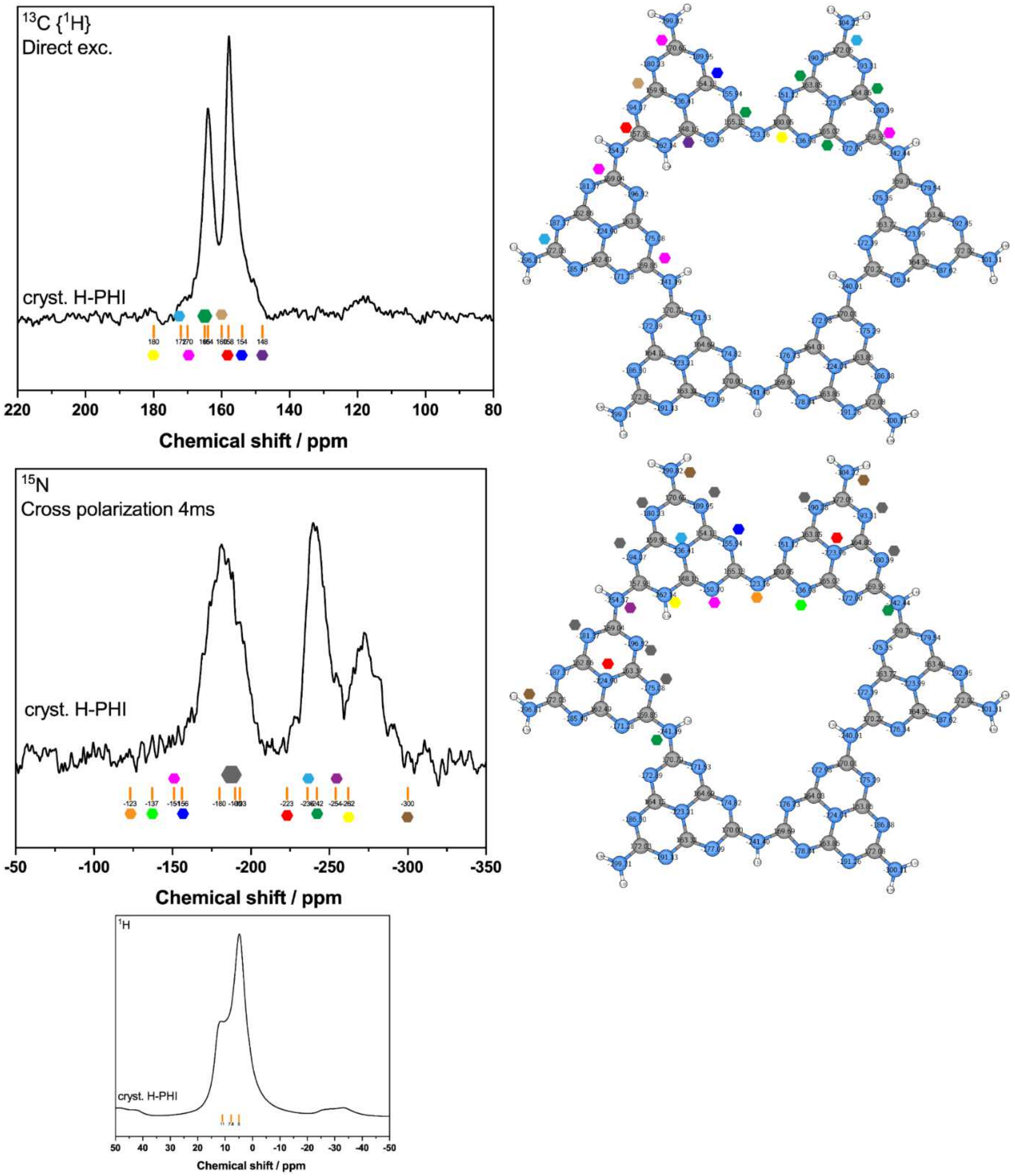

Figure A 21. ^{13}C- (direct exc.), ^{15}N-(CP) and ^1H- ssNMR spectra of protonated poly(heptazine imide) (H-PHI) and calculated NMR chemical shifts for a single protonated (neutral) heptazine pore, obtained on B97-2/pcsSeg-2//PBE0-D3/def2-TZVP level of theory. The proton is located at the heptazine ring farthest away from the bridging nitrogen atom. For better visualization, groups of atoms are marked with symbols in the corresponding pictures.

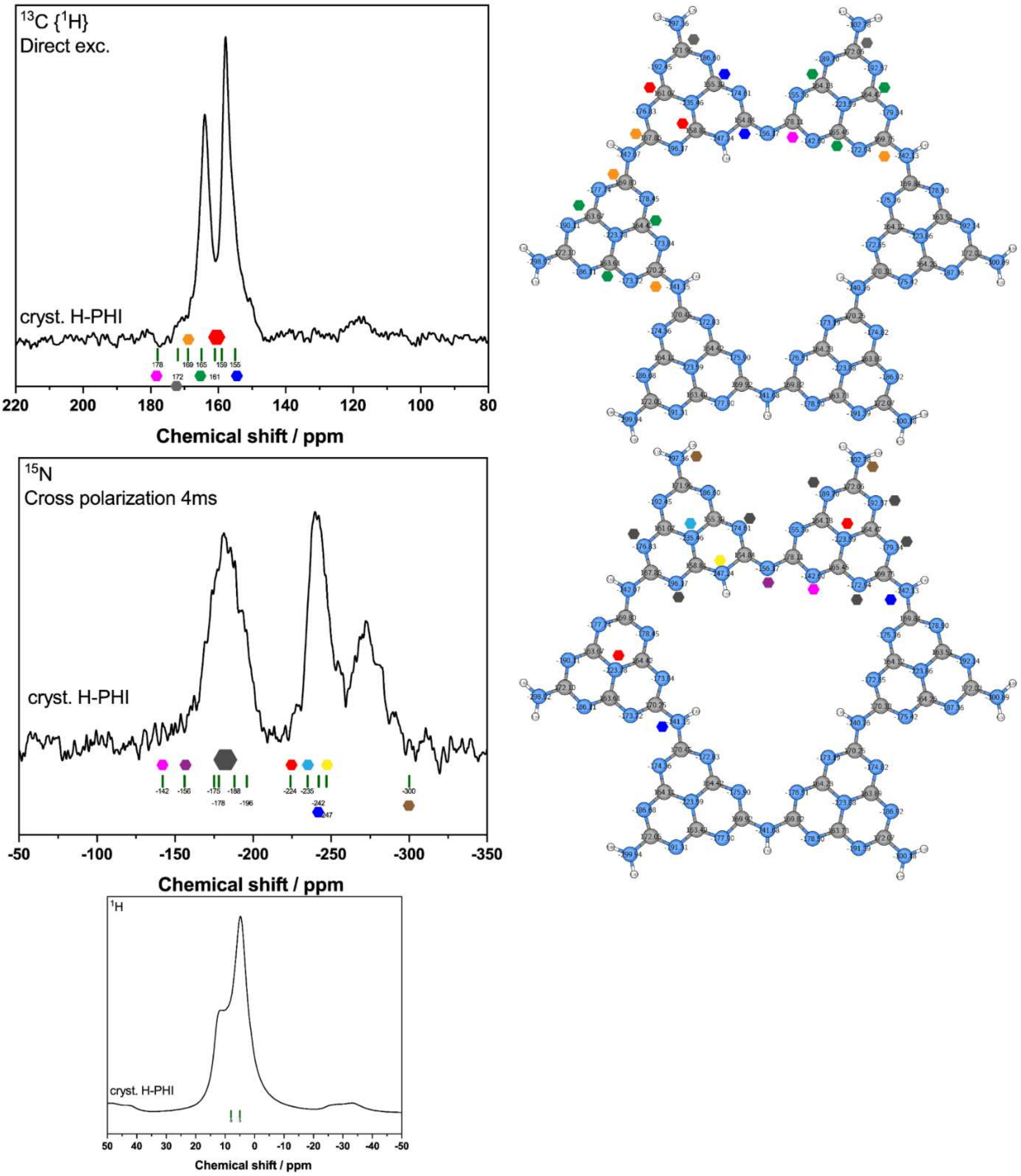

Figure A 22. ^{13}C- (direct exc.), ^{15}N-(CP) and ^{1}H- ssNMR spectra of protonated poly(heptazine imide) (H-PHI) and calculated NMR chemical shifts for a single protonated (neutral) heptazine pore, obtained on B97-2/pcsSeg-2//PBE0-D3/def2-TZVP level of theory. The proton is located at the heptazine ring next to the bridging nitrogen atom. For better visualization, groups of atoms are marked with symbols in the corresponding pictures.

K-PHI

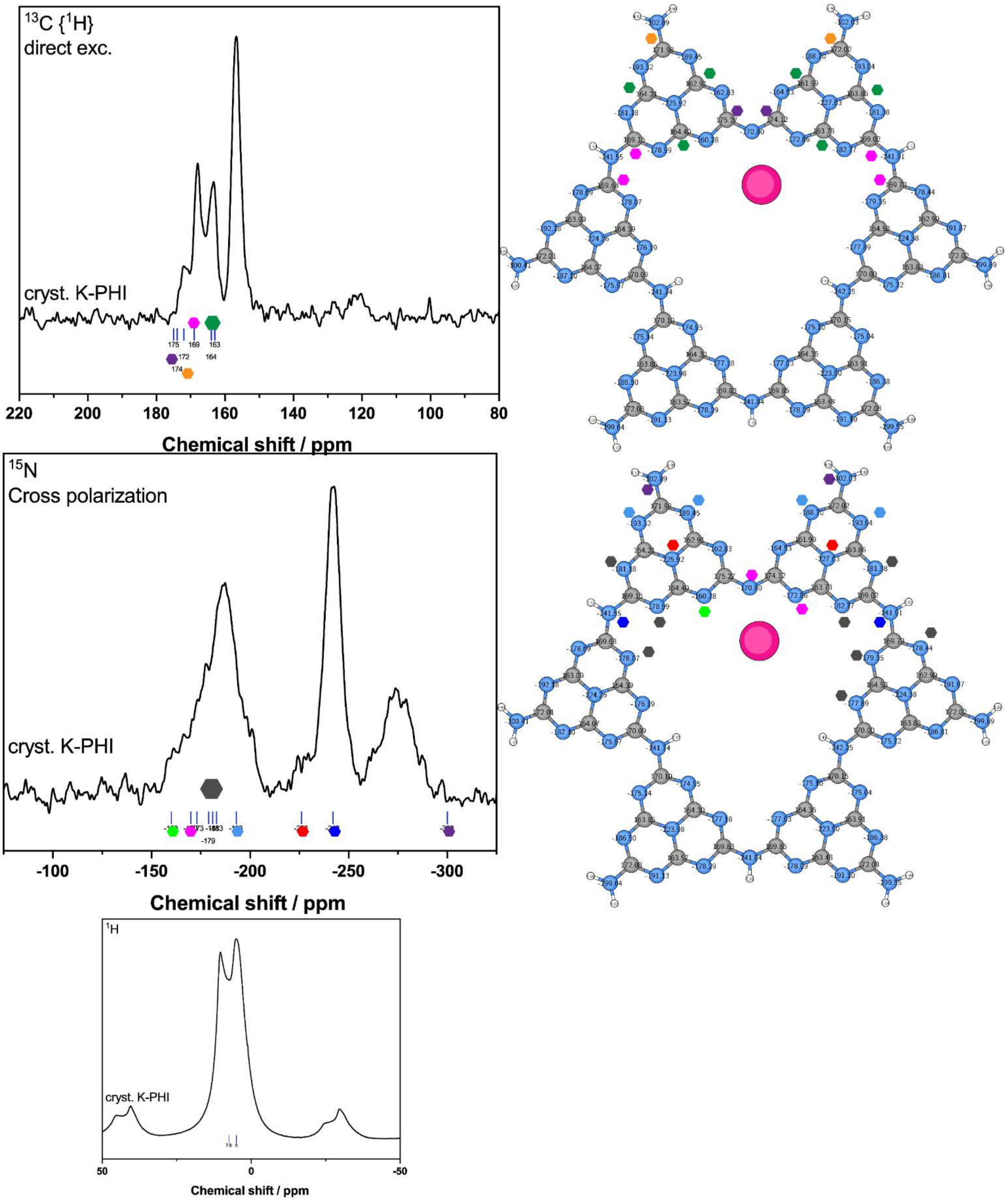

Figure A 23. ^{13}C- (direct exc.), ^{15}N-(CP) and ^{1}H- ssNMR spectra of potassium poly(heptazine imide) (K-PHI) and calculated NMR chemical shifts for a single a pore containing a potassium ion, obtained on B97-2/pcsSeg-2//PBE0-D3/def2-TZVP level of theory. The potassium ion is allocated near the heptazine units. This configuration fits the experimental results best. For better visualization, groups of atoms are marked with symbols in the corresponding pictures.

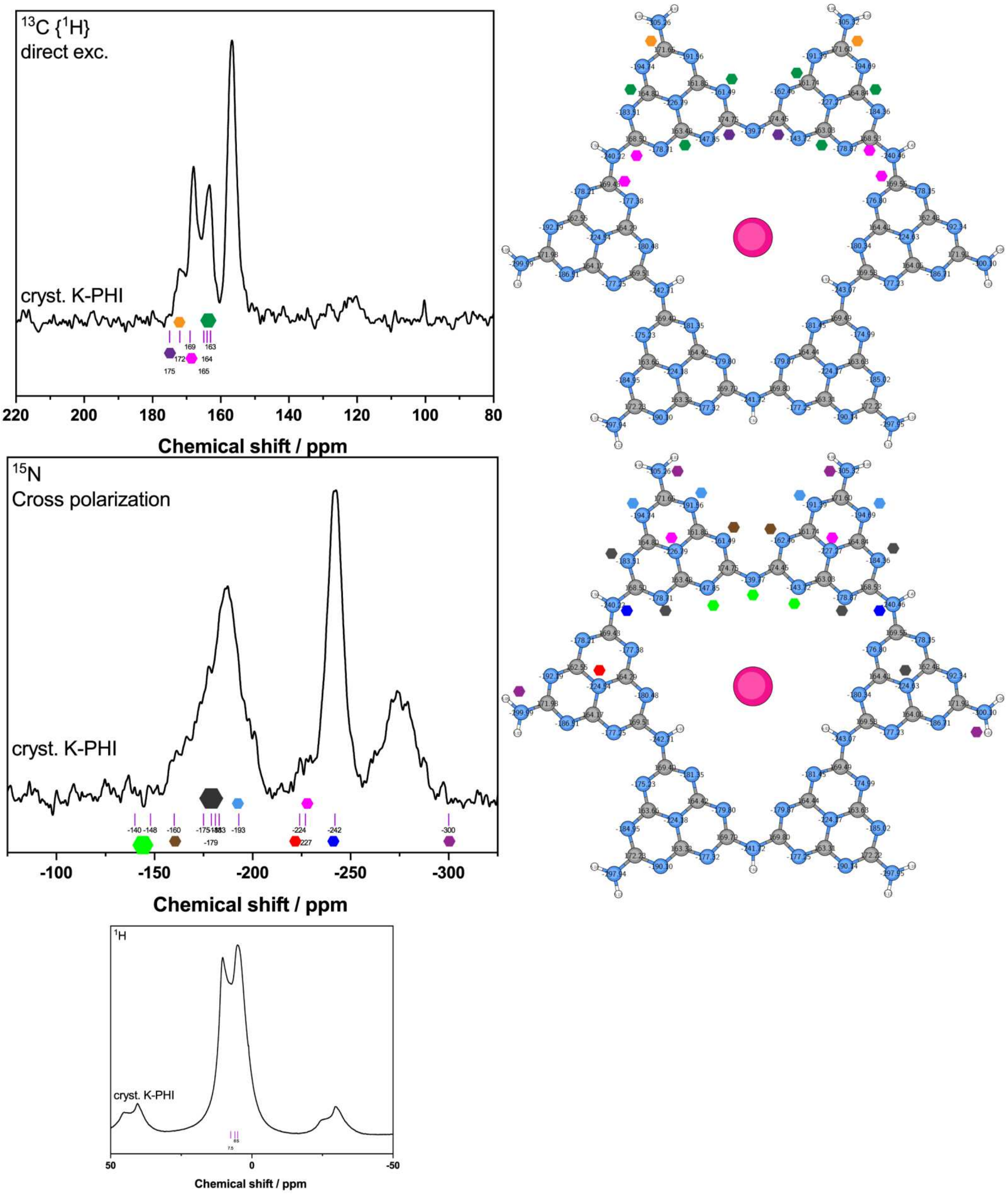

Figure A 24. ^{13}C- (direct exc.), ^{15}N-(CP) and ^{1}H- ssNMR spectra of potassium poly(heptazine imide) (K-PHI) and calculated NMR chemical shifts for a single a pore containing a potassium ion, obtained on B97-2/pcsSeg-2//PBE0-D3/def2-TZVP level of theory. The potassium ion is allocated centrally in the pore. This configuration is not very likely, because the distance to nitrogen atoms of the heptazines for a reasonable interaction is too far. For better visualization, groups of atoms are marked with symbols in the corresponding pictures.

Solvation shell model for potassium:

A solvated potassium ion model was constructed by running a molecular dynamics simulation with a single potassium ion in a solvated water box. The observed solvation shell (Figure A 25, left) shows 7 water molecules within the closest proximity and is line with experimentally available data.[25]

Potassium to oxygen distances were then extracted from the trajectory to compare with experimental PDFs for K-PHI (Main text, Figure 2.3c), confirming the occurrence of a water-K^+ coordination within the pores of K-PHI.

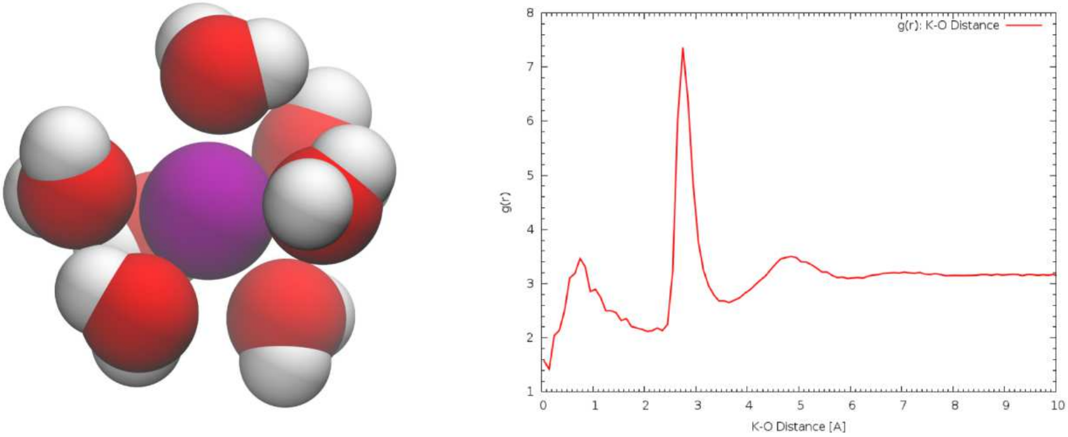

Figure A 25. Exemplary geometry for a potassium ion (purple) coordinated by 7 water molecules as extracted from a molecular dynamics trajectory (left) and the corresponding pair distribution function (right). The intense peak in the PDF at 2.7-3.3 Å represents typical, most observed K-O distances.

6.9 TGA-XRD experiments

Thermogravimetric (TG) analyses were performed using a STA 449 F5-Jupiter (Netzsch) device. The sample was heated up in a corundum crucible in a dynamic argon (50 mL/ min) atmosphere to 300, 350 or 400 °C with a heating rate of 10 K min^{-1} respectively. An empty corundum crucible was used as a reference. Corrections of instrumental effects and the buoyancy were performed with Al_2O_3 as an inert reference material during a separate measurement.

TGA in combination with *ex-situ* XRPD was carried out to investigate the thermal behavior of H-PHI, in particular the release of water molecules located in the pores of the poly(heptazine imide) network. The sample was heated up with a heating rate of 10 °Cmin^{-1} in an argon gas flow to 300, 350 and 400 °C. Directly after the respective temperature was reached the sample was removed from the oven and the powder was filled in a capillary that was immediately sealed afterwards. In Figure A 26 the TG-curve is depicted. The temperatures where the heating was stopped for XRPD analysis (Figure A 27) are indicated by red, filled circles.

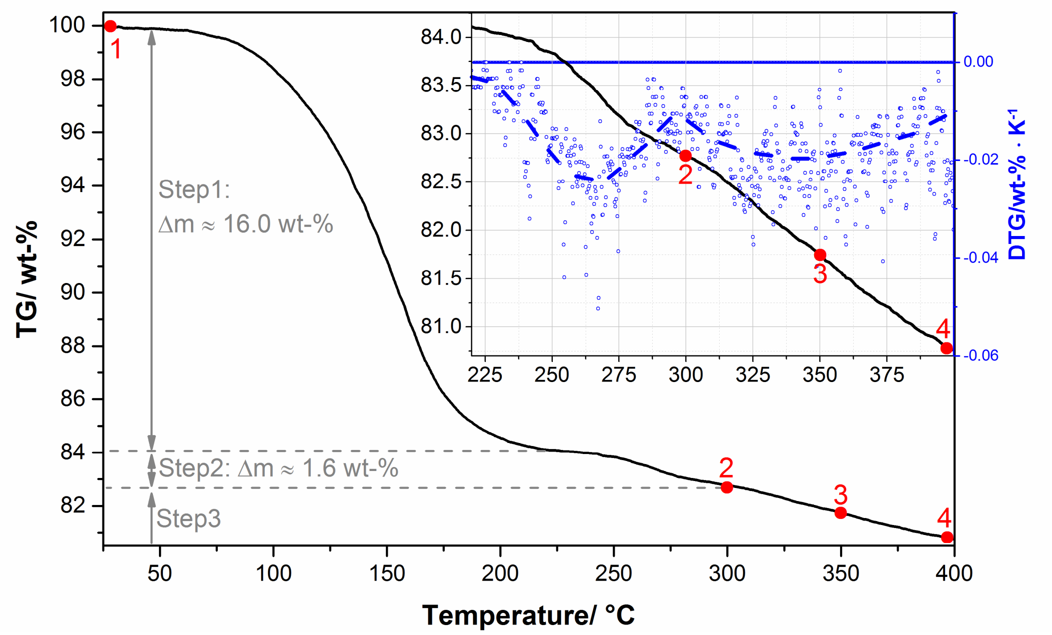

Figure A 26. Measured TG-curve of the H-PHI material. In the inset the second and third mass-loss step, as well as the 1st derivative of the TG-curve (blue circles and blue, dashed trend line) are presented. Temperatures at which ex-situ XRPD analyses were performed (Figure A 27) are indicated by red circles and red numbers.

Three distinct mass loss steps can be observed in the TG graph (Figure A 26, black line), which are attributed to the release of pore-water-molecules. The first water release step starts at ca. 75 °C and at 225 °C a small plateau indicates completion of this step, with a total mass loss of 16 wt%. During the first step water, which is most likely not or only loosely bound to the poly(heptazine imide) network is released. The second and third mass loss step vastly overlap and can only be distinguished by inspecting the first derivative of the TG-curve (Figure A 26, inset, blue circles and line). During the second step approx. 1.6 wt-% of the sample mass is released. In the *ex-situ* XRPD pattern (Figure A 27, orange pattern) the $\bar{1}10$ and the 010 reflections indicating 2-dimensional intra-layer ordering are still apparent. Therefore, the second decomposition step cannot be attributed to hydrolysis of the poly(heptazine imide) network, but to the release of more tightly bound pore water. In the diffraction pattern the 001 basal reflection is located almost at the same position.

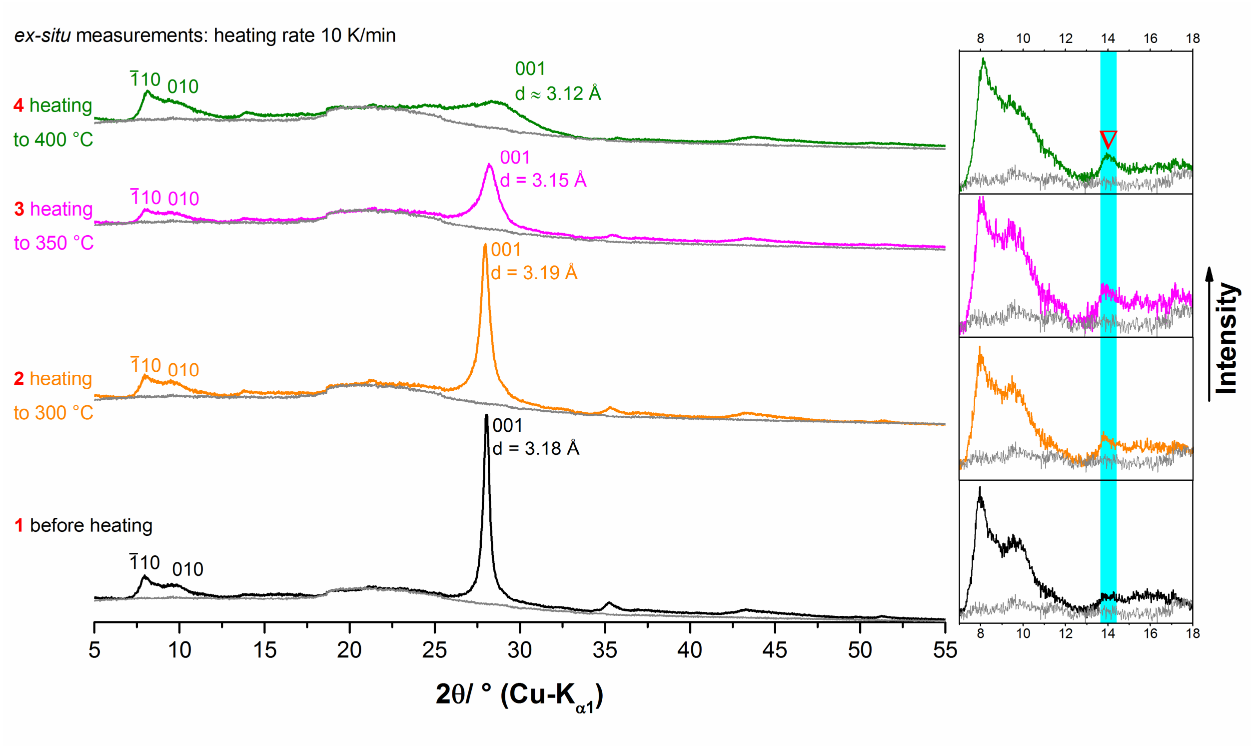

Figure A 27. Ex-situ XRPD analysis of the residue of H-PHI before and after heating up in the TGA-device to different temperatures. In order to illustrate the instrumental background effects, an empty capillary of the same batch was measured applying the same conditions (grey patterns). The low angle region of the XRPD pattern is presented in the inset. The expected position of the diffraction line, indicating eclipsed stacking is highlighted with cyan background.

The third mass loss step was investigated by ex-situ XRPD at 350 °C, which corresponds to the peak of the mass release and at 400 °C at which the decomposition step is almost completed. In the diffraction patterns (Figure A 27, magenta and green patterns) the $\bar{1}10$ and the 010 are slightly broadened but still clearly apparent. This indicates 2-dimensional coherence of the material, i.e. the poly(heptazine imide) layers are not completely depolymerized by hydrolysis. Therefore, the third mass loss step can be attributed mainly to the release of strongly bound pore water molecules. The 001 reflection is shifted towards smaller d-values, as the complete removal of pore water molecules leads to a shortening of the interlayer distances. The symmetrical, vast broadening of this reflection indicates a loss of three dimensional coherence in the crystal lattice, i.e. before heating H-PHI large stacks of poly(heptazine imide) layers were apparent and by removal of pore water the layers get partially exfoliated. Thus, only small stacks of a few nm (≈ 3-9 layers) remain. In addition, in the diffraction patterns at around 14 ° 2θ (Figure A 27, inset, cyan background) a Bragg peak (red triangle) arises from the diffuse scattering present in this region of the pattern. This peak indicates small domains (≈ 3-9 layers) of eclipsed stacked layers (see **6.12 Implications on the 3-dimensional structure of the poly(heptazine imide) framework from X-ray powder diffraction** data) after complete removal of pore-water, which is in accordance with the observations from SAED (see Figure 2.1 in the main text, and **6.3 Transmission electron microscopy (**TEM)).

6.10 Structure modeling based on XRPD

Indexing/Rietveld refinement:

XRPD reflections were indexed to a triclinic cell. The cell metric was verified by Pawley refinement, which resulted in a pseudohexagonal cell with lattice parameters a = b = 12.78 Å, c = 4.31 Å, α = β = 109.63°, and γ = 120°, R_{wp} = 3.87%, Figure A 28. Anisotropic peak broadening was accounted for by using a modification for cylindrical domain morphology[26] oriented along the c-axis. Additional broadening was described using a Lorentzian-type microstrain parameter, with additional corrections for the instrumental profile. A second Pawley phase of equally spaced reflections was used for the background. This cell was also suitable for describing the remaining diffraction features in the H-PHI pattern as well, Figure A 29. In this case, strain broadening was described using a hexagonal-type Stephens' model.[27]

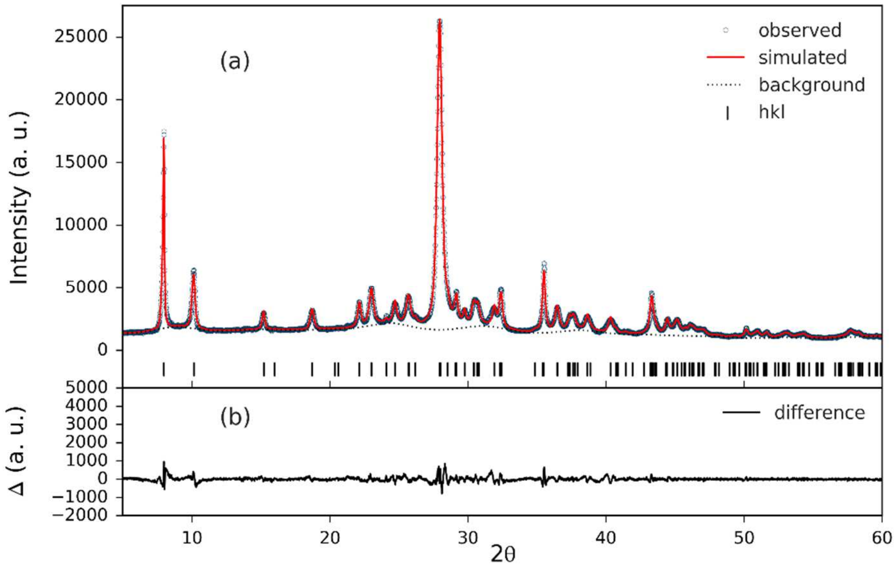

Figure A 28. (a) Resulting fit from Pawley refinement to the K-PHI dataset measured with CuK$_{\alpha 1}$ radiation. The reflection positions and background function are also plotted. (b) The difference curve is plotted for reference.

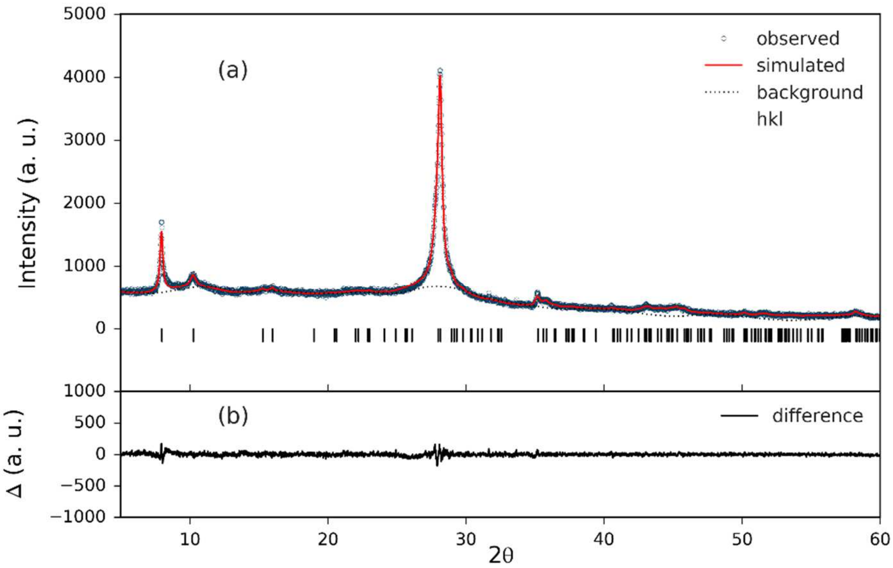

Figure A 29. (a) Resulting fit from Pawley refinement to the H-PHI dataset measured with $CuK_{\alpha1}$ radiation. The reflection positions and background function are also plotted. (b) The difference curve is plotted for reference.

A structure model for Rietveld refinement was based upon the previously solved structure of poly(triazine imide) reimagined for polymerized heptazine imide sheets.[28] The cell indexing indicates a single layer per cell, which given the non-90° α/β, must stack in a staggered fashion. A planar heptazine dimer was defined as a rigid body and oriented in the x-y plane, forming large triangular pores with two heptazine units on each side, and an interlayer distance of approximately 3.2 Å.

To obtain reasonable intensities, it was necessary to include atoms to account for the pore content. In all refinements for K-PHI, a single K atom was included in the pore with site position refined. Modeling of the additional species was attempted using different methods. First, the additional electron density in the pore was described using a pseudo-atom, i.e. a single atom with refined scattering contribution, and ADPs refined either isotropically or anisotropically, Figure A 30 a). This approximation was not sufficient for achieving a satisfactory fit. The second method involved sequentially adding oxygen atoms to represent water molecules, which were freely refined within the pore, Figure A 30 b). The final result used 7 oxygen atoms. 1 K and 7 O atoms corresponds roughly to 7 wt% K and 20 wt% water which is consistent with estimates from elemental analysis. Bond distance constraints, determined from DFT relaxations, were defined to maintain reasonable distances between O-O, K-O and O-C/N pairs. The fit, R_{wp} = 8.61%, indicates that this is a plausible crystallographic model, Figure A 31. Pawley and Rietveld refinements were performed using TOPAS v6.[29]

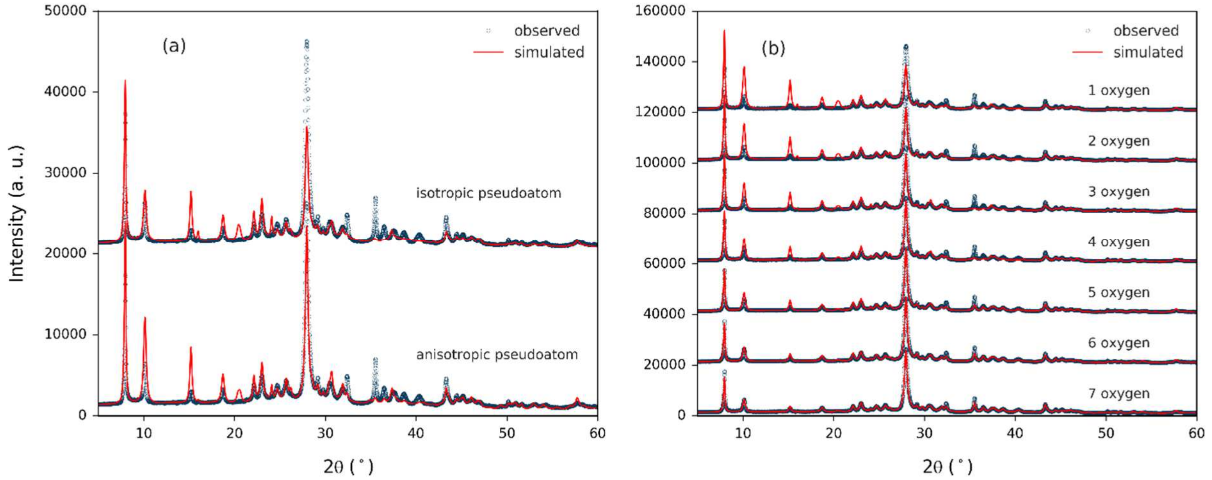

Figure A 30. (a) Rietveld refinement results from simulation of pore content by potassium and a single pseudo-atom of arbitrary electron number with site positions and ADPs refined. (b) Rietveld refinement results from simulation of pore content by potassium and various number of oxygen atoms with site positions refined and ADPs fixed.

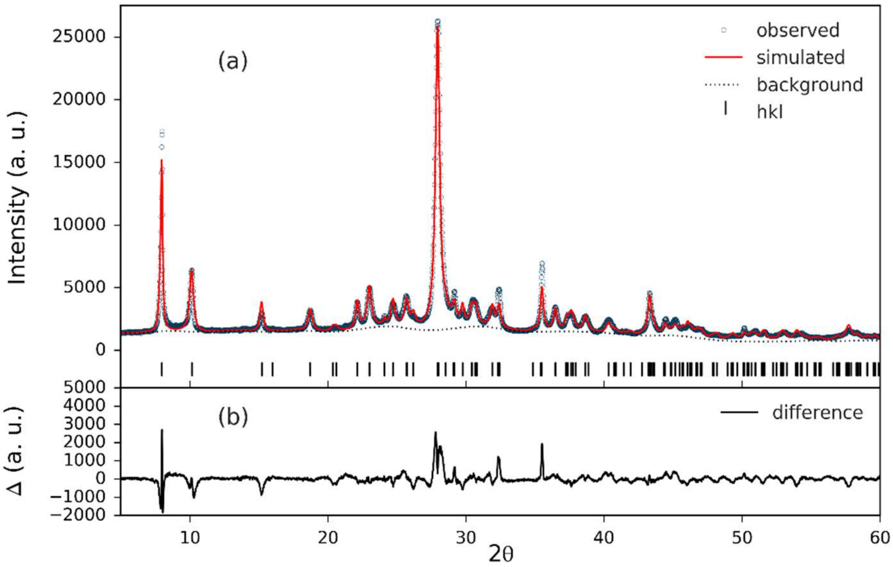

Figure A 31. (a) Final Rietveld refinement to the K-PHI dataset measured with CuK$_{\alpha 1}$ radiation. The reflection positions and background function are also plotted. (b) The difference curve is plotted for reference.

6.11 Pair distribution function (PDF) analysis

Data processing:

The raw 2D data from BNL and ESRF were corrected for polarization effects, masked, and azimuthally integrated into 1D powder diffraction intensities using FIT2D[30] and pyFAI[31] respectively. Further correction, normalization, and Fourier transformation of the data to the PDF, $G(r)$, was performed using PDFgetX3[32], within xPDFsuite.[33]

The total scattering structure function $S(Q)$ is obtained from the coherent scattering intensities $I_c(Q)$, after removal of the self-scattering, by,

$$S(Q)=\frac{I_c(Q)-\langle f_i(Q)^2\rangle+\langle f_i(Q)\rangle^2}{\langle f_i(Q)\rangle^2}. \tag{1}$$

Q is the magnitude of the scattering momentum transfer ($Q = 4\pi \sin\theta / \lambda$ for elastic scattering, where λ is the wavelength, and 2θ is the scattering angle). $f_i(Q)$ is the atomic form factor for atom i, and averaging denoted by $\langle \ldots \rangle$ is performed stoichiometrically over all atom species in the sample. The experimental PDF, $G(r)$, is obtained via truncated Fourier transformation of the reduced total structure function $F(Q) = Q[S(Q) - 1]$, by

$$G(r)=\frac{2}{\pi}\int_{Q_{min}}^{Q_{max}} F(Q)\sin(Qr)\,dQ \tag{2}$$

$$= 4\pi r[\rho(r)-\rho_0\gamma_0], \tag{3}$$

where ρ_0 is the average atomic number density and $\rho(r)$ is the local atomic pair density, which is the average density of neighboring atoms at a distance r from an atom at the origin. γ_0 is the characteristic function of the diffracting domains which equals 1 for bulk crystals, but has an r-dependence for nano-sized domains.[30] The maximum ranges of diffraction data used in the Fourier transform for the different measurements were Q_{max} = 25.0 Å^{-1} and 8.5 Å^{-1}.

Data comparison:

The reduced total scattering data and resulting pair distribution functions are shown in Figure A 32 and Figure A 33, for both the high Q_{max}/low Q_{res} and the high Q_{res}/low Q_{max} measurements at BNL. The former measurement gives high real space resolution, allowing for resolving distinct nearest neighbor atom-pair correlations from within the heptazine units. The latter measurement results in much lower real space resolution, and therefore specific intramolecular characteristics cannot be discerned. However, the higher reciprocal-space resolution of the measurement allows the real space structure information to be observed over longer distances, thus allowing for comparison of density modulations between the stacked layers to be compared between samples. It is clear that despite the loss of orientational coherence between stacked layers in the H-PHI sample, there is still a robust packing relationship between the layers, which is maintained at least up to 20-30 nm or more.

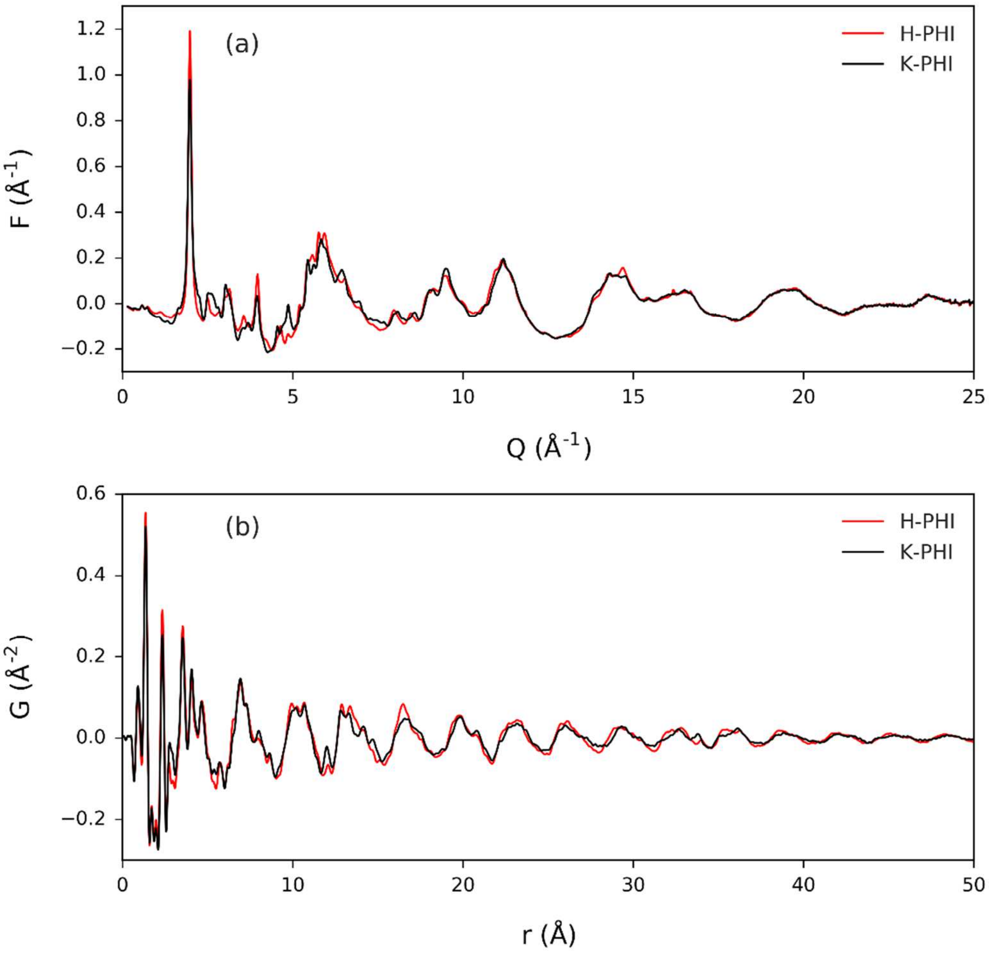

Figure A 32. (a) Reduced total scattering data for H-PHI and K-PHI measured with short detector distance (high Q_{max}/low Q_{res} setup, Q_{max} = 25.0 Å^{-1}), (b) Resulting PDFs compared up to 50 Å.

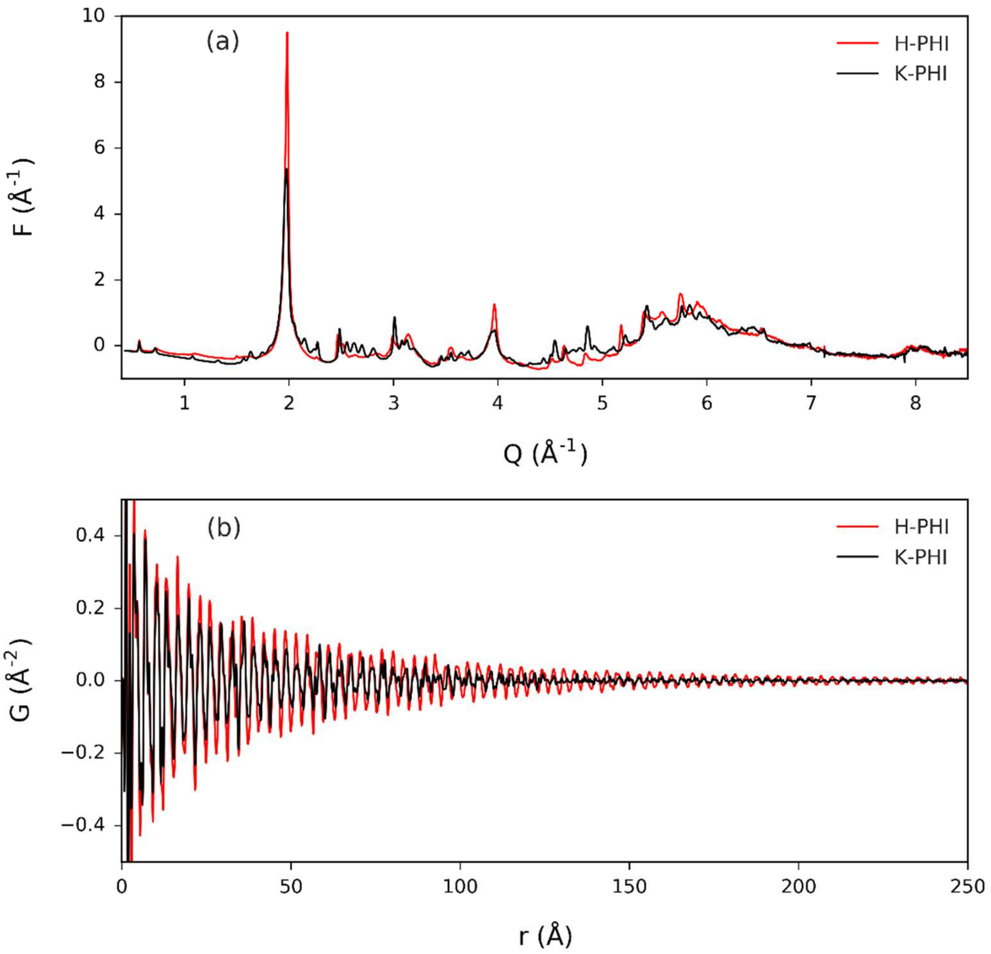

Figure A 33. (a) Reduced total scattering data for H-PHI and K-PHI measured with far detector distance (high Q_{res}/low Q_{max} setup, Q_{max} = 8.5 Å^{-1}) (b) Resulting PDFs compared up to 250 Å.

Data modeling – single molecule, single layer, crystal structure:

Simulation of the PDF for a single layer was performed using Diffpy-CMI.[34] Further PDF refinements, and co-refinement of XRD/PDF data were carried out using TOPAS v6.[29] The PDF was calculated from a crystallographic model by,

$$G(r) = \frac{1}{rN}\sum_{i}\sum_{j\neq i}\left[\frac{f_i f_j}{\langle f\rangle^2}\delta(r - r_{ij})\right] - 4\pi r\rho_0, \qquad (4)$$

$$R_w = \sqrt{\frac{\sum_{i=1}^{n}[G_{obs}(r_i) - G_{calc}(r_i, P)]^2}{\sum_{i=1}^{n} G_{obs}(r_i)^2}}. \qquad (6)$$

For XRD/PDF corefinement, R_w was minimized for both datasets simultaneously, fitted to the same structure. In this case, different weightings of the XRD and PDF were attempted, and a suitable result was found using a weighting of 100:1 PDF:XRD to account for the relative order of magnitudes of the peak intensities in each dataset. The XRD/PDF corefinement of synchrotron measured K-PHI sample is shown in Figure A 34, showing that the model can be consistently refined in both reciprocal and real space. Slightly improved fits to the PDF data were obtained by single dataset refinement for both K-PHI and H-PHI, shown in Figure A 35.

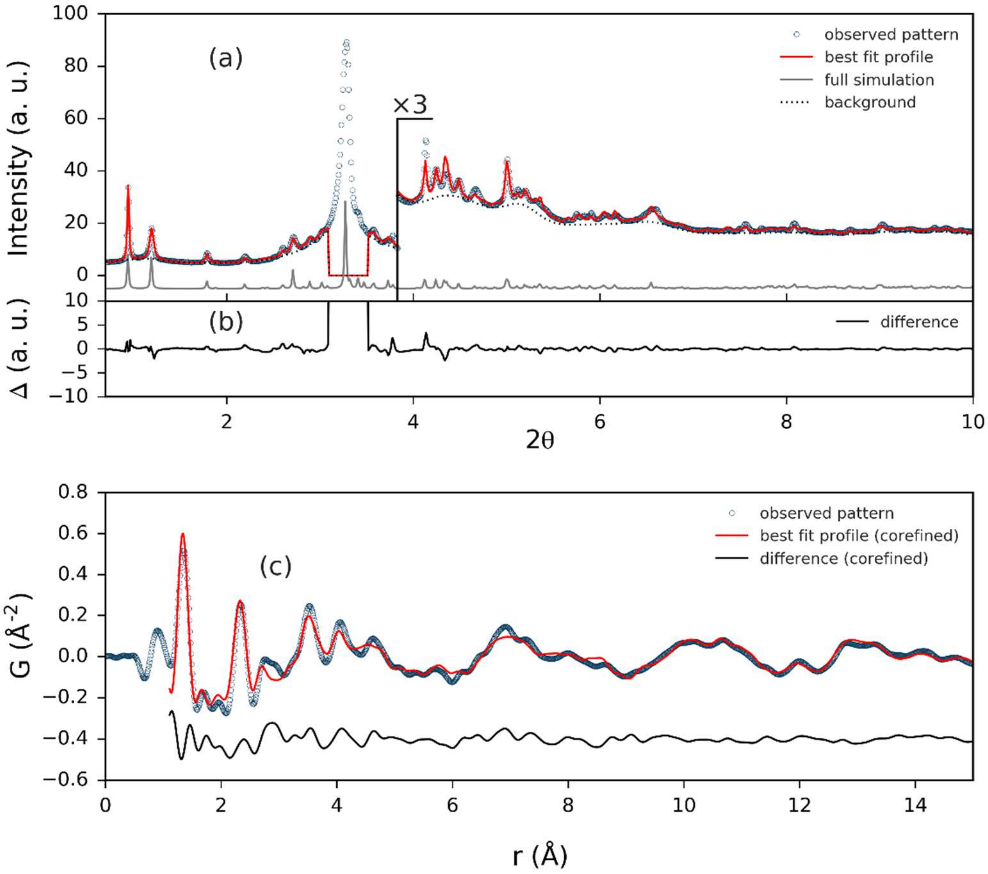

Figure A 34. Corefinement of K-PHI model to synchrotron XRD and PDF measurements. (a) Fit to the high Q resolution XRD dataset. The (001) peak was excluded due to an over-biasing effect on the refinement result. (b) The residual is shown for reference. (c) The resulting fit to the real space PDF from 1-15 Å.

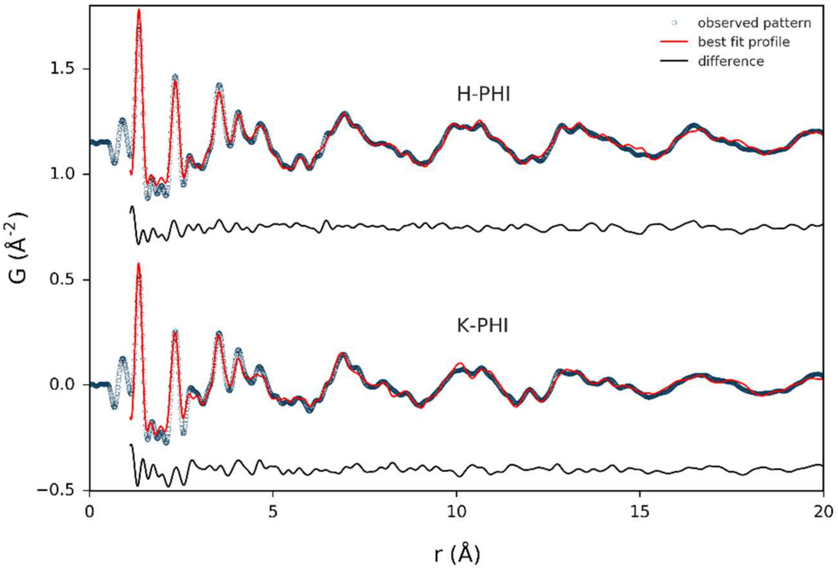

Figure A 35. PDF-only refinements to the H-PHI and K-PHI measurements. K-PHI contained 7 O and 1 K atom in the pore. For H-PHI, the K atom was replaced by an eighth O atom. The model gives a suitable result in both cases.

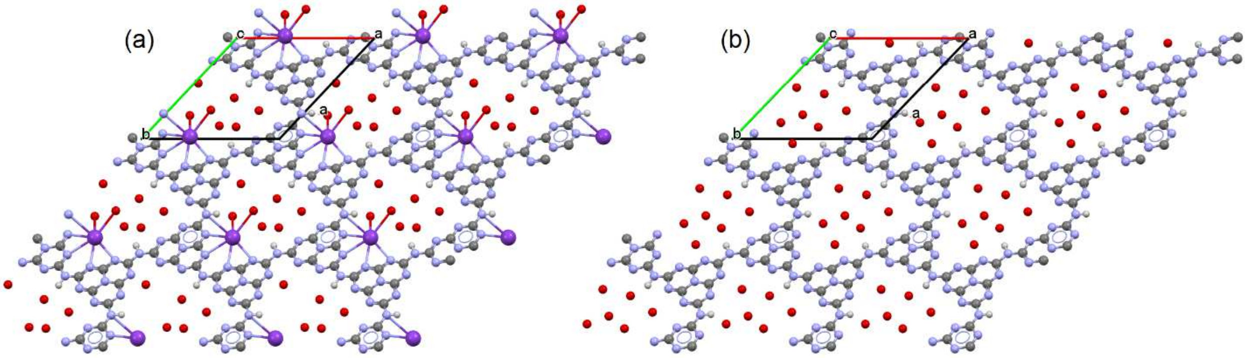

Figure A 36. Structures resulting from PDF-only refinements to the (a) K-PHI and (b) H-PHI measurements, both refined using the staggered stacking relationship determined from Rietveld refinement to K-PHI lab diffraction data.

Table A 2. PDF-only refinements to the H-PHI and K-PHI measurements. K-PHI contained 7 O and 1 K atom in the pore. For H-PHI, the K atom was replaced by an eighth O atom. The model gives a suitable result in both cases.

	Pawley		Rietveld	PDF*	
	K-PHI	H-PHI	K-PHI	K-PHI	H-PHI
wavelength	1.5406	1.5406	1.5406	0.1823	0.1823
refinement range	3.0-60.0 °	3.0-60.0 °	3.0-60.0 °	1.1-20.0 Å	1.1-20.0 Å
a=b	12.78	12.78	12.78	12.80	12.92
c	4.31	4.33	4.31	4.33	4.33
α=β	109.63	109.96	109.63	109.76	109.60
γ	120.0	120.0	120.0	120.0	120.0
R_{wp}	0.0387	0.0434	0.0861	0.2254	0.1901

*Separate samples prepared for PDF measurements.

Short range order:

By comparing PDF datasets measured for various K-PHI and H-PHI samples measured at BNL and ESRF, as well as Melem (with no ion content), we were able to observe an increase in the weighting of atom-pair correlations from approximately 2.5-3.2 Å with increasing ion concentration. These distances are found to correspond to the K-O coordination shell, as determined from DFT calculations, giving direct evidence that water coordination (either partial or full) of the K ions occurs within the pores. This distance range also corresponds to the distances expected for coordination of N atoms in K-azine complexes[35], meaning that there could be some contribution due to the off-centering of the K atoms within the pore.

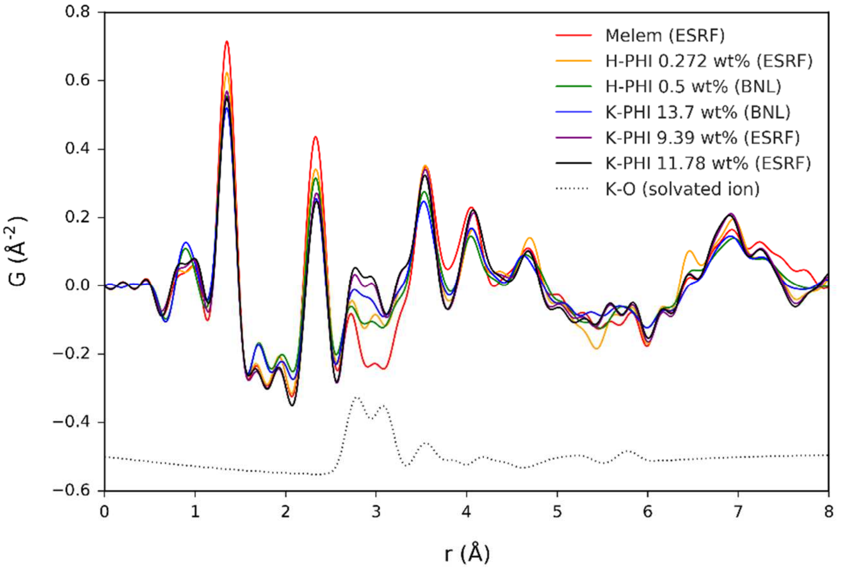

Figure A 37. Short range ordering of heptazine and pore contents as shown by the PDFs for H-PHI, K-PHI, and Melem samples measured at either BNL or ESRF.

6.12 Implications on the 3-dimensional structure of the poly(heptazine imide) framework from X-ray powder diffraction data

Information on the 3-dimensional structure of the poly(heptazine imide) framework can be extracted from the X-ray powder diffraction (XRPD) patterns, as these represent an averaged analysis of the bulk material. In contrast to ideal conventional crystalline material, the presence of different kinds of defects is expected in the PHI materials, such as: intralayer defects caused by incomplete polymerization, disorder of the pore material and planar defects occurring as stacking faults. Only the latter kind of faulting governs the structural coherence perpendicular to the poly(heptazine imide) planes. Hence the 3-dimensional structure of the poly(heptazine imide) framework can only be understood completely when these defects are taken into account. Therefore, systematic series of simulations of the diffraction patterns of the faulted poly(heptazine imide) using distinct faulting scenarios were performed and compared to the measured data in order to obtain qualitative information on the kinds and degree of faulting that is present in the material. Due to the presence of different kind of defects, as mentioned above, no attempt was made to fit the measured diffraction patterns with any faulting model.

Comparison of the powder patterns of K-PHI and H-PHI

A comparison of the diffraction patterns of K-PHI and H-PHI is presented in Figure A 38. In total H-PHI (black pattern) seems to exhibit less reflections than the potassium phase (blue pattern). The main reflections ($\bar{1}10$, 010, 001) in the hydrogen compound are situated at identical positions as in the pattern of K-PHI, which indicates that basic structural motifs such as the constitution of the poly(heptazine imide) layers are identical. The smaller number of reflection may indicate a higher symmetry of the structure of H-PHI but a close inspection of the diffraction pattern (Figure A 38, inset) reveals that there are many, but vastly broadened reflection apparent that almost merge with the background. Hence, there is much diffuse scatting in the diffraction pattern of H-PHI. The background itself and the basis of the $\bar{1}10, 010$ reflections exhibit a characteristic triangular shape, which is indicative for planar defects in the crystal structure.[36] Therefore, the lower number of reflections present in the diffraction pattern of H-PHI rather indicate a higher degree of disorder in the structure than a higher symmetry.

Diffuse scattering can also originate from the disorder of the solvent molecules present in the pores of the poly(heptazine imide) framework. In order to rule out the scattering contribution of the pore particles, diffraction patterns (Figure A 39) of fully ordered H-PHI were simulated using the structural model derived from the PDF-analysis (**6.10 Structure modeling based on** XRPD and **6.11 Pair distribution function (PDF)** analysis) with (black pattern) and without (blue pattern) the pore water related oxygen sites. Excluding the pore particles does not decrease the number of peaks in the diffraction pattern and therefore does not artificially increase the symmetry of the lattice. However, it affects the peak intensities in relation to the 001 basal reflection. In consequence systematic simulations of the diffractional effects of planar defects in the stacking of the poly(heptazine imide) framework without including the pore-water can be used to demonstrate which reflections are broadened due to the different faulting scenarios which are discussed in the next sections. But as the reflection intensities are affected by the pore particles, the simulations can only be used for a qualitative description of the 3-dimensional structure of the poly(heptazine imide) framework.

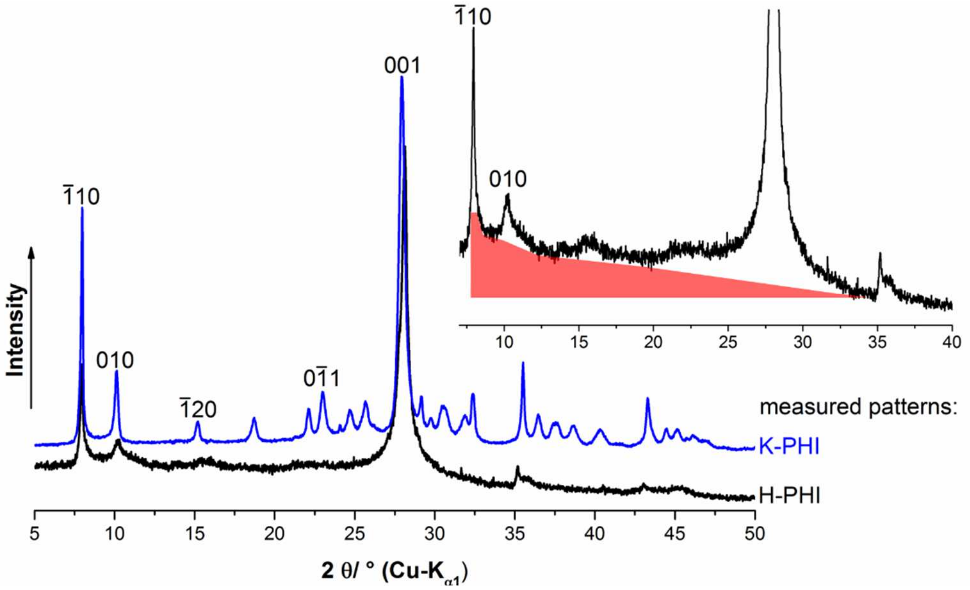

Figure A 38. Comparison of the measured powder patterns of K-PHI and H-PHI including selected reflection indices. Peak broadening appearing in a triangular shape that merges with the background in the pattern of H-PHI is highlighted by red color (inset).

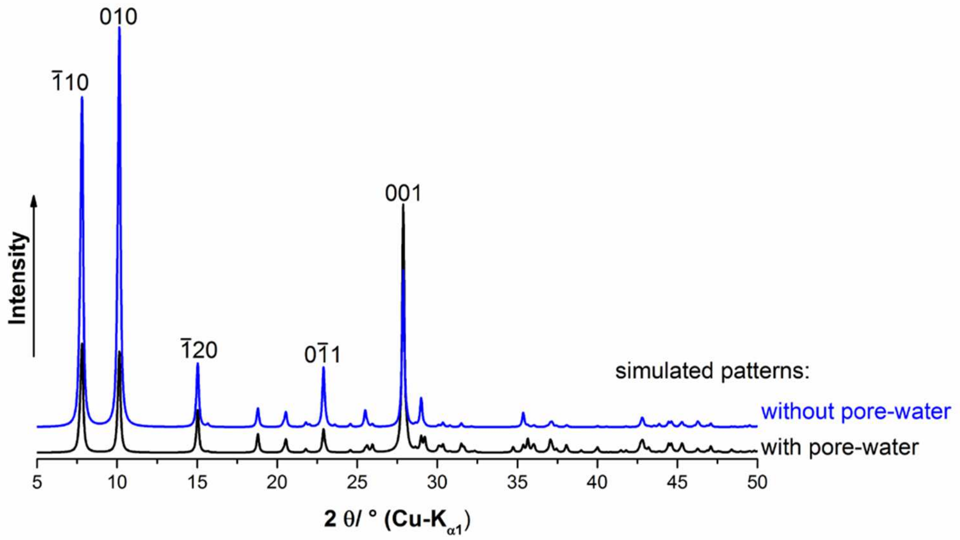

Figure A 39. Simulated diffraction patterns of H-PHI including and excluding pore water.

Possible arrangements of the poly(heptazine imide) layers

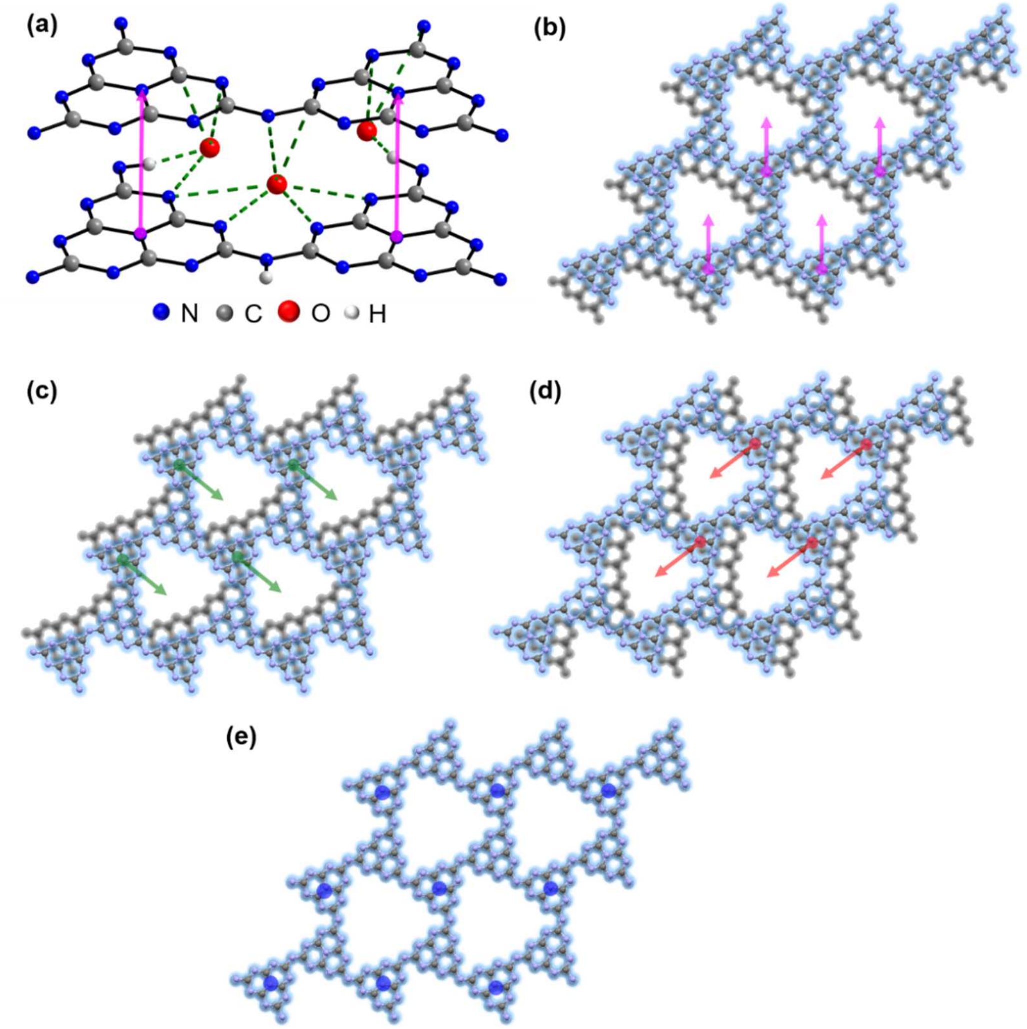

Figure A 40. (a) Interlayer interactions in the structural model of H-PHI mediated by water molecules (presented as oxygen atoms), possible attractive interactions between poly(heptazine imide) related nitrogen and hydrogen sites and pore water are indicated by green, dashed bonds, the stacking vector describing the layer-to-layer arrangement is represented by the magenta arrows. (b-e) Top view on possible layer to layer arrangements in the structure of H-PHI, molecules in the pore are omitted, the preceding layer is presented in grey and stacking vectors as colored arrows, (b) stacking order on the proposed structured model of H-PHI = pore I stacking, (c, d) alternative stacking order directed by one of the neighboring pores = pore II stacking, (e) completely eclipsed stacking.

Possible layer arrangements, i.e. stacking orders, in the poly(heptazine imide) material can be derived from the idealized structure model of H-PHI obtained by the PDF-analysis (see **6.10 Structure modeling based on** XRPD and **6.11 Pair distribution function (PDF)** analysis). Short N-H···O (1.7 Å to 1.9 Å) and N···O (2.8 Å to 3.7 Å) distances, as well the NMR- and TG- analyses (see **NMR section of main Text**, **6.7 Solid-state nuclear magnetic resonance (**ssNMR) and **6.9 TGA-XRD** experiments) indicate possible attractive interactions in terms of potential hydrogen bonds or dipole-dipole interactions between the poly(heptazine imide) backbone and the water molecules in the pores (Figure A 40, a, green, dashed bonds). These interactions occur both *within* a layer and *in-between* neighboring layers. Hence the position of a layer is shifted towards the pore of the preceding layer (Figure A 40, b). Due to the 3-fold symmetry of the heptazine SBU and the disorder of the pore water, the layer can be shifted towards each of the three neighboring pores (Figure A 40, b, c, d). In addition, a completely eclipsed stacking of the poly(heptazine imide) layers (Figure A 40, e) will be considered, as this stacking leads to a higher lattice symmetry and therefore to fewer peaks in the diffraction pattern.

Simulations of the diffractional effects of planar defects in the poly(heptazine imide) framework

For the simulations of the diffractional effects of planar defects in the poly(heptazine imide) lattice a supercell approach implemented into the TOPAS software[37] was used. Therefore, the unit cell of H-PHI had to be transformed into a pseudo-trigonal metric (Table A 3). The stacking sequence of the poly(heptazine imide) layers was described by *stacking vectors*. In the idealized, faultless model of the H-PHI phase the stacking vector is represented by the orientation of the crystallographic *c*-axis. For the simulations of the diffraction patterns of stacking faulted H-PHI four possible stacking-types were considered (Figure A 40, b-e) with each of them represented by an individual stacking vector that also had to be transformed into the pseudo-trigonal metric. In each simulation the diffractions patterns of 100 randomly created supercells each of them containing 200 poly(heptazine imide) layers using an array of up to four stacking vectors were calculated and averaged, which results in comparable simulation as obtained by the recursive *DIFFaX* routine.[38] The random creation of the stacking sequences was directed by *transition probabilities* that were systematically varied during one series of simulations (see below). In each series of the simulations a different set of transition probabilities, i.e. a different *transitions probability matrix* and different arrays of stacking vectors were used in order to represent different faulting scenarios.

Table A 3. Overview on the lattice parameters and the stacking vectors of the determined cell of H-PHI and of the transformed unit cell used for the simulations of the diffractional effects of planar defects using a supercell approach.

original cell		**transformed cell**	
Space group	$\mathrm{P}\bar{1}$	**Space group**	$P1$
V/ Å³	460	**V/ Å³**	$n \cdot 460$
a/ Å	12.963	**a'/ Å**	12.963
b/ Å	12.963	**b'/ Å**	12.963
c/ Å	4.319	**c'/ Å**	$n \cdot 3.1981$
α/ °	109.28	**α'/ °**	90
β/ °	109.28	**β'/ °**	90
γ/ °	≈ 120	**γ'/ °**	≈ 120
S	$\begin{pmatrix}0\\0\\1\end{pmatrix}$	**S**	$\in \left\{\begin{pmatrix}-0.22\\-0.22\\1\end{pmatrix}, \begin{pmatrix}0.22\\0\\1\end{pmatrix}, \begin{pmatrix}0\\0.22\\1\end{pmatrix}, \begin{pmatrix}0\\0\\1\end{pmatrix}\right\}$

n is the number of poly(heptazine imide) layers of the supercells

Faulting Scenario I

In the first faulting scenario, the diffractional effects of random transitions among pore directed stacking using only one pore (Figure A 40, b) and eclipsed stacking were simulated. For the transition from pore I directed stacking to eclipsed stacking the transition probability parameter P_x was defined, which was also used for the probability of transitions within the eclipsed stacking (Figure A 41). As the columns of the transition probability matrix (Table A 4) have to sum up to 1, all other layer-to-layer transitions are associated with a transition probability of $1-P_x$.

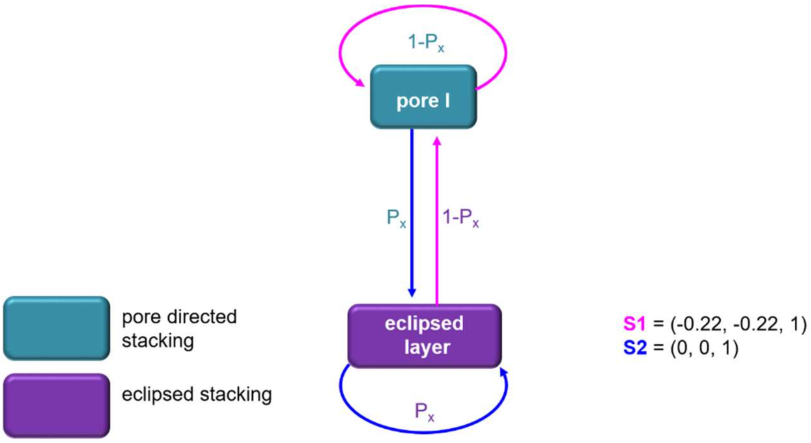

Figure A 41. Schematic illustration of the microstructural model used for the faulting scenario I, the transition probability matrix is given in Table A 4.

Table A 4. Transition probability matrix including the stacking vectors of faulting scenario I (Figure A 41).

from↓/ to→	**pore I**	**eclipsed layer**
pore I	$1-P_x$, **S1**	P_x, **S2**
eclipsed layer	$1-P_x$, **S1**	P_x, **S2**

In the simulation series the transition parameter P_x was gradually increased from 0 to 1 in order to simulate the transition from the pure, ordered pore directed stacking to eclipsed stacking (Figure A 42). An initial increase of the fault probability leads to a vast broadening of most reflections in the diffraction patterns. This is most pronounced for the 010 reflection, which is broadened but also shifted towards lower diffraction angles. At $P_x \approx 0.3$, this reflection begins to merge with the $\bar{1}10$ reflection which results in an overall triangular peak shape. Beginning at $P_x > 0.5$ new reflections appear and sharpen with increasing P_x, as a more and more ordered, eclipsed stacking is simulated. The reflections attributed to an ordered, eclipsed stacking (Figure A 42, grey background) are not apparent in the measured pattern (blue pattern). In addition, in the measured pattern the 010 reflection is still present, not shifted and not broadened to a high degree. As none of the simulated patterns is qualitatively good in agreement with the measured pattern, faulting scenario I does not represent the microstructure of the H-PHI sample.

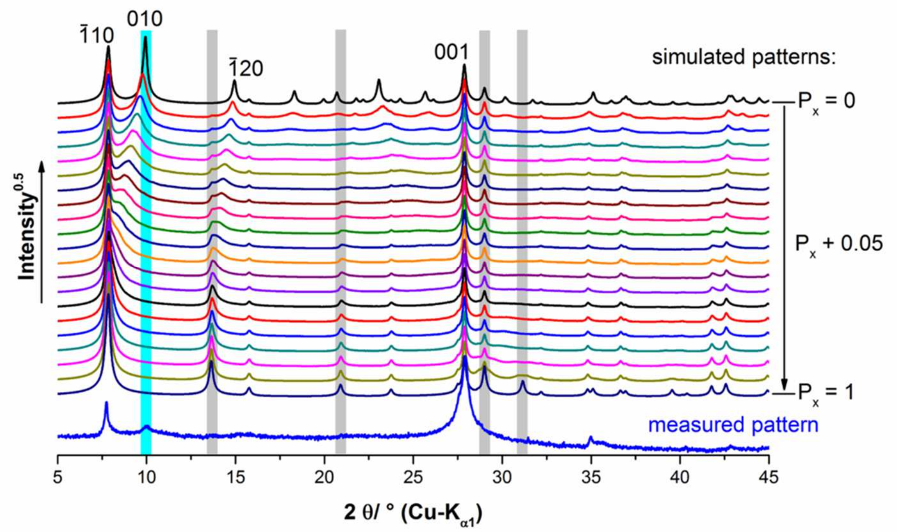

Figure A 42. Comparison of a series of simulated powder patterns of stacking faulted H-PHI using faulting scenario I (Figure A 41, Table A 4) in which the probability for eclipsed stacking, P_x, was gradually increased with the measured pattern. Reflections that are apparent in pure eclipsed stacking (P_x =1.0) but not in the measured pattern are highlighted with grey background, reflections that are apparent in the measured pattern but not in the simulated are highlighted with cyan background color.

Faulting Scenario II

In another faulting scenario transitions among the three different kinds of pore directed stacking (Figure A 40, b-d) were simulated (Figure A 43). The 3x3 transition probability matrix (Table A 5) was constraint by using one parameter, P_y, which describes the probability that there is a change in the direction of the stacking order.

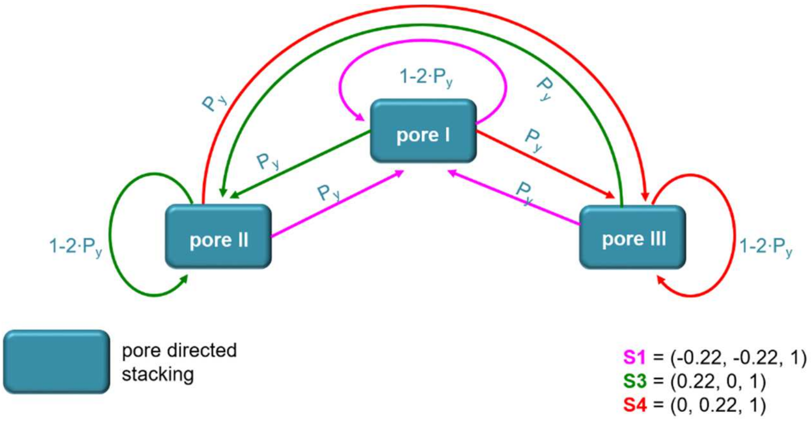

Figure A 43. Schematic illustration of the microstructural model used for the faulting scenario II, the transition probability matrix is given in Table A 5.

Table A 5. Transition probability matrix including the stacking vectors of faulting scenario II (Figure A 43).

from↓/ to→	pore I	pore II	pore III
pore I	$1\text{-}2{\cdot}P_y$, **S1**	P_y, **S3**	P_y, **S4**
pore II	P_y, **S1**	$1\text{-}2{\cdot}P_y$, **S3**	P_y, **S4**
pore III	P_y, **S1**	P_y, **S3**	$1\text{-}2{\cdot}P_y$, **S4**

In the simulation series the parameter P_y was gradually increased from 0.00 representing a complete ordered pore directed stacking to 0.33, which describes a complete random pore directed stacking (Figure A 44). An increased probability of a change in the stacking direction leads to broadening of almost all reflections present in the pattern of H-PHI except for the $\bar{1}10$ and the 001 reflection. The peak broadening is most pronounced for the 010 reflection. Nevertheless, it shows only a slight shift towards lower diffraction angles, it merges due to vast broadening with the $\bar{1}10$ reflections, which appears as a triangular peak shape at the basis. The simulated diffraction pattern of a complete random pore directed stacking (P_y = 0.33) exhibit strong similarities with the measured pattern (Figure A 44, blue pattern). A complete random pore directed stacking, however, leads to the disappearance of the 010 reflection, which is still present in the measured pattern (blue background). This indicates that the faulting scenario has to be extended by an additional element.

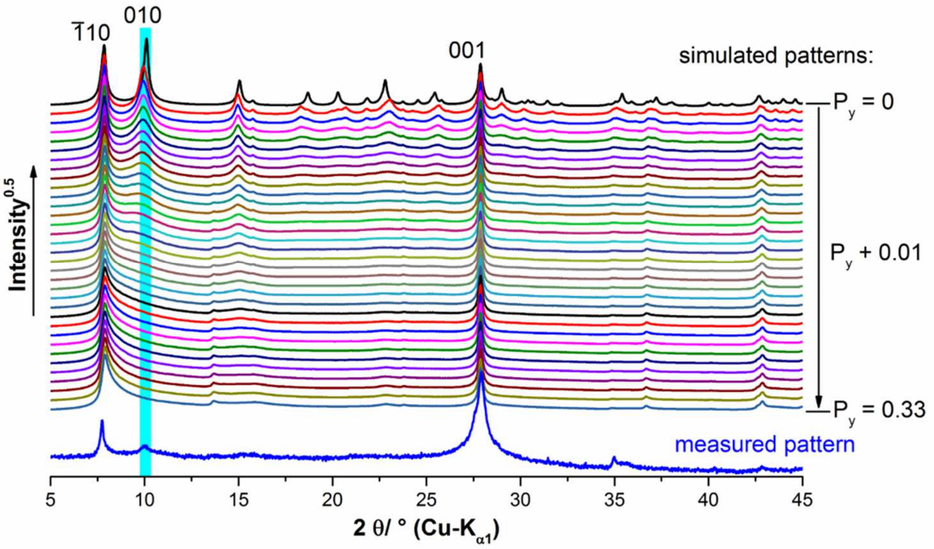

Figure A 44. Comparison of a series of simulated powder patterns of stacking faulted H-PHI using faulting scenario II (Figure A 43, Table A 5) in which the probability for a change in the direction of pore directed stacking, P_y, was gradually increased with the measured pattern. Reflections that are apparent in the measured pattern but not in the simulated for complete random pore directed stacking (P_y = 0.33) are highlighted with cyan background color.

Faulting Scenario III

In faulting scenario III, faulting scenario II was extended by adding the eclipsed layer stacking (Figure A 45). The transition probability matrix (Table A 6) was constraint by keeping the probability of a change in the direction of pore directed stacking constant at ⅓, which represents a complete random pore directed stacking. Within this stacking order eclipsed stacked layers were included as defects. Both the number of eclipsed stacked defects and the extension of the eclipsed stacked section were described by the parameter P_x (Figure A 45, Table A 6) that was gradually increased during the simulations.

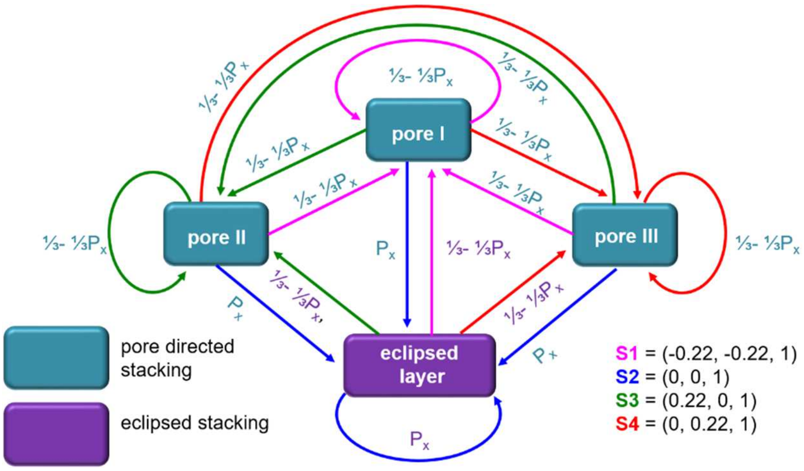

Figure A 45. Schematic illustration of the microstructural model used for the faulting scenario III, the transition probability matrix is given in Table A 6.

Table A 6. Transition probability matrix including the stacking vectors of faulting scenario III (Figure A 45).

from↓/ to→	pore I	pore II	pore III	eclipsed layer
pore I	⅓-⅓·P_x, **S1**	⅓-⅓·P_x, **S3**	⅓-⅓·P_x, **S4**	P_x, **S2**
pore II	⅓-⅓·P_x, **S1**	⅓-⅓·P_x, **S3**	⅓-⅓·P_x, **S4**	P_x, **S2**
pore III	⅓-⅓·P_x, **S1**	⅓-⅓·P_x, **S3**	⅓-⅓·P_x, **S4**	P_x, **S2**
eclipsed layer	⅓-⅓·P_x, **S1**	⅓-⅓·P_x, **S3**	⅓-⅓·P_x, **S4**	P_x, **S2**

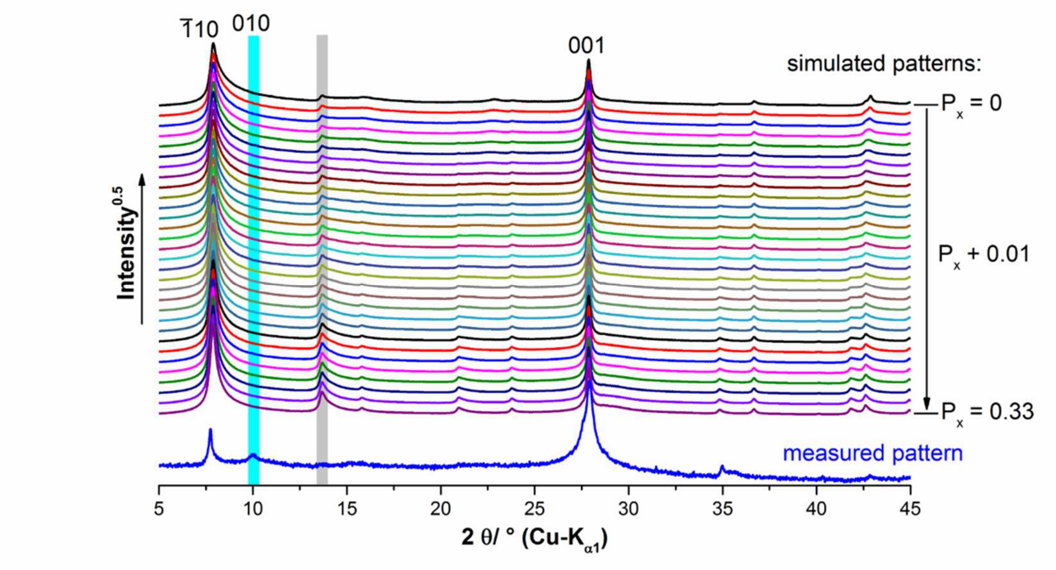

Figure A 46. Comparison of a series of simulated powder patterns of stacking faulted H-PHI using faulting scenario III (Figure A 45, Table A 6) in which the probability of eclipsed stacking, P_x, in a complete random pore directed stacking was gradually increased with the measured pattern. Reflections that appear during increasing the number and extension of eclipsed stacked layers (P_x) but are not in the measured pattern are highlighted with grey background, reflections that are apparent in the measured pattern, but not in the simulation, are highlighted with cyan background color.

The increase of the number and the extension of eclipsed stacked defects in a complete random pore directed stacking in H-PHI leads to the appearance of additional reflections. These reflections, however, are not present in the measured pattern, which is most striking at around 14 °2 θ (Figure A 46, grey background). This faulting scenario also does not explain the appearance of the residue of the 010 reflection in the simulated pattern (cyan background). Hence, extending the microstructural model of a complete random pore directed stacking by eclipsed stacking does not lead to a satisfying explanation for the observed diffractional effects.

Faulting Scenario IV

In faulting scenario IV only transitions among pore directed stacking were used to simulate a crystallographic intergrowth of a complete random pore directed stacked domain (P_y = ⅓) with an ordered pore directed stacked domain (Figure A 47). A probability parameter P_{dom} was defined that describes the *number* of ordered domains intergrown with a random domain directed stacking. After the transition from random pore directed stacking to an ordered domain, the stacking will continue in the same pore direction (Figure A 47, thick arrows). The parameter P_{ext} describes the probability for a transition from an ordered pore directed stacking to a randomly oriented pore directed stacking and therefore the *extension* of the ordered domain. The transition probability matrix is given in Table A 7.

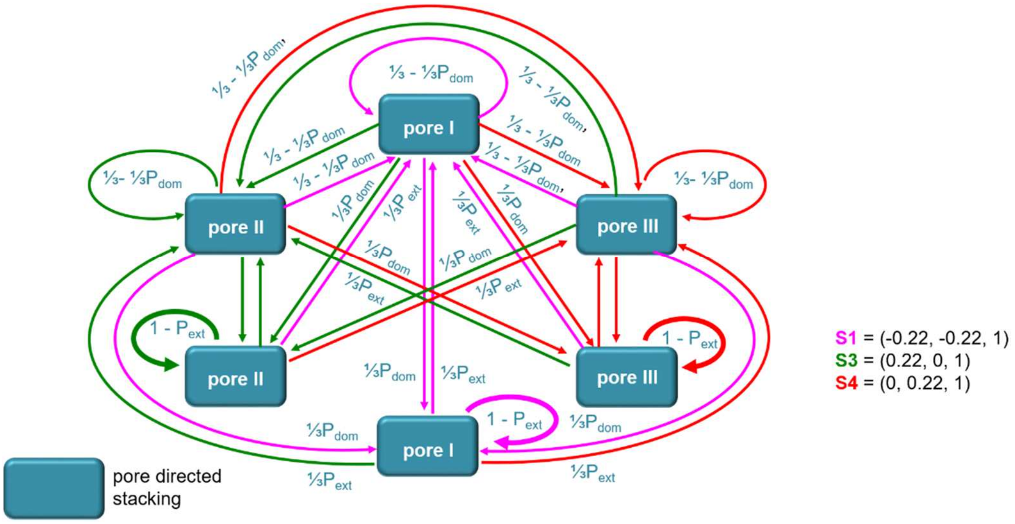

Figure A 47. Schematic illustration of the microstructural model used for the faulting scenario IV, the transition probability matrix is given in Table A 7.

Table A 7. Transition probability matrix including the stacking vectors of faulting scenario IV (Figure A 47).

from↓/ to→		random stacking			ordered domains		
		pore I	**pore II**	**pore III**	**pore I**	**pore II**	**pore III**
random stacking	**pore I**	⅓-⅓·P_{dom}, **S1**	⅓-⅓·P_{dom}, **S3**	⅓-⅓·P_{dom}, **S4**	⅓·P_{dom}, **S1**	⅓·P_{dom}, **S3**	⅓·P_{dom}, **S4**
	pore II	⅓-⅓·P_{dom}, **S1**	⅓-⅓·P_{dom}, **S3**	⅓-⅓·P_{dom}, **S4**	⅓·P_{dom}, **S1**	⅓·P_{dom}, **S3**	⅓·P_{dom}, **S4**
	pore III	⅓-⅓·P_{dom}, **S1**	⅓-⅓·P_{dom}, **S3**	⅓-⅓·P_{dom}, **S4**	⅓·P_{dom}, **S1**	⅓·P_{dom}, **S3**	⅓·P_{dom}, **S4**
ordered domains	**pore I**	⅓·P_{ext}, **S1**	⅓·P_{ext}, **S3**	⅓·P_{ext}, **S4**	1-P_{ext}, **S1**	-	-
	pore II	⅓·P_{ext}, **S1**	⅓·P_{ext}, **S3**	⅓·P_{ext}, **S4**	-	1-P_{ext}, **S3**	-
	pore III	⅓·P_{ext}, **S1**	⅓·P_{ext}, **S3**	⅓·P_{ext}, **S4**	-	-	1-P_{ext}, **S4**

In the series of simulation presented in Figure A 48 the probability for a backshift from an ordered to a random pore directed stacking was kept constant at P_{ext} = 3 %, which means that the ordered domain was kept at a high extension, i.e. after 22 layers ≡ 7 nm of ordered stacking there is a probability of > 50 % for a backshift to random pore directed stacking. The number of domains represented by the parameter P_{dom} was gradually increased. An increase of the number of ordered domains (P_{dom} > 0.03) leads to the appearance of the 010 reflection in the simulated patterns (Figure A 48, cyan background). Additional reflections become visible only after a further increase of the number of ordered domains (P_{dom} > 0.10). Hence, it can be concluded that faulting scenario IV (Figure A 48) is a suitable, qualitative approximation of the microstructure of the H-PHI phase.

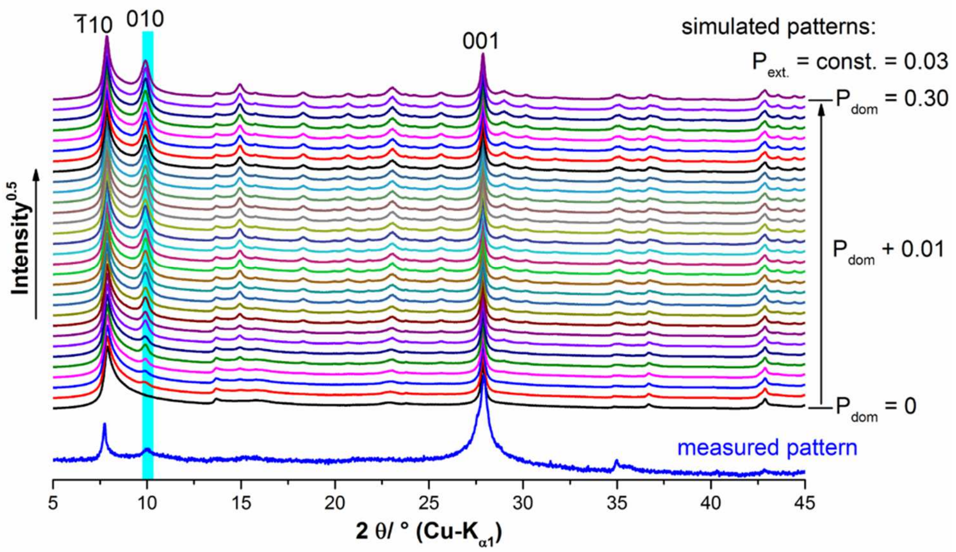

Figure A 48. Comparison of a series of simulated powder patterns of stacking faulted H-PHI using faulting scenario IV (Figure A 47, Table A 7) in which the probability of the occurrence of an ordered domain, P_{dom}, in a complete random pore directed stacking was gradually increased while the extension of the ordered domain was kept constant ($P_{ext.}$ = 0.03) with the measured pattern. The position of the 010 reflection is highlighted by cyan background.

Final evaluation

The absence of eclipsed stacking related reflections at (13.6, 15.8, 21.0 23.8, 29.0, 31.2)° 2θ in the measured patterns clearly indicated that there are no coherently scattering domains of eclipsed stacked poly(heptazine imide) layers in the H-PHI material. The presence of a few, isolated eclipsed stacked defects in the material, however, cannot be excluded. Systematic simulations indicated that the microstructure of H-PHI is mainly governed by pore directed stacking. Due to the intrinsic trigonal symmetry of the heptazine SBU, this type of stacking exhibits three fundamental directions. The vast broadening of the reflections indicated a non-coherent stacking, i.e. the stacking order is a complete random distribution of these three fundamental stacking directions. A remnant of the 010 reflection also points to the fact that few domains of ordered pore directed stacking are still apparent in the microstructure of the material (Figure A 49). As the scattering effect of the pore material, which modulates the peak intensities in relation to the intensity of 001 basal reflection, could not be included into the simulation series, quantitative information on the amount and extensions of the ordered stacked domains in the material, cannot be extracted.

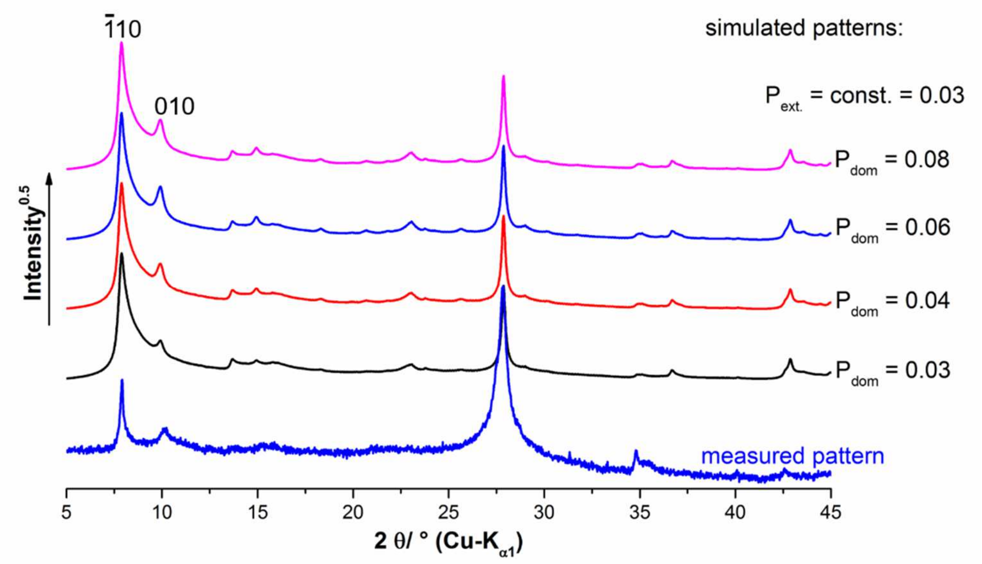

Figure A 49. Comparison of selected simulated diffraction patterns of faulting scenario IV (Table A 7, Figure A 47) with the measured pattern of H-PHI.

Synopsis: The 3-dimensional structure of the poly(heptazine imide) framework

The 3-dimensional structure of the poly(heptazine imide) framework, i.e. the arrangement of poly(heptazine imide) layers is governed by the ions and molecules (e.g. K^+ and H_2O) situated in the pores. By interactions between the pore particles and the poly(heptazine imide) backbone a stacking order in which the layers are arranged in a slightly staggered fashion, i.e. a layer is shifted towards the pore of the preceding layer, is more favorable than a complete eclipsed stacking. Due to the trigonal symmetry of the heptazine SBU, there are three symmetry equivalent pores per heptazine unit. In H-PHI the pores are exclusively filled with water molecules. According to the small spacial extension of water molecule and due to the interlayer spacing of $\approx$ 3.2 Å, water only mediates the interactions between two adjacent layers. In consequence there is no long-range order of the layer orientation in the structure of H-PHI. Hence, transitions among all three possible pore directed stackings occur in a complete random fashion. In contrast the powder pattern of K-PHI indicates a long-range order in *c*-direction. Due to the positive charge and the large ionic radius of potassium a partial hydration sphere is formed with the water molecule in the pores. Therefore, potassium directs the stacking order of at least three adjacent layers directly and by the arrangement of pore water molecules by forming the partial hydration sphere even more layers indirectly. The ordered domains that are present in the microstructure of H-PHI can be attributed to residual potassium (as indicated by elemental analysis showing 0.5 w% potassium for H-PHI) that was not completely exchanged during the conversion from K-PHI to H-PHI.

6.13 Protonation with different acids/concentrations

Figure A 50–Figure A 52 show that neither the type of acid, e.g. HCl, H_3PO_4, H_2SO_4 or $HClO_4$, nor the molarity of the acid is relevant for the transformation from K-PHI to H-PHI. Higher acid concentration most likely just result in a faster hydrolysis of attached functional groups. Also none of the anions could be found in the corresponding H-PHI. Thus, the formed salt from the acid/base reaction is washed out from the pores upon washing with water. This is not the case for the related poly(triazine imide) structure where "LiCl" is present within the pore.[28] As expected, all differently treated H-PHI samples performed similarly well in photocatalytic experiments. Additionally, we tried to extract the potassium ions by stirring the polymer in a crown-18-ether known to complex alkali ions. However, we could not detect any change in the structure after washing why we conclude that either the pores are not accessible to the cryptand or the potassium ions are bound to the network quite strongly.

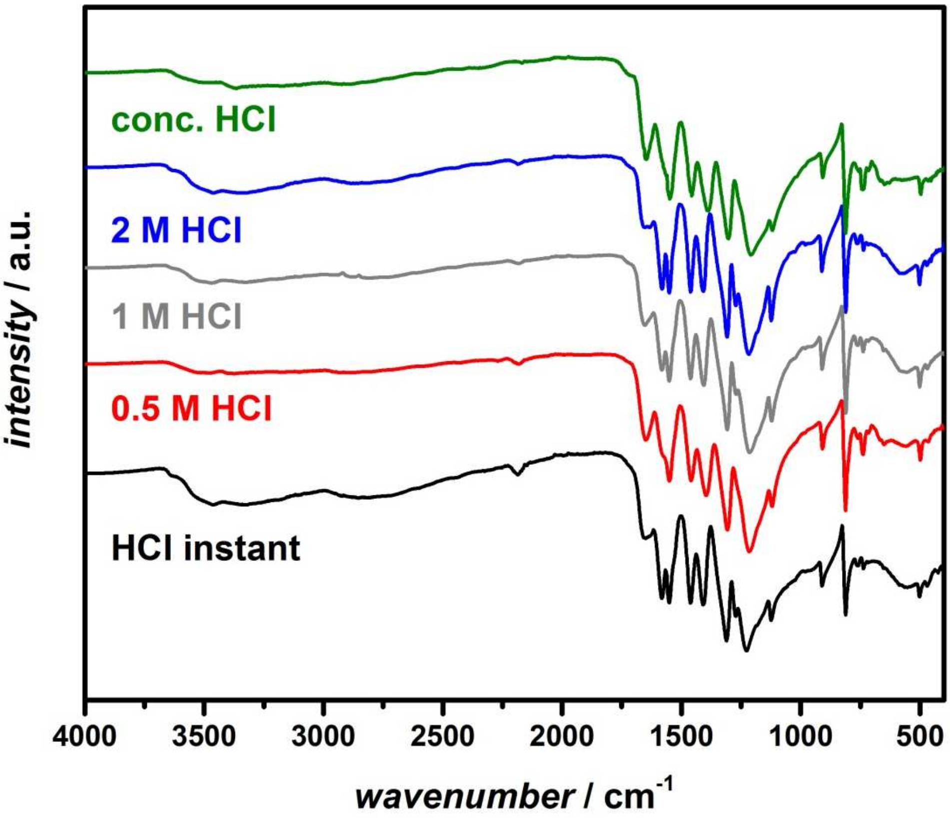

Figure A 50. IR spectra of K-PHI treated with different concentrations of hydrochloric acid. HCl instant was treated for only 5 min. while the rest was treated overnight. The major difference is the complete removal of the NCN-vibration at ca. 2170 cm^{-1} with higher concentrations.

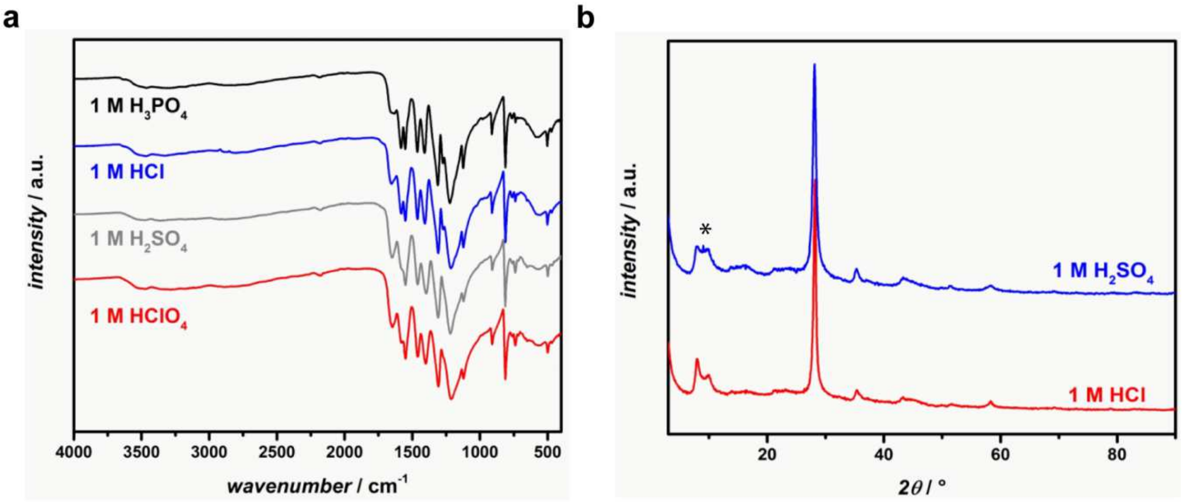

Figure A 51. (a) IR spectra and (b) powder XRD of K-PHI treated with HCl and H_2SO_4. We conclude that there is no significant influence of the acid that is used. Asterisk marks an artifact of the diffractometer.

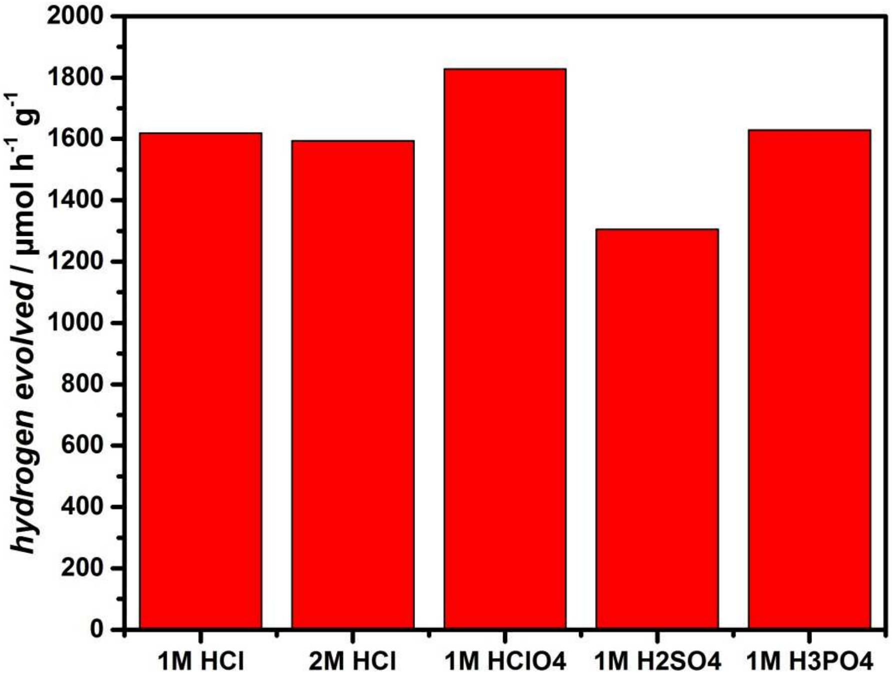

Figure A 52. Photocatalytic performance of K-PHI treated with various acids. The catalytic performance is neither dependent on the concentration of the acid nor their type.

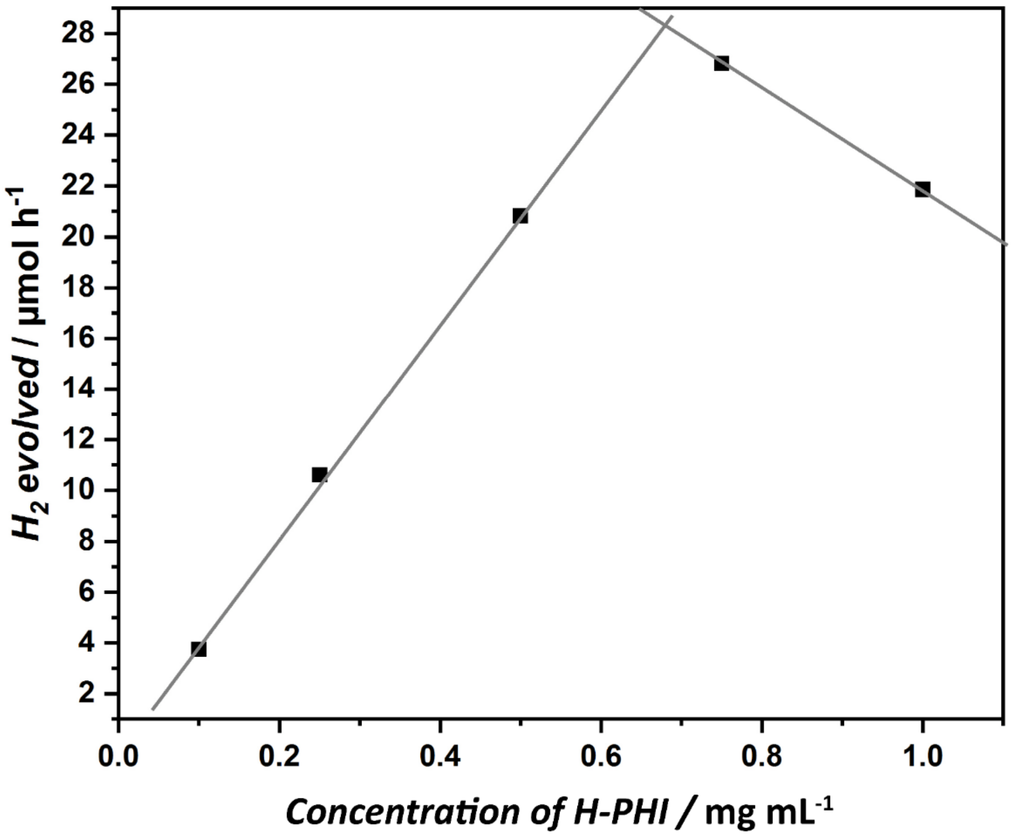

Figure A 53. Photocatalytic activity with respect to the H-PHI concentration in the suspension. According to this a concentration of approx. 0.7 mg/mL is suitable for optimal performance. The catalytic reaction was performed with Pt as co-catalyst (2 wt%) and methanol as sacrificial donor.

6.14 Base treated H-PHI

H-PHI may be treated with a base to reconvert it back to its anionic form and the corresponding alkali metal cation. The transformation from optimized K-PHI to H-PHI by stirring in diluted aqueous HCl and back to K-PHI by stirring in aqueous KOH is presented in Figure A 54. Although partial hydrolysis and hence degradation of the backbone and the functional NCN-groups may be expected, the main characteristic peaks in the analyses are retained. However, due to a likely loss of functional groups during the initial treatment with acids, the activity of the pristine K-PHI for H_2-Evolution is not totally recovered. Additionally, the increased tail in the diffuse reflectance spectrum (Figure A 54e) gives rise to the assumption of increased degradation of the photocatalyst, e.g. due to hydrolysis.

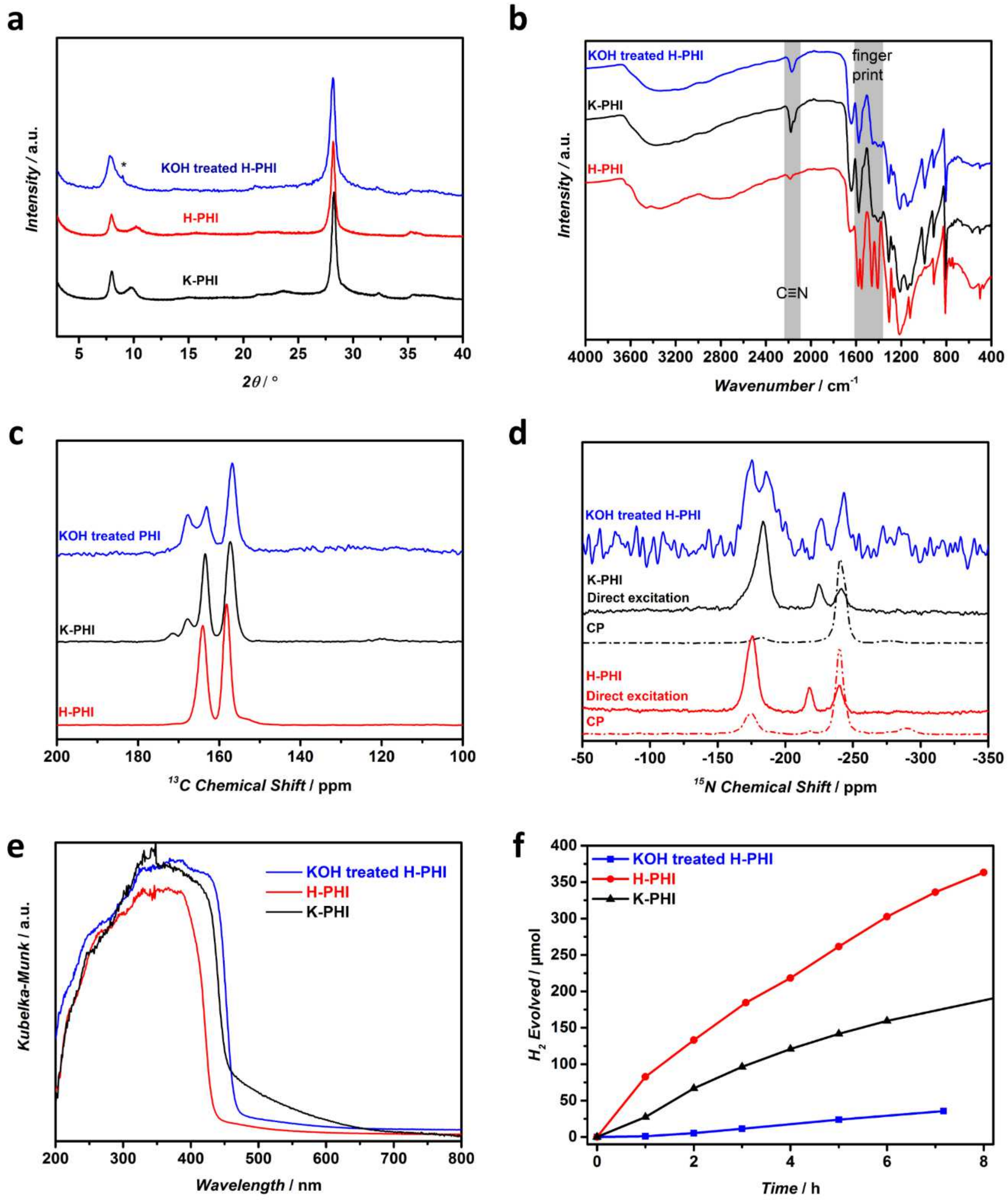

Figure A 54. (a) XRPD patterns, (b) FT-IR spectra, (c) ^{13}C cross-polarization (CP) MAS ssNMR spectra, (d) ^{15}N MAS ssNMR (direct and CP) (e) diffuse reflectance spectra and (f) photocatalytic performance of pristine optimized K-PHI, the acid treated H-PHI and the back-converted KOH treated H-PHI.

6.15 Elemental Analysis

Table A 8. Composition of crystalline K-PHI and optimized K-PHI determined by combustion analysis and ion coupled plasma (ICP) analysis. The values were averaged over several batches. Water was indirectly determined as the residual mass.

	Ampoule crystalline K-PHI		Crucible optimized K-PHI	
	wt%	mol%	wt%	mol%
C	27.6	34.9	26.2	32.6
N	46.3	50.1	43.6	46.5
K	13.7	5.3	9.0	3.4
S	2.0	0.9	0.4	0.2
H	(1.7)	-	(2.2)	-
H_2O[a)]	10.4	8.7	20.8	17.3
Total	100.0		100.0	100.0
N/C	**1.438**	$C_7N_{10}K_1S_{0.18}$	**1.426**	$C_7N_{10}K_{0.7}S_{0.04}$

[a)] All weight percents were added and the rest along with the hydrogen content was defined as water. This way the hydrogen content is not reliable and therefore not included in the chemical formula.

Table A 9. Composition of crystalline H-PHI and optimized H-PHI determined by combustion analysis and ion coupled plasma (ICP) analysis. The values were averaged over several batches. Water was indirectly determined as the residual mass.

	Ampoule crystalline H-PHI		Crucible optimized H-PHI	
	wt%	mol%	wt%	mol%
C	29.0	33.9	28.7	33.6
N	49.7	49.8	48.0	48.2
K	0.5	0.2	0.2	0.1
S	0.4	0.2	0	0
H	(3.0)	-	(3.1)	-
H_2O[a)]	20.4	15.9	23.1	18.1
Total	100.0		100.0	
N/C	**1.469**	$C_7N_{10.2}K_{0.04}S_{0.04}$	**1.434**	$C_7N_{10.2}K_{0.02}$

[a)] All weight percents were added and the rest along with the hydrogen content was defined as water. This way the hydrogen content is not reliable and therefore not included in the chemical formula.

As washing the substance with THF did not significantly impact the sulfur content, it is either covalently bound (doping in the backbone) or unaccessible in pores. However, when washed with diluted acids such as HCl a loss of sulfur is observed which may be explained by a delamination and successive removal of intraporous molecules/ions.

6.16 Water sorption

Water sorption isotherms were measured on an Autosorb-iQ surface analyzer with vapor option (Quantachrome Instruments, USA). To initially remove guest molecules the samples were outgassed in vacuum at 200 °C for 12 h. The measurements were performed at 273 K. The overall uptake of water is 340 ccm/g for optimized K-PHI, 417 ccm/g for optimized H-PHI, 169 ccm/g for crystalline K-PHI and 196 ccm/g for crystalline H-PHI. The desorption of water is reversible. However, at low pressures the initial amount is not reached and complete desorption of strongly bound water likely requires higher temperatures for these materials. This is expected since the ssNMR results also indicate a rather strong binding situation between water and the carbon nitride network. In the case of optimized H-PHI and K-PHI a significant uptake of water can be observed. The maximum adsorbed amount is somewhat larger in the case of H-PHI, which is in line with the other experimental data, since elemental analyses also show that more water is present in H-PHI. The lower adsorption volume for crystalline samples is expected due to the larger crystallites and therefore less accessible surface area and also follows the data from elemental analysis.

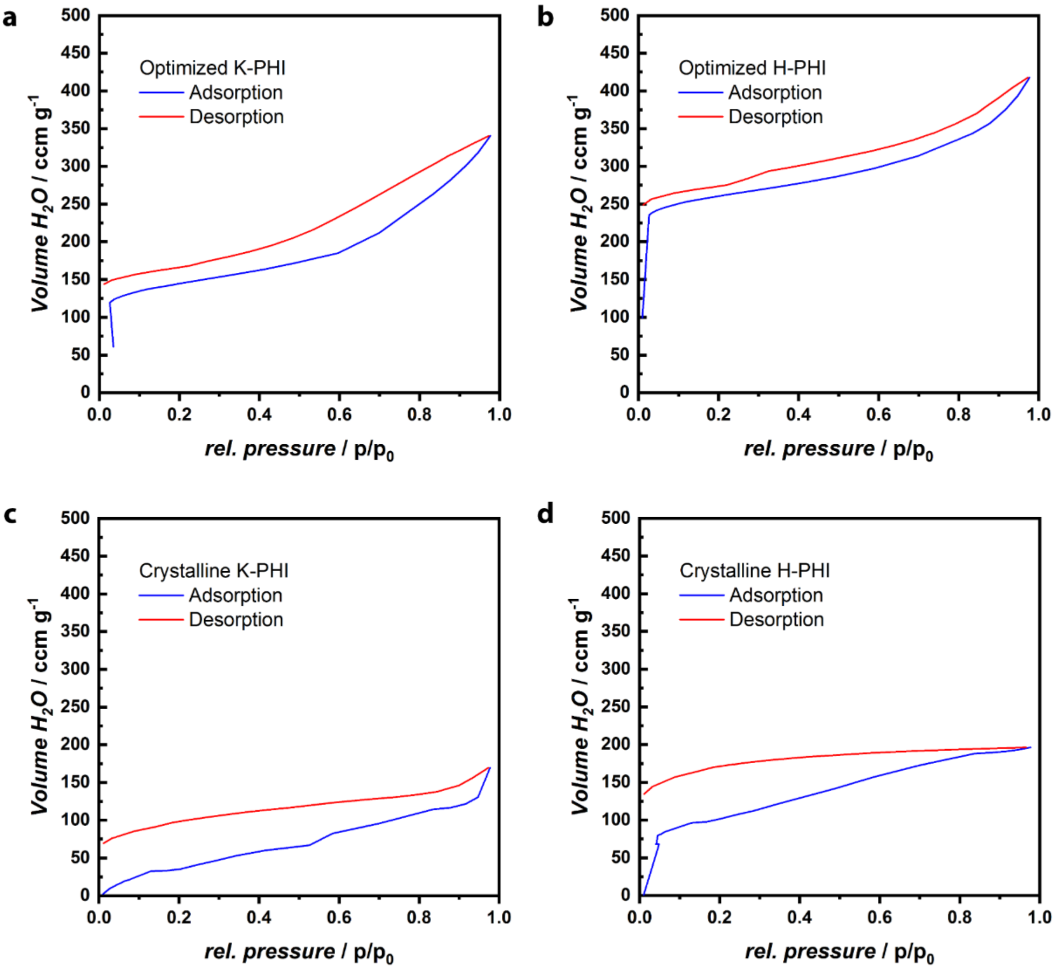

Figure A 55. Water sorption isotherms at 273 K for (a) optimized K-PHI, (b) optimized H-PHI, (c) crystalline K-PHI and (d) crystalline H-PHI.

6.17 Raman spectroscopy

The Raman spectra were recorded with an excitation wavelength of 532 nm and 633 nm. In general, K-PHI and H-PHI both show a strong luminescence background for both measured excitation wavelengths (Figure A 56). Some of the main signals are still distinguishable from the background, which are within the expected range for triazine or heptazine based systems.[39,40] No significant differences of those signals were observed for H-PHI and K-PHI. The weaker intensities in crystalline samples are likely to arise from looser packing in the capillary and therefore less substance in the focus of the laser.

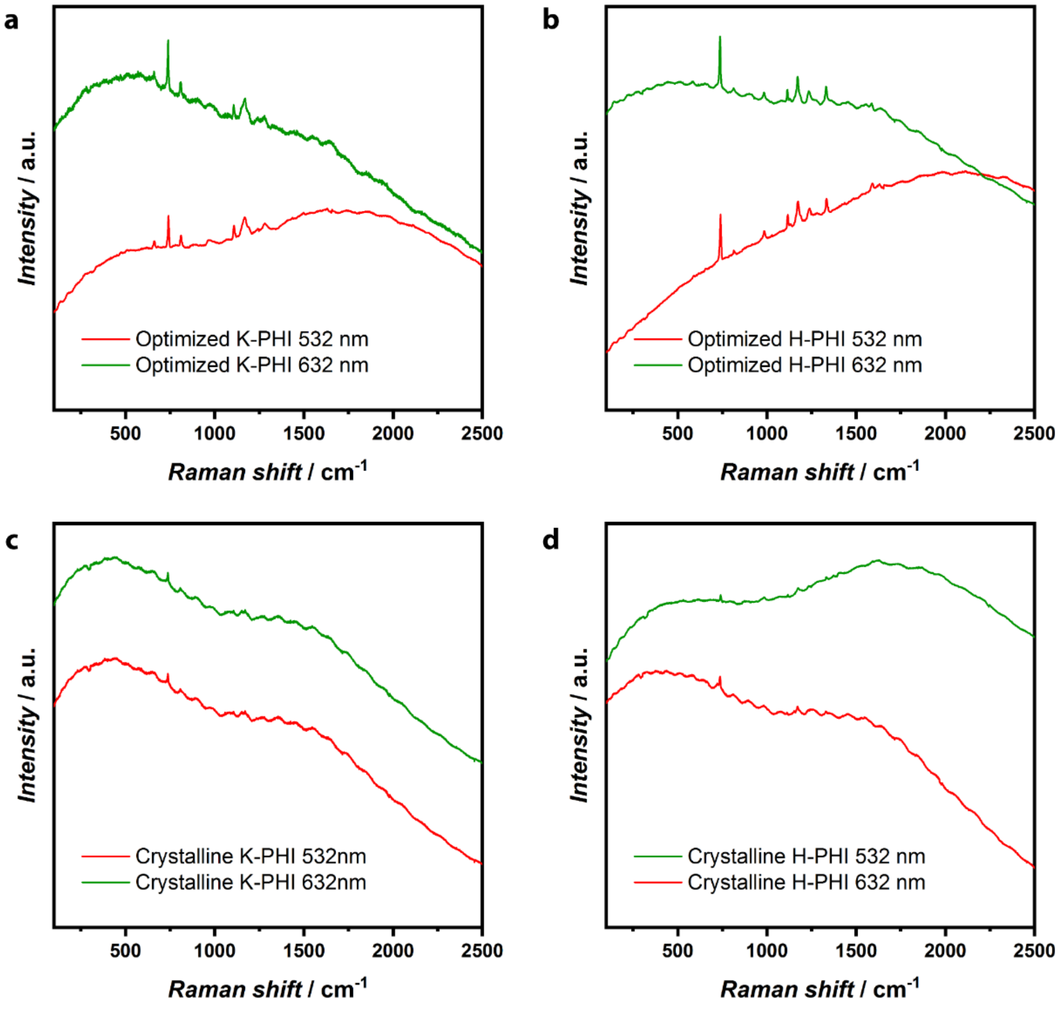

Figure A 56. Raman spectra Raman spectra of (a) optimized K-PHI, (b) optimized H-PHI, (c) crystalline K-PHI and (d) crystalline H-PHI recorded with a 532 nm and 632 nm laser, respectively. The signals are overlapped by a strong fluorescence for both wavelengths.

6.18 References

(1) Lau, V. W.-h.; Moudrakovski, I.; Botari, T.; Weinberger, S.; Mesch, M. B.; Duppel, V.; Senker, J.; Blum, V.; Lotsch, B. V. Rational design of carbon nitride photocatalysts by identification of cyanamide defects as catalytically relevant sites. *Nat. Commun.* **2016**, *7*, 12165. DOI: 10.1038/ncomms12165.

(2) Lau, V. W.-h.; Yu, V. W.-z.; Ehrat, F.; Botari, T.; Moudrakovski, I.; Simon, T.; Duppel, V.; Medina, E.; Stolarczyk, J.; Feldmann, J.; Blum, V.; Lotsch, B. V. Urea-Modified Carbon Nitrides: Enhancing Photocatalytic Hydrogen Evolution by Rational Defect Engineering. *Adv. Energy Mater.* **2017**, 1602251. DOI: 10.1002/aenm.201602251.

(3) Lau, V. W.-h.; Klose, D.; Kasap, H.; Podjaski, F.; Pignié, M.-C.; Reisner, E.; Jeschke, G.; Lotsch, B. V. Dark Photocatalysis: Storage of Solar Energy in Carbon Nitride for Time-Delayed Hydrogen Generation. *Angew. Chem. Int. Ed.* **2017**, *56* (2), 510–514. DOI: 10.1002/anie.201608553.

(4) Brinkmann, A.; Kentgens, A. P. M. Proton-selective ^{17}O-^{1}H distance measurements in fast magic-angle-spinning solid-state NMR spectroscopy for the determination of hydrogen bond lengths. *J. Am. Chem. Soc.* **2006**, *128* (46), 14758–14759. DOI: 10.1021/ja065415k.

(5) Levitt, M. H. Symmetry-Based Pulse Sequences in Magic-Angle Spinning Solid-State NMR. In *eMagRes*; R. K. Harris, R. L. Wasylishen, Eds.; Wiley, 2007.

(6) Chupas, P. J.; Qiu, X.; Hanson, J. C.; Lee, P. L.; Grey, C. P.; Billinge, S. J. L. Rapid-acquisition pair distribution function (RA-PDF) analysis. *J. Appl. Crystallogr.* **2003**, *36* (6), 1342–1347. DOI: 10.1107/S0021889803017564.

(7) David A. Case; Robin M. Betz; D.S. Cerutti; Thomas Cheatham; Thomas Darden; Robert E Duke; T.J. Giese; Holger Gohlke; Andreas W Götz; Nadine Homeyer; Saeed Izadi; Pawel A Janowski; J. Kaus; Andriy Kovalenko; Tai-Sung Lee; S. LeGrand; P. Li; C. Lin; Tyler Luchko; Ray Luo; B. Madej; D. Mermelstein; Kenneth Merz; Gérald Monard; Hung Nguyen; Hai Nguyen; I. Omelyan; Alexey Onufriev; Daniel R Roe; Adrian E. Roitberg; Celeste Sagui; Carlos Simmerling; Wesley M. Botello-Smith; Jason M Swails; R.C. Walker; J. Wang; R.M. Wolf; Xiongwu Wu; L. Xiao; Peter A. Kollman. *Amber 16, University of California, San Francisco*.

(8) Phillips, J. C.; Braun, R.; Wang, W.; Gumbart, J.; Tajkhorshid, E.; Villa, E.; Chipot, C.; Skeel, R. D.; Kalé, L.; Schulten, K. Scalable molecular dynamics with NAMD. *J. Comput. Chem.* **2005**, *26* (16), 1781–1802. DOI: 10.1002/jcc.20289.

(9) Stadelmann, P. A. EMS - a software package for electron diffraction analysis and HREM image simulation in materials science. *Ultramicroscopy* **1987**, *21* (2), 131–145. DOI: 10.1016/0304-3991(87)90080-5.

(10) Brivio, J.; Alexander, D. T. L.; Kis, A. Ripples and layers in ultrathin MoS_2 membranes. *Nano Lett.* **2011**, *11* (12), 5148–5153. DOI: 10.1021/nl2022288.

(11) Meyer, J. C.; Geim, A. K.; Katsnelson, M. I.; Novoselov, K. S.; Booth, T. J.; Roth, S. The structure of suspended graphene sheets. *Nature* **2007**, *446* (7131), 60–63. DOI: 10.1038/nature05545.

(12) Patterson, A. L. The Scherrer Formula for X-Ray Particle Size Determination. *Phys. Rev.* **1939**, *56* (10), 978–982. DOI: 10.1103/PhysRev.56.978.

(13) Cheary, R. W.; Coelho, A. A.; Cline, J. P. Fundamental Parameters Line Profile Fitting in Laboratory Diffractometers. *J. Res. Natl. Inst. Stand. Technol.* **2004**, *109* (1), 1–25. DOI: 10.6028/jres.002.

(14) Cheary, R. W.; Coelho, A. A fundamental parameters approach to X-ray line-profile fitting. *J. Appl. Crystallogr.* **1992**, *25* (2), 109–121. DOI: 10.1107/S0021889891010804.

(15) Coelho, A. A. TOPAS and TOPAS-Academic:An optimization program integrating computer algebra and crystallographic objects written in C++. *J. Appl. Crystallogr.* **2018**, *51* (1), 210–218. DOI: 10.1107/S1600576718000183.

(16) Adamo, C.; Barone, V. Toward reliable density functional methods without adjustable parameters:The PBE0 model. *J. Chem. Phys.* **1999**, *110* (13), 6158–6170. DOI: 10.1063/1.478522.

(17) Ernzerhof, M.; Scuseria, G. E. Assessment of the Perdew–Burke–Ernzerhof exchange-correlation functional. *J. Chem. Phys.* **1999**, *110* (11), 5029–5036. DOI: 10.1063/1.478401.

(18) Grimme, S.; Antony, J.; Ehrlich, S.; Krieg, H. A consistent and accurate ab initio parametrization of density functional dispersion correction (DFT-D) for the 94 elements H-Pu. *J. Chem. Phys.* **2010**, *132* (15), 154104. DOI: 10.1063/1.3382344.

(19) Schäfer, A.; Huber, C.; Ahlrichs, R. Fully optimized contracted Gaussian basis sets of triple zeta valence quality for atoms Li to Kr. *J. Chem. Phys.* **1994**, *100* (8), 5829–5835. DOI: 10.1063/1.467146.

(20) Wilson, P. J.; Bradley, T. J.; Tozer, D. J. Hybrid exchange-correlation functional determined from thermochemical data and ab initio potentials. *J. Chem. Phys.* **2001**, *115* (20), 9233–9242. DOI: 10.1063/1.1412605.

(21) Jensen, F. Segmented contracted basis sets optimized for nuclear magnetic shielding. *J. Chem. Theory Comput.* **2015**, *11* (1), 132–138. DOI: 10.1021/ct5009526.

(22) Ahlrichs, R.; Bär, M.; Häser, M.; Horn, H.; Kölmel, C. Electronic structure calculations on workstation computers:The program system turbomole. *Chem. Phys. Lett.* **1989**, *162* (3), 165–169. DOI: 10.1016/0009-2614(89)85118-8.

(23) Kussmann, J.; Ochsenfeld, C. Pre-selective screening for matrix elements in linear-scaling exact exchange calculations. *J. Chem. Phys.* **2013**, *138* (13), 134114. DOI: 10.1063/1.4796441.

(24) Peters, L. D. M.; Kussmann, J.; Ochsenfeld, C. Efficient and Accurate Born-Oppenheimer Molecular Dynamics for Large Molecular Systems. *J. Chem. Theory Comput.* **2017**, *13* (11), 5479–5485. DOI: 10.1021/acs.jctc.7b00937.

(25) Mähler, J.; Persson, I. A study of the hydration of the alkali metal ions in aqueous solution. *Inorg. Chem.* **2012**, *51* (1), 425–438. DOI: 10.1021/ic2018693.

(26) Ectors, D.; Goetz-Neunhoeffer, F.; Neubauer, J. A generalized geometric approach to anisotropic peak broadening due to domain morphology. *J. Appl. Crystallogr.* **2015**, *48* (1), 189–194. DOI: 10.1107/S1600576714026557.

(27) Stephens, P. W. Phenomenological model of anisotropic peak broadening in powder diffraction. *J. Appl. Crystallogr.* **1999**, *32* (2), 281–289. DOI: 10.1107/S0021889898006001.

(28) Wirnhier, E.; Döblinger, M.; Gunzelmann, D.; Senker, J.; Lotsch, B. V.; Schnick, W. Poly(triazine imide) with Intercalation of Lithium and Chloride Ions [$(C_3N_3)_2(NH_xLi_{1-x})_3\cdot LiCl$]: A Crystalline 2D Carbon Nitride Network. *Chem. Eur. J.* **2011**, *17* (11), 3213–3221. DOI: 10.1002/chem.201002462.

(29) Coelho, A. A. Deconvolution of instrument and K α 2 contributions from X-ray powder diffraction patterns using nonlinear least squares with penalties. *J. Appl. Crystallogr.* **2018**, *51* (1), 112–123. DOI: 10.1107/S1600576717017988.

(30) Hammersley, A. P.; Svensson, S. O.; Hanfland, M.; Fitch, A. N.; Hausermann, D. Two-dimensional detector software:From real detector to idealised image or two-theta scan. *High Press. Res.* **1996**, *14* (4-6), 235–248. DOI: 10.1080/08957959608201408.

(31) Ashiotis, G.; Deschildre, A.; Nawaz, Z.; Wright, J. P.; Karkoulis, D.; Picca, F. E.; Kieffer, J. The fast azimuthal integration Python library:PyFAI. *J. Appl. Crystallogr.* **2015**, *48* (Pt 2), 510–519. DOI: 10.1107/S1600576715004306.

(32) Juhás, P.; Davis, T.; Farrow, C. L.; Billinge, S. J. L. PDFgetX3:A rapid and highly automatable program for processing powder diffraction data into total scattering pair distribution functions. *J. Appl. Crystallogr.* **2013**, *46* (2), 560–566. DOI: 10.1107/S0021889813005190.

(33) Yang, X.; Juhas, P.; Farrow, C. L.; Billinge, S. J. L. *xPDFsuite:An end-to-end software solution for high throughput pair distribution function transformation, visualization and analysis*. http://arxiv.org/pdf/1402.3163v3.

(34) Juhás, P.; Farrow, C. L.; Yang, X.; Knox, K. R.; Billinge, S. J. L. Complex modeling:A strategy and software program for combining multiple information sources to solve ill posed structure and nanostructure inverse problems. *Acta Cryst. A* **2015**, *71* (Pt 6), 562–568. DOI: 10.1107/S2053273315014473.

(35) Amunugama, R.; Rodgers, M.T. Absolute alkali metal ion binding affinities of several azines determined by threshold collision-induced dissociation and ab initio theory. *Int. J. Mass Spectrom.* **2000**, *195-196*, 439–457. DOI: 10.1016/S1387-3806(99)00145-1.

(36) Warren, B. E. X-Ray Diffraction in Random Layer Lattices. *Phys. Rev.* **1941**, *59* (9), 693–698. DOI: 10.1103/PhysRev.59.693.

(37) Coelho, A. A.; Evans, J. S. O.; Lewis, J. W. Averaging the intensity of many-layered structures for accurate stacking-fault analysis using Rietveld refinement. *J. Appl. Crystallogr.* **2016**, *49* (5), 1740–1749. DOI: 10.1107/S1600576716013066.

(38) Treacy, M. M. J.; Newsam, J. M.; Deem, M. W. A General Recursion Method for Calculating Diffracted Intensities from Crystals Containing Planar Faults. *Proc. R. Soc. A* **1991**, *433* (1889), 499–520. DOI: 10.1098/rspa.1991.0062.

(39) Fan, C.; Miao, J.; Xu, G.; Liu, J.; Lv, J.; Wu, Y. Graphitic carbon nitride nanosheets obtained by liquid stripping as efficient photocatalysts under visible light. *RSC Adv.* **2017**, *7* (59), 37185–37193. DOI: 10.1039/C7RA05732F.

(40) Miller, T. S.; Jorge, A. B.; Suter, T. M.; Sella, A.; Corà, F.; McMillan, P. F. Carbon nitrides:Synthesis and characterization of a new class of functional materials. *Phys. Chem. Chem. Phys.* **2017**, *19* (24), 15613–15638. DOI: 10.1039/c7cp02711g.

7 Appendix B

Experimental Details

Melon:

Dicyandiamide (Sigma-Aldrich, 99 %) was ground in a mortar and transferred into an open crucible which was heated in a muffle furnace (10 °C/min, 550 °C, 4 h, slow cooling to ambient temperature). The resulting pale, yellow solid was ground and washed four times with DI water.

Potassium melonate:

Melon and potassium thiocyanate (Gruessing, 99 %) were thoroughly ground in a mortar and transferred into a crucible covered with a lid which was placed in a preheated muffle furnace (550 °C, 4 h, slow cooling to ambient temperature). The resulting bright yellow solid was washed three times with DI water. The volume of the combined transparent filtrate was then reduced by rotary evaporation and potassium melonate penta-hydrate precipitated overnight. Filtration yielded a colorless needle shaped compound which was recrystallized from a mixture of water/acetone.

K-CN-phase:

Dicyandiamide (97 mg, 1.14 mmol, Sigma-Aldrich >98%), KSCN (18 mg, 0.19 mmol, Gruessing 99 %) and potassium melonate penta-hydrate (79 mg, 0.16 mmol) were ground in a mortar and transferred into a Duran glass ampoule, which was subsequently purged four times with argon and then dried under high-vacuum. The ampoule was then flame-sealed and placed into a tube furnace (6 °C/min, 500 °C, 6 h, 1 °C/min, rt). In a final step the yellow solid was washed four times with DI water and then dried at 60 °C.

H-CN-phase (protonation):

Finely ground cryst. K-CN-phase (100 mg) was treated with 100 mL of 1 M HCl and stirred for 15 min. The suspension was filtered and the residue washed four times with DI water to yield H-PHI. The powder was dried overnight.

Backconverted K-CN-phase (deprotonation):

Finely ground H-CN-phase was treated in a solution of K_2CO_3 (300 mg, 2.17 mmol) in 10 mL dest. water and subsequently filtered and washed five times with 25 mL of DI water to remove excess K2CO3. The powder was dried overnight.

Photocatalytic experiments

In a typical photocatalytic experiment 10 mg (note that rates (μmol/gh) were normalized according to the used amount of catalyst) carbon nitride material, 9 mL DI water, 1 mL (10 vol%) of methanol as sacrificial donor and 6 μL of dihydrogen hexachloroplatinate (Sigma-Aldrich, 8 wt% solution in H_2O), which forms the platinum cocatalyst *in-situ*, were transferred into a glass reactor with a quartz window. The suspension was stirred and sonicated prior to illumination. Additionally, the headspace was evacuated and backfilled with argon several times. A 300 Xenon arc-lamp (Newport, 300 W) equipped with a 1.5 Global AM filter illuminated the suspension with 100 mW/cm^2 and from the headspace samples were periodically taken and quantified by gas-chromatography (Thermo Scientific TRACE GC Ultra) equipped with a TCD detector using argon as the carrier gas. The reaction was thermostated at 25 °C during illumination as in previous works.

Electrochemical experiments

The electrochemical measurements were performed with plasma-cleaned FTO as a substrate. The contacts were sealed with epoxy resin and the final area of the electrodes ca. 1.5 cm^2. 2 mg of the carbon nitride material, 50 µL milipore water, 30 µL iso-propanole and 20 µL Nafion 117 (5% solution) were mixed into a slurry, which was subsequently sonicated for 1 h. The suspension was dropcasted on the wired FTO and dried at 60 °C over night. The measurements were performed in an aqueous 1 M KCl solution and referenced against a Ag/AgCl (sat. KCl) electrode while a platinum wire was used as a counter electrode. The electrolyte was purged for 30 min with nitrogen prior to the experiments.

Instrumental details:

Solid state ^{1}H, ^{13}C and ^{15}N magic angle spinning (MAS) NMR experiments were performed on a Bruker Avance-III 400 MHz instrument at the frequencies of 400, 100.61 and 40.53 MHz, respectively (B_0 = 9.4 T). All ^{1}H and ^{13}C spectra are referenced indirectly with respect to tetramethylsilane (TMS) using adamantane as secondary reference and the ^{14}N and ^{15}N to nitromethane using glycine and/or NH_4Cl as a secondary reference. MAS frequencies were between 6.5-14.0 kHz in a 4 mm ZrO_2 rotor.

Transmission electron microscope: Powders, ground and suspended in butanol, were distributed onto a holey carbon/copper grid and studied with a Philips CM 30 ST microscope (300 kV, LaB6 cathode). Images were taken with a TVIPS TemCam-F216 CMOS Camera.

Laboratory X-ray powder diffraction (XRPD) patterns of K-CN-phase and H-CN-phase were collected using a STOE Stadi P diffractometer with CuK$_{\alpha 1}$ radiation (λ = 1.540598 Å) equipped with a MYTHEN 1 K detector (Dectris Ltd.) and a curved Ge(111) monochromator.

Thermogravimetric (TG) analyses were performed using a STA 449 F5-Jupiter (Netzsch) device. The K-CN-phase sample was heated up in a corundum crucible in a dynamic argon (50 mL/ min) atmosphere to 600 °C with a heating rate of 5 °C min^{-1}. An empty corundum crucible was used as a reference.

Combustion analysis for detection of C, H, N, S was performed on a Elementar Analysensysteme GmbH – Vario micro elemental analyzer.

Inductively coupled plasma atomic emission spectroscopy (ICP-AES) data was obtained from a Varian Vista RL CCD simultaneous ICP-ACS device. The sample was dissolved in concentrated HNO_3 in the microwave oven at 150 °C, before injecting into the plasma.

Diffuse reflectance UV-Vis spectra were collected on a Cary 5000 spectrometer referenced to PTFE or barium sulfate as reference.

Infrared (IR) spectra were recorded on a JASCO Fourier transform infrared spectrometer equipped with a diamond attenuated total reflectance (ATR) unit and a resolution of 4 cm^{-1}.

Electron paramagnetic resonance (EPR) spectra were measured on a Bruker EMXnano X-band device operating at an excitation frequency of ~9.6 GHz and 100 mW microwave power.

Electrochemical experiments were performed with an Ivium technologies compactstat potentiostat with platinum wire as a counter electrode and an Ag/AgCl (sat. KCl) reference electrode.

Transmission electron microscopy

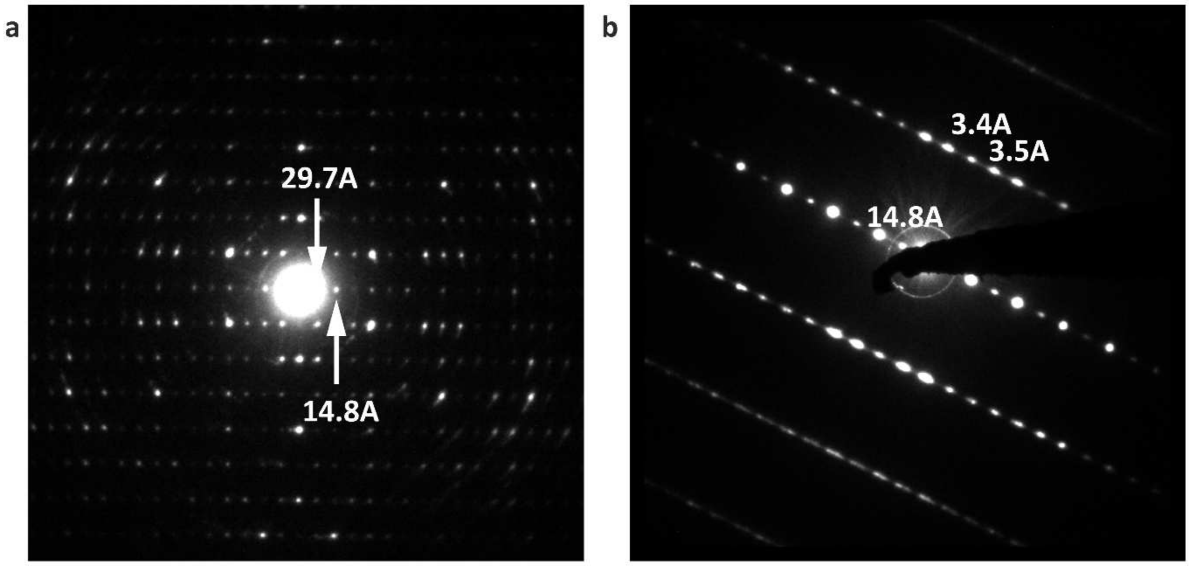

Figure B 1. (a) Precession electron diffraction image of the [001] zone axis. The arrows mark the (020) reflection (14.8 Å) along the b-axis and the systematically absent (010) reflection (29.7 Å). The primary beam is covering the first 29.7 Å reflection spot. (b) Electron diffraction image featuring a zone axis that presumably contains the stacking reflection (3.4-3.5 Å). The streaking of the intensities of the diffractions parallel to the central line could indicate a turbostratic disorder of the stacked polymer strands or the presence of very thin crystallites of only a few nanometers.

Pair distribution function analysis

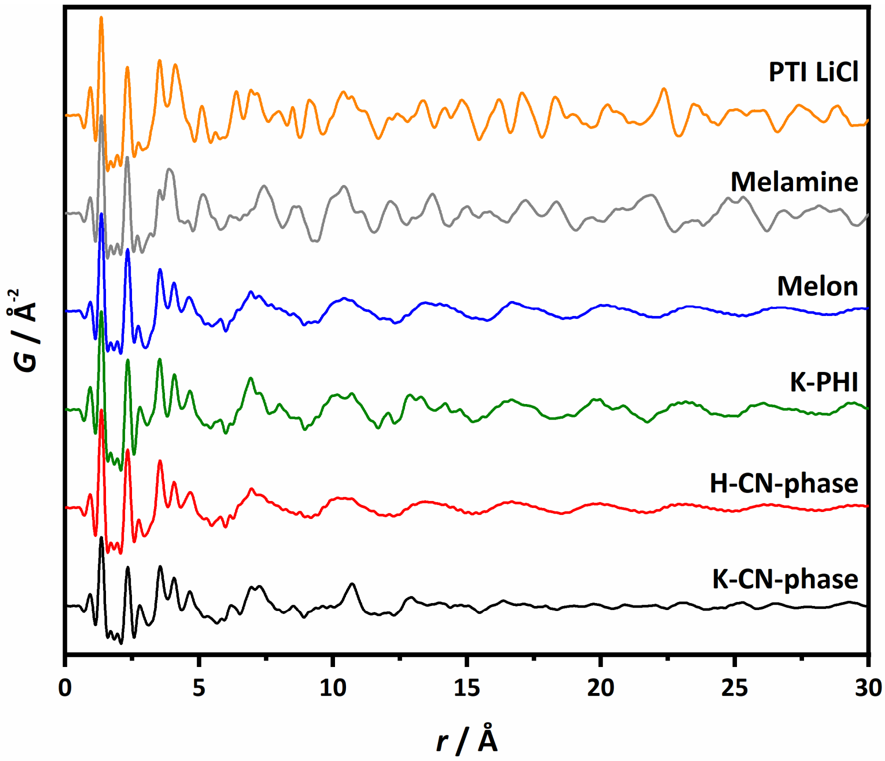

Figure B 2. PDF of various known carbon nitrides polytriazine imide (PTI LiCl), melamine, melon and potassium polyheptazine imide (K-PHI) as a direct comparison to the newly synthesized K-CN- and H-CN-phase. The large similarities <2 Å are caused by the similar C-N bonding situation in all of the examined substances.

X-ray powder diffraction

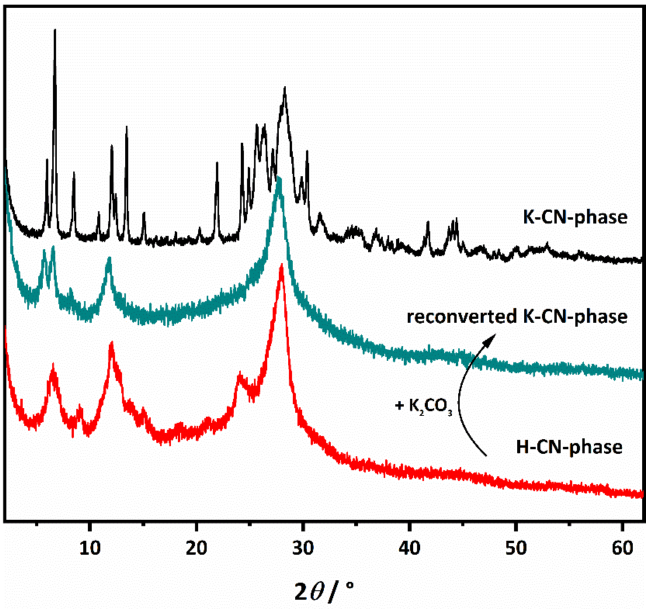

Figure B 3. X-ray powder diffraction patterns of H-CN-phase (red) and the reconversion with K_2CO_3 to K-CN-phase (cyan). The original pattern from the pristine K-CN-phase (black) is shown for comparison. A few of the main reflections for reconverted K-CN-phase can be observed, but the crystallinity that was lost cannot be regained just by introducing the potassium cations. The same can be observed for the reconversion of H-PHI to K-PHI with potassium carbonate (cf. chapter 2).

Infrared spectroscopy

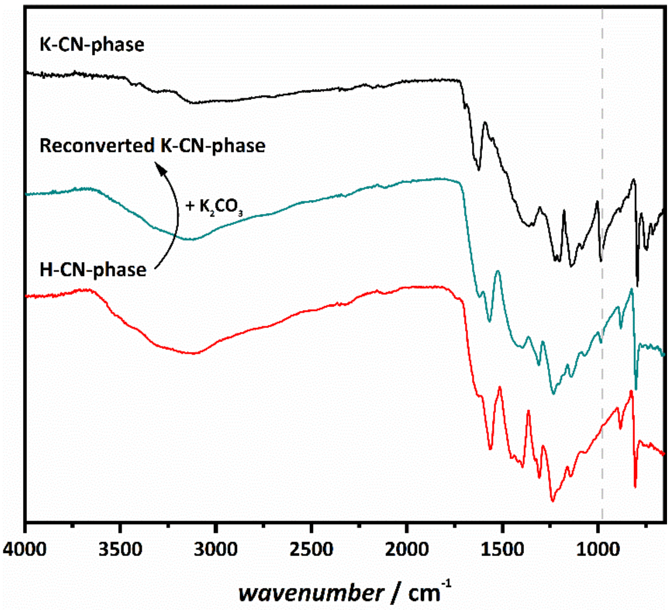

Figure B 4. Infrared spectra of H-CN-phase (red) and the "reconversion" with K_2CO_3 to K-CN-phase (cyan). The original pattern from the pristine K-CN-phase (black) is shown for comparison. It is obvious that not all vibrational modes are present for the reconverted sample with respect to the pristine sample. However, some vibrations like the one at approx. 980 cm^{-1} (grey dashed line) are observed, which implicates that most likely only a partial conversion is achieved.

Elemental analysis

Table B 1. Elemental analysis obtained from combustion analysis and ICP/AE spectroscopy for K-CN-phase and H-CN-phase, respectively. For the H-CN-phase no potassium could be detected by ICP/AE spectroscopy.

	K-CN-phase		H-CN-phase	
	wt%	mol%	wt%	mol%
C	29.6	30.2	30.8	25.1
N	52.2	45.6	52.8	37.8
K	13.0	4.1	-	-
H	1.4	17.4	2.8	28.0
O[a)]	3.8	2.8	13.6	9.0
Total	100.0	100.0	100.0	100.0
N/C	**1.51**	**$C_6N_9H_{2.5}K_{0.8} \cdot 0.5\ H_2O$**	**1.47**	**$C_6N_9H_{2.5} \cdot 2\ H_2O$**

[a)] All relative amounts were summed up and the rest was defined as oxygen, which is likely to be present in the form of water inside the structure. The sum formula represents a possible composition based on the elemental analysis data.

Additional ssNMR spectra

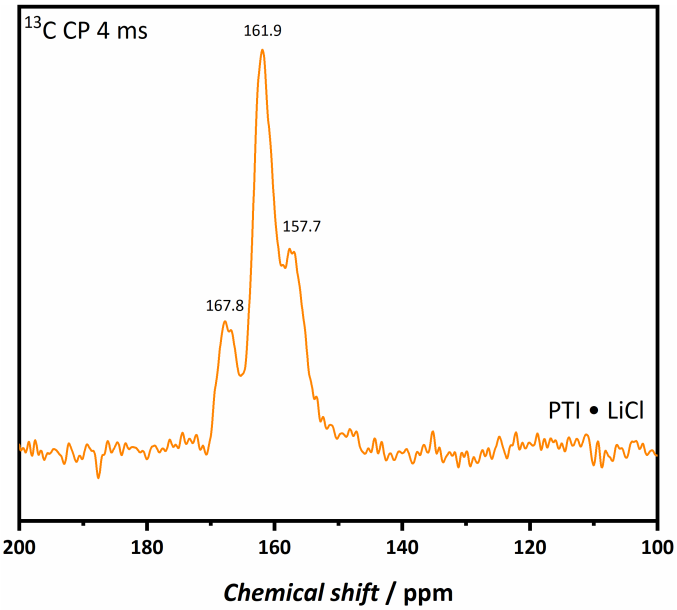

Figure B 5. ^{13}C cross-polarization ssNMR spectrum of poly(triazine imide) · LiCl with 4 ms contact time. The chemical shift range is narrower than those observed for heptazine-based structures. Therefore, we conclude K-CN-phase to be heptazine-based.

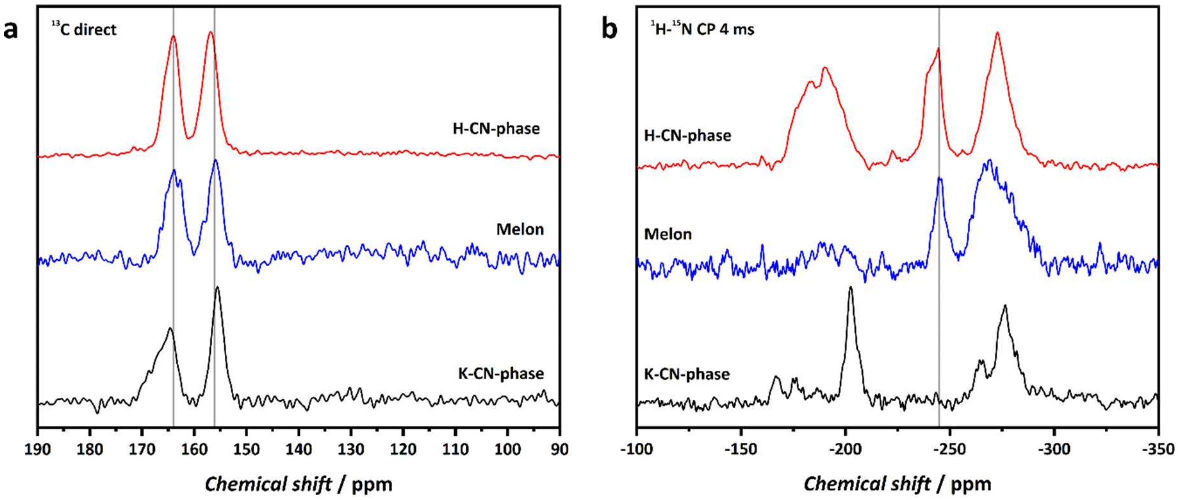

Figure B 6. (a) ^{13}C direct excitation ssNMR spectrum showing the close similarities between the acid treated H-CN-phase and melon, being a 1D strand polymer. (b) ^{15}N cross-polarization ssNMR spectrum of the same compounds. Note that melon has been recorded with a different set of device parameters and therefore the intensities should not directly be compared between those. The chemical shifts, however, are directly comparable. It is remarkable that during the protonation of the K-CN-phase leads to a signal at approx. 240 ppm, which corresponds to the bridging nitrogen in melon. This corroborates that this nitrogen atom was deprotonated in K-CN-phase previously.

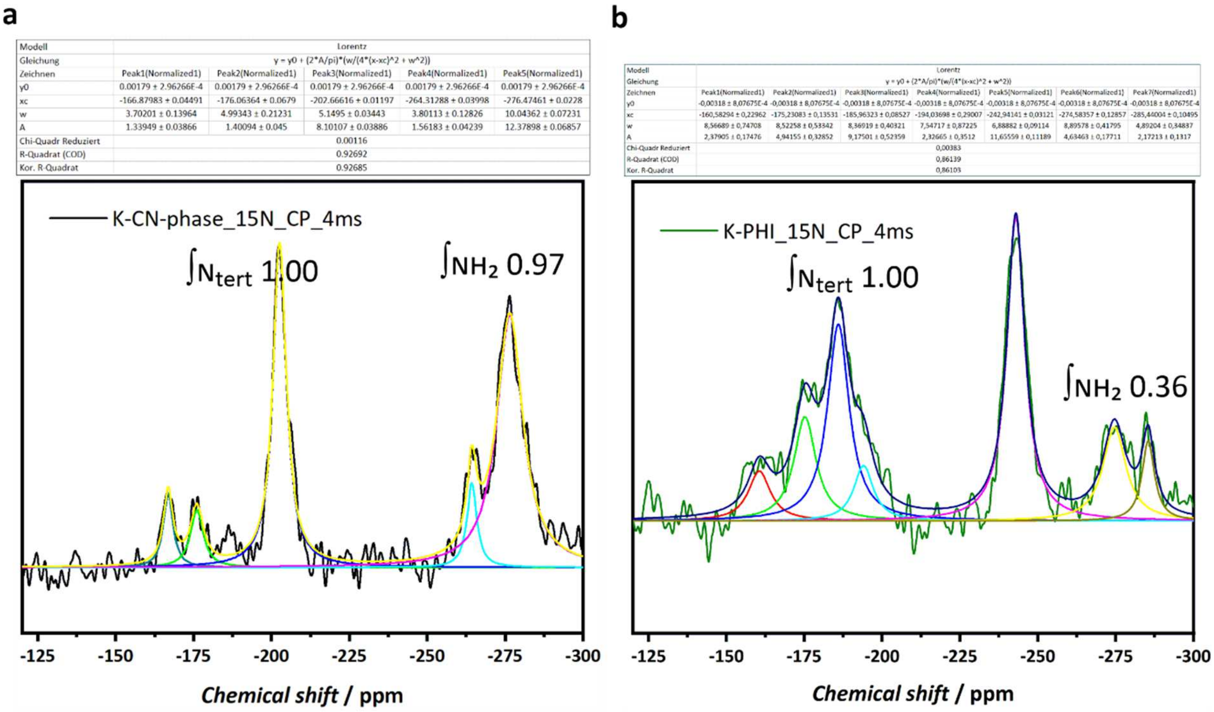

a

Modell	Lorentz				
Gleichung	y = y0 + (2*A/pi)*(w/(4*(x-xc)^2 + w^2))				
Zeichnen	Peak1(Normalized1)	Peak2(Normalized1)	Peak3(Normalized1)	Peak4(Normalized1)	Peak5(Normalized1)
y0	0.00179 ± 2.96266E-4	0.00179 ± 2.96266E-4	0.00179 ± 2.96266E-4	0.00179 ± 2.96266E-4	0.00179 ± 2.96266E-4
xc	-166.87983 + 0.04491	-176.06364 + 0.0679	-202.66616 + 0.01197	-264.31288 + 0.03998	-276.47461 + 0.0228
w	3.70201 ± 0.13964	4.99343 ± 0.21231	5.1495 ± 0.03443	3.80113 ± 0.12826	10.04362 ± 0.07231
A	1.33949 ± 0.03866	1.40094 ± 0.045	8.10107 ± 0.03886	1.56183 ± 0.04239	12.37898 ± 0.06857
Chi-Quadr Reduziert	0.00116				
R-Quadrat (COD)	0.92692				
Kor. R-Quadrat	0.92685				

b

Modell	Lorentz						
Gleichung	y = y0 + (2*A/pi)*(w/(4*(x-xc)^2 + w^2))						
Zeichnen	Peak1(Normalized1)	Peak2(Normalized1)	Peak3(Normalized1)	Peak4(Normalized1)	Peak5(Normalized1)	Peak6(Normalized1)	Peak7(Normalized1)
y0	-0,00318 ± 8,07675E-4	-0,00318 ± 8,07675E-4	-0,00318 ± 8,07675E-4	-0,00318 ± 8,07675E-4	-0,00318 ± 8,07675E-4	-0,00318 ± 8,07675E-4	-0,00318 ± 8,07675E-4
xc	-160,58294 ± 0,22962	-175,23083 ± 0,13531	-185,96323 ± 0,08527	-194,03698 ± 0,29007	-242,94141 ± 0,03121	-274,58357 ± 0,12857	-285,44004 ± 0,10495
w	8,56689 ± 0,74708	8,52258 ± 0,53342	8,36919 ± 0,40321	7,54717 ± 0,87225	6,88882 ± 0,09114	8,89578 ± 0,41795	4,89204 ± 0,34837
A	2,37905 ± 0,17476	4,94155 ± 0,32852	9,17501 ± 0,52359	2,32665 ± 0,3512	11,65559 ± 0,11189	4,63463 ± 0,17711	2,17213 ± 0,1317
Chi-Quadr Reduziert	0,00383						
R-Quadrat (COD)	0,86139						
Kor. R-Quadrat	0,86103						

Figure B 7. ^{15}N CP ssNMR spectra of (a) K-CN-phase and (b) K-PHI taken with equal contact times of 4 ms. The integrations have been made by Lorentz peak fitting. In both spectra the integral over the tertiary nitrogen atoms have been arbitrarily chosen to be 1.00. The signals belonging to NH$_2$ groups in the K-CN-phase have a much larger area relative to the corresponding signals in K-PHI. Since the contact times are equal, this finding implies that K-CN-phase has more terminating amino groups, hence exhibiting a less condensed structure. This observation points to the structural arrangement in PHI strands opposed to 2D interconnected units like in K-PHI.

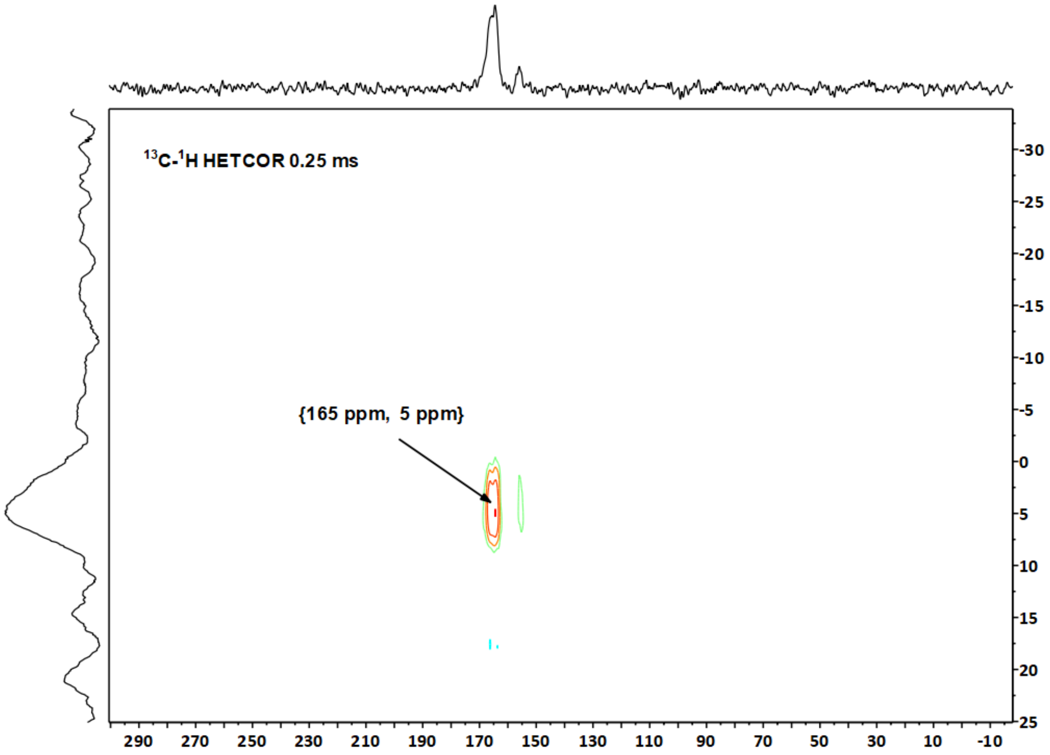

Figure B 8. ^{13}C-^{1}H-HETCOR MAS NMR spectrum of the K-CN-phase recorded at 12.5 kHz and a contact time of 0.25 ms.

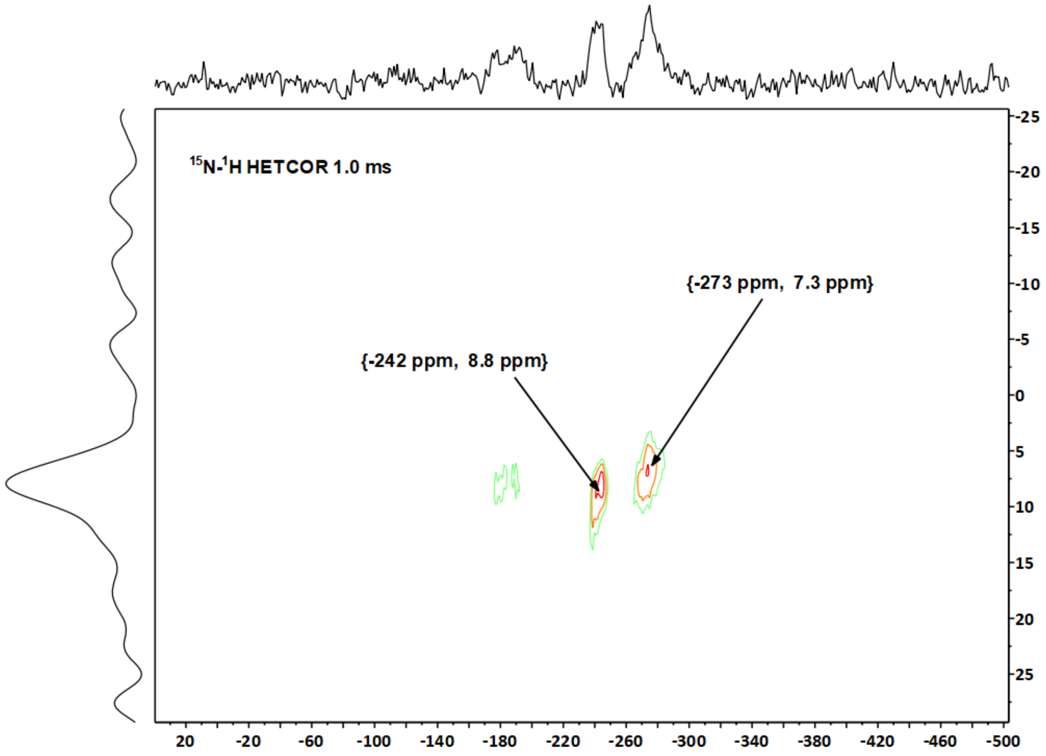

Figure B 9. ^{15}N-^{1}H-HETCOR MAS NMR spectrum of the H-CN-phase recorded at 12.5 kHz and a contact time of 1.0 ms.

Photocatalysis

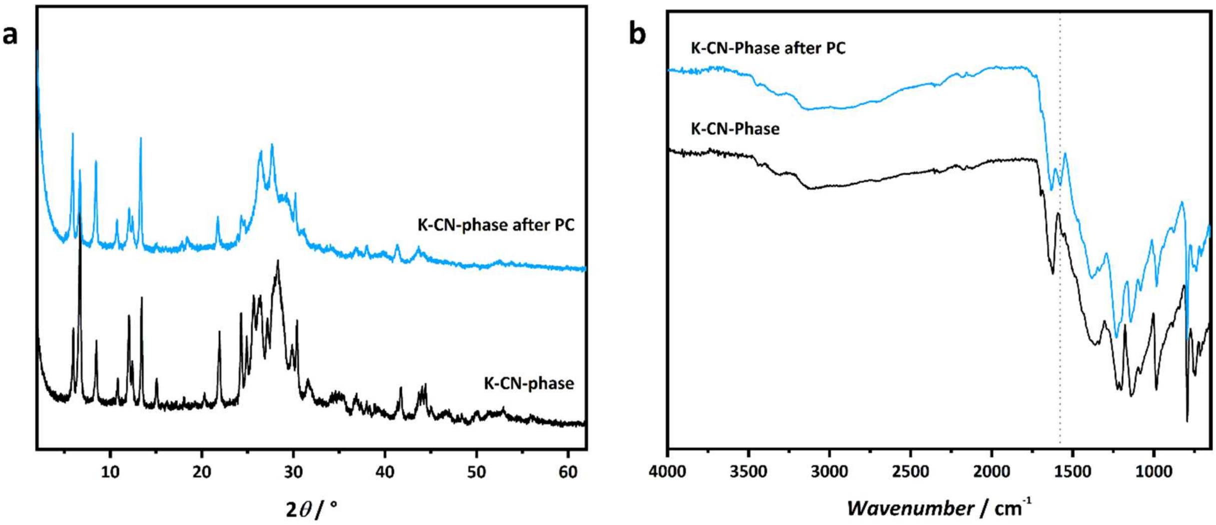

Figure B 10. (a) XRD pattern of K-CN-phase before and after photocatalysis for >6 h. A visible loss of long-range order is observable through broader Bragg reflections and also changes in signal intensity can be observed. These could hint at a transformation to H-CN-phase under the harsh photocatalytic conditions and the prolonged stirring in water. (b)Infrared spectrum for the K-CN-phase before and after photocatalysis for >6 h. The features of the spectrum are largely retained, expect for a new peak emerging at 1575 cm^{-1}, which can be related to a vibrational band in the H-CN-phase. Therefore, a beginning transformation under the harsh photocatalytic conditions may be observed.

An ICP/AES measurement after photocatalysis for >6 h yielded a reduced content of ca. 10 wt% opposed to the pristine sample with 14 wt%. The beginning loss of structurally incorporated potassium is responsible for the intensity changes in the diffraction pattern.

Photocatalysis

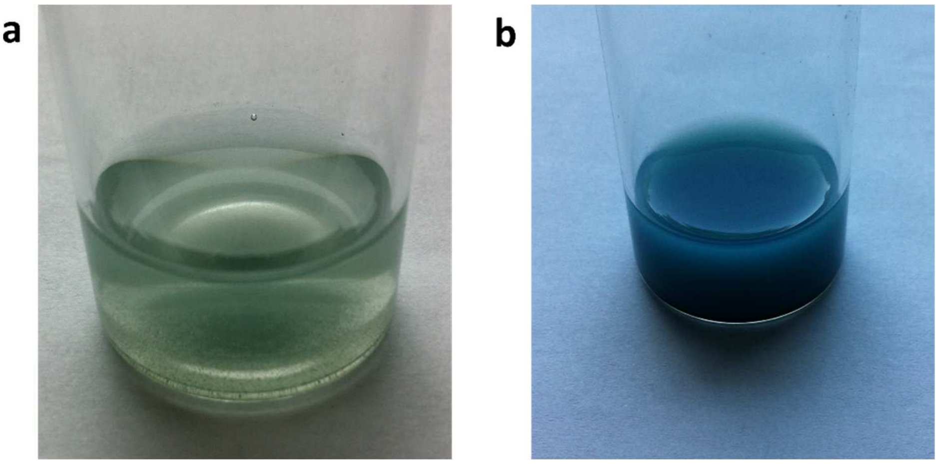

Figure B 11. (a) Crystalline K-PHI versus (b) amorphous optimized K-PHI in the presence of 4-MBA as electron donor irradiated by Xe-lamp. It is obvious that the crystalline version contains lower concentrations of photoreduced species.

Electrochemistry

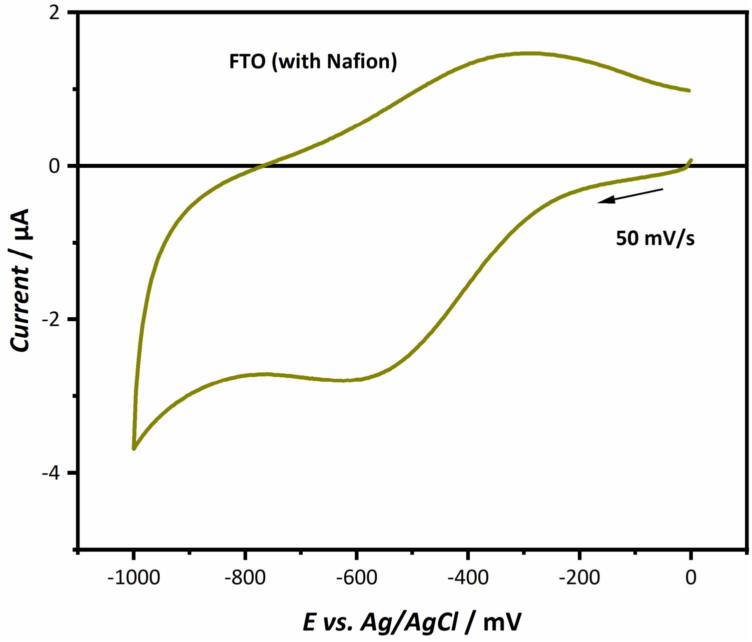

Figure B 12. Cyclic voltammogram of a blank FTO electrode coated with Nafion 117; scanrate 50 mV/s. Scan was performed in the dark.

Cyclic voltammetry (CV) of fluorine-doped tin oxide (FTO) electrode coated only with Nafion 117 as a blind experiment. The potential was swept from 0 mV to -1000 mV against a Ag/AgCl (sat. KCl) reference electrode and reversely. The electrode had an area of 1.4 cm^2 in contact with the 1 M KCl electrolyte, which had been degassed for 1 h with nitrogen prior to the measurement. The curve shows only a very low current, which increases until the potential of -1000 mV is reached. At this potential, a starting decomposition of the electrolyte (water electrolysis) is observed as the redox potential for hydrogen evolution vs. Ag/AgCl locates at ca. -610 mV at pH 7 without overpotential.[1] The other detectable, reversible redox peak at approx. -450 mV probably stems from an impurity in the electrolyte as it is also visible in the CVs with K-PHI and the K-CN-phase. Note, that this reversible peak is also observed for a blank FTO electrode without Nafion coating and could also not be removed by excessive degassing with nitrogen. Apart from this feature, the shape of the voltammogram suggests a capacitive behavior as would be expected for a non-reactive electrode surface.

7.1 References

(1) Wang, L.; Lee, C.-Y.; Schmuki, P. Solar water splitting: preserving the beneficial small feature size in porous α-Fe_2O_3 photoelectrodes during annealing. *J. Mater. Chem. A* **2013**, *1* (2), 212–215. DOI: 10.1039/C2TA00431C.

8 Appendix C

Experimental details

Dicyandiamide (190 mg, 2.25 mmol) and an eutectic melt of $NiCl_2$ (394 mg, 3.05 mmol) and KCl (605 mg, 8.11 mmol) was ground and transferred into a Duran glass ampoule which was purged three times with argon. The powder was further dried in vacuo and subsequently flame sealed and subjected to the following temperature program in a tube furnace (6 °C/min, 500 °C, 6 h, 1 °C/min, rt). The obtained solid was ground and washed five times with DI water and subsequently dried at 60 °C.

Instrumental details

Laboratory X-ray powder diffraction (XRPD) patterns of H-PHI and K-PHI were collected using a STOE Stadi P diffractometer with $CuK_{\alpha 1}$ radiation (λ = 1.540598 Å) equipped with a MYTHEN 1 K detector (Dectris Ltd.) and a curved Ge(111) monochromator.

Transmission electron microscope: Powders, ground and suspended in butanol, were distributed onto a holey carbon/copper grid and studied with a Philips CM 30 ST microscope (300 kV, LaB6 cathode). Images were taken with a TVIPS TemCam-F216 CMOS Camera.

Thermogravimetric (TG) analyses were performed at using a STA 449 F5-Jupiter (Netzsch) device. The sample was heated up in a corundum crucible in a dynamic argon (50 mL/min) atmosphere from room temperature to 800 °C with a heating rate of 5 $\mathrm{Kmin^{-1}}$, respectively. An empty corundum crucible was used as a reference. Corrections of instrumental effects and the buoyancy were performed with Al_2O_3 as an inert reference material during a separate measurement. The gas stream injected at various times and was analyzed via mass spectrometry.

For the evolved gas analysis thermogravimetric analysis (TGA, Netzsch STA F449 F3) coupled with gas chromatography (GC, Agilent 8890 GC System) and mass spectroscopy (MS, Agilent 5977 GC/MSD) was applied. The sample (5 mg) was loaded into a Al_2O_3 crucible and heated with a constant rate of 5 K/min to 800 °C in a He (5.0) flow of 70 mL/min. GS-MS injections were triggered at 75 °C (background) and 800 °C (high temperature background), and at the inflection points of the TG curve at 490 °C, 630 °C. The evolved gas was constantly transported through a heated transfer line (290 °C) to a VICI valve box (250 °C) until injection was triggered. A volume of 250 µL gas was then injected into a split injector (5:1) at inlet temperature of 300°C. The GC was equipped with an Agilent HP5MS UI column (30 m × 250 µm × 0.25 µm). The column was heated to 45 °C for 15 min and subsequently heated to 100 °C (20 K/min) for 5 min. The eluted gases were detected with an MS in the scan range of 10-550 m/z and selected ion monitoring (SIM) was performed at 16, 17, 26, 27, 28, 36, 52, and 58 m/z. The MS source was heated to 230 °C, the quadrupole to 150 °C.

Solid state ^{13}C and ^{15}N magic angle spinning (MAS) NMR experiments were performed on a Bruker Avance-III 400 MHz instrument at the frequencies of 400 and 100.61 MHz, respectively

($B_0 = 9.4$ T). All ^1H and ^{13}C spectra are referenced indirectly with respect to tetramethylsilane (TMS) using adamantane as secondary reference. MAS frequencies were between 6.5-14.0 kHz in a 4 mm ZrO_2 rotor.

Diffuse reflectance UV-Vis spectra were collected on a Cary 5000 spectrometer referenced to PTFE as background. The scan was performed from 800 to 250 nm. At 340 nm the switching of the light source from tungsten halogen lamp to deuterium arc lamp causes an artefact in the measurement visible as a non-monotonic step.

Electron paramagnetic resonance (EPR) spectra were measured on a Bruker EMXnano X-band device operating at an excitation frequency of ~9.6 GHz and 100 mW microwave power.

Infrared (IR) spectra were recorded on a JASCO Fourier transform infrared spectrometer equipped with a diamond attenuated total reflectance (ATR) unit and a resolution of 4 cm^{-1}.

XPS analyses were performed with a monochromized Al-$K_{\alpha1}$ radiation source (1486.6 eV) on an Axis Ultra system (Kratos). Detailed scans were acquired using a pass energy of 20 eV while 80 eV was used for the survey scan. Due to charging of the non-conductive sample, it was coated with small amounts of polydimethylsiloxane (PDMS) as an internal reference and pressed into an indium foil. The reference binding energy of PDMS (silicon) was set to 102.0 eV. The peaks were fitted with a Gauss/Lorentz ratio of 30% after subtraction of a Shirley background.

CO_2 sorption measurements were performed on a Autosorb-iQ surface analyzer with vapor option (Quantachrome Instruments, USA). To initially remove guest molecules the samples were outgassed in vacuum at 120 °C for 12 h. The measurements were performed at 298 K.

Pair distribution function analysis

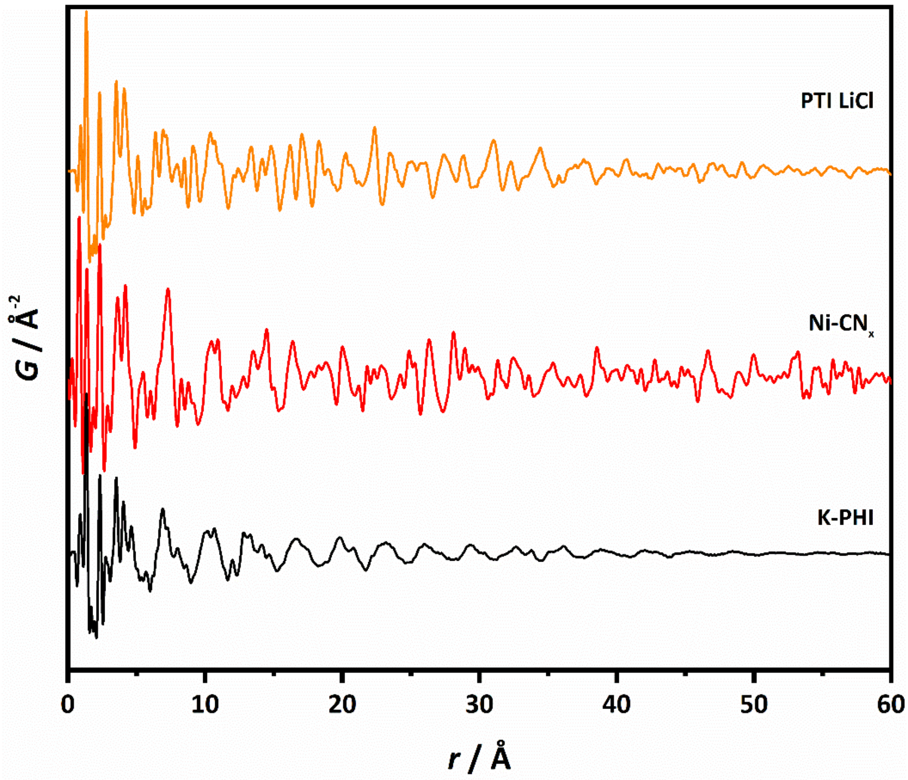

Figure C 1. Pair distribution function data for PTI LiCl (orange), Ni-CN$_x$ (red) and K-PHI (black) compared up to 60 Å. PTI · LiCl and Ni-CN$_x$ show no visible modulation of intensity as is the case for K-PHI. In K-PHI these modulations are caused by a repetition of identical structural motifs within each plane stacked in a staggered AA-fashion. PTI · LiCl the stacking order is AB-type and thus more complicated manifesting in a more irregular pattern above r = 5 Å.

Transmission electron microscopy

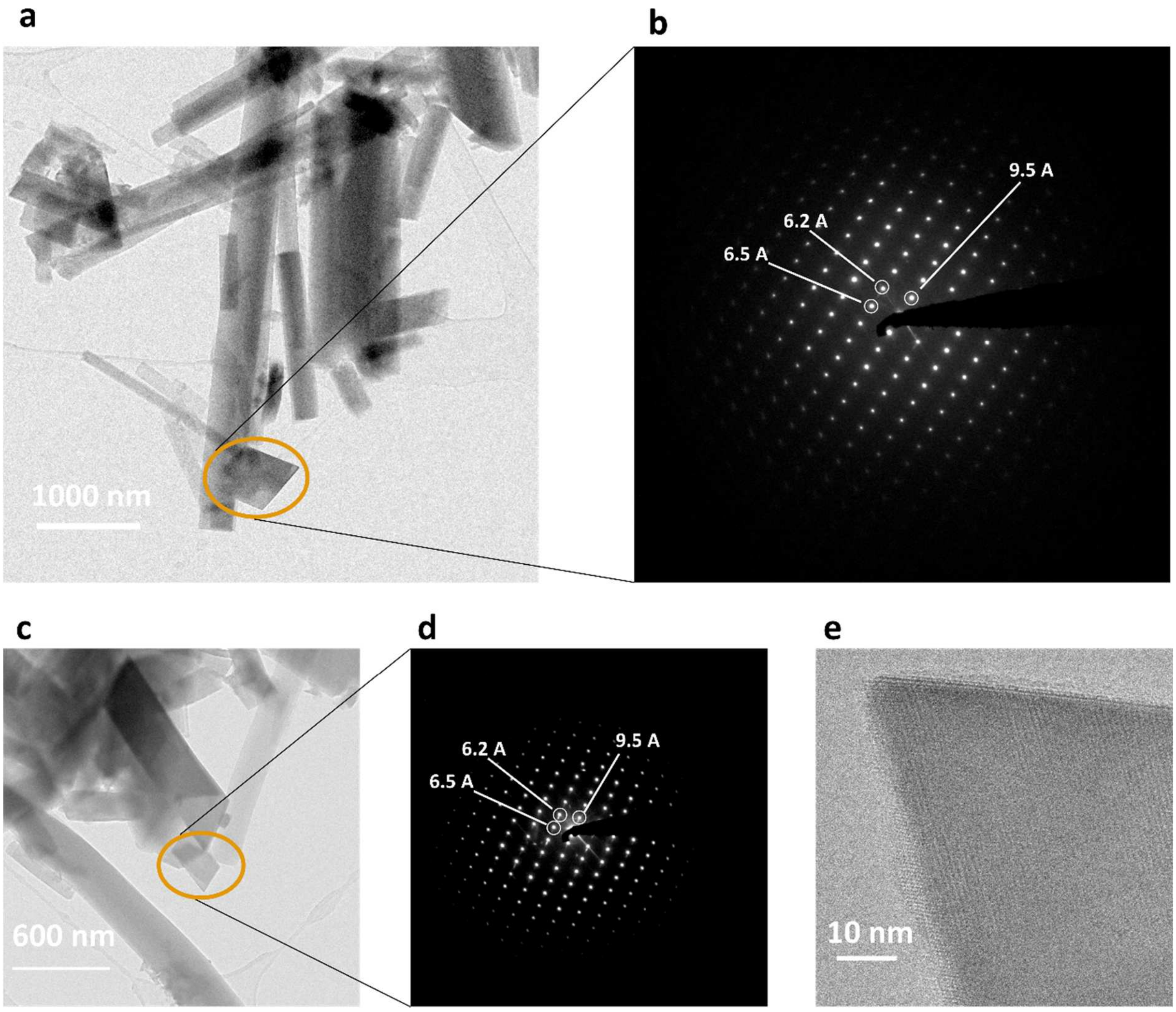

Figure C 2. (a), (c) TEM micrographs of the crystalline side phase reavealing diamond-shaped crystallites. (b), (d) corresponding SAED patterns of the marked crystallites. The d-spacings (6.2 Å, 6.5 Å and 9.5 Å) do not match the ones observed in the bulk XRD of Ni-CN$_x$, which is why it is considered an impurity. (e) High-resolution TEM image of the crystal with very sharp cell edges as compared to the usual needle-shaped crystallites.

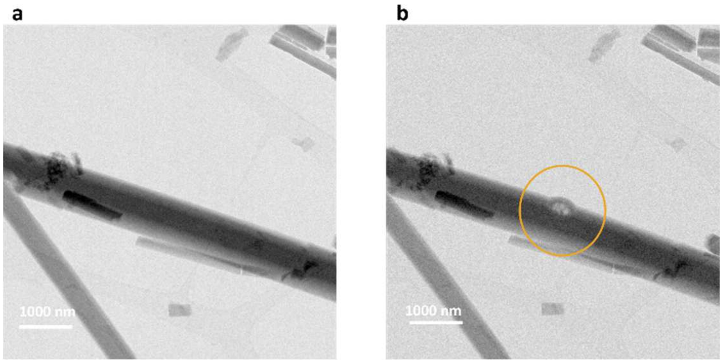

Figure C 3. (a) Before and (b) after attempt of electron diffraction and HR-TEM imaging. The beam damage of the needle-shaped crystal is apparent as a bubble is forming. This could indicate either a melting or "boiling" of the constituting polymer/monomers.

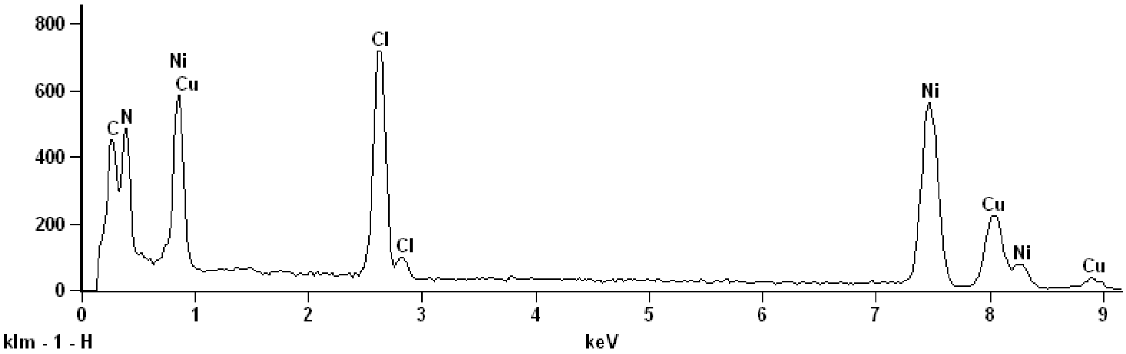

Figure C 4. EDX spectrum of Ni-CNx of the majority, needle-shaped phase. The Ni:Cl content is calculated to be approx. 44:56, matching the ICP/AES and titration results quite well.

X-ray diffraction and infrared spectroscopy after acidic treatment

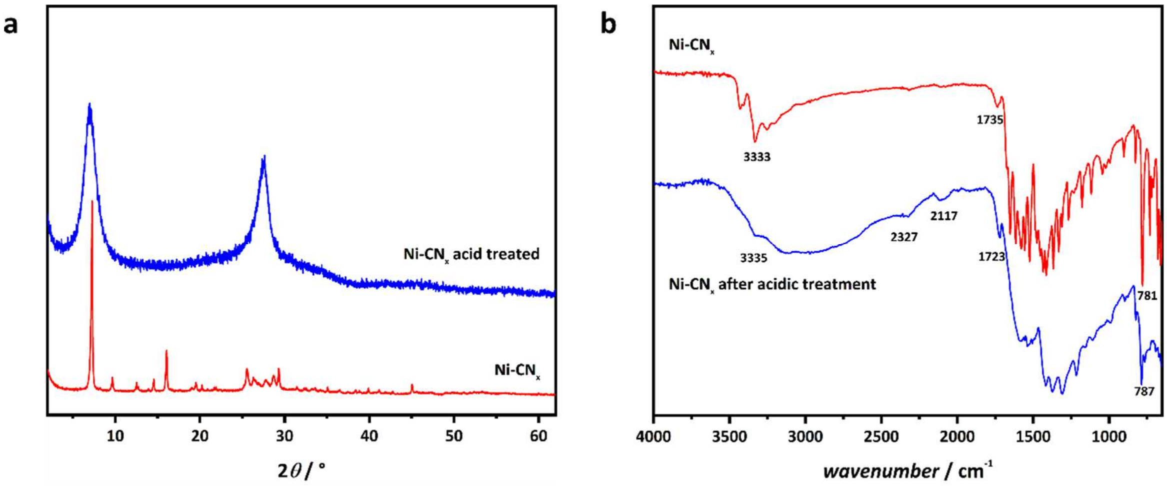

Figure C 5. (a) XRD pattern of pristine Ni-CN$_x$ and acid treated Ni-CN$_x$. To a large degree the sample is amorphized over the treatment with conc. hydrochloric acid, but the strong main feature as well as the "stacking reflection" is retained, which could imply that the general structure remains intact. (b) Infrared spectrum largely showing a similar vibrational bands, but much broader bandwidths, which may again be attributed to an increased degree of freedom the individual constituents can occupy. Strikingly an increase in the region around 3000 cm^{-1} could indicate the uptake of water or suggest beginning hydrolysis of the compound. A new vibration at 2117 cm^{-1} could indicate the presence of a cyanamide moiety whose vibration could have been formerly suppressed in the deprotonated state. Other small shifts may also be attributed to changes in vibrational frequencies due to protonation.

Liquid NMR spectroscopy after acidic treatment

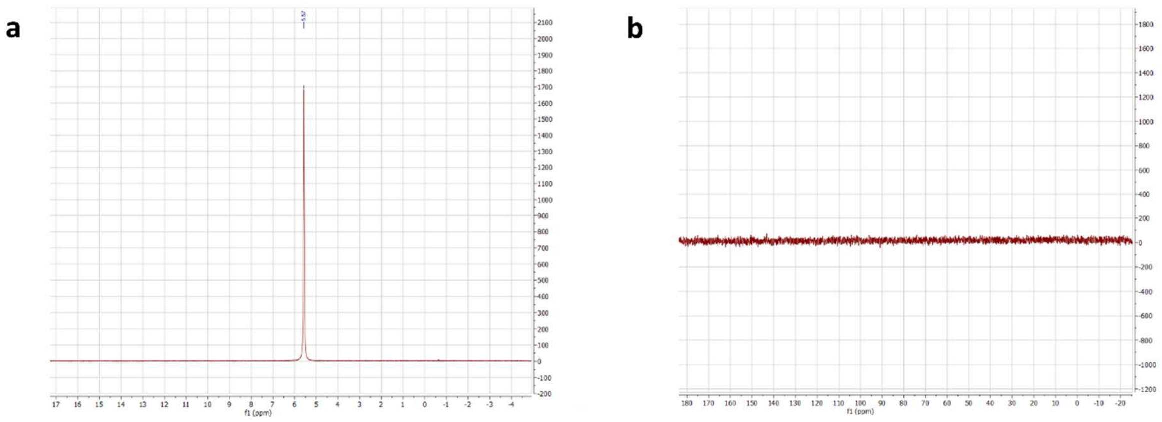

Figure C 6. (a) Proton- and (b) ^{13}C- liquid NMR spectrum of the filtrate obtained after treating Ni-CN$_x$ powder in conc. deuterated hydrochloric acid. However, no signal (except for the solvent peak at ca. 5.5 ppm) could be detected.

Mass spectrometry

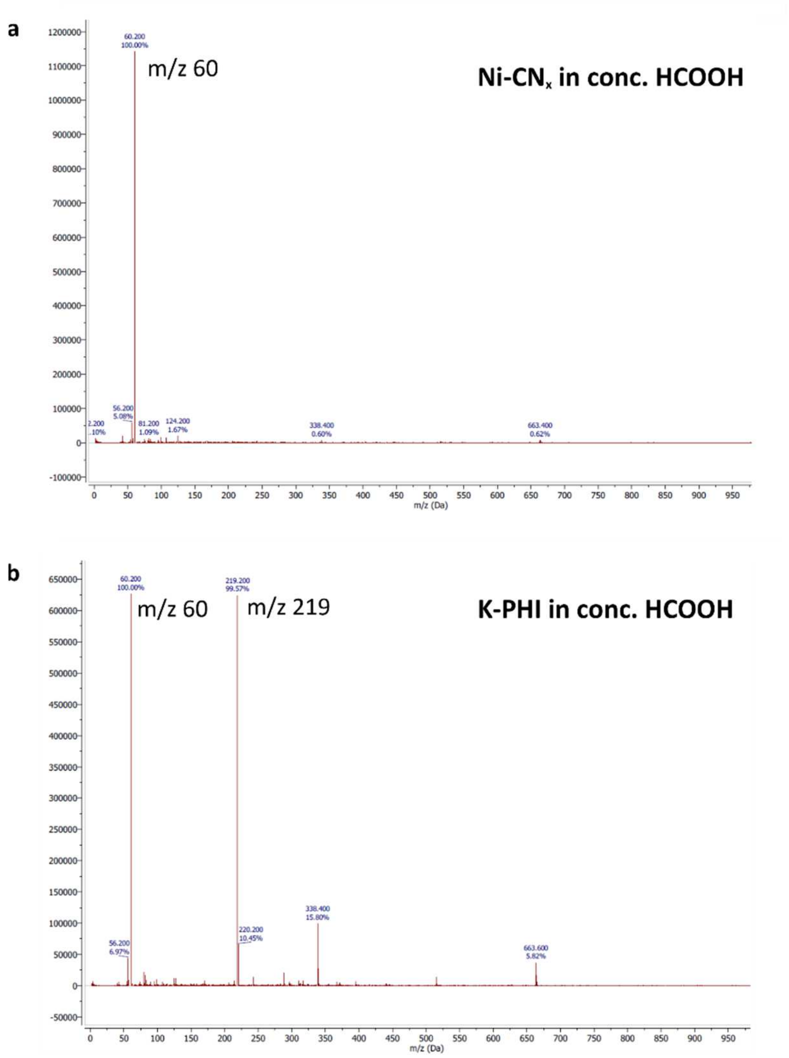

Figure C 7. Mass spectra of (a) filtrate of Ni-CNx and (b) K-PHI, as a typical carbon nitride polymer, suspended in conc. formic acid. m/z = 60 corresponds to the prot. Acid while only for K-PHI a signal was obtained at m/z = 219 corresponding to a protonated melem unit.

Electron paramagnetic resonance

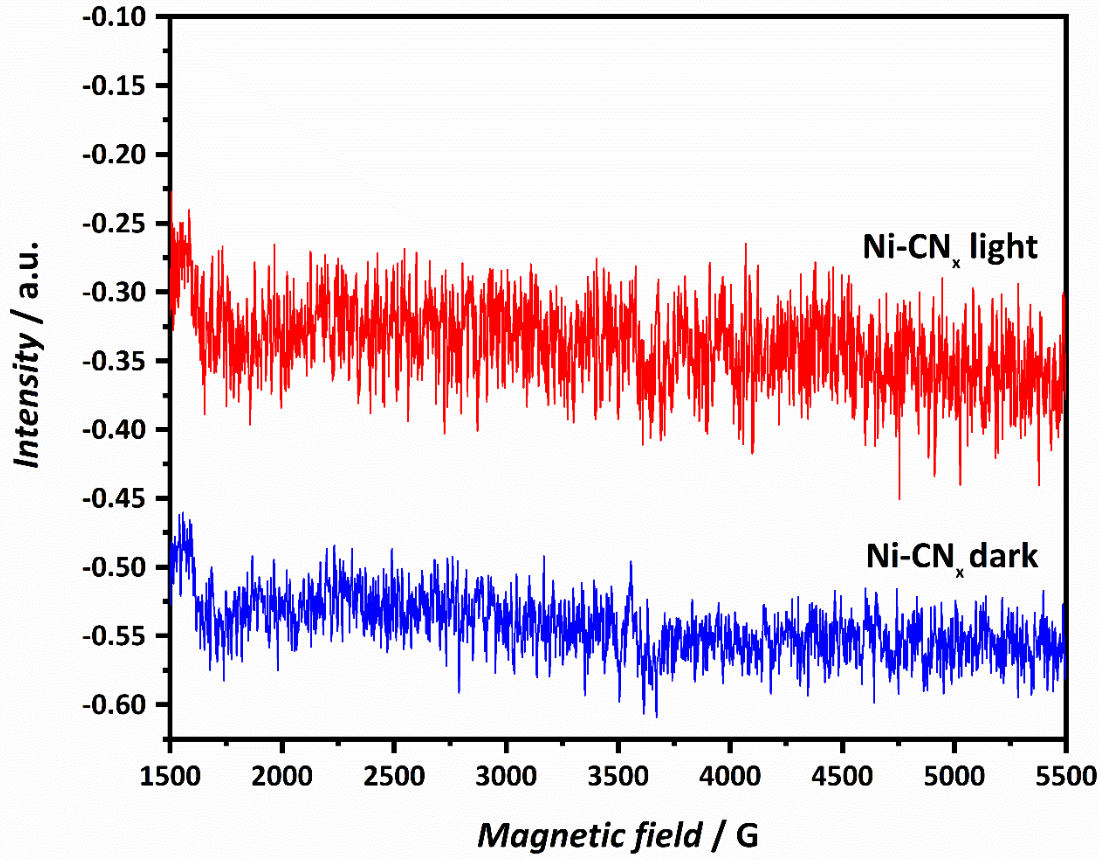

Figure C 8. EPR spectrum of Ni-CN$_x$ in the dark (blue) and illuminated (red) with a Xe-lamp.

The EPR spectrum of Ni-CN$_x$ does not show distinct peaks that could correspond to unpaired electrons within the structure. However, it could be that small impurities with Ni(0) could cause such disturbance that no signal may be obtained. Another issue could be that all electrons in the nickel atoms are paired, thus causing no signal. This would be the case for instance in a planar coordination of the nickel cationic centers, if nickel is in oxidation state +2. It can also be that the concentration is not high enough to observe a clear signal. At ca. 3500 G corresponding to a g-factor of 1.93 could be interpreted as a peak, but for an unambiguous assignment this signal is not suitable. The lack of a clear signal either indicates that no unpaired electrons (or in too low concentration) are present within the structure or that the background noise is too high to observe the signals.

X-ray photoelectron spectroscopy

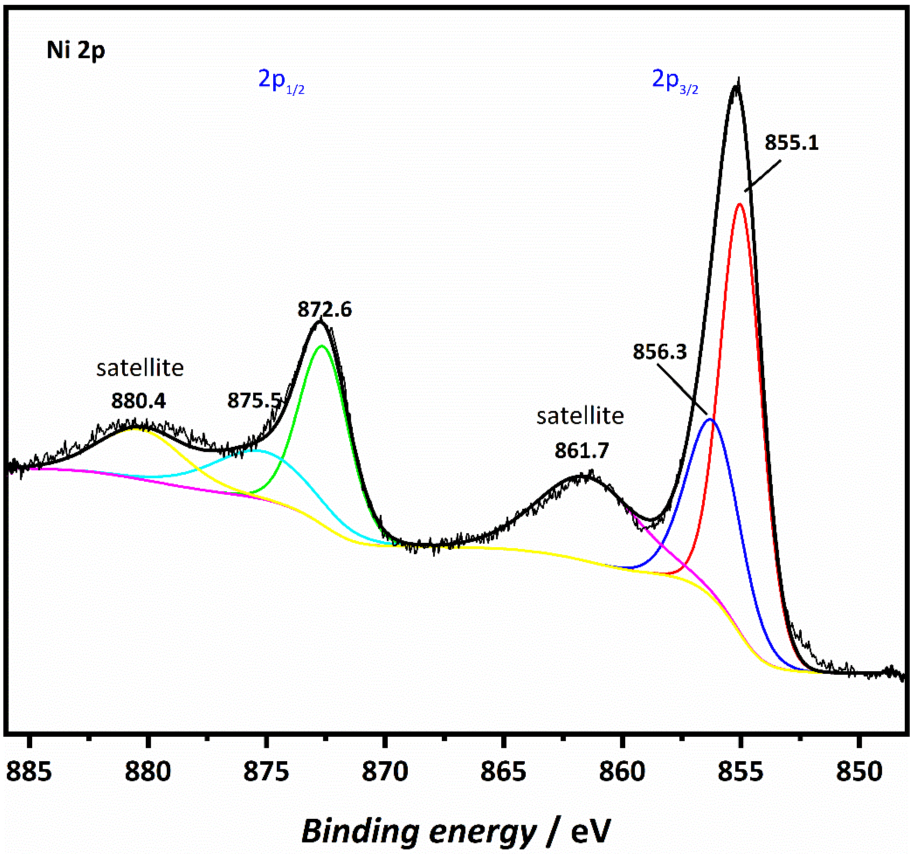

Figure C 9. X-ray photoelectron spectrum of Ni-CN_x of the Ni 2p orbitals. The experimental pattern could be fitted best with two distinct peaks.

The photoelectron spectrum reveals the presence of two nickel species at binding energies for the $2p_{3/2}$ orbital of 855.1 eV and 856.3 eV, respectively. There is also a broad shake-up satellite at 861.7 eV. For instance, studies on nickel oxide particles decorated on carbon nitride polymers have also found multiple Ni-species among which the higher binding energies belonged the more oxidized Ni-atom.[1] However, as no significant amounts of nickel oxide species are detectable, – both in TEM images and the overall low oxygen content from EDX analyses – it may be that there are also various other nickel species in the same oxidation state, but differently coordinated. Due to the relatively high binding energies of both species one could expect an octahedral environment for nickel.[2] On the other hand this assignment should be taken with a grain of salt, because the unconductive nature of the Ni-CN_x sample could have caused charging during the measurement, which may have resulted in a shifted binding energy. Additionally, the oxidation state of nickel is notoriously difficult to assign, which further prevents clear assignments.

CO_2 reduction

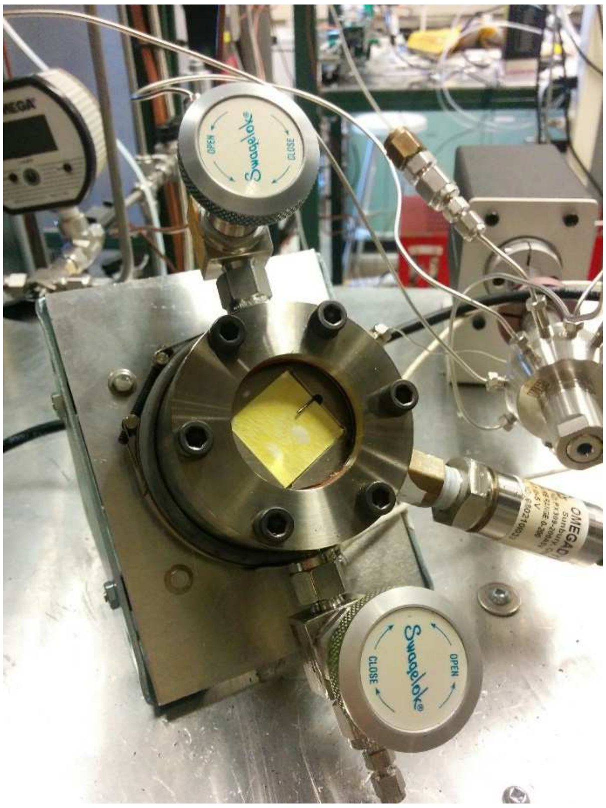

Figure C 10. Reactor for CO_2 reduction. Measurements were performed during research stays of Dr. L. Diehl at Prof. G. A. Ozins lab at the University of Toronto in December 2016 and June 2017. The yellow square is the catalyst loaded silicate filter (in this case melon). The batch reactor is filled with 1 bar H_2 and 1 bar $^{13}CO_2$, monitored by a pressure gauge. During the experiment the reactor's temperature is controlled by a heating element at its back. After the reaction cycle has been completed the headspace is connected to a gas chromatograph with serial mass spectrometer.

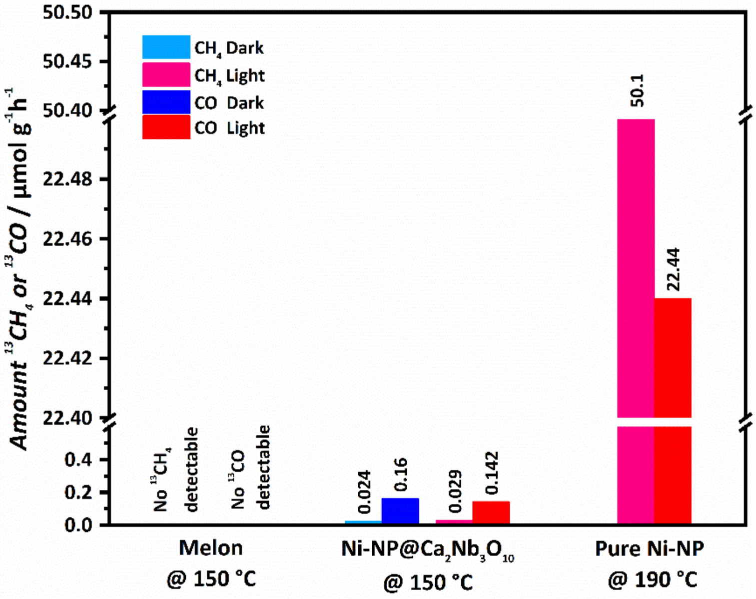

Figure C 11. CO_2 reduction experiments with the archetypical type carbon nitride: melon, which yielded neither $^{13}CH_4$ nor ^{13}CO. Another experiment with Ni-nanoparticles deposited on a calcium niobate support showed only modest activity. A control experiment with purchased nickel nanoparticles showed a relatively high activity but with substantially more $^{13}CH_4$. Note, however, that the nickel as the active catalytic center in Ni-CN_x makes up only 27% of the compound's mass, which should be considered when comparing the activity of Ni-NP. If normalized to the amount of nickel and comparing with the Ni-CN_x measurement at 187 °C, Ni-CN_x even has a superior CO evolution rate.

8.1 References

(1) Niu, W.-J.; He, J.-Z.; Wang, Y.-P.; Sun, Q.-Q.; Liu, W.-W.; Zhang, L.-Y.; Liu, M.-C.; Liu, M.-J.; Chueh, Y.-L. A hybrid transition metal nanocrystal-embedded graphitic carbon nitride nanosheet system as a superior oxygen electrocatalyst for rechargeable Zn–air batteries. *Nanoscale* **2020**, *12* (38), 19644–19654. DOI: 10.1039/D0NR03987J.

(2) Matienzo, J.; Lo Yin, I.; Grim, S. O.; Swartz, W. E. X-ray photoelectron spectroscopy of nickel compounds. *Inorg. Chem.* **1973**, *12* (12), 2762–2769. DOI: 10.1021/ic50130a005.

9 Contributions and publications

In chapter 2, Hendrik Schlomberg developed a new synthetic pathway to yield crystalline K/H-PHI, characterized the material and was substantially involved in the coordination of the project. Julia Kröger performed photocatalytic measurements and was involved in numerous discussions on the manuscript, which led to shared first authorship. Gökcen Savasci performed quantum-chemical calculations for NMR chemical shifts. Igor Moudrakovski and Renée Siegel conducted solid-state NMR experiments and helped with interpretation of these data. Maxwell W. Terban investigated the material's structure by Rietveld refinement and PDF analysis. Sebastian Bette modelled stacking sequences and fitted them to diffraction data. Filip Podjaski tested long-term stability measurements of the photoreduced state and helped with photocatalytic experiments. Viola Duppel performed TEM microscopy on the material and helped with interpretation thereof. H.S. screened literature and wrote the main part of the manuscript including introduction, conclusion, TEM section and NMR section, M.W.T. wrote the PDF and XRPD section, S.B. wrote the stacking sequence section, J.K. wrote the catalysis section. All authors revised the manuscript. The work was supervised by Bettina Lotsch.

In chapter 3, Hendrik Schlomberg conceived and designed this study. H.S. synthesized, characterized the new K-CN-phase and interpreted the data. Maxwell W. Terban performed pair distribution analysis and attempted structure solution on X-ray powder diffraction data. Igor Moudrakovski performed solid-state NMR spectroscopy and helped with interpretation thereof. Viola Duppel collected TEM images/electron diffraction data and helped with discussions. Christian Minke supplied SEM images and EDX spectra Sascha Harm supported the project with many discussions on structural analysis. Hendrik Schlomberg wrote the manuscript. Leo Diehl revised the manuscript. The work was supervised and revised by Bettina Lotsch.

In chapter 4, Hendrik Schlomberg in collaboration with Leo Diehl, conceived and designed this study. H.S. synthesized and structurally characterized the Ni-CN_x species, while Leo Diehl performed photothermal catalysis experiments for CO_2 hydrogenation in the lab of Geoffrey A. Ozin at the University of Toronto. Maxwell W. Terban further investigated the compound by PDF analysis. Viola Duppel performed electron microscopy and electron diffraction on this material and helped with discussions. XPS was performed and analyzed by Kathrin Küster. Stefan Trenker collected CO_2 sorption data. Lars Grunenberg performed LCMS measurements. Jakob Blahusch and Christian Schneider conducted TGA and TG-MS measurements respectively. Igor Moudrakovski performed ssNMR spectroscopy. Christian Minke collected SEM images and EDX spectra. Hendrik Schlomberg wrote the manuscript. Leo Diehl revised the manuscript. The work was supervised and revised by Bettina Lotsch.

Publications

1. Structural Insights into Poly(Heptazine Imides): A Light-Storing Carbon Nitride for Dark Photocatalysis
H. Schlomberg, J. Kröger, G. Savasci, M. W. Terban, S. Bette, I. Moudrakovski, V. Duppel, F. Podjaski, R. Siegel, J. Senker, R. E. Dinnebier, C. Ochsenfeld, B. V. Lotsch
Chem. Mater. **2019**, *31*, 7478–7486; DOI: 10.1021/acs.chemmater.9b02199.

2. **Interfacial Engineering for Improved Photocatalysis in a Charge Storing 2D Carbon Nitride: Melamine Functionalized Poly(heptazine imide)**
J. Kröger, A. Jiménez-Solano, G. Savasci, P. Rovó, I. Moudrakovski, K. Küster, H. Schlomberg, H. A. Vignolo-González, V. Duppel, L. Grunenberg, C. B. Dayan, M. Sitti, F. Podjaski, C. Ochsenfeld, B. V. Lotsch
Adv. Energy Mater. **2021**, *11*, 2003016; DOI: 10.1002/aenm.202003016.

3. Defying Thermodynamics: Stabilization of Alane Within Covalent Triazine Frameworks for Reversible Hydrogen Storage
V. Stavila, S. Li, C. Dun, M. A. T. Marple, H. E. Mason, J. L. Snider, J. E. Reynolds III, F. El Gabaly, J. D. Sugar, C. D. Spataru, X. Zhou, B. Dizdar, E. H. Majzoub, R. Chatterjee, J. Yano, H. Schlomberg, B. V. Lotsch, J. J. Urban, B. C. Wood, M. D. Allendorf
Angew. Chem. **2021**, *60*, 25815; DOI: 10.1002/anie.202107507.

4. Von der Jahrmarktattraktion zur Energiequelle: Kohlenstoffnitride
H. Schlomberg, F. Podjaski, J. Kröger, B. Lotsch
Nachr. Chem. **2018**, *66*, 1157–1161; DOI: 10.1002/nadc.20184065088.

5. Homonuclear Mixed-Valent Cobalt Imidazolate Framework for Oxygen-Evolution Electrocatalysis
E. A. Flügel, V. W-h. Lau, H. Schlomberg, R. Glaum, B. V. Lotsch
Chem. Eur. J. **2016**, *22*, 3676; DOI: 10.1002/chem.201504151.

Other

6. StickLiS – Stickstoffhaltige Kohlenstoffe für hochkapazitive zyklenstabile Lithium-Schwefel-Kathoden
J. Maschita, H. Schlomberg, F. Haase, B. V. Lotsch
Schlussbericht – Technische Informationsbibliothek Hannover, **2019**; 10.2314/KXP:1688798692.

7. Patent application: ELECTROCHEMICAL DEVICE, BATTERIES, METHOD FOR HARVESTING LIGHT AND STORING ELECTRICAL ENERGY, AND DETECTION METHODS
Filip Podjaski, Bettina V. Lotsch, Julia Kröger, Andreas Gouder, Hendrik Schlomberg
International application No.: PCT/EP2019/050448; Filing date: 09.01.2019.